Design Tools for Magnetic Bearings

Ritchie, Ewen; Bjerregaard, Henning; Sloth, Kristian; Thygesen, Rune Ryberg

Publication date:
2014

Document Version
Publisher's PDF, also known as Version of record

DeepWind Deliverable

Grant Agreement number: 256769

Project title: Future Deep Sea Wind Turbine Technologies

Deliverable No.: D3.31

Deliverable title: Design tools for magnetic bearings

Deliverable status: submitted

Name of lead beneficiary: AALBORG UNIVERSITET

Nature of deliverable: Report

Dissemination level: PU

Due date from Annex 1: Month 37

Actual submission date: June 30th 2014

Deliverable status: Submitted

Author: Ewen Ritchie

Quality check approval by: date: June 30 2014

DeepWindWP3 D31 - Technical Report – Bearings and seals for 5MW 10MW and 20MW versions

Contents

Introduction

Bearings have been a source of failure in wind turbine machinery throughout the history of modern wind power generation, [1]. Notoriously, this has been related to gearbox bearings, but it has also been attributed to the general lack of knowledge of the static and dynamic loads applied to the bearings.

The Deep Wind project poses a number of challenges not present in the case of Horizontal Axis Wind Power Generators. It is clear that in the case of the Deep Wind project efforts will be required to predict the loads applied to the bearings and the available dimensions, in order to facilitate bearing design. Prediction of some of these loads is a function of WP3. However prediction of other applied loads is outside the scope of WP3 and will be provided by those WPs concerned with blade and turbine design, the forces applied to the underwater part of the structure, the anchoring system etc.

It will be necessary to know the magnitude and direction of all the forces applied to the bearing in order to consider the design.

Other factors affecting the design of the bearings are related to the ambient conditions, that is the depth, temperature and composition of the sea water, and also the probable growth of life on the structure in the neighbourhood of the bearing.

If the bearing is regarded as the only load transmission component, transmitting load from the

ANSI/AGMA/AWEA 6006-A03
Design and Specification of Gearboxes for Wind Turbines

This standard is intended to apply to wind turbine gearboxes. It provides information for specifying, selecting, designing, manufacturing, procuring operating and manufacturing reliable speed increasing gearboxes for wind turbine generator system service. Annex information is supplied on: wind turbine architecture, wind turbine load description, quality assurance, operation and maintenance, minimum purchaser gearbox manufacturing ordering data, lubrication selection and monitoring, determination of an application factor from a load spectrum using equivalent torque, and bearing stress calculations. Replaces AGMA 921-A97.

rotating part to the stationary part, all forces must be transmitted by the bearing. These forces may be resolved into radial components and thrust components. Additional aspects of the load may be that the load is present, absent or different for various conditions of operation. Care must be taken that the static load conditions applying at start can be met. During acceleration and deceleration the loads may be varying and dynamic. Resonance conditions may arise. At normal duty conditions, the bearing must operate continuously. Finally the bearing must survive overspeed conditions for short periods. For all these situations, the bearing must operate without suffering damage.

The preceding remarks address the specification of the requirements for the bearing. We should now determine what performance is required of the bearing.

It is necessary to consider the physical method of supporting the forces applied and what the consequences of applying this method in the required environment may be.

This report will rely on studying the literature, and relating the characteristics of the various bearing types to the requirements of the specification. It will conclude by making a recommendation and a proposal for bearing design within the limits imposed by current knowledge of the operating conditions. Recommendations will be made for studies thought to be necessary to complete the design.

Task 3.4 A concept for watertight journal and thrust magnetic bearings

The following is the task description as formulated in the DeepWind project work plan.

A concept for watertight journal and thrust magnetic bearings (TL AAU, RIS).

Develop a concept for watertight journal and thrust magnetic bearings, including mechanical design, magnetic functional concept, and cooling. This task will also consider and propose solutions for sealing the generator and power converter against the ingress of salt water. This type of watertight bearing is intended for the 5 MW and 20 MW versions.

Objective

Consider and propose a bearing system for the bearings of the DeepWind wind turbine generator system. This system should be capable of functioning continuously at a depth of 200 m under the surface of the sea.

This will provide a basis for provide a basis for future design work on real machines.

Initial consideration

The DeepWind operating conditions are characterised by the bearing loads, the shaft torque and speed, the ambient conditions and the dynamic loading. The bearings will be required to carry loads while the shaft is stationary, during acceleration and under all operating conditions. The ambient conditions include the water pressure and temperature, the chemical composition of the water and the presence of life in the water.

The load bearing capacity of a bearing is a function of the operating speed, the torque and the forces applied to the shaft. Forces applied to the bearing must be resolved into components along the tube axis and components normal to the tube axis. Components along the axis are known as thrust components and components normal to the axis are known as radial components. A bearing that supports thrust components is called a thrust bearing and one that supports radial components is called a journal bearing. It will be interesting to know the eigenvalues of the tube and the turbine, the expected forcing frequencies arising from the interaction of the wind and the waves, forces arising from the action of the generator, and the response of the bearing to these.

Different types of bearings

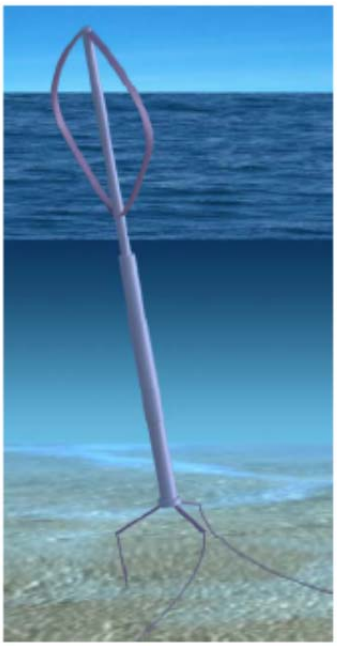

Fig. 1 Artist's impression of DeepWind Turbine neglecting Generator.

Plain bearings

Plain bearings comprise a close-fitting sleeve directly around the shaft. They require some form of lubricant that prevents the two from making direct contact. The lubricant may be pressurised using an external pump and the bearing is referred to as hydrostatic. Alternatively the lubricant may be pressurised by the rotation of the bearing and the bearing is referred to as hydrodynamic. The lubricant may be a liquid or a gas. The liquid here could be water, possibly Sea Water. This is a solution often applied to the journal (radial) bearings of ship's propeller shafts. The thrust (axial) bearing is usually oil lubricated as it is inside the seal system.

Rolling bearings

Rolling bearings have been applied on many wind turbine assemblies. These have been spherical roller bearings, cylindrical roller bearings and tapered roller bearings. Over the years problems have been experienced with reliability of these bearings. The problems have been attributed to misalignment and a general lack of knowledge of the dynamic loading of the bearings. The introduction of ANSI/AGMA/AWEA 6006-A03 was acclaimed as a great step forward in the effort to improve the reliability of wind turbine generators.

Magnetic bearings

Magnetic bearings may be sorted into four main categories:-

- Permanent magnet magnetic bearings
- Resonant magnetic bearings
- Controlled, or active magnetic bearings
- Superconducting magnetic bearings

Permanent magnet magnetic bearings

The current cost spiral of permanent magnets is a serious disadvantage. It may be necessary to apply permanent magnets to excite the generator. Permanent magnets could also be used to generate excitation current to excite magnetic bearings. This may require somewhat less expensive permanent magnet material compared to the PM material required to exciter the generator itself. It will be an advantage to avoid the use of a large quantity of permanent magnet material.

Resonant magnetic bearings

Resonant magnetic bearings are dependent on the resonant frequency matching the dynamic loading. This may be a disadvantage in the wind turbine application, as the speed and load will be changing constantly.

	2 MW	20MW
Power	2 MW	20 MW
Rotor Diameter	67 m	240 m
Reference rotor Height	75 m	240 m
Chord (blades number)	3.2 m (2)	11.0 m(2)
Rotational speed at rated conditions	15.0 rpm	4.1 rpm
Radius of the rotor tower	2.0 m	3.0 m
Maximum radius of the submerged part	3.5 m	6.5m
Total tower length (underwater part)	183 m (93m)	340 (105)
Displacement	3000 tons	13000 tons

Fig. 2 Table showing some predicted key figures for DeepWind. Paulsen [5]

Controlled magnetic bearings

In order to design a magnetic bearing that supports the shaft reliably in the housing, it will be necessary to control the forces generated by the bearing somehow. This is because the relationship between the magnetic force and the distance is in unstable equilibrium.

Superconducting magnetic bearings

Superconducting magnetic bearings have been proposed. These could be using superconducting coils or superconducting blocks. In any case, a weakness of superconducting materials is that they need to be cooled to cryogenic temperatures. The system to achieve this would detract considerably from the reliability, and this is the prime reason for rejecting superconducting magnetic bearings.

Sub-Conclusion and selection of bearing type for further study

Considering the arguments presented above, the controlled magnetic bearings were selected for further study.

Watertight seals

The bearing and generator housing may be sealed at the shaft entry to prevent the ingress of sea water. The seal has not yet been considered in detail, as it depends on the agreed construction of the assembly of the generator to the shaft.

Alternative to watertight seals

As a possible alternative to sealing the shaft, the construction may be open. In this case, two versions may be considered. One possibility is where the sea water fills the generator and one where the generator is filled with an alternative fluid.

Remarks

It would be an advantage if small segments of the bearing could be removed individually for maintenance purposes.

Fig. 3 Diagram showing a simplified version of the DeepWind system.

Design proposal

As mentioned in the previous section, the proposed bearing design under study is the controlled, or active magnetic bearing. This is because it can be controlled to respond well to the changing loading conditions expected in the DeepWind application. Obvious disadvantages are that it will require a control system and power supply, and the windings will need to be insulated and may require maintenance.

Introduction - Consideration of a controlled electromechanical system of a rotor supported on bearings

In order to consider a rotor supported in bearings it is necessary to develop a mathematical model. This will take its origin from the physical system of the rotating mechanical system and the loads applied to it, and the controller and power converter system. The DeepWind problem is especially interesting as it comprises a very long rotor with distributed forces applied to it, and supported at one end only. A simple model of a rigid rotor

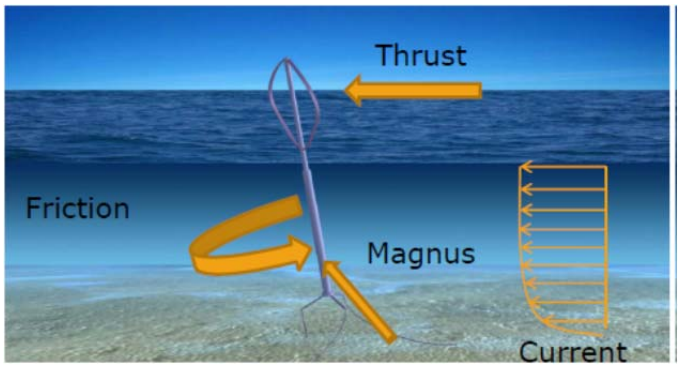

Fig. 5 Estimated application of forces on the tower according to Paulsen, [5].

will be developed, to promote understanding of the problems involved. This could be developed further at a later stage to encompass a model of a flexible rotating system.

System description

The general layout of the system is as shown in [5]. Forces F_A and F_R are a combination of forces from many sources. Here, the thrust due to the wind is predicted, for a 2 MW model, to be approximately 240 kN, and the maximum angle 14.7 degrees from the vertical. Additionally, a controller will be needed, with a power converter for each direction in which forces may be applied by the bearing.

Here a 5MW windmill design is presented with some general data, such as the expected mass, forces acting on the windmill system, and the overall topology. The design presented here is in a process of reiteration; hence changes may be expected to occur when the design of all parts of the windmill system is improved and specified further. The Darrieus windmill is built as a floating spar structure, anchored to the seabed. An outline of the design is shown in Fig. 4. Above water level the structure consists of two blades and one shaft, which is called the turbine rotor. The blades have an aerofoil shape. Initially, this is the NACA0018 standard shape, which is symmetric about the foil chord. The blade contour follows a modified troposkien curve, which is not presented here, thus the circular shape shown in the figures is not an accurate representation. The shaft is hollow all the way through, giving buoyancy to the structure. Below water level the shaft continues and the radius increases. The shaft end continues into the generator housing. The generator housing contains the generator and bearing, and connects the windmill to the seabed via cables. The generator housing design is nearly non-existent at this time, since this design, and the generator housing placement depends highly on the choice of generator and bearing type. The shaft itself may form the outer housing of the generator, with the rotor fitted to the inner surface of the shaft. The stator would then be the inner member of the generator, supported by the bearing and attached to the anchor chains. An alternative construction would be for the generator housing to contain the stator of the generator, and for the shaft to pass into the housing with the rotor fitted to the outer surface of the shaft. Since the windmill floats in the water, anchored by cables, it may be expected to exhibit significant pitch, yaw and roll. This will cause the bearing load to vary with wind speed, wave motion, and rotor orientation relative to the wind direction.

α	L per meter [kN/m]	Aerodynamic Thrust [kN]	Friction Power [kW]	Generated Power [kW]	Friction/Generated power
1.4 (5.5rpm)	9.950	65.81	3.71	0.0	/
2.9 (11rpm)	23.72	186.85	16.69	1050	0.012(1.2%)
3.9 (15rpm)	**25.15**	**239.65**	43.20	1960	**0.022(2.2%)**

Fig. 4 Table of forces applied to Deep Wind Tower and Floater [5] Forces have been revised since the time of publishing.

Model of the Deep Wind, wind turbine

To make a model that may be used to dimension the bearing system, initially the rotor is modelled as a rigid body with loads applied at well-defined points. Later the model may be developed to represent a flexible rotor with distributed loads. An additional assumption is that a two dimensional model is considered. Loads applied to the journal bearings arise from the action of the wind against the turbine blades and the rest of the structure above the water line. Below the water line, forces arise because of the rotation of the shaft in the water and the updrift, because of buoyancy. During operation the wind turbine will heel over because of these forces, making it necessary to resolve all forces perpendicular to and along the shaft. All these forces are applied to the bearings and the reaction to them is applied by the mooring system, see Fig. 1. For modelling purposes, these forces were represented in a free body diagram as shown in Fig. 6. The model is a mathematical representation of the free body diagram shown in **Error! Reference source not found.**

Rigid rotor

Consider a rigid rotor of mass$M$. The rotor is defined in a system of axes $0\xi\eta\zeta$ such that one axis 0ζ is the axis of rotation.

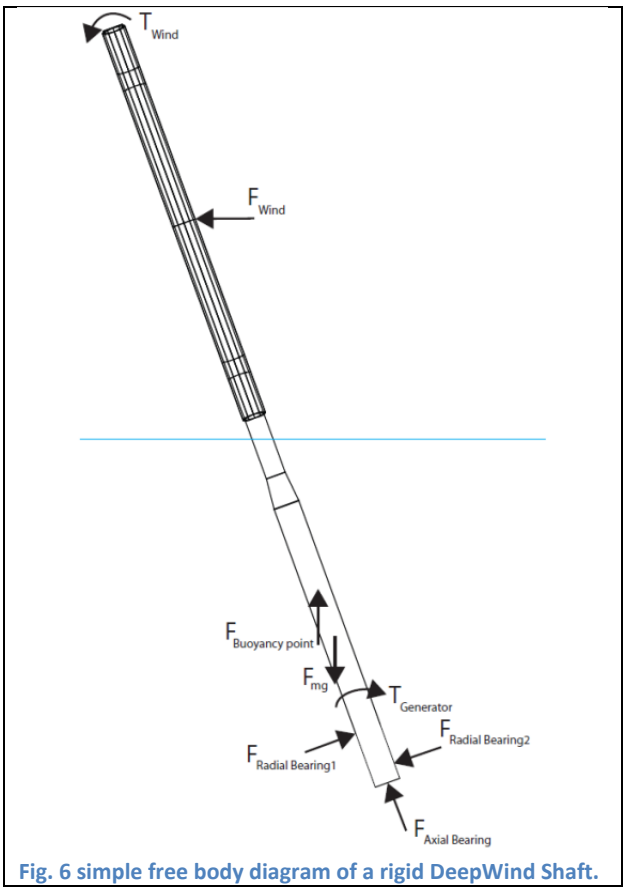

Fig. 6 simple free body diagram of a rigid DeepWind Shaft.

Fig. 7 Forces applied to the DeepWind wind turbine system.

Bearing Loads

A first approximation of the bearing load may be obtained from a free body model. Forces arising will act in various directions, see Fig. 6. To analyse the bearing loads they must be resolved into forces acting along the axis of rotation of the bearing, and forces acting in two directions normal to this.

Thrust from the wind on the turbine is assumed to act at the centre of the turbine and horizontally. The axis of rotation is assumed to incline at angle γ to the vertical. This angle will vary due to the wind and current. Thrust will be applied under water due to the Magnus effect and currents, and will also be assumed to act at a point on the underwater part of the tube.

The buoyancy is expected to be in equilibrium with the weight of the structure. However, some restraining force will be applied by the anchorage system. Harmonic variations of the forces due to the action of wave motion may be expected.

Definition of the Forces acting on the system

The forces acting on the simplified system are depicted in Fig. 6. The tower is assumed to be a rigid beam. Each Force is assumed to act at a point. The generator is assumed to be a rigid body. For the wind turbine system to remain in a given position under steady state operation all forces must be balanced, both horizontally and vertically. As the purpose here is to build a model to enable estimation of the loads acting on the bearing, all forces will be resolved into components acting axially along the tower, and components acting radially to the axis of the tower.

A consequence of assuming the tower to be a rigid body is that forces are assumed to act at known points on the tower, unaffected by bending of the tower. The tower is inclined at angle γ to the vertical. The force arising from the wind blowing on the turbine is assumed to contain horizontal and vertical components. The force is assumed to act at two points, namely the top and bottom fixing points of the turbine blades. The division of the wind force between these two points is assumed to be independent of the angle of inclination.

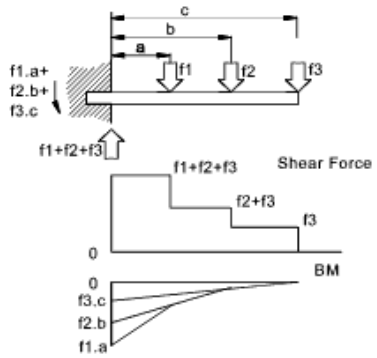

Fig. 8 General diagram of a cantilever loaded by several forces acting at several points. [6]

General for a cantilever

The DeepWind tower is here considered as a two-dimensional cantilever beam anchored at the main bearing of the generator. A general diagram of the loading of a cantilever beam is shown in [6]. When considering the bearing loading, the main journal bearing will be loaded by the sum of the normal components of the applied forces.

The radial side-load on the main bearing of the generator is given by the sum of the forces acting normally to the axis of the tower. The axial thrust load is given by the sum of the components of the forces acting along the axis of the tower.

The generator will be provided with two bearings. The main bearing of the generator is expected to be the upper bearing of the two as it is situated very close to the point of attachment of the mooring system. This bearing will take the radial load and the axial thrust load imposed by the turbine. The non-drive end or lower journal bearing of the generator is expected to be loaded by forces dependent on the distance between the two bearings because of the relatively large moment component of the forces.

For DeepWind

In the case of the 5 MW simulations of the DeepWind Generator the load at the upper bearing is predicted by other work packages. This is summarised as given in Appendix 1 and Appendix 2 of this report.

Mathematical Model of the Mechanical System

The model of the mechanical system for use with estimating the bearing loads was derived using the Lagrange formulation of the generalised equations of motion.

$$\overrightarrow{Q_j} = \frac{d}{dt}\left(\frac{\partial T}{\partial \dot{q}_j}\right) - \left(\frac{\partial T}{\partial q_j}\right) \quad , \quad \mathbf{L} = T\text{-}V$$

Where $\mathbf{L}$ is the Lagrangian, T is the kinetic energy, and V is the potential energy. The rigid shaft is considered to be a free body with five degrees of freedom. These are three rotational degrees of freedom and two translational. It is assumed that the shaft cannot move in the axial direction.

When expressions for the kinetic energy and potential energy are developed, the system Lagrangian becomes:

$$\mathbf{L} = T_{trans} + T_{rot}\text{-}V$$
$$= \frac{1}{2}\cdot m\cdot(\dot{x}^2+\dot{y}^2) + \frac{1}{2}\cdot I_{xx}\cdot\left(\dot{\theta_y}^{\,2}+\dot{\theta_x}^{\,2}\right) + \frac{1}{2}\cdot I_{zz}\cdot\left(\omega^2 - 2\cdot\omega\cdot\dot{\theta_y}\cdot\dot{\theta_x}\right)$$

and taking the time derivatives of the Lagrangian:

$$\frac{\partial \mathbf{L}}{\partial \dot{\vec{q}}} = \begin{bmatrix} m\cdot\dot{x} \\ m\cdot\dot{y} \\ I_{xx}\cdot\dot{\theta}_x \\ I_{xx}\cdot\dot{\theta}_y - I_{zz}\cdot\omega\cdot\theta_x \end{bmatrix}$$

$$\frac{\partial \mathbf{L}}{\partial \vec{q}} = \begin{bmatrix} 0 \\ 0 \\ -I_{zz}\cdot\omega\cdot\dot{\theta}_y \\ 0 \end{bmatrix}$$

Finally, the Lagrangian becomes:

$$\frac{d}{dt}\left(\frac{\partial \mathbf{L}}{\partial \dot{\vec{q}}}\right) - \frac{\partial \mathbf{L}}{\partial \vec{q}} = \begin{bmatrix} m & 0 & 0 & 0 \\ 0 & m & 0 & 0 \\ 0 & 0 & I_{xx} & 0 \\ 0 & 0 & 0 & I_{xx} \end{bmatrix}\cdot\ddot{\vec{q}} + \begin{bmatrix} 0 & 0 & 0 & 0 \\ 0 & 0 & 0 & 0 \\ 0 & 0 & 0 & -I_{zz}\cdot\omega \\ 0 & 0 & -I_{zz}\cdot\omega & 0 \end{bmatrix}\cdot\dot{\vec{q}}$$

Or

$$\vec{Q} = M\cdot\ddot{\vec{q}} + G\cdot\dot{\vec{q}}$$

Where the matrix M is the mass matrix and the matrix G is the gyroscopic matrix.

This model is described in detail in [7].

Magnetic circuit

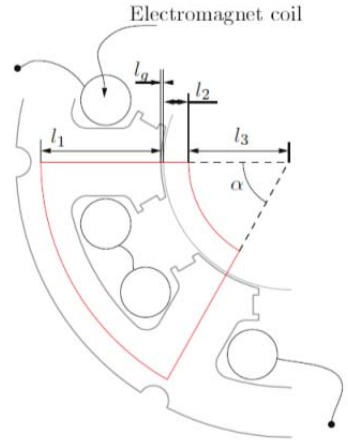

Fig. 9 Mean flux path of one electromagnet of the laboratory model controlled magnetic bearing

Principle of Bearing Magnetic circuit

The main idea of the proposed bearing design is to have wound magnetic salient poles on the stator, an air-gap and a smooth, round, soft magnetic rotor. Excitation of the magnetic field would be by current flow in the pole windings. The return path for the magnetic field would be in the back-iron of the stator and the rotor. The magnetic circuit of a single electromagnet is shown in Fig. 9. A whole bearing of the laboratory model comprises three such electro-magnets around the circumference.

The bearing for the full size 5 MW system will have many such electromagnets, arranged to support the shaft in three, four or five directions. A system providing journal bearing support in

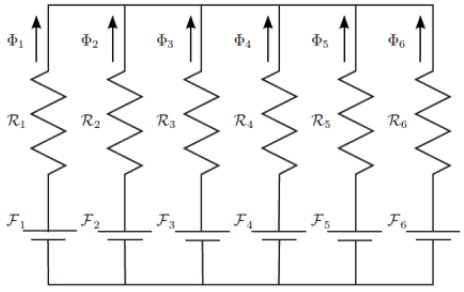

Fig. 10 Magnetic equivalent circuit of a journal bearing

three directions is proposed and considered here.
By injecting current into the winding of this electromagnet, the shaft will be attracted towards the centre of the electromagnet. By exerting such a controlled attraction in a combination of three directions around the shaft, forces may be applied to the shaft in any direction. The shaft will be held in the middle, the rotation axis. The number of functional directions will be a matter for optimisation on the full size version. An electromagnet will be required for each direction in which it is required to apply attractive force.
The equations used to solve the magnetic equivalent circuit are an adaptation of Kirchhoff's laws for electric circuits, using Ampere's circuital law. Provision is made in the model to allow for displacement of the centre of the shaft as it is a necessary function of the bearing that the shaft be displaced as a function of the bearing load. The magnetic circuit is related to an electric circuit, as the magnetic field is induced by current flowing in the coils. Ultimately, the electric circuit model is given by the voltage equation:

$$\vec{u} = R_{ohm} \cdot \vec{\imath} + \mathrm{L}(\vec{\mathrm{q}}) \cdot \frac{\mathrm{d}\vec{\imath}}{\mathrm{dt}} + \sum_{k=1}^{2} \left(\frac{\partial L(\vec{q})}{\partial q_k} \cdot \frac{dq_k}{dt} \right) \cdot \vec{\imath}$$

And the force is related to the change of energy stored in the air gap:

$$W = \frac{1}{2} \cdot i^{-T} \cdot L(\vec{q}) \cdot \vec{\imath}$$

$$Q_n = \frac{\partial W}{\partial q_n}; n = 1{,}2$$

Sensors

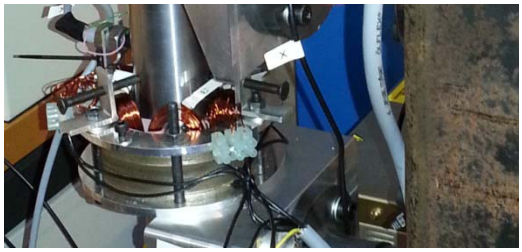

Fig. 11 Laboratory model controlled magnetic bearing

For the bearing controller, sensors are required to measure the actual position of the shaft relative to the bearing. They should be sufficiently sensitive, i.e. provide a large signal for the allowed shift in shaft position relative to the bearing. The frequency response of the combined measurement system should be adequate to enable control of the shaft position within the required limits at all times and under all dynamic conditions. A sensor is required for each direction in which the attractive force will be applied.

Controller

The controller compares the signal from the position sensor with the required reference position signal, and adjusts the output power demand signal accordingly. The output power demand signal is applied to the power supply system and in this way the current in the electromagnet, and hence the force applied by the electromagnet is controlled. Again, the sensitivity and the frequency response must be adequate. A controller is required for each direction in which the attractive force will be applied.

Power supply

The power supply amplifies the output signal of the controller. It may be assumed that the amplifier will use Pulse Width Modulation as the basic power control strategy. Again, the sensitivity and the frequency response must be adequate. A power supply is required for each direction in which the attractive force will be applied.

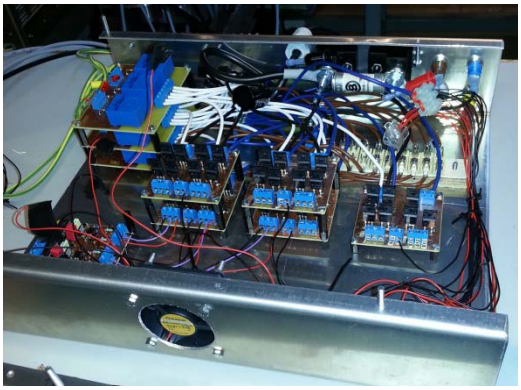

Fig. 12 Controlled Power Supply for three axes on the bearing and three axes on each of two load actuators..

Test Bench

A test bench was made in the laboratory comprising a test magnetic bearing and two load applying bearings. The purpose was to verify the mathematical model of the bearing.

System description

The test rig was built with a single magnetic bearing and two load actuators on the same shaft. Each actuator is able to apply force in three directions, under control. The whole system comprises nine control systems. The mechanical rig is sketched in Fig. 14, and a photo of the magnetic bearing is shown in **Error! Reference source not found.**. The assembly of nine control systems is shown in **Error! Reference source not found.**, and the nine power supplies are shown in Fig. 12

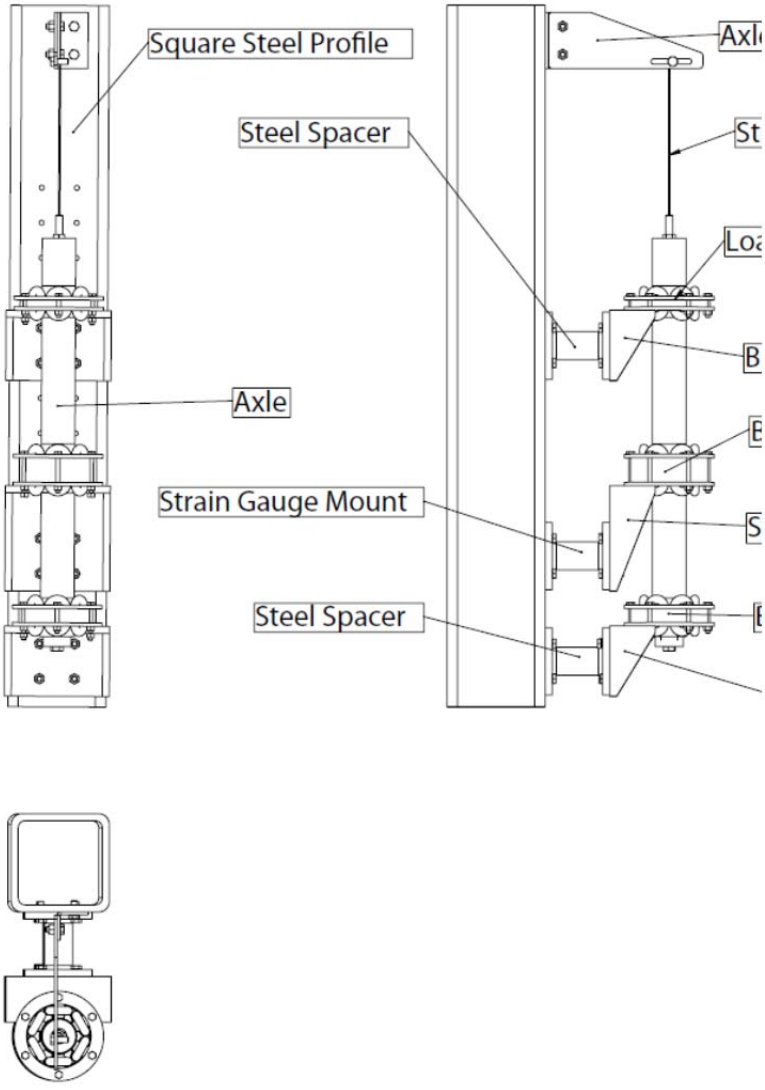

Fig. 13 Laboratory arrangement of journal bearings.

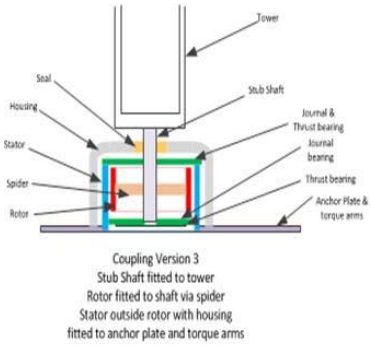

Fig. 15 Showing bearing and generator mounting selected by RIS for further work.

DeepWind Bearing and Seal Design 5MW

The DeepWind bearing design is based on the construction shown diagrammatically in Fig. 15. A stub shaft is fitted to the bottom of the floater (referred to as 'tower' in the sketch). This shaft transmits the driving torque to the generator and the supporting forces from the mooring

system to the floater. In this report only the forces will be considered. Two journal bearings are proposed, one each at the top and the bottom of the generator. Two thrust bearings are also required to support axial loads along the floater and shaft.

Shaft diameter for the 5 MW version

The floater enters the bearing and generator assembly at the top and follows on down through the assembly as the shaft. The rotor of the generator is attached to the shaft, and the journal bearings run freely on the shaft, holding it in position relative to the generator stator. The thrust bearings provide reaction to the forces acting along the direction of the shaft axis. It is general practice for electrical machines that the air-gap between the rotor and the stator is not allowed to vary by more than 10% of its nominal size, 6 [mm], i.e. ±0.6 [mm]. Several shaft diameters have been considered, ranging from 5.884 [m], where the generator rotor would be a snug fit on the shaft, to 1.5 [m], corresponding to the largest diameter that Wärtsila could offer. The Wärtsila bearing is a plain bearing lubricated by pressurised sea water. An early version is shown in the sketch attached to Troels Friis Pedersen's e-mail of 2013-09-24, and selecting the 3 [m] reduced floater diameter as shaft diameter, the shaft diameter used for bearing design was [3] m, see*: Appendix 3 Sketch by Troels Friis Pedersen, from e-mail 2013-09-24*.

Input Design forces, speed

The values given are extracted from an e-mail written by Helge Aagaard Madsen dated 2014-02-18.

Helge Aagaard Madsen dated 2014-02-18 (copied from HAMA e-mail)

We have run simulations with an updated rotor model with a sectionized tower design with decreased tower weight.

However, the major difference is that we now extract the shaft forces at the entrance to the generator in a stationary frame of reference – y is in the streamwise direction and x is perpendicular to the free stream.

The data are shown in the figures and in the tables.

The fy is mainly dominated by the thrust of the rotor (at 10m/s we estimate by hand 600kN)so it seems reasonable.

The fx is mainly due to the Magnus force and the strong increase from 14 to 16m/s is simply due to change in water current.
So it is seen that the Magnus force contributes quite much to the bearing forces.

As concerns the fz it can very much be regulated by the mass and the buoyancy of the generator house.

Finally it can also be noted that the dynamic content is small compared with the mean value.
The opposite was seen for the forces in the rotating frame of reference.

Table 1 Forces from Helge Aagaard Madsen e-mail 2014-02-19

m/s	Fx [kN]	std.dev [kN]	Fy [kN]	std.dev [kN]	Fz [kN]	std.dev [kN]
6	763.67	275.3	171.22	209.79	-1050.93	108.71
8	909.81	173.93	327.06	138.4	-1097.75	75.13
10	951.38	97.57	374.83	110.97	-1119.04	57.46
14	979.82	138.59	325.82	143.6	-1140.79	70.87
16	1901.93	154.49	466	162.46	-1548.26	86.24
18	1912.07	173.96	460	168.66	-1550.37	86.46
22	1906.05	244.24	454.28	199.63	-1545.72	103.03

Table 2 Moments from Helge Aagaard Madsen e-mail 2014-02-19

m/s	Mx [kNm]	std.dev [kNm]	My [kNm]	std.dev [kNm]	Mz [kNm]	std.dev [kNm]
6	2687.43	2572.37	-9122.16	2900.34	1769.27	729.06
8	5436.98	1461.51	-10754.27	1737.29	2912.98	1099.39
10	6844.9	669.38	-11120.87	868.22	4241.15	1234.23
14	7440.08	859.55	-11188.7	1137.15	6856.53	1200.02
16	9272.13	1031.45	-21876.28	1417.1	7461.68	1357.98
18	9469.9	998.22	-21995.65	1394.65	7927.12	1587.66
22	9939.78	1285.41	-22034.5	1897.21	8603.22	2309.34

External Forces Applied at the generator

Interpretation of Table 1 and Table 2 for calculation of the bearing: (bearing design run numbers 39 & 40

%% Applied Forces at the generator
%2nd iteration design – for load purposes, all forces and moments are interpreted as positive
Fz_mean_WindTurbine=1545.72e3;%Newton Fig. from Helge e-mail dated 2014-01-14

%Forces at the generator
%% New Values from Helge Aagaard Madsen dated 2014-02-19
Fx_mean=1906.05e3; %Newton
Fx_sigma=244.24e3e3; %Newton
Fy_mean=454.28e3; %Newton

Fy_sigma=199.63e3; %Newton
Fz_mean=Fz_mean_WindTurbine+AxialLoadDueToRotorWeight; %Newton
Fz_sigma=103.03e3; %Newton

%Moments applied at the generator
Mx_mean=9939.78e3; %Newton meter
Mx_sigma=1285.41e3; %Newton meter
My_mean=22034.5e3; %Newton meter
My_sigma=1897.21e3; %Newton meter
Mz_mean=8603.22e3; %Newton meter
Mz_sigma=2309.34e3; %Newton meter

%Internal magnetic forces in the generator due to unbalanced magnetic pull
Fgen=362e3; %Newton

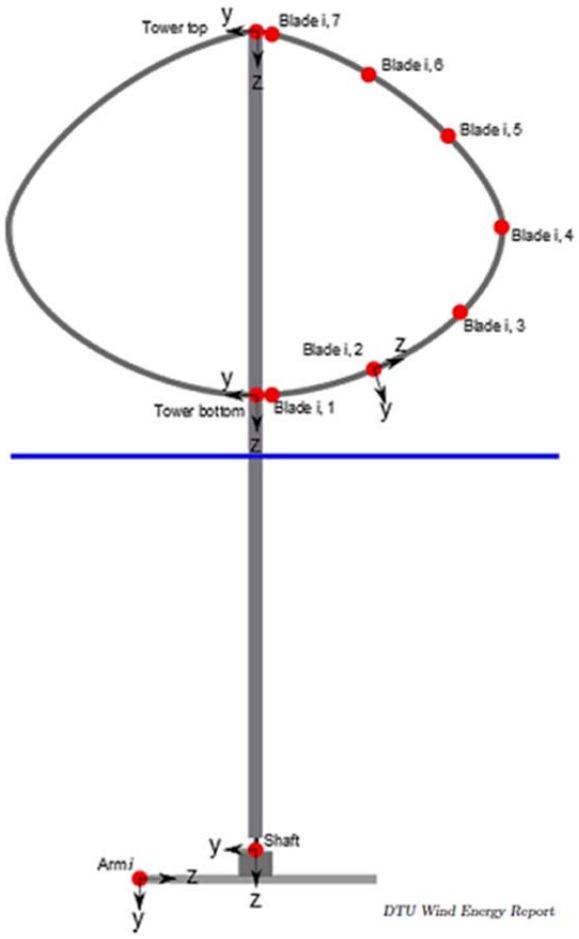

Fig. 16 Showing positions for the calculation of forces, Error! Reference source not found.**. The bearing described here is located at the point marked 'shaft'.**

Further interpretation for bearing calculations:

----------Design Load Forces Radial Bearing----------
Bearing 1 F radial mean 4364.16 [kN]
Bearing 2 F radial mean 2404.72 [kN]
Bearing 1 F radial max 5289.26 [kN]
Bearing 2 F radial max 2747.16 [kN]

Internal forces arising in the generator

Internal forces arise in the generator because of imperfect centring of the rotor in the stator bore. This is known as Unbalanced Magnetic Pull (UMP). This force may become very large if the rotor is eccentric in the stator bore. Eccentricities may arise from manufacturing imperfections, or from static or dynamic loading of the shaft and bearings. This arises independent of the type of bearing used. As we are proposing a controlled magnetic bearing, it is possible to specify the eccentricity of the shaft at the bearing. Other factors affecting the UMP are the flux density in the air-gap of the generator and the surface area of the stator bore. Here, a simple equation was used to estimate the UMP, using the air-gap flux density at No-Load condition, as this is the conservative choice; the air-gap flux density from the permanent magnets is greatest under this condition. For the calculations, the eccentricity was specified as 10% of the air-gap length, which is the maximum allowed.

$$F_{UMP} = \epsilon \cdot \frac{B_{gap}^2}{2 \cdot \mu_0} \cdot \pi \cdot D_{gap} \cdot \frac{L_{EFF}}{2}$$

Shaft speed and peripheral speed

The shaft speed is the same as that used for the generator design, 5.73 [rpm]. This is not given in the aeroelastic report 'report_2nd_iteration_loads_17052013.pdf', but was obtained from Uwe e-mail 2013-09-24.

Bearing design

The bearings were designed using the principles studied and laid down in [7], using a specially written, in house, design program 'DWControlledMagBrg' to synthesise the dimensions required. The control system algorithm for journal bearings is designed and was built and tested in the laboratory. The final version of the control system must be tuned to suit the DeepWind 5 MW mechanical arrangement and operating conditions. It remains to dimension the power controllers and the control system. The mean power required for the journal bearings and for the thrust bearings is dependent on the actual bearing design and may be a total of about 100 [kW]. This is a rather large power, some 2% of the 5 [MW] rated output power. However, this is offset by the fact that magnetic bearings dissipate no friction loss. Further studies of the dynamic behaviour may enable the mean required power to be reduced, by reducing the air-gap. This will also reduce the performance requirements of the power controllers.
See Appendix 4 for the detailed results.

Bearing Control System

The control system for the 5MW bearings will comprise 8 controllers. 3 controllers for each journal bearing and one for each thrust bearing. Each controller will comprise a position sensor, a regulator and a power controller.

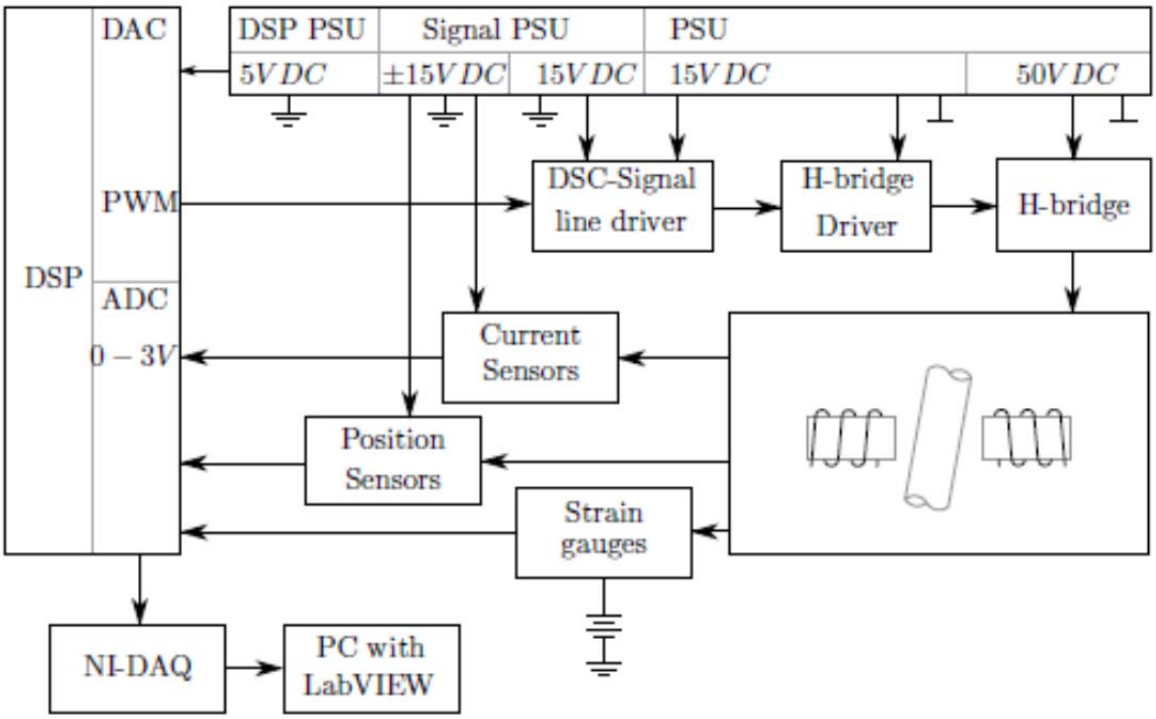

Fig. 17The electrical system for actuators, sensors, and data logging on the magnetic bearing arrangement. Left: DSC with ADC and DAC. Top: Power supplies with two common points. Lower right: Active Magnetic Bearings.

As the time constants of the mechanical system are very long compared with the speed of the DSP, one DSP will suffice for all 8 regulators. The power controllers will be H-bridge DC controllers, as an Active Magnetic Bearing of this type is not sensitive to the direction of the current in its windings. Each power controller for the journal bearings and the thrust bearings will be rated for the estimated average power, continuous, It will be necessary to provide the mean power of to excite all of the DeepWind 5MW bearings, with a peak power that will be required only rarely.

Summary of Results

Results are summarised here for bearings with various different shaft diameters ranging from 1.5 [m] to 5.8 [m], and with various lengths between bearing centres.

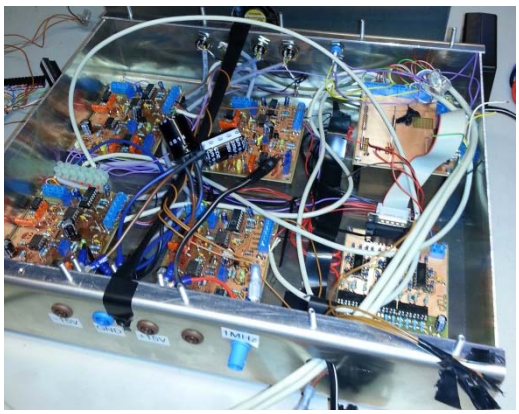

Fig. 18 photo of laboratory measurement system and control system for three axes of three bearings.

A long length between bearing centres along the shaft gives added leverage against the moments and requires smaller bearings. Disadvantages include that the length of the floater is increased and the stability of the mooring may be adversely affected.

A larger shaft diameter reduces the size of spider needed to attach the generator rotor to the shaft, and also reduces the length of each individual journal bearing. Disadvantages include increased power required to energise the bearings, and increased diameter of axial bearings.

All things considered, the overall picture is unclear. The final decision must be made as a result of simultaneous

engineering and optimisation of the total material cost. The material cost should weighted by the diameters required as precision manufacturing at large diameters increases both the labour cost and the cost of investment in machine tools.

	Case A0 **Shaft diameter equal to the inner diameter of the generator rotor** **Length between centres of Radial bearings 7.14 [m]**	**Case A1** **Shaft diameter equal to the inner diameter of the generator rotor** **Length between centres of Radial bearings 24.1 [m]**	**Case A3** **Shaft diameter equal to the inner diameter of the generator rotor** **Length between centres of Radial bearings 8.1 [m]** **Corrected version of case A0 to be physically possible**	**Case B0** **Shaft diameter equal 1.5 [m]** **Length between centres of Radial bearings 7.14 [m]**	**Case B1** **Shaft diameter equal 1.5 [m]** **Length between centres of Radial bearings 19.14 [m]**	**Case C0** **Shaft diameter equal 3.0 [m]** **Length between centres of Radial bearings 15 [m]**
	Bearing output files #39 & 40 Note that in this case, **no** additional spider will be necessary to connect the generator rotor to the shaft	Bearing output files #44 & 45 Note that in this case, **no** additional spider will be necessary to connect the generator rotor to the shaft	Bearing output files #58 & 59 Note that in this case, **no** additional spider will be necessary to connect the generator rotor to the shaft	Bearing output files #41 & 42 Note that in this case, **an additional spider will be necessary** to connect the generator rotor to the shaft	Bearing output files #43 & 44 Note that in this case, **an additional spider will be necessary** to connect the generator rotor to the shaft	Bearing output files #43 & 44 Note that in this case, **an additional spider will be necessary** to connect the generator rotor to the shaft
Dimensions of upper radial bearing (1 required)						
Shaft Diam	5.8840 [m]	5.8840 [m]	5.8840 [m]	1.5000 [m]	1.5000 [m]	3.0 [m]
Outer Diam	6.1164 [m]	6.1164 [m]	6.1164 [m]	1.7508 [m]	1.7508 [m]	3.251 {m]
Bore Diam	5.8900 [m]	5.8900 [m]	5.8900 [m]	1.5060 [m]	1.5060 [m]	3.006 [m]
Air Gap	0.0030 [m]	0.0030 [m]	0.0030 [m]	0.0030 [m]	0.0030 [m]	0.0030 [m]
Core Length	3.9911 [m]	1.8561 [m]	3.6327 [m]	15.6095 [m]	8.1756 [m]	4.708 [m]
Overall Length	4.2765 [m]	2.1414 [m]	3.9180 [m]	15.9015 [m]	8.4676 [m]	5.001 [m]
Number of Slots	102	102	102	24	24	48
Number of coils	51	51	51	12	12	24
Number of Poles	102	102	102	24	24	48
Number of sectors	3	3	3	3	3	3
Max Power	187 [kW]	101.4 [kW]	172.4 [kW]	154.8 [kW]	84.3 [kW]	101.7 [kW]
----------Material weights----------						
Weight of 1 bearing core	61.9229 [ton]	28.7977 [ton]	56.3609 [ton]	71.4924 [ton]	37.4450 [ton]	41.313 [ton]

Weight of Copper in winding	1.5534 [ton]	0.8439 [ton]	1.4343 [ton]	1.2645 [ton]	0.6885 [ton]	0.848 [ton]
Weight of 1 bearing TOTAL	63.4763 [ton]	29.6416 [ton]	57.7952 [ton]	72.7570 [ton]	38.1334 [ton]	42.161 [ton]
Dimensions of lower radial bearing (1 required)						
Shaft Diam	5.8840 [m]	5.8840 [m]	5.8840 [m]	1.5000 [m]	1.5000 [m]	3.0 [m]
Outer Diam	6.1164 [m]	6.1164 [m]	6.1164 [m]	1.7508 [m]	1.7508 [m]	3.251 {m]
Bore Diam	5.8900 [m]	5.8900 [m]	5.8900 [m]	1.5060 [m]	1.5060 [m]	3.006 [m]
Air Gap	0.0030 [m]	0.0030 [m]	0.0030 [m]	0.0030 [m]	0.0030 [m]	0.0030 [m]
Core Length	2.0729 [m]	0.0621 [m]	1.7144 [m]	8.1073 [m]	0.6735 [m]	0.95 [m]
Overall Length	2.3583 [m]	0.3474 [m]	1.9998 [m]	8.3993 [m]	0.9655 [m]	1.242 [m]
Number of Slots	102	102	102	24	24	48
Number of coils	51	51	51	12	12	24
Number of Poles	102	102	102	24	24	48
Number of sectors	3	3	3	3	3	3
Max Power	110 [kW]	29.8 [kW]	95.8 [kW]	83.6 [kW]	16.3 [kW]	41.1 [kW]
----------Material weights----------						
Weight of 1 bearing core	32.1618 [ton]	0.9635 [ton]	26.5997 [ton]	37.1320 [ton]	3.0846 [ton]	8.3321 [ton]
Weight of Copper in winding	0.9160 [ton]	0.2478 [ton]	0.7968 [ton]	0.6832 [ton]	0.1071 [ton]	0.2596 [ton]
Weight of 1 bearing TOTAL	33.0777 [ton]	1.2112 [ton]	27.3966 [ton]	37.8152 [ton]	3.1916 [ton]	8.5917 [ton]
Dimensions of each axial bearing (2 required)						
Shaft Diam	5.8840 [m]	5.8840 [m]	5.8840 [m]	1.5000 [m]	1.5000 [m]	3.000 [m]
Axial Brg. Outer Diam	6.2644 [m]	6.2644 [m]	6.2644 [m]	2.6836 [m]	2.6836 [m]	3.7071 [m]
Bore Diam	5.8900 [m]	5.8900 [m]	5.8900 [m]	1.5060 [m]	1.5060 [m]	3.0060 [m]
Air Gap	0.0030 [m]	0.0030 [m]	0.0030 [m]	0.0030 [m]	0.0030 [m]	0.0030 [m]
Overall Diam	6.5047 [m]	6.5047 [m]	6.5047 [m]	2.9279 [m]	2.9279 [m]	3.9512 [m]
Axial Brg. Total length	0.3205 [m]	0.3205 [m]	0.3205 [m]	0.3480 [m]	0.3480 [m]	0.3473 [m]
Number of Slots	102	102	102	24	24	48
Number of coils	51	51	51	12	12	24
Number of Poles	102	102	102	24	24	48
Number of sectors	1	1	1	1	1	1
Max Power (per bearing)	37.6 [kW]	37.6 [kW]	37.6 [kW]	13.9 [kW]	13.9 [kW]	22.3 [kW]
----------Material weights----------						
Weight of 1 axial bearing core	8.5978 [ton]	8.5978 [ton]	8.5978 [ton]	10.4868 [ton]	10.4868 [ton]	9.8535 [ton]

Weight of Copper in axial bearing winding	0.3139 [ton]	0.3139 [ton]	0.3139 [ton]	0.1142 [ton]	0.1142 [ton]	0.1819 [ton]
Weight of 1 axial thrust plate	8.5978 [ton]	8.5978 [ton]	8.5978 [ton]	10.4868 [ton]	10.4868 [ton]	9.8535 [ton]
Weight of 1 axial bearing	17.5095 [ton]	17.5095 [ton]	17.5095 [ton]	21.0879 [ton]	21.0879 [ton]	19.8890 [ton]
----------Total Bearing weights and costs (including controllers)----------						
Total Bearing Weight	131.6 [ton]	65.9 [ton]	120.201 [ton]	152.8 [ton]	83.5 [ton]	90.531 [ton]
Total power capacity	372.2 [kW]	206.4 [kW]	343.4 [kW]	266.2 [kW]	128.4 [kW]	187.4 [kW]
Total material cost, bearings		€ 179,050.00	€ 363,957,42		€ 189,945.00	€ 240,780.00

Conclusion

This report gives a discussion of the bearing system for the Deep Wind project. The loads on the bearing will be a combination of the static loads applied by the wind and the buoyancy, etc., and the dynamic loads applied by the motion of the system. A mathematical model of the mechanical system, based on the Lagrangian energy formulation is proposed and described in this report. The actual mechanical model described here is a model of the laboratory test rig built to test the bearings and verify the model. The electromagnetic system generating the bearing forces is also modelled. A linearised analytic model based on magnetic equivalent circuits of the bearing is described here relating the dimensions and materials to the forces available in the bearing. In the case of the 5 MW DeepWind construction, the aeroelastic team at Risø were responsible for calculating the external forces applied to the bearings.

The detailed reporting of the bearing modelling, verification of the model and design strategy may be found in [7].

Further Studies Required

When the mechanical and electromagnetic models of the bearing have been verified using the laboratory test rig, they will need to be modified to include all degrees of freedom anticipated for the Deep Wind system. Then the models will be used to design and predict the performance of the 5 MW and 20 MW journal bearing and thrust bearing versions. A thrust bearing will be required to support the axial loads applied to the anchoring system.

Additional consideration is required for the sealing of the generator shaft. This will be dependent on the final design of the assembly.

Additional work id required to define the abnormal load situations and specify the input and performance in these cases.

References

[1] D. Robb, "*The role of bearings in gearbox failure*," Windpower Monthly, pp, 53-55, 57-58, Nov. 2005.

[2] ANSI/AGMA/AWEA 6006-A03, *Design and Specification of Gearboxes for Wind Turbines,*

[3] Yuri N. Zhuravlyov, "*Active Magnetic Bearings"*; Helsinki University of Technology, 1992

[4] Akira Chiba, Tadashi Fukao, Osamu Ichikawa *Magnetic Bearings And Bearingless Drives*

[5] Uwe Schmidt Paulsen, '*DeepWind – Tomorrow's Concept for Large Offshore Wind Power*', North America Offshore Wind Conference, Washington D.C., USA, April 2011.

[6] Roy Beardmore*, Shear Force and Bending Moment Diagrams, www.roymech.co.uk, 2012-02-15.*

[7] Design of Active Electromagnetic Bearing for Darrieus Type Wind Turbines, Henning Bjerregaard, Kristian Sloth, Rune Ryberg Thygesen, MSc thesis, Aalborg University, June 2013 (will be made available to the partners at the Deep Wind teamsite when complete and approved.

[8] DeepWind 2nd Iteration

[9] DeepWind-Mooring

Appendices

Appendix 1 5MW Radial bearing design data

An example of the output of the design program 'DWControlledMagBrg' is included as Appendix 1 for the journal (radial) bearing and Appendix 2 for the thrust (axial) bearing.

DeepWind Radial Bearing Design Version Number 8
DeepWindRadialBearingversion_8.txt

Dept. of Energy Technology, AAU
Krisztina Leban Ewen Ritchie

24-Sep-2013

----------Input Dimensions----------
Shaft Diam 3.00 [m] Length between bearings 14.69 [m]
Length of air gap 0.01 [m]

----------Input Bearing Forces Radial Bearing----------
Fx mean -144.01 [kN] Std. dev. 89.99 [kN]
Fy mean -228.59 [kN] Std. dev. 49.95 [kN]
Fz mean -1500.00 [kN] Std. dev. 10.70 [kN]

----------Input Bearing Moments at generator----------
Mx mean -1601.27 [kNm] Std. dev. 97.04 [kNm]
My mean 1014.55 [kNm] Std. dev. 246.53 [kNm]

----------Design Load Forces Radial Bearing----------
Bearing 1 F radial mean 264.17 [kN] Bearing 2 F radial mean 6.00 [kN]
Bearing 1 F radial max 859.07 [kN] Bearing 2 F radial max 262.71 [kN]

----------Design Rules for Radial Bearing----------
Factor of Safety 2 Max induction in gap 1.07 [T]
Max current density in winding 8.00 [A/mm^2]
Max force density in air gap 455.54 [kN/m^2]
Tooth width/Tooth pitch 0.75
Tooth width required 0.14
Slot height/slot width 1.00
Max Bearing slot fill 0.50
Creepage 97.50 [mm]
----------Materials----------
Soft Magnetic Material: dk66
Shaft Material: Free Cutting Iron
Winding Material: Copper
----------Dimensions----------
Shaft Diam 3.0000 [m] Outer Diam 3.4127 [m]
Bore Diam 3.0200 [m] Air Gap 0.0100 [m]
Core Length 1.6007 [m] Overall Length 1.8939 [m]

Number of Slots 48 [m] Number of coils 24 [m]
Number of Poles 48 [m] Number of sectors 3 [m]
----------Winding----------
Cold Resistance per sector 13.82 [Ohm] Inductance per sector 21.60 [H]
Max Current 56.4266 [A] Max Voltage 0.7801 [kV]
Max Power 132.0 [kW]
Mean Current 17.3414 [A] Mean Voltage 0.2397 [kV]
Mean Power 12.5 [kW]
----------Material weights----------
Weight of 1 bearing core 23.6376 [ton]
Weight of Copper in winding 1.0785 [ton]

Appendix 2 5MW Axial Bearing Design Data

DeepWind Axial Bearing Design Version Number 8
DeepWindAxialBearingversion_8.txt

Dept. of Energy Technology, AAU
Krisztina Leban Ewen Ritchie

24-Sep-2013

----------Input Dimensions----------
Shaft Diam 3.00 [m] Length of air gap 0.01 [m]

----------Input Bearing Forces Axial Bearing----------
Fx mean -144.01 [kN] Std. dev. 89.99 [kN]
Fy mean -228.59 [kN] Std. dev. 49.95 [kN]
Fz mean -1500.00 [kN] Std. dev. 10.70 [kN]

----------Input Bearing Moments at generator----------
F axial mean -1.50 [MN] Std. dev. 10.70 [kN]
F axial max -3.06 [MN]
----------Design Rules----------
Factor of Safety 2 Max induction in gap 1.07 [T]
Max current density in winding 8.00 [A/mm^2]
Max force density in air gap 572.96 [kN/m^2]
Tooth width/Tooth pitch at bore 0.75
Tooth width required at bore 0.14
Slot height/slot width 1.00
Max Bearing slot fill 0.50
Creepage 97.50 [mm]
-------Axial Bearing Materials----------
Soft Magnetic Material: dk66
Thrust plate Material: Free Cutting Iron
Winding Material: Copper
--------Axial Bearing Dimensions----------
Shaft Diam 3.0000 [m] Axial Brg. Outer Diam 3.1569 [m]
Bore Diam 3.0200 [m] Air Gap 0.0100 [m]
Overall Diam 3.4014 [m] Axial Brg. Total length 0.3559 [m]
Number of Slots 48 [m] Number of coils 24 [m]
Number of Poles 48 [m] Number of sectors 1 [m]
----------Winding----------
Cold Resistance 13.42 [Ohm] Inductance per sector 0.38 [H]
Max Current 62.4149 [A] Max Voltage 0.8377 [kV]
Max Power 52.3 [kW]
Mean Current 30.5537 [A] Mean Voltage 0.4101 [kV]
Mean Power 37.6 [kW]
----------Material weights----------
Weight of 1 axial bearing core 1.5887 [ton]
Weight of Copper in axial bearing winding 0.4285 [ton]

Appendix 3 Sketch by Troels Friis Pedersen, from e-mail 2013-09-24

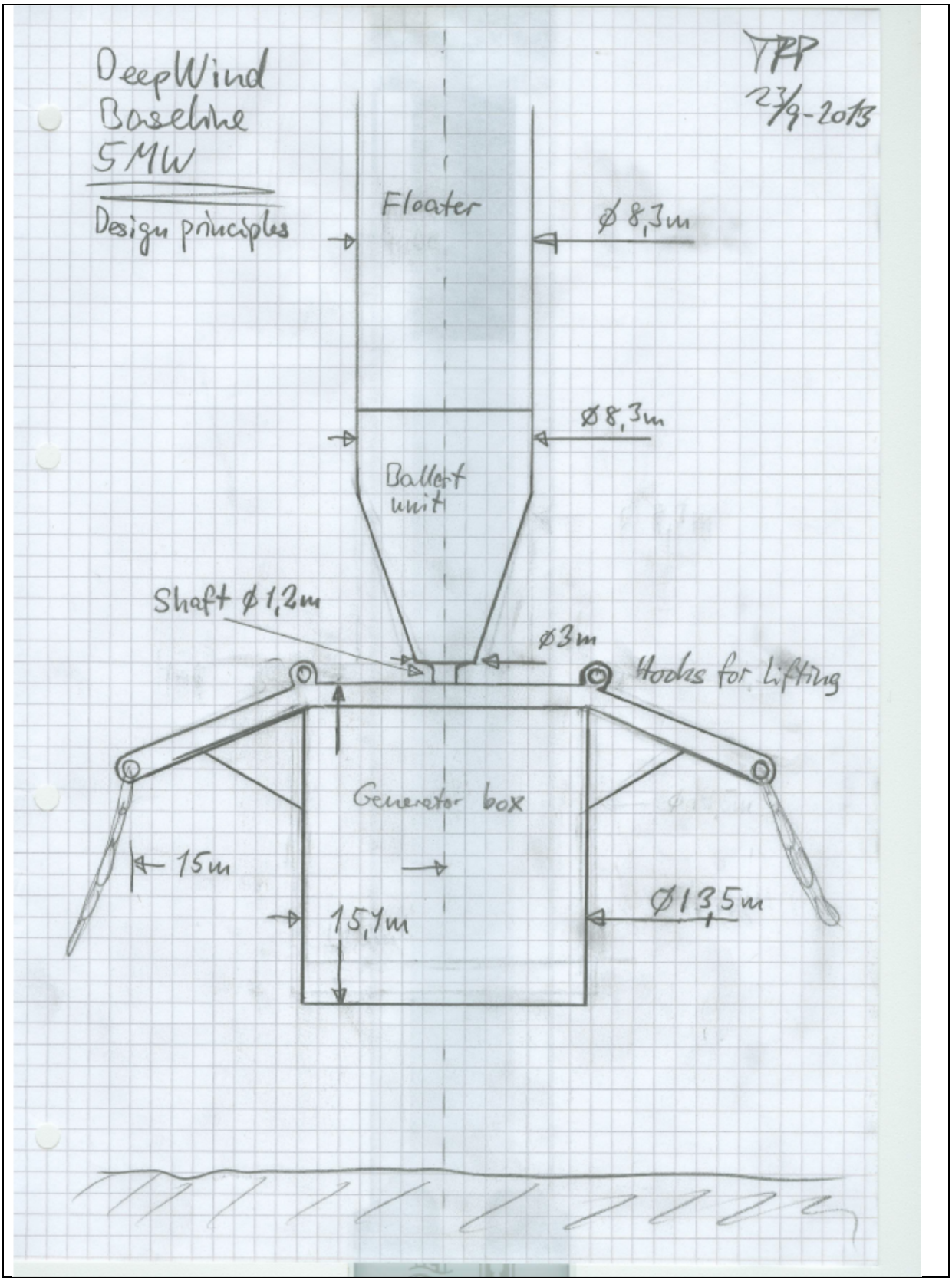

Appendix 4 Results of calculations for various designs

Case A Shaft diameter equal to the inner diameter of the generator rotor

Bearing output files #39 & 40

Note that in this case, no additional spider will be necessary to connect the generator rotor to the shaft

Length between centres of Radial bearings 7.14 [m]

Dimensions of upper radial bearing

----------Dimensions----------

Shaft Diam 5.8840 [m]	Outer Diam 6.1164 [m]
Bore Diam 5.8900 [m]	Air Gap 0.0030 [m]
Core Length 3.9911 [m]	Overall Length 4.2765 [m]
Number of Slots 102	Number of coils 51
Number of Poles 102	Number of sectors 3

Max Power 187 [kW]

----------Material weights----------

Weight of 1 bearing core 61.9229 [ton]

Weight of Copper in winding 1.5534 [ton]

Weight of 1 bearing TOTAL 63.4763 [ton]

Dimensions of lower radial bearing

----------Dimensions----------

Shaft Diam 5.8840 [m]	Outer Diam 6.1164 [m]
Bore Diam 5.8900 [m]	Air Gap 0.0030 [m]
Core Length 2.0729 [m]	Overall Length 2.3583 [m]
Number of Slots 102	Number of coils 51
Number of Poles 102	Number of sectors 3

Max Power 110 [kW]

----------Material weights----------

Weight of 1 bearing core 32.1618 [ton]

Weight of Copper in winding 0.9160 [ton]

Weight of 1 bearing TOTAL 33.0777 [ton]

Dimensions of each axial bearing (2 required)

--------Axial Bearing Dimensions----------

Shaft Diam 5.8840 [m]	Axial Brg. Outer Diam 6.2644 [m]
Bore Diam 5.8900 [m]	Air Gap 0.0030 [m]
Overall Diam 6.5047 [m]	Axial Brg. Total length 0.3205 [m]
Number of Slots 102	Number of coils 51
Number of Poles 102	Number of sectors 1

Max Power 37.6 [kW] (per bearing)

----------Material weights----------
Weight of 1 axial bearing core 8.5978 [ton]
Weight of Copper in axial bearing winding 0.3139 [ton]
Weight of 1 axial thrust plate 8.5978 [ton]
Weight of 1 axial bearing TOTAL 17.5095 [ton]

Case B0 Shaft diameter equal 1.5 [m] Length between centres of Radial bearings 7.14 [m]

Bearing output files #43 & 44
Note that in this case, an additional spider will be necessary to connect the generator rotor to the shaft

Dimensions of upper radial bearing

----------Dimensions----------

Shaft Diam 1.5000 [m]	Outer Diam 1.7508 [m]
Bore Diam 1.5060 [m]	Air Gap 0.0030 [m]
Core Length 15.6095 [m]	Overall Length 15.9015 [m]
Number of Slots 24	Number of coils 12
Number of Poles 24	Number of sectors 3

Max Power 154.8 [kW]
----------Material weights----------
Weight of 1 bearing core 71.4924 [ton]
Weight of Copper in winding 1.2645 [ton]
Weight of 1 bearing TOTAL 72.7570 [ton]

Dimensions of lower radial bearing

----------Dimensions----------

Shaft Diam 1.5000 [m]	Outer Diam 1.7508 [m]
Bore Diam 1.5060 [m]	Air Gap 0.0030 [m]
Core Length 8.1073 [m]	Overall Length 8.3993 [m]
Number of Slots 24	Number of coils 12
Number of Poles 24	Number of sectors 3

Max Power 83.6 [kW]

----------Material weights----------
Weight of 1 bearing core 37.1320 [ton]
Weight of Copper in winding 0.6832 [ton]
Weight of 1 bearing TOTAL 37.8152 [ton]

Dimensions of each axial bearing (2 required)

--------Axial Bearing Dimensions----------

Shaft Diam 1.5000 [m]	Axial Brg. Outer Diam 2.6836 [m]
Bore Diam 1.5060 [m]	Air Gap 0.0030 [m]
Overall Diam 2.9279 [m]	Axial Brg. Total length 0.3480 [m]
Number of Slots 24	Number of coils 12
Number of Poles 24	Number of sectors 1

Max Power 13.9 [kW]

----------Material weights----------
Weight of 1 axial bearing core 10.4868 [ton]
Weight of Copper in axial bearing winding 0.1142 [ton]
Weight of 1 axial thrust plate 10.4868 [ton]
Weight of 1 axial bearing TOTAL 21.0879 [ton]

Case B1 Shaft diameter equal 1.5 [m] Length between centres of Radial bearings 19.14 [m]

Bearing output files #43 & 44
Note that in this case, an additional spider will be necessary to connect the generator rotor to the shaft
Length between centres of Radial bearings 19.14 [m]

Dimensions of upper radial bearing

----------Dimensions----------

Shaft Diam 1.5000 [m]	Outer Diam 1.7508 [m]
Bore Diam 1.5060 [m]	Air Gap 0.0030 [m]
Core Length 8.1756 [m]	Overall Length 8.4676 [m]
Number of Slots 24	Number of coils 12
Number of Poles 24	Number of sectors 3

Max Power 84.3 [kW]

----------Material weights----------
Weight of 1 bearing core 37.4450 [ton]
Weight of Copper in winding 0.6885 [ton]
Weight of 1 bearing TOTAL 38.1334 [ton]

Dimensions of lower radial bearing

----------Dimensions----------

Shaft Diam 1.5000 [m]	Outer Diam 1.7508 [m]
Bore Diam 1.5060 [m]	Air Gap 0.0030 [m]
Core Length 0.6735 [m]	Overall Length 0.9655 [m]
Number of Slots 24	Number of coils 12
Number of Poles 24	Number of sectors 3

Max Power 16.3 [kW]

----------Material weights----------
Weight of 1 bearing core 3.0846 [ton]
Weight of Copper in winding 0.1071 [ton]
Weight of 1 bearing TOTAL 3.1916 [ton]

Dimensions of each axial bearing (2 required)

--------Axial Bearing Dimensions----------

Shaft Diam 1.5000 [m]	Axial Brg. Outer Diam 2.6836 [m]
Bore Diam 1.5060 [m]	Air Gap 0.0030 [m]

Overall Diam 2.9279 [m]	Axial Brg. Total length 0.3480 [m]
Number of Slots 24	Number of coils 12
Number of Poles 24	Number of sectors 1

Max Power 13.9 [kW]

----------Material weights----------
Weight of 1 axial bearing core 10.4868 [ton]
Weight of Copper in axial bearing winding 0.1142 [ton]
Weight of 1 axial thrust plate 10.4868 [ton]
Weight of 1 axial bearing TOTAL 21.0879 [ton]

Case C0 Shaft diameter equal 3.0 [m] Length between centres of Radial bearings 15 [m]

DeepWind Radial Bearing Design Version Number 60 CASE C0 – Upper Radial Bearing
DeepWindRadialBearingversion_60.txt

Dept. of Energy Technology, AAU
Krisztina Leban Ewen Ritchie

24-Mar-2014

----------Input Dimensions----------
Shaft Diam 3.000 [m] Length between bearings 15.000 [m]
Length of air gap 0.0030 [m]

----------Input Bearing Forces Radial Bearing----------
Fx mean 1906.05 [kN] Std. dev. 244.24 [kN]
Fy mean 454.28 [kN] Std. dev. 199.63 [kN]
Fz mean 1761.12 [kN] Std. dev. 103.03 [kN]

----------Input Bearing Moments at generator----------
Mx mean 9939.78 [kNm] Std. dev. 1285.41 [kNm]
My mean 22034.50 [kNm] Std. dev. 1897.21 [kNm]

----------Design Load Forces Radial Bearing----------
Bearing 1 F radial mean 2591.23 [kN] Bearing 2 F radial mean 631.79 [kN]
Bearing 1 F radial max 3184.34 [kN] Bearing 2 F radial max 642.23 [kN]

----------Design Rules for Radial Bearing----------
Factor of Safety 1 Max induction in gap 1.20 [T]
Max current density in winding 8.00 [A/mm^2]
Max force density in air gap 572.96 [kN/m^2]
Tooth width/Tooth pitch 0.75
Tooth width required 0.14
Slot height/slot width 1.00
Max Bearing slot fill 0.65
Creepage 97.50 [mm]
----------Materials----------
Soft Magnetic Material: dk66
Shaft Material: Free Cutting Iron
Winding Material: Copper
----------Dimensions----------
Shaft Diam 3.0000 [m] Outer Diam 3.2511 [m]
Bore Diam 3.0060 [m] Air Gap 0.0030 [m]
Core Length 4.7081 [m] Overall Length 5.0007 [m]

Number of Slots 48 Number of coils 24
Number of Poles 48 Number of sectors 3
----------Winding----------
Cold Resistance per sector 154.51 [Ohm] Inductance per sector 349.39 [H]
Max Current 14.8124 [A] Max Voltage 2.2887 [kV]
Max Power 101.7 [kW]
Mean Current 13.3501 [A] Mean Voltage 2.0628 [kV]
Mean Power 82.6 [kW]
----------Material weights----------
Weight of 1 bearing core 41.3126 [ton]
Weight of Copper in winding 0.8482 [ton]
Weight of 1 bearing TOTAL 42.1608 [ton]
----------Material costs----------
Cost of 1 bearing core 123937.9136 €
Cost of Copper in winding 12722.7307 €
Cost of 1, 3 direction controller 6102.2627 €
Cost of 1 radial bearing TOTAL 142762.9069 €

DeepWind Radial Bearing Design Version Number 61 CASE C0 – Lower Radial Bearing
DeepWindRadialBearingversion_61.txt

Dept. of Energy Technology, AAU
Krisztina Leban Ewen Ritchie

24-Mar-2014

----------Input Dimensions----------
Shaft Diam 3.000 [m] Length between bearings 15.000 [m]
Length of air gap 0.0030 [m]

----------Input Bearing Forces Radial Bearing----------
Fx mean 1906.05 [kN] Std. dev. 244.24 [kN]
Fy mean 454.28 [kN] Std. dev. 199.63 [kN]
Fz mean 1761.12 [kN] Std. dev. 103.03 [kN]

----------Input Bearing Moments at generator----------
Mx mean 9939.78 [kNm] Std. dev. 1285.41 [kNm]
My mean 22034.50 [kNm] Std. dev. 1897.21 [kNm]

----------Design Load Forces Radial Bearing----------
Bearing 1 F radial mean 631.79 [kN] Bearing 2 F radial mean 631.79 [kN]
Bearing 1 F radial max 642.23 [kN] Bearing 2 F radial max 642.23 [kN]

----------Design Rules for Radial Bearing----------
Factor of Safety 1 Max induction in gap 1.20 [T]
Max current density in winding 8.00 [A/mm^2]
Max force density in air gap 572.96 [kN/m^2]
Tooth width/Tooth pitch 0.75
Tooth width required 0.14
Slot height/slot width 1.00
Max Bearing slot fill 0.65
Creepage 97.50 [mm]
----------Materials----------
Soft Magnetic Material: dk66
Shaft Material: Free Cutting Iron
Winding Material: Copper
----------Dimensions----------
Shaft Diam 3.0000 [m] Outer Diam 3.2511 [m]
Bore Diam 3.0060 [m] Air Gap 0.0030 [m]
Core Length 0.9496 [m] Overall Length 1.2421 [m]

Number of Slots 48 Number of coils 24
Number of Poles 48 Number of sectors 3
----------Winding----------
Cold Resistance per sector 47.29 [Ohm] Inductance per sector 70.47 [H]
Max Current 14.8124 [A] Max Voltage 0.7005 [kV]
Max Power 31.1 [kW]
Mean Current 14.6902 [A] Mean Voltage 0.6947 [kV]
Mean Power 30.6 [kW]
----------Material weights----------
Weight of 1 bearing core 8.3321 [ton]
Weight of Copper in winding 0.2596 [ton]
Weight of 1 bearing TOTAL 8.5917 [ton]
----------Material costs----------
Cost of 1 bearing core 24996.3580 €
Cost of Copper in winding 3893.8513 €
Cost of 1, 3 direction controller 1867.6261 €
Cost of 1 radial bearing TOTAL 30757.8353 €

DeepWind Axial Bearing Design Version Number 60 CASE C0 – Axial Bearing (2 required)
DeepWindAxialBearingversion_60.txt

Dept. of Energy Technology, AAU
Krisztina Leban Ewen Ritchie

24-Mar-2014

----------Input Dimensions----------
Shaft Diam 3.00 [m] Length of air gap 0.00 [m]

----------Input Bearing Forces Axial Bearing----------
Fx mean 1906.05 [kN] Std. dev. 244.24 [kN]
Fy mean 454.28 [kN] Std. dev. 199.63 [kN]
Fz mean 1761.12 [kN] Std. dev. 103.03 [kN]

----------Input Bearing axial forces at generator----------
F axial mean 1.76 [MN] Std. dev. 103.03 [kN]
F axial max 1.97 [MN]
----------Design Rules----------
Factor of Safety 1 Max induction in gap 1.20 [T]
Max current density in winding 8.00 [A/mm^2]
Max force density in air gap 572.96 [kN/m^2]
Tooth width/Tooth pitch at bore 0.75
Tooth width required at bore 0.14
Slot height/slot width 1.00
Max Bearing slot fill 0.65
Creepage 97.50 [mm]
-------Axial Bearing Materials----------
Soft Magnetic Material: dk66
Thrust plate Material: Free Cutting Iron
Winding Material: Copper
--------Axial Bearing Dimensions----------
Shaft Diam 3.0000 [m] Axial Brg. Outer Diam 3.7071 [m]
Bore Diam 3.0060 [m] Air Gap 0.0030 [m]
Overall Diam 3.9512 [m] Axial Brg. Total length 0.3473 [m]
Number of Slots 48 Number of coils 24
Number of Poles 48 Number of sectors 1
----------Winding----------
Cold Resistance 105.45 [Ohm] Inductance per sector 8.87 [H]
Max Current 14.5429 [A] Max Voltage 1.5336 [kV]
Max Power 22.3 [kW]
Mean Current 13.7601 [A] Mean Voltage 1.4510 [kV]
Mean Power 20.0 [kW]
----------Material weights----------
Weight of 1 axial bearing core 9.8535 [ton]
Weight of Copper in axial bearing winding 0.1819 [ton]
Weight of 1 axial thrust plate 9.8535 [ton]
Weight of 1 axial bearing TOTAL 19.8890 [ton]
----------Material costs----------
Cost of 2 axial bearing core 59121.0935 €
Cost of Copper in 2 windings 5457.8850 €
Cost of 2, 1 direction controllers 2676.2723 €
Cost of 2 axial bearings TOTAL 67255.2509 €

Appendix 5 – Sketches of Case A3 and Case C0

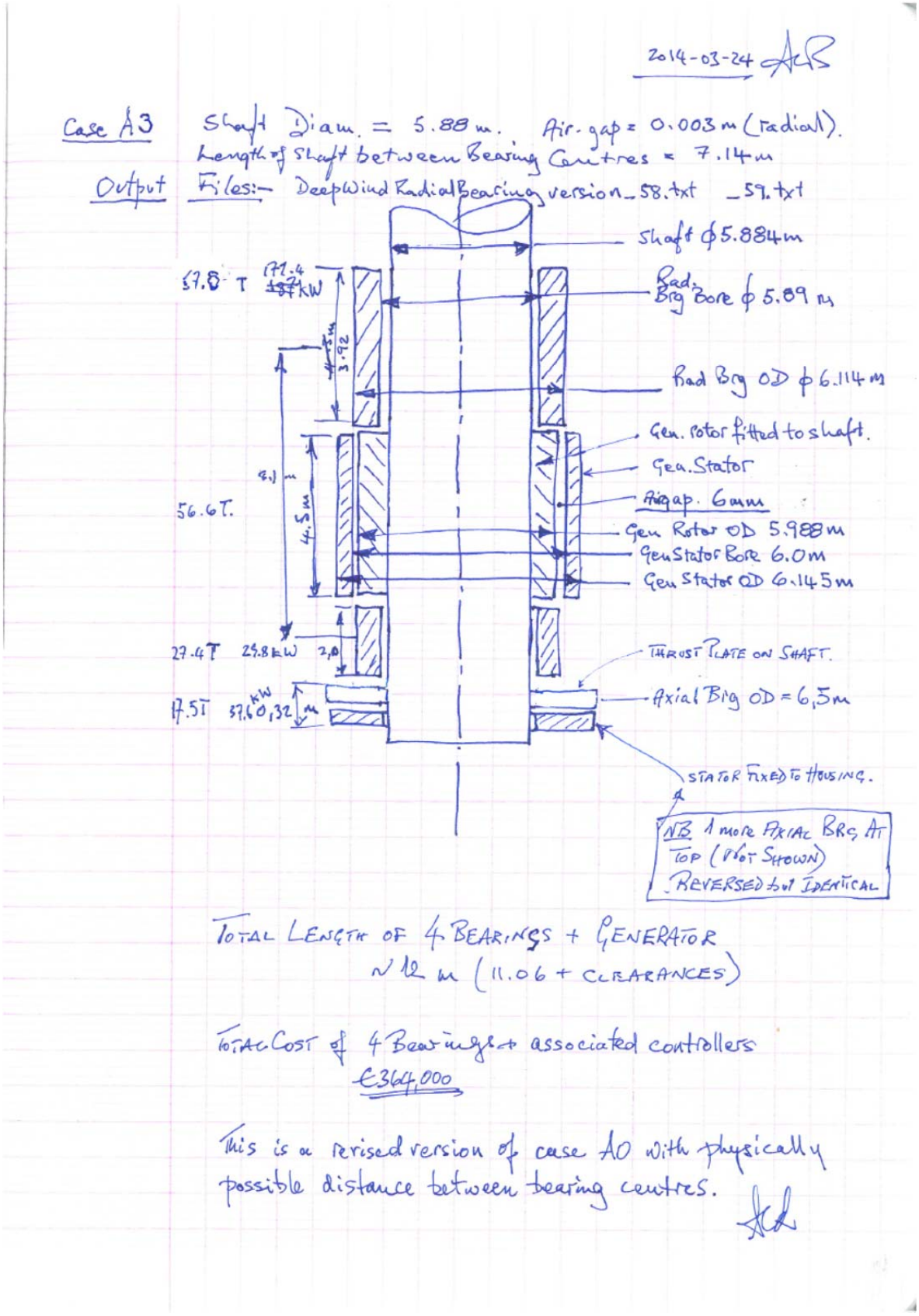

Fig. 19 Freehand sketch of Case A3.

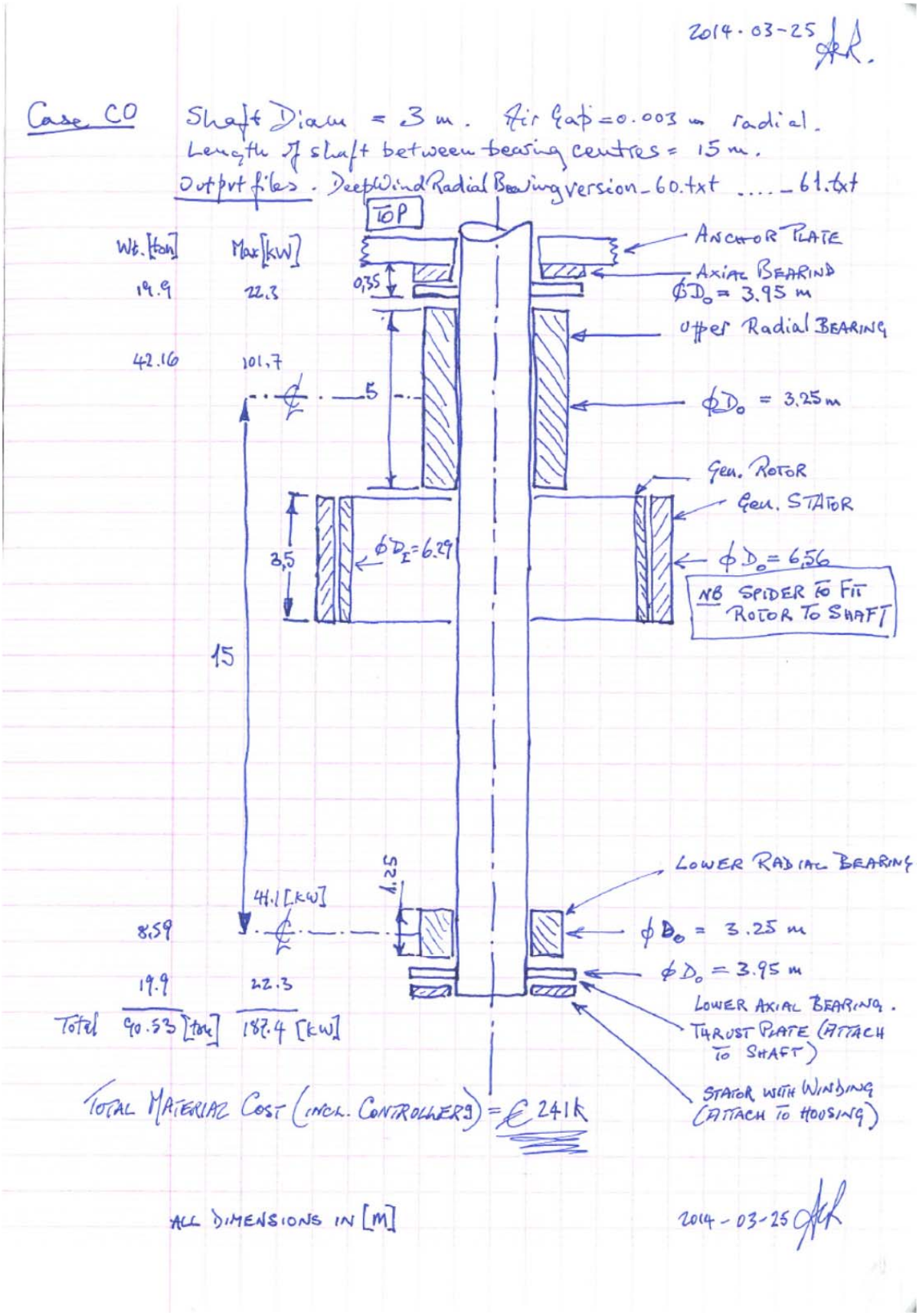

Fig. 20 Freehand sketch of Case C0.

Appendix 6 – reference [7]

Design of Active Electromagnetic Bearing for Darrieus Type Wind Turbines, Henning Bjerregaard, Kristian Sloth, Rune Ryberg Thygesen, MSc thesis, Aalborg University, June 2013 (made available to the partners at the Deep Wind teamsite; complete and approved.

EMSD3-44

Analysis of Active Electromagnetic Bearing for Darrieus Type Wind Turbines

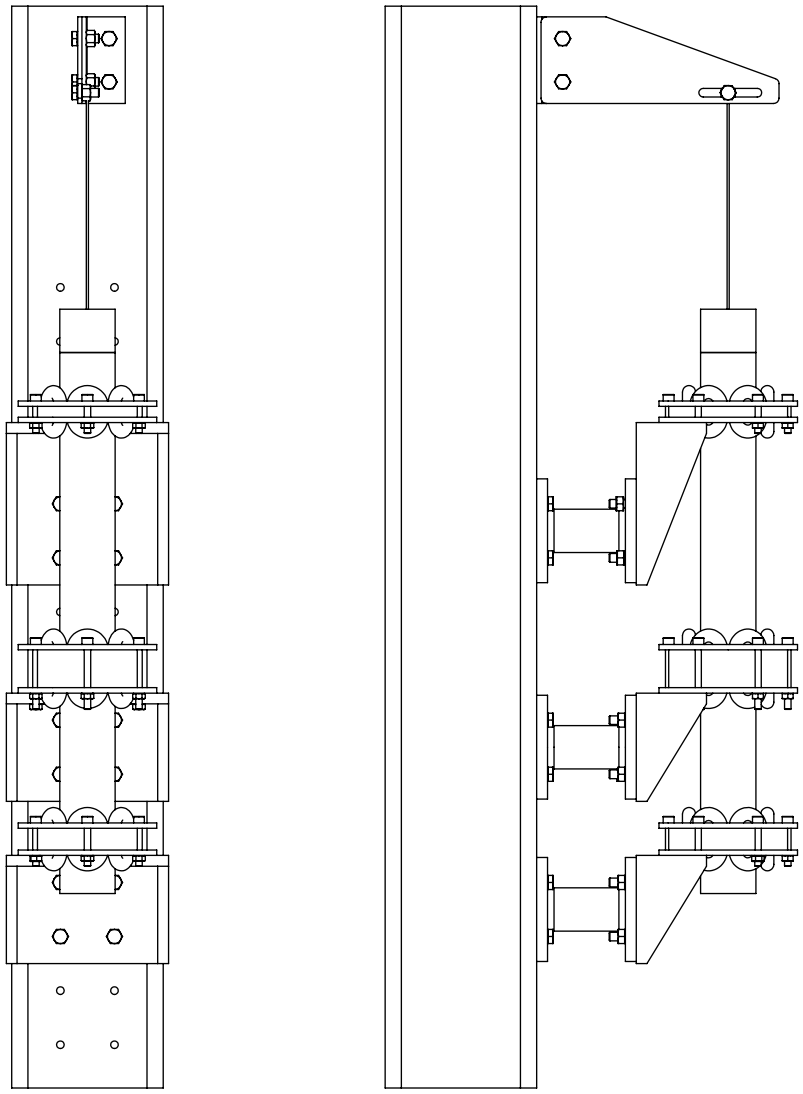

AALBORG UNIVERSITY

Master thesis

9th and 10th semester

September 1st 2012 - June 4th 2013

Title: Analysis of Active Electromagnetic Bearing for Darrieus Type Wind Turbines
Semester: 9th and 10th semester
Theme: Master Thesis
Project period: September 1st 2012 to June 4th 2013
ECTS: 55 point
Supervisor: Ewen Ritchie and Krisztina Monika Leban
Project group: EMSD3-44

Group members:

Henning Bjerregaard

Kristian Sloth

Rune Ryberg Thygesen

Number of copies: 5
Number of pages: 134
Appendix: A - I

Synopsis:

In this Master thesis an active magnetic bearing is modeled, and verified on an experimental setup. The results and tools will be used, by the DeepWind research group, to determine the applicability and feasibility for the use in offshore vertical axis wind turbines. If deemed applicable the models can be expanded and scaled to design the full scale bearing arrangement, and its dynamic response to the loads simulated.
For model verification an experimental setup is designed and built from scratch, where a digital signal processor controls nine coils by use of power electronics. As feedback both currents, forces and positions are utilized. For position feedback four inductive sensors are designed and manufactured. The electric, magnetic and mechanical models are verified simultaneously on this setup, by comparing the non-linear response with experimental data. A range of control strategies are designed, tested and compared. Finally a preliminary design for a full-scale bearing is designed and presented.

By signing this document each student confirms that every group member has taken an equal part in the project, and that everyone is liable for the contents of the report.

AALBORG UNIVERSITY

Study board of Industry and Global business development
Fibigerstræde 16
DK 9220 Aalborg Øst
Tel +45 99 40 93 09 Fax +45 98 15 16 75
swe@me.aau.dk http://www.industri.aau.dk/

Preface

This report is written by group EMSD3-44 from September 1st 2012 to June 4th 2013 at Aalborg University.

Reading guide

All figures and formulas are numbered as (A.B), where 'A' denotes the chapter number and 'B' denotes the formula/figure number in the chapter.
References to formulas are done with the use of parenthesis, whereas references to figures are done without the use of parenthesis.
All figures and tables are accompanied by an explanatory text and, unless cited, the figures are made by the students themselves.
References to literature are done by use of the Harvard method, where references are denoted as [Author, year].
In some instances additional reading might be available, but has been moved to an appendix instead of being in the actual report for ease of reading. If this is the case, the appendix will be referenced.

A CD is supplied in addition to the report and the table of contents of the CD can be found in appendix A.

Executive summary

The DeepWind project is a research project that currently are designing a $5MW$ Vertical Axis Wind Turbine (VAWT) exclusively for offshore use. The research group, located at Aalborg University, is responsible for the generator and bearing design. This thesis is based on a project proposal from this group. Specifically to explore the possibilities of using Active Magnetic Bearings (AMBs) for this application.

To do this, an experimental model of an AMB is designed and built. First a structural design is presented, and the system is designed and verified using a simple structural Finite Element Method (FEM) analysis, where the maximum deflections are determined. Furthermore the magnetic part of the experimental setup is designed. This being two axial bearings, and to actuate the system a third magnetic actuator is added.

A control system is also designed. This includes the design and fabrication of distance sensors and power electronics, consisting of current sensors, H-bridge drivers, and semi passive H-bridges.

Furthermore, to gather the requisite information from the system, data acquisition is set up with load transducers being strain gauges and a National Instruments - Data Acquisition (NI-DAQ) device. The control system is run using a Digital Signal Controller (DSC), and a number of controllers has been implemented for testing.

A number of problems appeared when creating the system, e.g. the first iteration of a galvanic isolation system based on optocouplers. The parasitic capacitance, of these devices, rendered the entire sensor system useless because of noise. Therefore a line driver, based on optical transmitters, was build. Also a number of problems, with noise in the control signals, occurred. These has been significantly abated by shielding and grounding.

In parallel with the experimental model, a mathematical model was set up for the system. A Reluctance Network Model was set up to describe the magnetic circuit. The forces calculated by the model was compared to measurements, conducted with strain gauges, and by tuning the model parameters it showed good accordance to the measurements.

Furthermore a mechanical and an electrical model was set up. A simple proportional current controller was developed and used along with a PD controller to verify the magnetic, electric and mechanical model. A dynamic verification of the system is shown in Figure 1, and the model shows good accordance with the experimental setup.

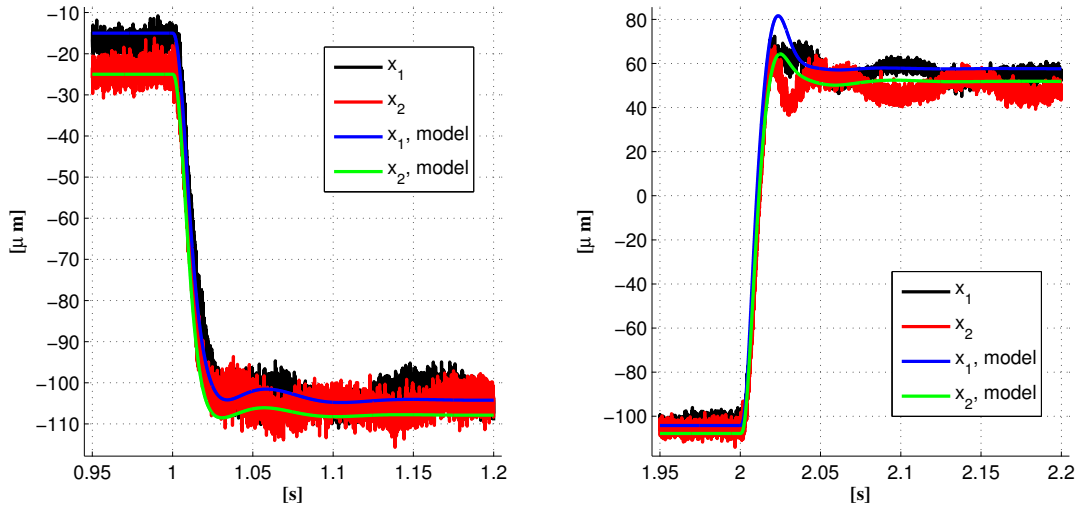

(a) Step of $-50\mu m$ *(b) Step of $100\mu m$*

Figure 1: *Position for a series of steps for model verification.*

The experimental system is inherently unstable, which replicates the VAWT system. Five different controllers, that stabilize the system, are developed, where both transfer function and state space based methods are utilized. Quantitative measures, for the performance of the controllers, are set up, and the results are shown in Figure 2.

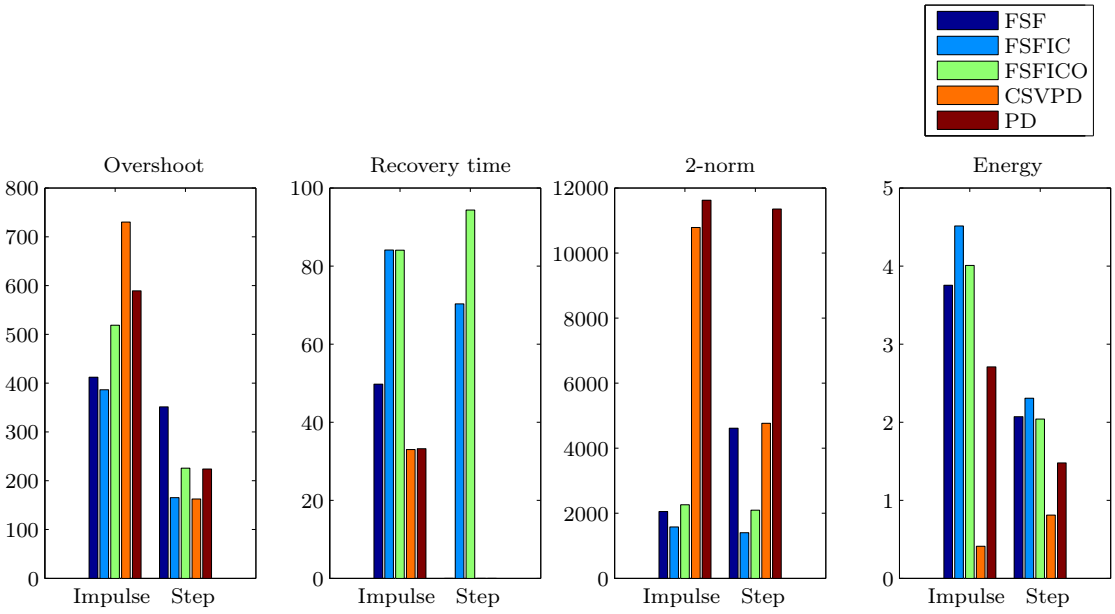

Figure 2: *Bar plot of the controllers performance.*

Full size design proposal

Based on dynamic loads recieved from the DeepWind research group, together with the mechanical interfaces supplied, a preliminary full scale design of an AMB is made. This design proposes two radial bearings, each with 12 pole pairs, and an axial bearing with 10 pole pairs. The bearing power consumption was evaluated to $14.16kW$, which is 2.832‰ of the $5MW$ the windmill is designed to produce. This power consumption seems acceptable and the AMB bearing solution worth pursuing.

Table of Contents

Introduction 1

DeepWind is a 4 year research project, run by Technical University of Denmark (DTU) Risø and 11 international partners. The project was funded by FP7 - Future Emerging Technologies in October 2010 and runs until September 2014.

Due to the fact that the offshore wind energy play an increasing role, as a source of energy, it is logical to develop a dedicated technology for the offshore wind turbines. The goal of the project is, by designing a wind turbine specifically for the offshore environment, to achieve a much better efficiency than existing technologies.

More specifically the project is limited to concern a floating vertical axis rotor with a floating foundation. There is not one defined wattage of the design. The mission of the project is to develop a tool for development and analysis of large wind turbines based on the VAWT concept.

The initial concept is shown in Figure 1.1. The VAWT consists of a two blade rotor, attached on a long tube connecting the rotor to a generator and bearing which are submerged. The bottom generator is attached to an anchoring system which in turn is attached to the sea-bed.

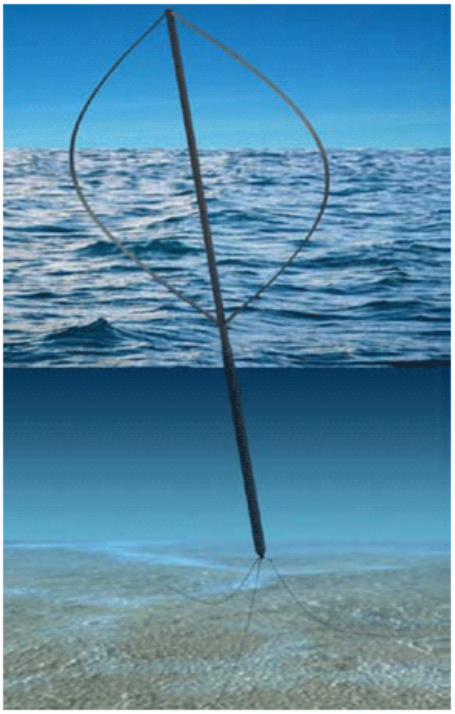

Figure 1.1: *Offshore VAWT concept drawing [DTU Risø, 2012]*

The DeepWind project has main focus in developing technologies for individual components, in order to evaluate the concept against other technologies. Therefore models evaluating the energy production, dynamics and loads are of main importance. Additionally design tools for blades, anchoring, generator, and control should be developed, and last a proof of principles and testing should be carried out by building a kW scale model. It all should end up in a specific design of a $5MW$ VAWT [DTU Risø, 2012].

The technologies needed, for designing the VAWT, are numerous and each area require research. The research concerning bearing and generator design is situated at Aalborg University, where different topologies are analyzed before choosing a candidate solution.

1.1 5MW Darrieus type wind turbine

The $5MW$ VAWT is presented in this section. The design presented is the first iteration, hence changes occur when the design is improved and specified further.

The VAWT is build as a floating structure anchored to the seabed. An outline of the design is shown in Figure 1.2. The structure above water level consists of two blades and an axle - the rotor. The blades airfoil shape is the NACA0018 standard shape, which is symmetric about the foil chord. The blade contour follows a modified troposkien curve, which is not presented here, thus the circular shape shown in Figure 1.2 is not a correct representation. The axle is hollow, all the way through, giving buoyancy to the structure.

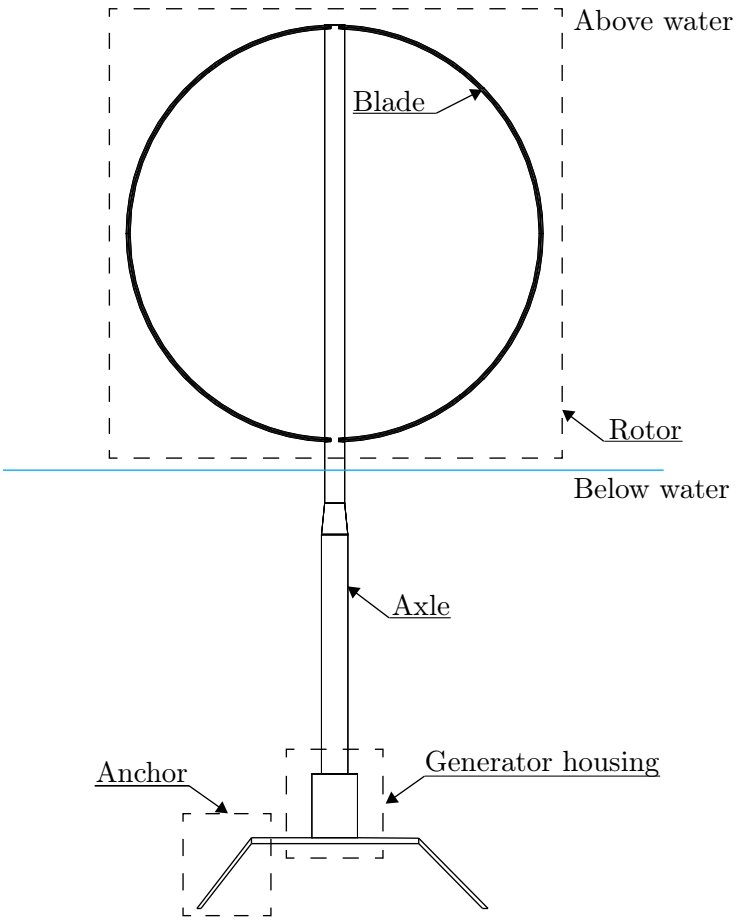

Figure 1.2: *5MW Darrieus turbine design outline.*

Below water level the axle continues, and the radius increases. The axle end continues into a generator housing. The generator housing contains the generator and bearing, and connects the rotating structure to a stationary structure mounted on the seabed via mooring lines. The generator housing design is nearly non existent at the moment, since this design, along with the generator housing placement, relies highly on the choice of generator and bearing type. Since the turbine floats, only anchored by cables, it has significant pitch, yaw and roll, thus the bearing load varies with wind speed, waves and rotor orientation.

The VAWT pitches or yaws up to 14° during operation, because the mooring anchor is flexible the angle increases until the mooring resists the rotating adequately.

1.2 Master Thesis

The project group will, as their master thesis, focus on the use of AMBs for the connection between the rotor and the stator of a VAWT. The bearings will have to transfer significant forces, and because of the near to zero friction, in magnetic bearings, and negligible mechanical wear, it is seen as a candidate technology for use in the VAWT.

Longevity of the bearing system is of high importance, since repair and maintenance is highly troublesome after deployment of the wind turbine at sea. Longevity, of a

conventional journal bearing, requires a clean environment and a supply of lubricant. Thus requiring the submerged generator housing to be sealed, creating the challenge of developing a seal with high lifespan. The electromechanical system of the magnetic bearing, the coils and iron core itself, does not need a clean environment or a clean supply of lubricant. It contains no moving parts in contact. The potentially troublesome part of the magnetic bearing system is the control and power electronic systems. Potential failure of these systems would be critical, thus safeguards and redundancies are needed. Failure of one of the redundant systems does not render the wind turbine useless, since another system is ready to take over. The project group expects that a conventional journal bearing breakdown would affect the construction critically, where the AMB only need replacement of the electric system affected. These considerations highlights the possibilities of using AMBs for this type of wind turbine. The project group will not compare feasibility of the AMBs solution to other bearing solutions. Doing this would required extensive knowledge of each bearing type, including load capabilities, maintenance costs, investment cost etc. Instead the AMB technology will be studied and applied to the wind turbine.

Being able to asses the capabilities of the AMB technology, design and development of control systems requires a mathematical model of the bearing. Such a model is set up and verified using an experimental set up developed and build by the project group. This test set up will also be used for testing control strategies and access the challenges and uncover potential pitfalls of AMB development and use.

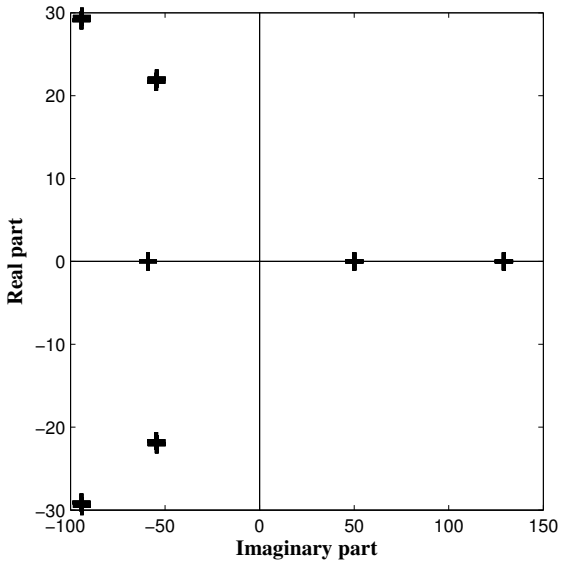

Figure 1.3: *Pole plot of the magnetic, electrical and mechanical system of an linearized active magnetic bearing. A total of 14 are plotted, but seems like seven because they are pairwise very close.*

Using the reluctance principle for a bearing is highly non-linear qua the fact that electromagnets, without the use of Permanent Magnets (PMs), are only capable of generating attractive forces. Furthermore a magnetic bearing is unstable, as seen in Figure 1.3 where the poles of the linearized system are plotted. Clearly there are poles in the right half plane, and the system is unstable. Therefore when designing an AMB the use of control theory, to stabilize the bearing, is necessary. The aforementioned non-linearities

makes control design a challenge. Thus much effort it spent developing and testing control strategies for the AMB. Efficiency via good control, presupposes a good overall topology for the bearing, that enables the magnetic flux to flow, where it is needed. Consequently both a good magnetic design and controller design is needed for an effective bearing.

This section concludes the introductory chapter of this report. The problem statement is presented in the next chapter.

Problem statement 2

The DeepWind research group is evaluating different bearing technologies for a VAWT, and needs tools for modeling of the magnetic, electrical and mechanical system of an AMB. The project group will, as their master thesis, study this application and develop these tools. The main goals of this thesis are outlined in the following problem statement:

- - - - - - - - - - - -

How can the electromechanical system, of an AMB, be modeled and controlled? Can a bearing topology, for a full size wind turbine, carry the dynamic loads that are applied during operation?

- - - - - - - - - - - -

Based on this, the project is executed as shown in the flowchart Figure 2.1.

To analyze the problem, in a reliable way, a mathematical model is set up, and an experimental setup is build. The purpose of the experimental setup is for model verification. Then gaining knowledge of the model precision, enables the possibility of applying the model to full scale AMBs. Designing and constructing the experimental setup enables the project group to obtain empirical knowledge of AMB technology.

For the experimental setup the control system has to be build. This involves design and implementation of the signal processing system, power electronics system, and data acquisition system.

For the control system, a number of control strategies has to be developed. The mathematical model is used for this task, both for the design process and the following controller testing.

A design based on the information available for the large scale DeepWind turbine is lastly designed. This design is used to obtain approximate figures for bearing size and efficiency, leaving room for improvement, but making the reader able to assess if use of an AMB for the wind turbine is realistic. This report should then be used by the wind turbine designer to set up a magnetic bearing model and control system, in addition to their own dynamical models, and finish the bearing design.

In the two following chapters the experimental setup is presented. In Chapter 3 the general design and mechanical parts of the setup are presented and in Chapter 4 the control system for the setup is presented.

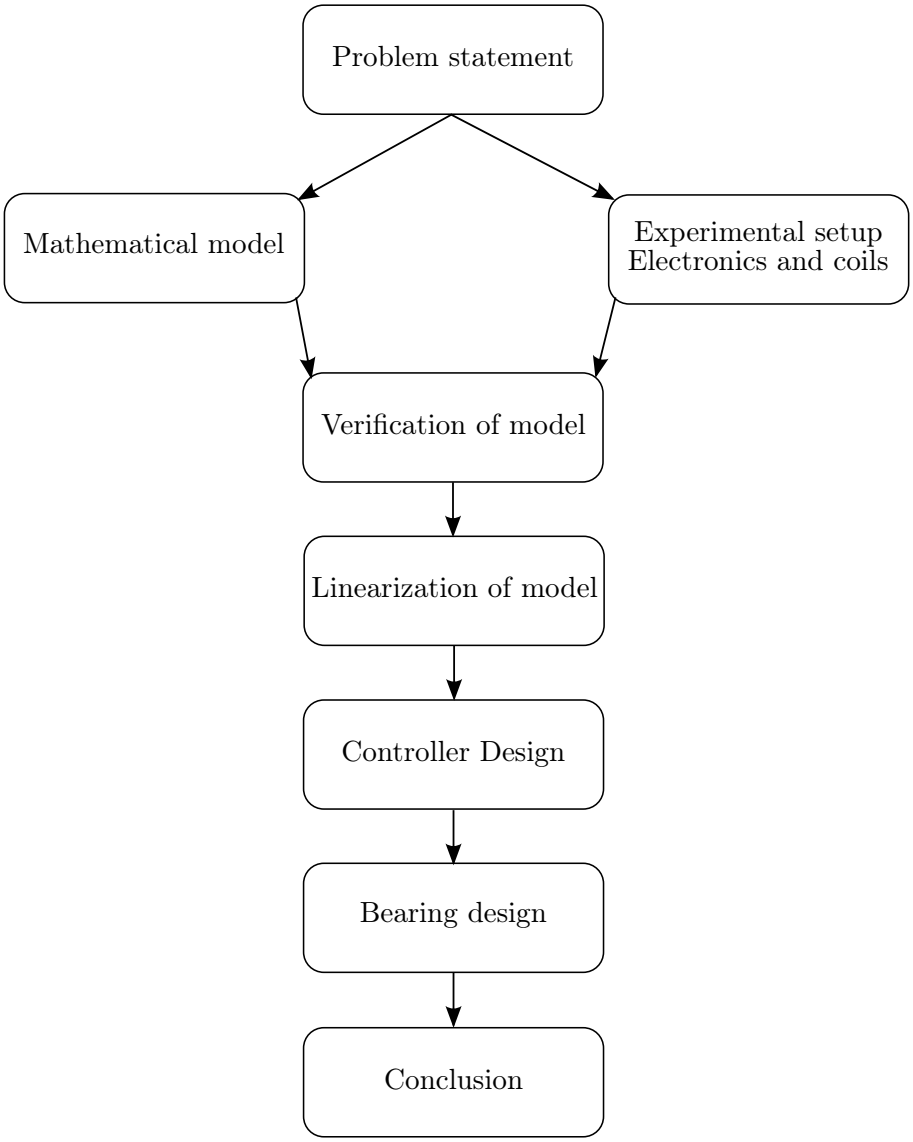

Figure 2.1: *Flowchart of the thesis subjects.*

Experimental Setup 3

To verify the accuracy of the AMB model, get acquainted with the practical issues, and controller testing, an experimental setup is designed and constructed.

The experimental setup is designed based on a number of demands of the system. Therefore a number of demands are listed and sorted according to their importance as "Must have" or "Nice to have".

Must have:

1. Current and position feedback.
2. Force transducer for model verification.
3. At least two radial bearings.
4. I/O's controlled by a DSC.
5. Flexibility of bearing placement.

Nice to have:

1. Load actuator to model dynamic loads.
2. Rotational actuator and feedback, to verify the dynamic model.
3. Both axial and radial magnetic bearings.
4. Force feedback on every bearing.
5. Ability to expand experimental setup with extra features.

A number of iterations and designs, working with these demands, ended up with the experimental setup as shown in Figure 3.1. In Table 3.3 the terminology of the experimental setup is presented. A number of drafts for the design is presented and evaluated in Appendix B.1.

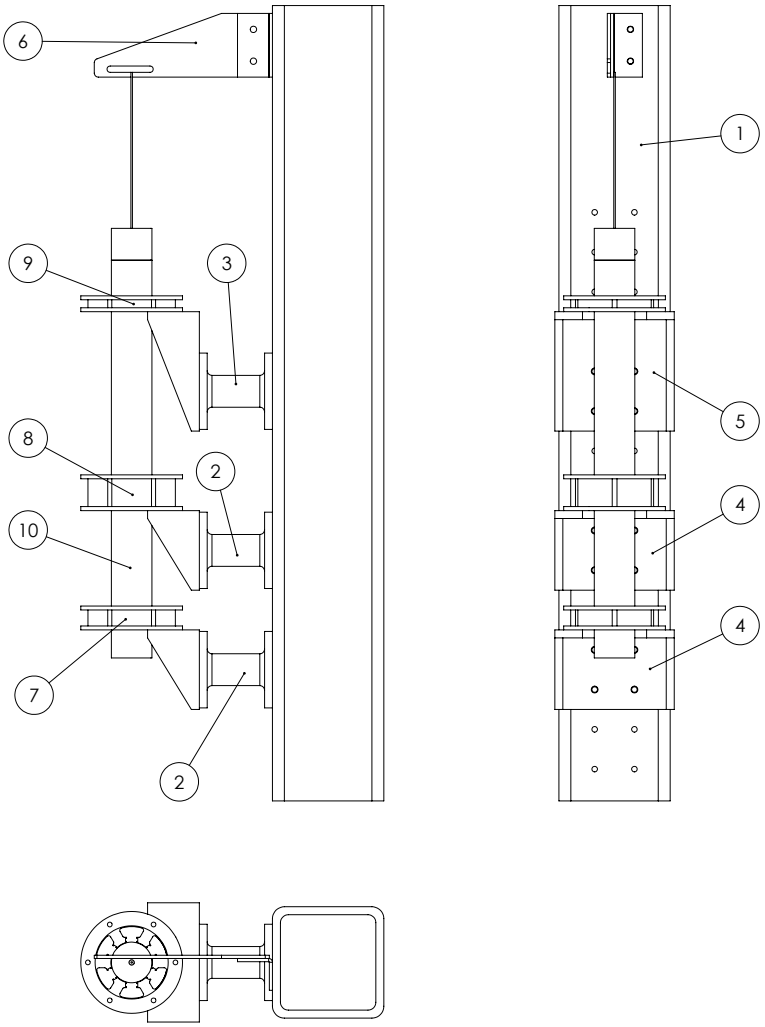

Figure 3.1: *Experimental setup schematic with reference number of parts. Parts are defined in Table 3.3.*

Reference number	Part	Reference number	Part
1	Square Steel Profile	6	Axle Rig
2	Steel Spacer	7	Bearing One
3	Strain Gauge Mount	8	Bearing Two
4	Aluminum Bracket	9	Load Actuator
5	Strain Gauge Aluminum Bracket	10	Axle

Table 3.1: *Terminology related to experimental set up.*

The experimental setup consists of two radial bearings and an actuator, where the actuator in principle is identical to the radial bearings. The two radial bearings emulated the radial bearings of a VAWT. The load actuator is used to apply a force varying force corresponding to a wind force, thereby emulating the VAWT load. The load actuator is additionally used for model verification.

For holding the bearing in place, and aligning the bearings in one direction, a square steel

beam is used. On one side the beam has been machined for alignment purposes. A row of threaded holes are placed in a pattern along the machined side of the beam. This gives flexibility of bearing and load actuator placement. Furthermore it provides the possibility of adding an electric motor, driving the axle, or to add a different kind of load actuator.

The two bearings are placed on steel spacers, this to make it possible to mount Strain Gauges (SGs) on the magnetic actuator and measure the force it exerts. The slightly different "Strain Gauge Bracket" acts as a moment arm for better resolution on the SG. The experimental setup is placed with the axle in a vertical position to eliminate the gravitational effects from the axle. Thereby avoiding using what bearing force is available on gravitational axle force, but on control and stabilization of the axle with respect to the load. The next sections will present and describe the parts of the experimental setup, their function, and document the design. Technical documentation of the parts are present on the attached CD.

3.1 Axle

For ease of manufacturing and keeping costs low, the axle is a solid piece of ferromagnetic steel. Thus the core material of the magnetic bearing is not sheet steel manufactured for use in electric machinery, this will results in higher eddy current losses, but this is accepted since the experimental setup axle is not rotating.

3.2 Magnetic bearings

Each bearing and actuator is made from a switch reluctance motor, where the sheet metal is reused. Therefore the geometry of the sheet metal for the magnetic bearings are given. The sheets are $0.5mm$ thick and a number of 130 sheets are available. Because of the decision to recycle the sheet, the bearings are radial. The sheets are shown in Figure 3.2.

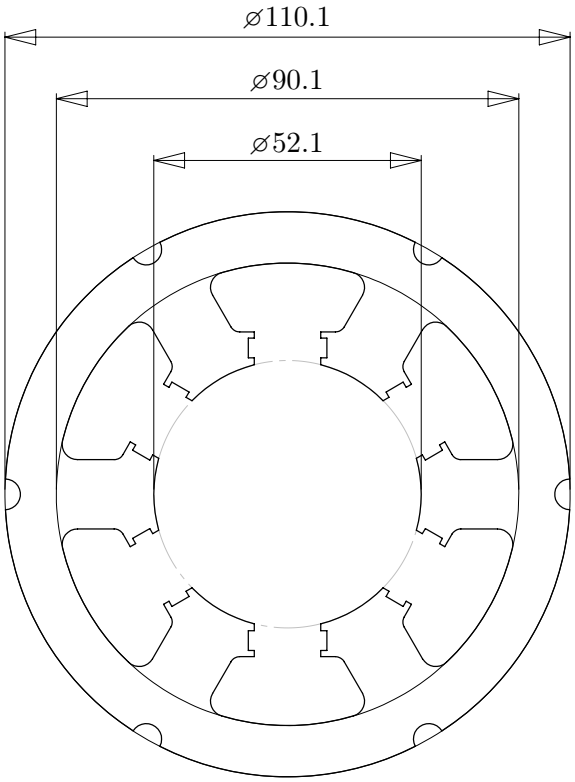

Figure 3.2: *Dimensions of the switch reluctance motor sheets used for radial bearings.*

The available sheet steel is divided to form three actuators. Two of the stacks form the magnetic bearings, the remaining are used for the load actuator. The ratio of sheet steel in the respective bearings are calculated in appendix B.2, based on a statically equilibrium of forces. The height of each actuator is shown in Table 3.2.

Load Actuator	$h_{actuator}$	$10mm$
Bearing 2	h_2	$35mm$
Bearing 1	h_1	$20mm$

Table 3.2: *Height of individual magnetic actuators*

The coils of the magnetic bearings are wound with 150 windings each, and a wire thickness of $0.63mm$, thus an electromagnet consists of two coils of 150 windings each. Combining the coils in pairs, simplifies the power electronics by halving the number of H-Bridges required. The airgap is chosen to be $0.5mm$. Due to machining tolerances of the axle the actual air gap is measured to be $0.475mm$. The choice of airgap is somewhat arbitrary. The smaller the airgap is, the more economical the machine becomes, because less current is required to generate the equivalent amount of flux in the airgap, thus resulting in less ohmic loss. A smaller airgap also lessens the leakage flux and makes the model assumptions more accurate. But a small airgap also makes control harder and the demands on the displacement sensors more severe. The $0.5mm$ is thus a compromise between control freedom, sensor demands and model accuracy. Since the experimental setup is for purely scientific purposes, the ohmic loss is not of great importance.

The number of windings is chosen such that saturation of the sheet steel is possible. Then the effects of working in the non-linear area can be investigated. The magnetic circuit of

one of the electromagnets in the bearing is presented in Figure 3.3.

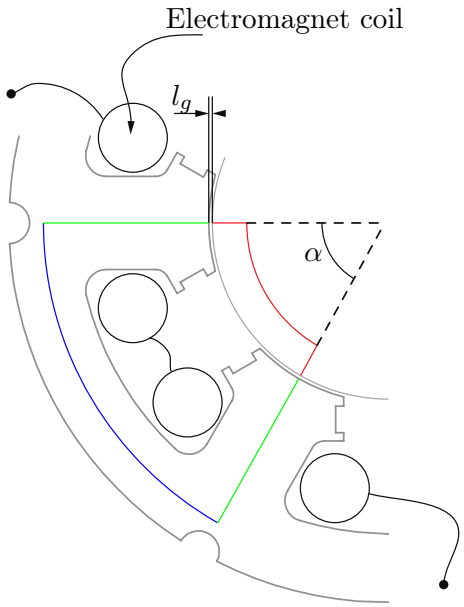

Figure 3.3: *Mean flux path of one electromagnet. The rotor flux path is highlighted in red, the pole flux path is green and the stator flux path is blue.*

From the mean flux path the circuit equations, for the Magnetomotive force (MMF), are set up and shown in equation (3.2.3).

$$\begin{aligned} \mathcal{F}_{stator} &= H_{stator} \cdot (2 \cdot L_p + L_s) \\ \mathcal{F}_{rotor} &= H_{rotor} \cdot L_r \\ \mathcal{F}_{airgap} &= 2 \cdot \frac{B_{max}}{\mu_0} \cdot l_g \end{aligned} \tag{3.2.1}$$

Where L_p, L_s and L_r is the lengths of the mean flux paths for pole, stator and rotor respectively. Summing up the MMF for stator, rotor and airgap:

$$N \cdot I_{max} = \mathcal{F}_{stator} + \mathcal{F}_{rotor} + \mathcal{F}_{airgap} \tag{3.2.2}$$

Choosing a maximum current and a maximum flux density the number of windings required is calculated.

$$N = \frac{\mathcal{F}_{stator} + \mathcal{F}_{rotor} + \mathcal{F}_{airgap}}{I_{max}} \tag{3.2.3}$$

The current is chosen to be $5A$. This is little more than half of the maximum current limit set by the electronics, which leaves room for saturating the magnetic materials and operation outside the linear range. The maximum flux density is chosen as $1T$, this from the BH-curves generated by experiments documented in Appendix B.3 and shown in Figure 3.4.

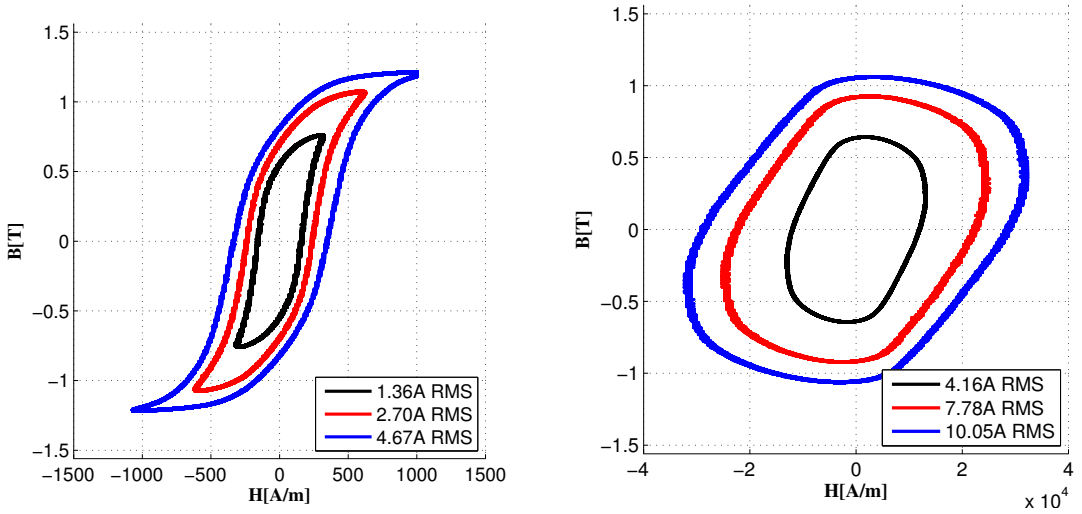

(a) Experimentally determined B-H curve for radial bearing sheet steel.

(b) Experimentally determined B-H curve for solid rotor steel.

Figure 3.4

$1T$ is in the non-linear area of the sheet steel and at the limits of the steel axle. The required number of windings are calculated as:

$$N = \frac{500\frac{A}{m}\left(2 \cdot 0.0240 + 0.0524\right)m + 3000\frac{A}{m} \cdot 0.0215m + 2 \cdot 1T \cdot 4.75 \cdot 10^{-4}m \cdot \frac{1}{\mu_0}}{5A}$$
$$= 165 \tag{3.2.4}$$

This is therefor the minimum required winding number to obtain 1T at $5A$ current.

The remaining restricting parameter is the coil resistance. Limiting copper loss is not of vital importance since the bearing is used in an experimental setting and the coils are placed in open space and connected to aluminum surfaces creating good cooling conditions. 150 windings per coil were chosen as a fitting number based on practical considerations, fill factor, available copper thread in the laboratory, safety factor and acceptable resistance. The coil resistances are shown in Appendix F.1.

3.3 Load Actuator

Using a magnetic actuator it is possible to exert force in every direction in the xy-plane, dynamically, and to mimic different loads, e.g. wind load. Applying the same calculations as in the former section each load actuator coil are also wound with a 150 windings.

3.4 Load transducer

To be able to calculate and verify the force exerted on the axle from one of the magnetic bearings, a load transducer is designed. The transducer piece along with SG placement is shown in Figure 3.5. The "Strain Gauge Mount" is hollow contrary to the steel spacers, to allow sufficient deformation of the strain gauge. Since the tube is short and wide, the displacement of the tube can be neglected, which makes the relation between bearing force

and gauge strain linear. This is because it can be assumed that the points of attack of the forces remains unchanged, due to small displacements [Gere and Goodno, 2004]. A short tube also keeps the displacement of the force transducer at a minimum, to ensure that the bearing position remains as constant as possible. If the bearing displacement is too large the alignment of the bearings in the experimental setup is compromised.

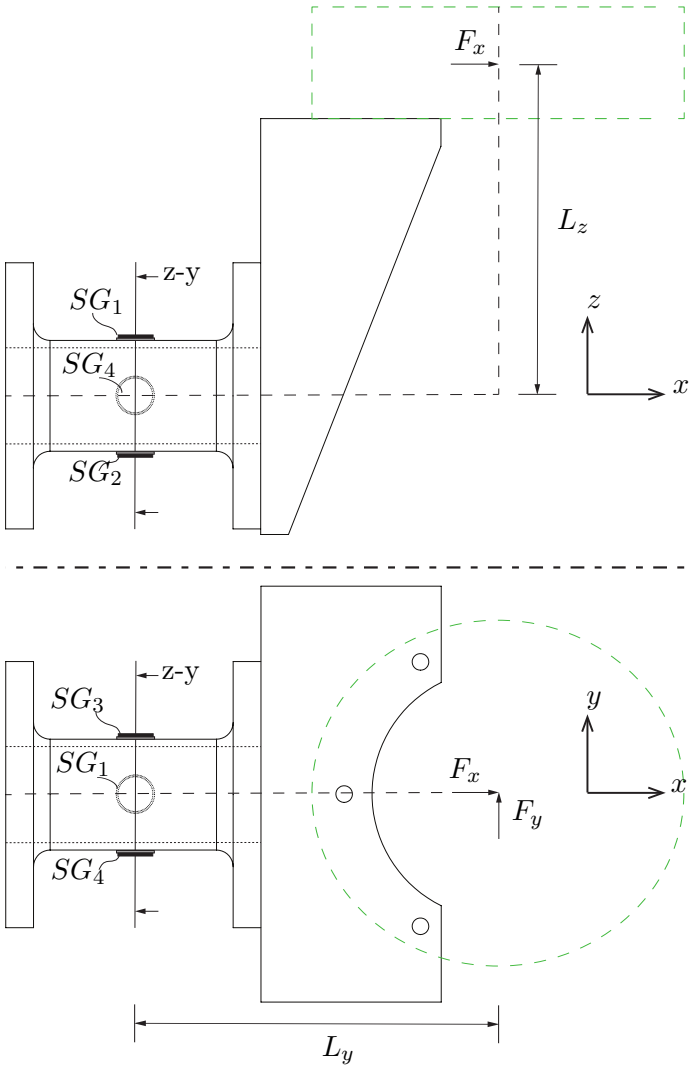

Figure 3.5: *Schematic showing the strain gauge's placement on the strain gauge spacer, with indication of forces and coordinate systems.*

Biaxial strain gauges are used, one of the strain gauges are show in Figure 3.6. Using biaxial strain gauges cancellation of superimposed torsional strain is possible [Hoffmann, 1989].

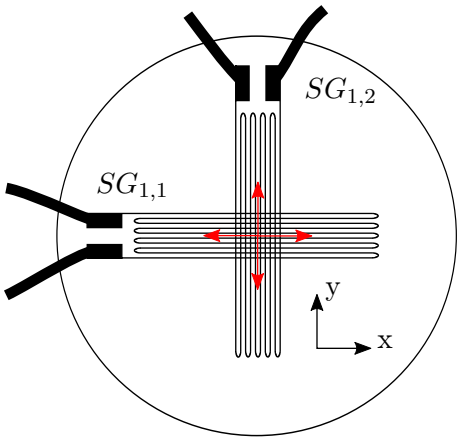

Figure 3.6: *The biaxial SG_1 with active directions indicated by the red arrows.*

Strain gauges opposite each other are coupled into a full Wheatstone bridge. Bridge one is SG_1 coupled with SG_2 and bridge two SG_3 couples with SG_4. Thus the force transducer consists of two Wheatstone bridge circuits. Bridge one is unbalanced by F_x and bridge two unbalanced by F_y.

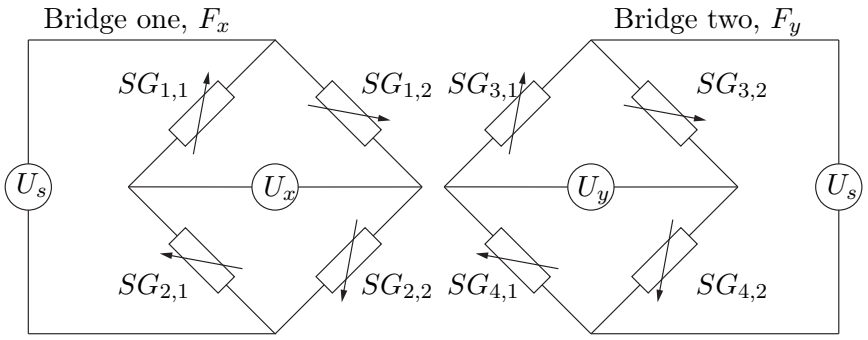

Figure 3.7: *The two wheatstone bridges configured to measure pure moment in the strain gauge mount, which is proportional to the applied magnetic forces via geometric relations.*

The two Wheatstone bridges are shown Figure 3.7. The relation between bridge supply voltage and bridge voltage is shown in equation (3.4.1) [Hoffmann, 1989].

$$\begin{aligned}
\frac{\Delta R}{R} &= k_{gauge} \cdot \epsilon_{gauge} \\
U_x &= \frac{(\epsilon_{1,1} - \epsilon_{2,1} + \epsilon_{2,2} - \epsilon_{1,2})}{4} \cdot k_{gauge} \cdot U_s \\
U_y &= \frac{(\epsilon_{3,1} - \epsilon_{4,1} + \epsilon_{4,2} - \epsilon_{3,2})}{4} \cdot k_{gauge} \cdot U_s
\end{aligned} \tag{3.4.1}$$

When the strain gauges along the x-axis deform from normal forces they all deform equally and the resistance change is equal, thus the bridge remain balanced. If the tube is subject to torsion the resistance change of the gauges placed along the x-axis and the strain gauges perpendicular to the tube and the x-axis are equal and the bridge remains balanced. This because the gauges are placed 45^o from the principal direction of strain in torsion. Using the same logic, temperature disturbances, if assumed equal in all the strain gauges, are also canceled out.

As bridge amplifiers two Hottinger Baldwin Messtechnik (HBM) strain meters are used, DMD 20 and DMD 20A. These are chosen because they along with indicating the bridge difference digitally also supply an analog output, proportional to the strain.

The strain gauges are calibrated using a Newton meter. The relation between force and output voltage is presented in Figure 3.8.

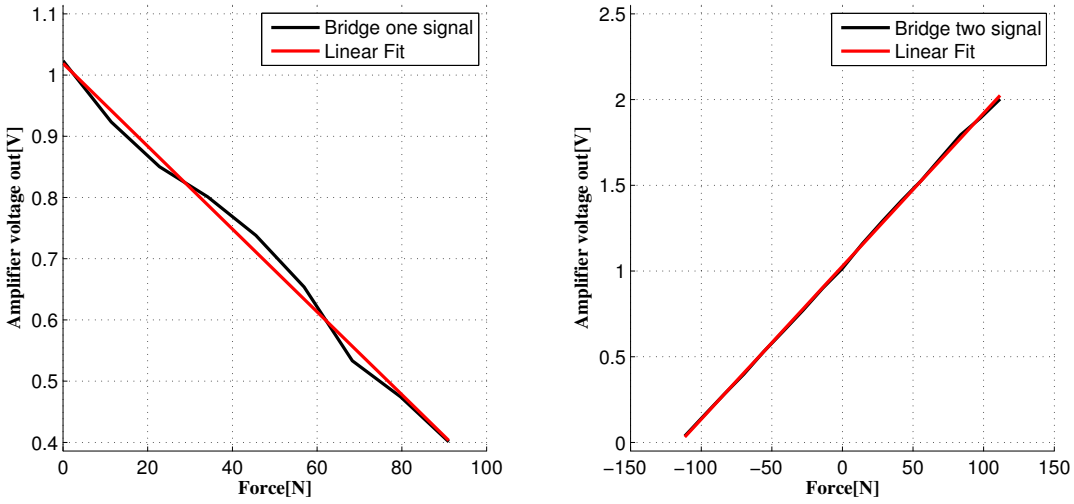

(a) *Bridge one amplifier signal plotted with relation to force, F_x.*

(b) *Bridge two amplifier signal plotted with relation to force, F_y.*

Figure 3.8: *Force transducer calibration using a Newton meter to apply loads.*

Thus the linear relationship between force and strain gauge output is confirmed and the relation constants found and shown (3.4.3). The offset of the linear fit is disregarded. Using the equipment one should calibrate the offset of the signal to a desired value each time before beginning force measurement.

$$F_x = k_{x1} \cdot U_x; \quad k_{x1} = -147.9 \tag{3.4.2}$$

$$F_y = k_{y1} \cdot U_y; \quad k_{y1} = 112.0 \tag{3.4.3}$$

Figure 3.9 shows the amplifier output from both bridges when a force along one axis is applied. The relevant bridge should show a linear relationship with regard to the applied force, while the other bridge signal should remain unchanged. Which they for the most part are, thus cross coupling between direction should be minimal.

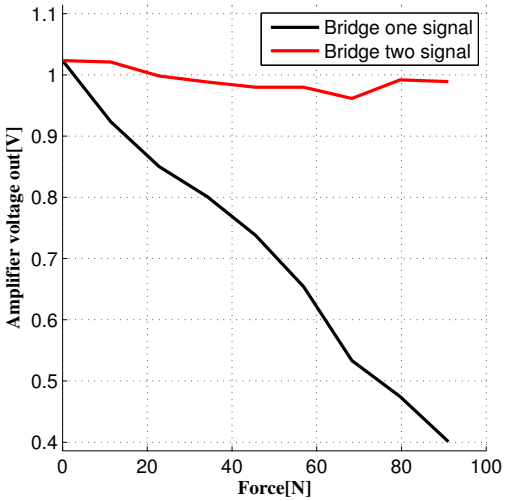

(a) Bridge amplifier signals plotted with relation to force, F_x.

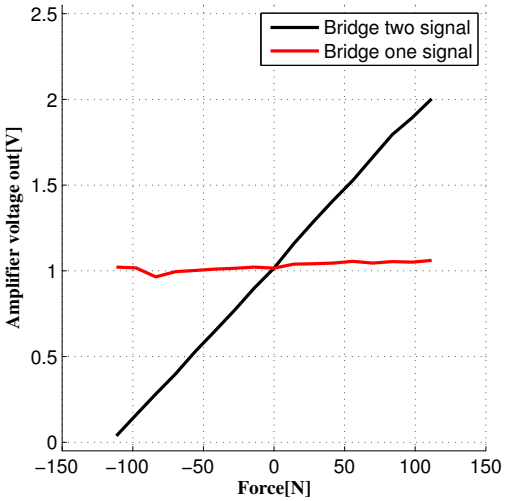

(b) Bridge amplifier signals plotted with relation to force, F_y.

Figure 3.9: *Force transducer output plotted against the applied force, to showcase cross coupling.*

3.5 Structural design of experimental setup

The airgap of the magnetic bearings and the actuator is $0.5mm$ and this determines the stiffness requirements of the experimental setup. Steel has been chosen as the main material because of its availability and stiffness. The brackets are aluminum, because of its permeability, to avoid unintentionally affecting the flux paths of the magnetic circuits.

To verify that the magnetic bearing brackets does not deform excessively, a static Finite Element Analysis (FEA) is performed on the larger bearing, bearing two, and the load actuator assemblies. This analysis assumes that the bolt connections allow transfer of both tensile and compressive stress, and that the electromagnetic force can be modeled as a pressure attacking the surface of the bearing. It is also assumed that the sheet metal is a single lump of metal and that the square steel profile is infinitely stiff.

The electromagnet shown to yield the largest total deflection when maximum force is applied is number one, which is the electromagnet compromised of coil one and two. The red lines in Figure 3.11 indicate the poles of electromagnet one, where the pressure is applied. A pressure of $0.8MPa$ is applied, equal to the twice the pressure generated by the electromagnet when operating at $1T$, maximum flux density. An analysis result is presented in Figure 3.10, to show the model discretization and contour lines. The deformations of the points indicated Figure 3.11 are presented in Table 3.3, for bearing two and the load actuator. These points indicate deformation of the magnetic poles, which are seen as the most critical deformations. These show that the total deformation does not exceed a tenth of a millimeter with a safety factor of two applied to the load pressure. This is deemed an acceptable stiffness since this deflection is present only at maximum force, which will rarely be applied during operation.

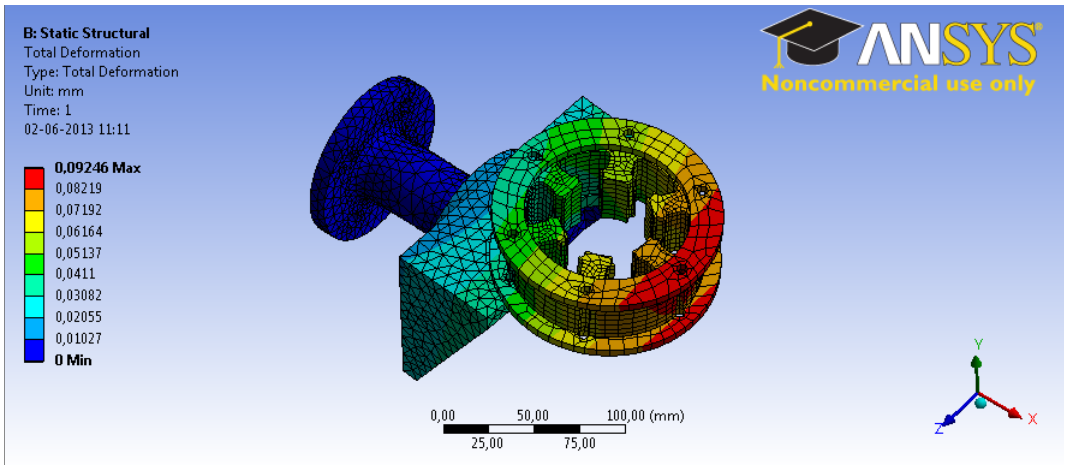

Figure 3.10: *Static FEA of the middle bearing and mount showing total deflection.*

Bearing Two	Total Deformation[μm]	Load Actuator	Total Deformation[μm]
1	70.8	1	68.8
2	64.5	2	61.6
3	51.8	3	51.2
4	42.3	4	49.6
5	46.9	5	56.7
6	62.0	6	65.4

Table 3.3: *Total deformation of selective points of FEA.*

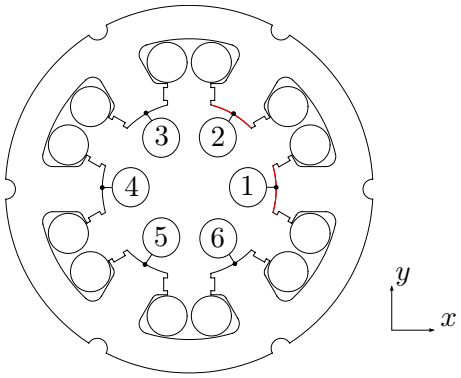

Figure 3.11: *Cross section of the magnetic bearing and actuator, indicating probing points for the total deflections shown Table 3.3. The red lines indicate the pole areas where pressure loads were applied in the FEA.*

3.5.1 Problem with mechanical vibrations during operation and possible solutions

During use of the experimental setup mechanical vibrations occurred. These vibrations disturb the position feedback, especially the differential term of the PD controller. The mechanical vibrations occur around $200Hz$ to $300Hz$. This is a problem, because these disturbances lie outside the signal filtering ranges and above the bandwidth of the controllers. Thus the controller sees the disturbances but cannot damp them. A solution to this problem has been removing the steel spacers and reinforcing the sensor brackets.

An eigenfrequency analysis was performed using the model shown in Figure 3.12. The model was developed using the Computer Aided Design (CAD) drawings already available from the experimental setup manufacturing. The results were obtained using SolidWorks Simulation.

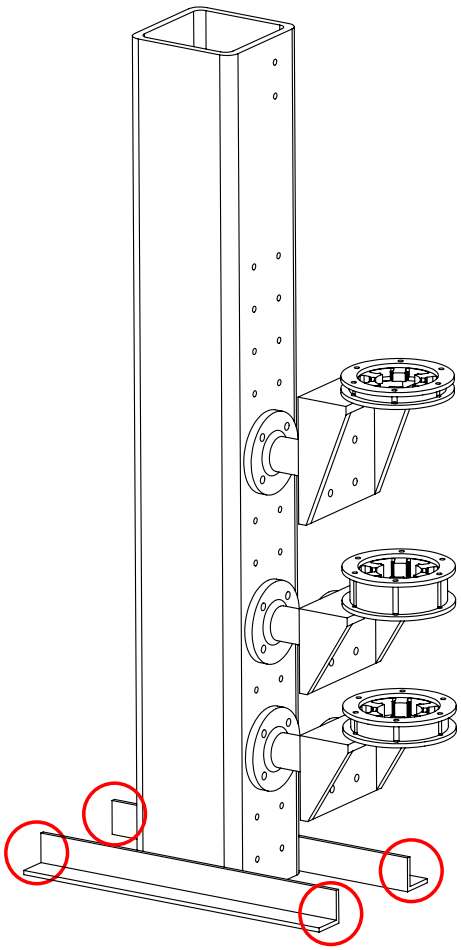

Figure 3.12: *Eigenfrequency analysis was done on this CAD model. The L profiles were fixed at their ends, indicated by the red circles.*

Table 3.4 shows the results of the analysis. The first two eigenmodes were oscillations in the L-bracket, used for mounting the experimental setup. The remaining mode all affect the magnetic bearings. This is a simple analysis, but it supports the theory of bearing oscillations around $200Hz$ to $300Hz$ being a problem.

Mode number	Frequency[Hz]	Mode number	Frequency[Hz]
1	27.849	6	283.57
2	49.192	7	284.42
3	208.76	8	343.94
4	250.33	9	349.32
5	262.57	10	417.63

Table 3.4: *Eigenfrequencies of the experimental setup, based on a FEA.*

This problem was detected late in the project period, therefore a real solution to the problem was not devised. The oscillations were removed by mounting the bearing brackets

directly on the experimental setup column. If more time had been available, using accelerometers to detect which modes of oscillations were being exited and then altering the stiffness or mass of the experimental setup, to avoid these modes, would be one solution to the problem. Lowering the frequency of the exited mode and making it controllable could also be a solution.

Control system 4

The control system is the active part of the experimental setup, comprised of all the sensors and actuators that are necessary to control the axle position. In order to be able to test and use control strategies, on the experimental setup, all of the parts, presented in this section, are needed. The interface, to the control system, is a DSC, which is programmed in C. This interface enables the actuators to be controlled as a function of the input from the sensors. All the hardware needed for the experimental setup has been designed, produced and tested by the project group.

As most control systems the components breaks in to two categories: Sensors and actuators. The actuators are the nine electromagnets, that are controlled by the DSC via a galvanic isolation, a H-bridge driver and finally the semi-passive H-bridge. Figure 4.1 is a diagram of the control system, starting from the Digital to Analog Conversion (DAC) module of the DSC.

On the sensor side currents, positions and forces are measured with their respective circuits, and connected to the Analog to Digital Conversion (ADC) module of the DSC as depicted in Figure 4.1. The top bar in this figure depicts the power supplies that are used in order to power all of the sensors and actuators.

As presented in Chapter 3 the experimental setup contains three magnetic actuators. As one DSC can only control six coils, because the available unit only has 6 modules for Pulse Width Modulation (PWM) signal generation. An advantageous approach would be to control the two bearings with one DSC, and then configure a second DSC for the load actuator. This configuration allows for force feedback in the load actuator, and a closed loop force controller can be set up, while testing controllers in the bearings.

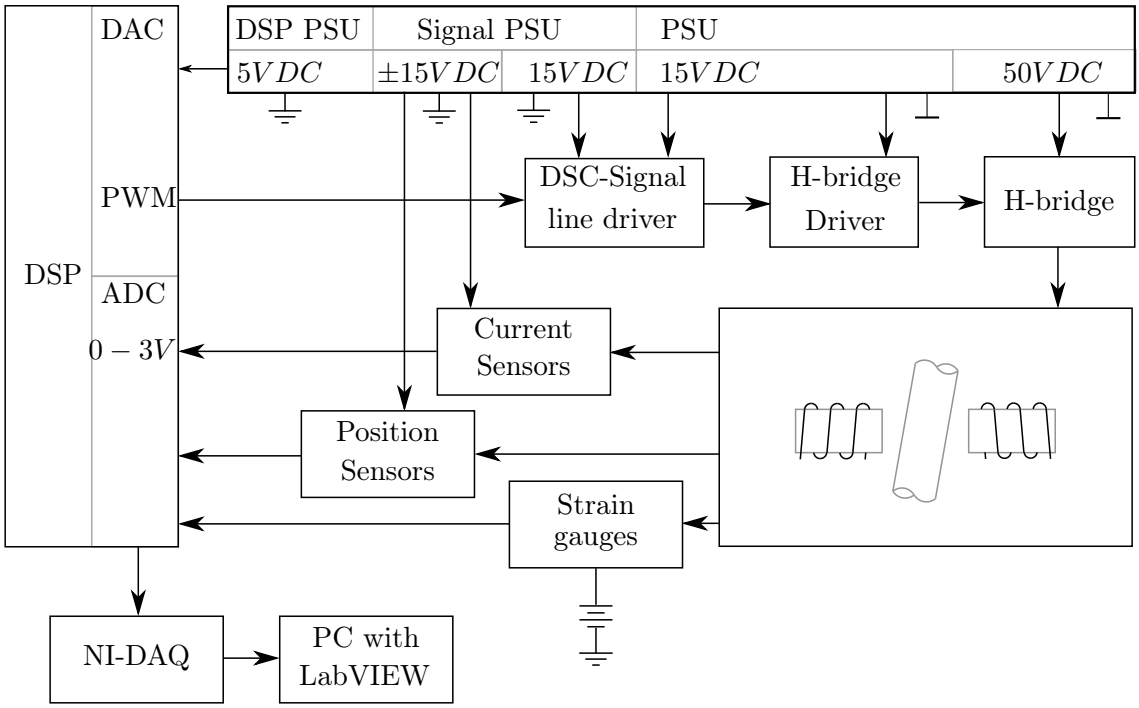

Figure 4.1: *The electrical system for actuators, sensors, and data logging on the magnetic bearing experimental setup. Left: DSC with ADC and DAC. Top: Power supplies with two common points. Lower right: AMB experimental setup.*

The system has two galvanically isolated electrical systems, with their respective common points, as illustrated in the above figure. This is introduced to avoid high voltage to destroy any of the sensitive components in the system, e.g. the DSC. Practically this is done with fiber-optic cable before the digital signal from the DSC is amplified.

4.1 Galvanic isolation

To isolate the two common points of the system, the sensitive components e.g. DSC, distance sensors and their power supply are located physically apart from the power electronics. To connect the PWM signal from the DSC to the H-bridge driver, while keeping them galvanically isolated, a fiber-optic cable is utilized. This requires a transmitter and a receiver board, where a fiber-optic cable can be used between them, also allowing for a greater distance between the two systems. Initially this isolation was achieved with an optocoupler circuit, but the parasitic capacitance of this device made it ineffective for decoupling. This problem with optocouplers was identified with the help of Schneiders Practical Installation guidelines, [Schneider, 2000], and the original board that was used for decoupling, can be found in Appendix C.3.

4.2 H-bridge Driver and H-bridge

The power circuit consists of a semi-passive H-bridge circuit and a driver circuit for the bridge. They are both depicted in Figure 4.2. The Semi-Passive H-bridge makes control of the coil voltage, by PWM, possible, since the electromagnet is an inductive load, the current can be controlled, to near DC values, using a sufficiently high PWM frequency.

The bridge consists of two N-Channel Metal-Oxide-Semiconductor Field-Effect Transistors (MOSFETs) and two diodes, indirectly four diodes since the MOSFETs contain diodes. The two transistors are paired and are both either on or off simultaneously. When both transistors are turned on, the coil is excited with the full DC-link voltage. When both transistors are turned off the voltage drop across the coil is reversed to minus the DC-link voltage. The reason for using a semi-passive H-bridge is that only current in one direction is needed in an electromagnet. Flux in the air gap can only pull the rotor towards the stator pole, no matter the current/flux direction. For supplying the coil a laboratory power supply of up to $50V$ is used. A driver circuit, for the N-channel MOSFETs in the bridge circuit, is needed to bootstrap the voltage for the high side MOSFET. The circuit diagram of the driver circuit can be found on attached CD.

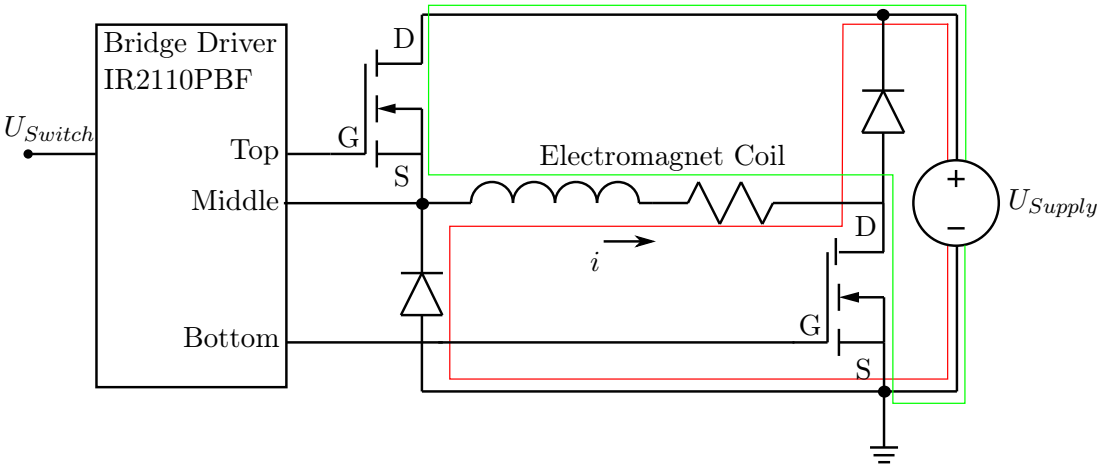

Figure 4.2: *Semi Passive H-bridge for applying $\pm U_{supply}$ to the coils. Green line indicating current path with transistors on and red line indicating it with the transistors off.*

To ensure that the MOSFETs can dissipate the power loss, that occur during the on state and state switching, the highest allowable switching frequency is found. A good approximation of the power loss in a switch can be obtained using (4.2.1) and (4.2.2) [Mohan et al., 2003].

$$P_{switch} = \frac{1}{2} \cdot U_{Supply} \cdot I_{max} \cdot f_{switch} \cdot (t_{on} + t_{off}) \tag{4.2.1}$$

$$P_{on} = R_{on} \cdot I_{max}^2 \cdot \frac{t_{high}}{t_{cycle}} \tag{4.2.2}$$

Using values from the component data sheets the maximum operating frequency of the MOSFET at I_{max} of $9.5A$ and a U_{Supply} at $40V$, before reaching the dissipation capabilities of a passively cooled MOSFET, is found in equation (4.2.3). Where the sum of the power described is solved for the maximum operating frequency. $38W$ is the power the component can dissipate at room temperature without any additional modifications. $\frac{t_{high}}{t_{cycle}}$ is the dutycycle of the PWM.

$$\frac{2(38W - 0.36\Omega \cdot 9.5A^2 \cdot 1)}{40V \cdot 9.5A \cdot (248ns + 320ns)} = 51.0 \cdot 10^3 Hz \tag{4.2.3}$$

The highest switching frequency (4.2.3) far exceeds what is necessary to control the bearings. Also the calculations are conservative since the dutycycle is a 100% and the

current is the maximum rating of the component. This situation will never occur on the test setup since the current is limited by fuses, with a rating lower than the component maximum rating, to avoid over current. For a conservative figure, a duty cycle of a 100% is used, even though there would be no switching in practice, and thus zero switching loss.

4.2.1 RC Snubbers

The semiconductor devices in the H-bridge are sources for both large $\frac{dV}{dt}$ and $\frac{di}{dt}$, which introduces noise and excessive voltage levels at the switches because of the stray inductance in the wires and Printed Circuit Board (PCB). To reduce these effects, snubbers are added to the circuits based on NXP Semiconductors [2012]. Most of the $\frac{dV}{dt}$ problems experienced in the H-bridge circuit arise from ringing. Ringing occurs during and after reverse recovery of the semiconductors. The parasitic capacitance of the MOSFET and the inductance of the PCB trace effectively create an oscillation circuit. To damp the oscillation an RC circuit is used to dissipate the energy oscillating in the LC circuit. The capacitance is added to avoid a short circuit, bypassing the MOSFET. A simplified circuit of the left leg of the H-bridge circuit is shown Figure 4.3. This simplified circuit is valid when the MOSFET is turned off, and in this model the MOSFET is replaced by a stray capacitance, and the trace inductance is added. The RC snubber consists of R_S and C_S.

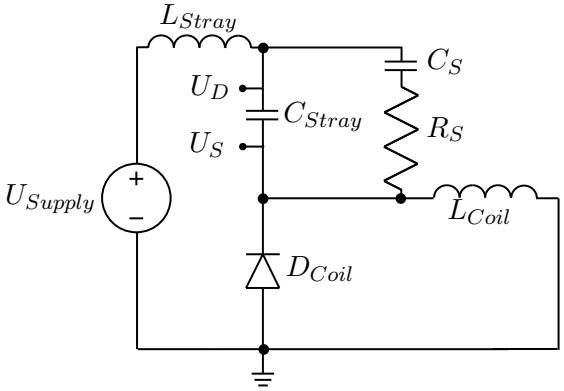

Figure 4.3: *Simplified H-bridge model for design of RC snubber.*

To find L_{Stray} and C_{Stray}, two measurement are made, at this point no snubber is present. U_D to U_S is measured during turn-off, then a small known capacitor is added in parallel to C_{Stray} to change the capacitance of the LC circuit. Noting the two different ringing frequencies, and using equations (4.2.5) C_{Stray} is found.

$$x = \frac{f_{original}}{f_{altered}} \tag{4.2.4}$$

$$C_{Stray} = \frac{C_{add}}{x^2 - 1} \tag{4.2.5}$$

$f_{original}$ is found from Figure 4.4 as the unaltered ringing frequency. It is found to be around $10MHz$. A temporary capacitance of $2.2nF$ is added and the altered frequency is measured and found to be $3.7MHz$. Thus C_{Stray} is found to be $0.36nF$.

Knowing that the ringing frequency of a LC circuit can be found using (4.2.6), the

inductance is found.

$$f_{original} = \frac{1}{2\pi\sqrt{L_{Stray}C_{Stray}}} \tag{4.2.6}$$

Using the aforementioned values the inductance L_{Stray} is $0.712\mu F$.

Deciding which snubber components to use are now a matter of damping the LC-circuit. The damping is increased through the added resistance of the snubber. The resistor is chosen using equation (4.2.7), where the resistance is derived as a function of damping. Choosing critical damping $\zeta = 1$ should yield a non oscillating circuit.

$$R_S = \frac{1}{2\zeta}\sqrt{\frac{L_{Stray}}{C_{Stray}}} \tag{4.2.7}$$

Choosing a snubber capacitor is not as straight forward. The snubber capacitance alters the LC circuit and thus the ringing frequencies and if chosen poorly can also disturb the PWM signal. A recommendation from the source of this design guide is used. Which advises to choose the capacitor such that the R_S and C_S cut off frequency is $f_{original}$. Thus C_S is found using.

$$C_S = \frac{1}{2\pi R_S \cdot f_{original}} \tag{4.2.8}$$

The snubber capacitance is found to be 0.7nF.

With the snubber implemented the ringing is reduced significantly, as shown in Figure 4.4. Though it is not critically damped as the design suggests, for the purpose of reducing the Electromagnetic interference (EMI), this snubber is adequate.

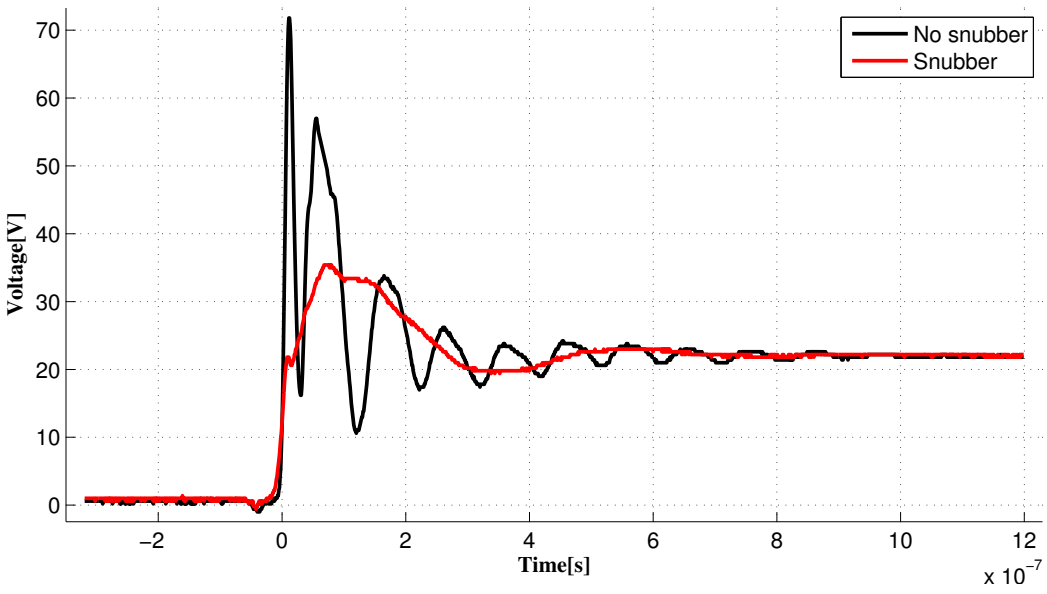

Figure 4.4: *Voltage drop across the high side MOSFET without and with a snubber circuit added.*

4.3 Current sensor

In this section the current sensor electronics for the control system is presented. For current sensing LA 25-NP Hall Effect sensors are used. The measurement circuit is

seen Figure 4.5. These sensors provide galvanic isolation of the DSC circuits from the power electronics. The sensor works as a variable current source generating a current nearly linearly dependent of the input current. The input current to output current relationship is determined by how the measured current is fed through the LA 25-NP sensor module. Different ratios can be obtained through different connection schemes. Choosing a maximum current of $9A$ yields a ratio of $4 \cdot 10^{-}3$ between input and output current, according to the module data sheet.

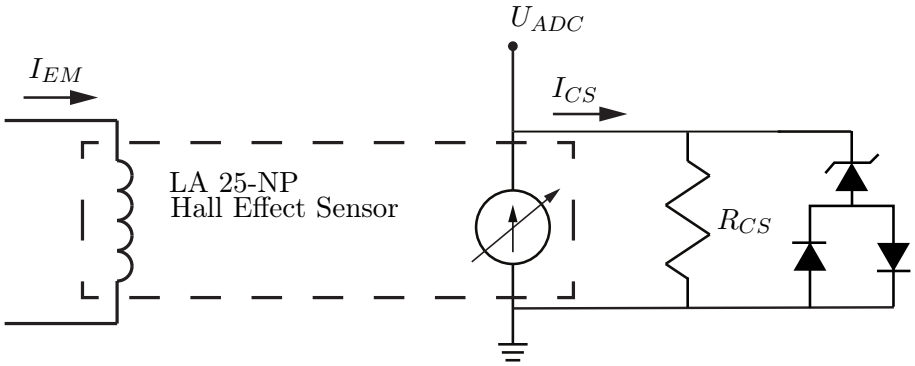

Figure 4.5: *Current sensor circuit. The hall sensor galvanically isolated the measurement circuit from the power electronics.*

A resistance is placed in series with the current source and is chosen such that the highest source current corresponds to the highest voltage the ADC modules of the DSC can handle. The Zener diode and the diodes act as over voltage protection with respect to the DSC. The Zener diode has a breakdown voltage of approximately four volts, thus U_{ADC} is limited between approximately -0.7 and 4 volts.

	Relevant performance values
Bandwidth	150kHz
Linearity	$\pm$ 0.2 %
Response time (90% of current)	< 1 μ s

Table 4.1: *Table of relevant data on the LA 25-NP Hall Effect sensor.*

The current sensors were initially placed close to the power electronics. This caused unforeseen noise in the measurements and in the power supply that supplies the current sensors. This noise propagated too the distance sensors, practically rendering them inoperable. To avoid this issue, the current sensors were moved to the experimental setup chassis and mounted close to the coils instead of close to the power electronics. Further decoupling of the DC supply and a relocation of the measuring resistor to a board close to the DSC reduced the noise, and its propagation to the other measuring circuits.

4.4 Distance sensor

In the design of a feedback control system for a magnetic bearing, the most obvious parameter to control is the position of the axle, with a fixed setpoint where the axle and bearings are coincident. Instead of choosing a commercially available position sensor, the

sensor topology is chosen, designed, tested and manufactured by the project group. It may seem ill advice to design and build the distance sensors, but since the project is educational, this endeavor is used as a challenge and a learning experience. A secondary benefit of this is saving money since commercially available sensor for these kinds of systems are not cheap. For this kind of no-contact distance sensors a range of different technologies are available [Kaman Sensors, 2012].

4.4.1 Candidate technology

It seems that the inductive Eddy current technology offers the best resolution and speed, given that the axle material can conduct electrical current [Kaman Sensors, 2012]. This technology is made commercially available, with a sensor circuit that oscillates at medium to high frequency. The sensor induces a voltage in the target material, and a magnetic field arises due to the eddy currents, that interacts with the sensors magnetic field. A change in the sensor air gap, then changes the magnetic circuit and thus the inductance of the sensor. This change in inductance is measured and converted into a DC voltage. To measure this change an AC impedance bridge, driven by a sine wave, is used. Measuring the relative change in impedance of the sensor directly relates to the relative change in inductance.

4.4.2 Measuring displacement with an AC impedance bridge.

A Wheatstone bridge is used for measuring small changes in resistance, e.g. in strain gauges where the ohmic resistance in the gauge increases linearly with strain. If the bridge in Figure 4.6, is driven by a sine wave at points A-C, the balance in the bridge will shift if one of the inductances change, and this change will cause a voltage difference between D-B. In this configuration the bridge will be referred to as a AC impedance bridge.

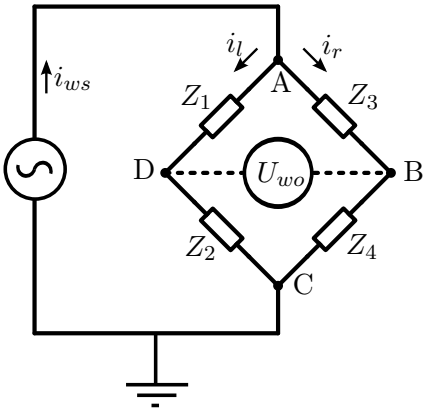

Figure 4.6: *AC impedance bridge for measuring relative change of inductance, and thus position for the distance sensor.*

The frequency of the sine wave is set to $1MHz$, for a few reasons, primarily that the sensor coil needs to induce a voltage in the target material, which will increase with frequency. Furthermore the signal has to be rectified and filtered, and a good filter performance is easier to achieve, with regards to ripple and bandwidth of the sensor, when using a high frequency. An even higher frequency signal would have even better performance, but the

chosen medium frequency of $1MHz$ is the best trade-off between performance, and what is achievable with the available electrical components.

Referring to Figure 4.6, Z_4 is the sensor coil, and Z_2 a reference coil identical to the sensor coil. The purpose of the reference coil is to cancel out the temperature drift in the bridge, by placing it close to the sensor coil, where it cannot be affected by the target material, only temperature. Impedances Z_1 and Z_3 are purely resistive, ideally, and the difference in voltage drop over these resistances will in effect be the measured output U_{wo}.

For the purpose of choosing appropriate values for the bridge, its equations must be set up and solved for i_r and i_l. The output, U_{wo}, is assumed to draw no current, as this voltage difference is measured with a very high impedance.

The equivalent impedance, Z_{eq}, for the parallel circuit is:

$$Z_{eq} = \left(\frac{1}{Z_1 + Z_2} + \frac{1}{Z_3 + Z_4} \right)^{-1} \tag{4.4.1}$$

$$i_{ws} = i_l + i_r \tag{4.4.2}$$

$$-Z_3 i_r - Z_4 \cdot i_r + Z_1 \cdot i_l + Z_2 \cdot i_l = 0 \tag{4.4.3}$$

$$U_{ws} - z_{eq} \cdot i_{ws} = 0 \tag{4.4.4}$$

Solving (4.4.3) and (4.4.4) for i_r and i_l yields:

$$i_l = \frac{U_{ws}}{Z_1 + Z_2} \tag{4.4.5}$$

$$i_r = \frac{U_{ws}}{Z_3 + Z_4} \tag{4.4.6}$$

The output from the bridge is then given by the voltage difference between points D and B, as earlier mentioned:

$$U_{wo} = Z_1 \cdot i_l - Z_3 \cdot i_r = \frac{Z_1 \cdot U_{ws}}{(Z_1 + Z_2)} - \frac{Z_3 \cdot U_{ws}}{(Z_3 + Z_4)} \tag{4.4.7}$$

Using RMS values, the four impedances in the bridge are:

$$Z_1 = R_1 \tag{4.4.8}$$

$$Z_2 = R_{ref} + R_2 + 2 \cdot \pi \cdot f \cdot L_{ref} \tag{4.4.9}$$

$$Z_3 = R_3 \tag{4.4.10}$$

$$Z_4 = R_{sensor} + R_4 + 2 \cdot \pi \cdot f \cdot L_{sensor} \tag{4.4.11}$$

Where:

R_1 to R_4 are resistances.
R_{ref} and R_{sensor} are the coil resistance for the reference and sensor coil respectively.
L_{ref} and L_{sensor} are the corresponding inductances.

Inserting this into equation (4.4.7) yields:

$$U_{wo} = \frac{R_1 \cdot U_{ws}}{(R_1 + R_{ref} + R_2 + 2 \cdot \pi \cdot f \cdot L_{ref})} - \frac{R_3 \cdot U_{ws}}{(R_3 + R_{sensor} + R_4 + 2 \cdot \pi \cdot f \cdot L_{sensor})} \tag{4.4.12}$$

In this application the objective is to measure a displacement, and this displacement changes the inductance of the sensor coil. Getting a large signal from the AC bridge is advantageous, and according to (4.4.12), getting a large signal, $\frac{dV}{dL_{sensor}}$, requires small resistances under the conditions that R_1 and R_3 cannot be omitted, so that a too large current is not drawn from the source. A large voltage difference in the bridge, relative to the change in sensor inductance is desirable, as this larger sensor signal requires less amplification in the sensor circuit. Generally, the smaller the gain necessary to condition the signal for the ADC, the smaller the problems with ripple and noise.

4.4.3 Principle of signal conditioning

The principle of obtaining the signal itself, the result of a voltage difference in a AC impedance bridge, was explained in the previous section, but it is roughly in the range of $0 - 10mV$, and therefore needs amplification to utilize the full resolution of the ADC. This principle is visualized with a flowchart in Figure 4.7. The next steps in the signal conditioning are explained here chronologically, because of prior explanation the sensor and the bridge itself are omitted:

- Instrumentation Amplifier (Inamp):
  To measure the voltage difference between the two signals an Inamp is used. This device consists of three Operational Amplifiers (Opamps), and features a very high input impedance, and thus it is ideal for use in measurement bridges. The high input impedance prevents pollution of the small measurement signal.

- Inverting amplifier:
  This Opamp stage is used for amplifying the signal. It is used in an inverting configuration and therefore also inverts the signal(Recommended by the component manufacturer).

- Inverting rectifier:
  As the voltages in this system are relatively small, further amplification is necessary. A precision rectifier is chosen to rectify the signal, and is also used to provide an additional gain to the signal. The voltage drop occurring from use of a conventional rectifier bridge is eliminated, and as mentioned also adds an additional amplification stage.

- Filter:
  Filters the rectified signal to obtain a DC voltage.

- Inamp:
  For the sensor circuit to be useful, it must be able to amplify and offset the filtered

DC signal, this makes it possible to use the sensors in different operating ranges, thus facilitating sensor calibration. This is done by using an Inamp in a configuration with potentiometers.

- DSC protection:
  The last active stage of the system has a rail-to-rail supply of $\pm 15V$, and is thus able to supply voltages well out of the range of the DSC, that can handle voltages from 0 to $3V$. This final function of the sensor electronics, protects the DSC from these voltages, during calibration, start up or malfunction.

These overall stages of the system and their components, will be elaborated in their respective sections.

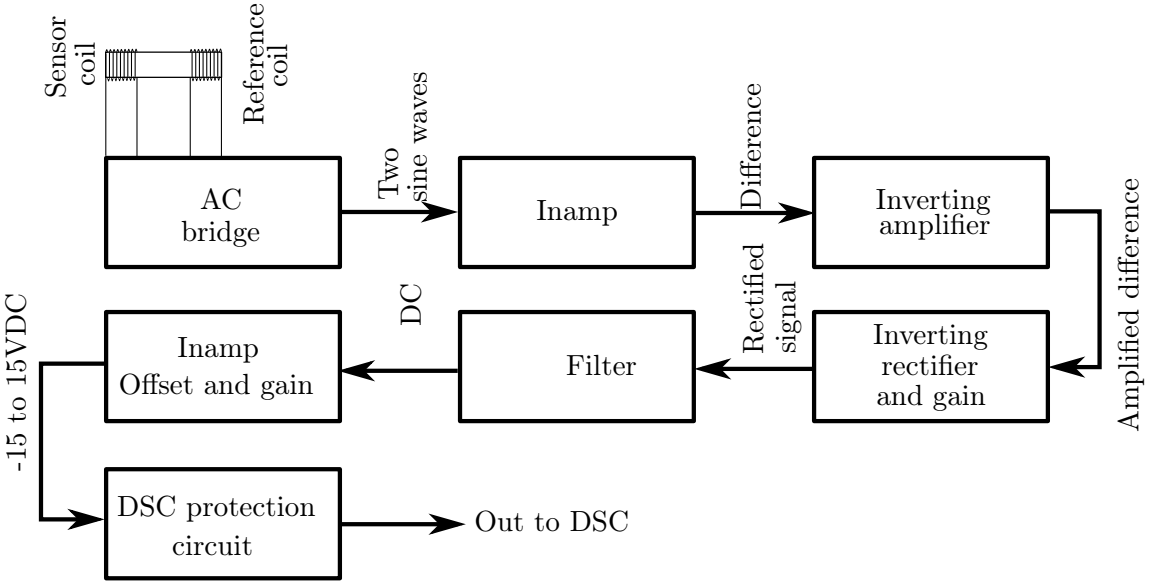

Figure 4.7: *Working principle of the distance sensor. A relative change in position increases the difference between the reference coil and the sensor coil inductance, and this signal is converted into a DC voltage.*

For visualization purposes, some important signals from the system are shown in Figure 4.8, where the amplification of the signal between the stages also are clear. The data are from the SPICE model of the system, and this exhibits some oscillations in the precision rectifier stage, that are not present in the actual system.

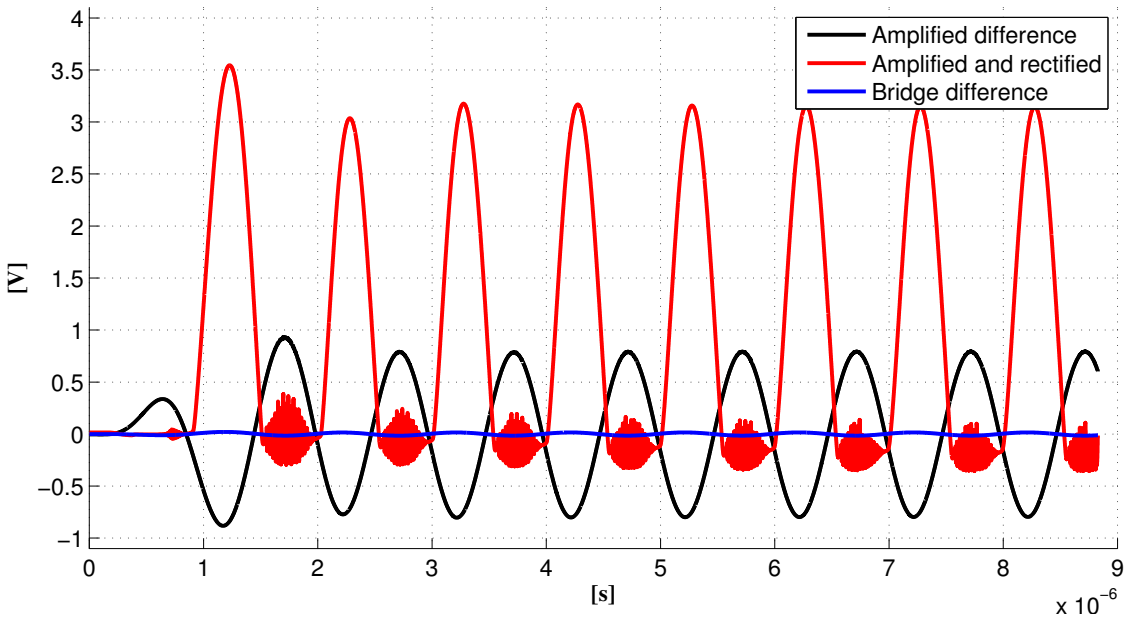

Figure 4.8: *Simulation result showing the small signal being amplified and rectified in the three stages after the AC impedance bridge.*

4.4.4 Sensor base and coils

The physical sensor that is to be placed in close proximity of the axle, in order to determine its position is a small piece of machined polymer, with grooves for the two coils and thread for mounting the sensor on the experimental setup, the sketch for this is depicted in Figure 4.10. The four wires of the sensor are soldered to a shielded cable, and the other end is fitted with a Deutsches Institut für Normung (DIN) connector, for connecting it with the PCB through the aluminum box that holds the measuring electronics. The effective measurement distance for a coil of this type, is ≈ 0.5 times the diameter. A diameter of $\approx 5mm$ was chosen [Kaman Sensors, 2012]. Not much effort was put into investigating and analyzing the sensor dimensions and the coils. The coils were simply wound with 25 turns each and this resulted in a satisfactory signal. A sensor can be seen in Figure 4.9, mounted with two nuts to a aluminum bracket. The coils are not visible as they are protected by electrical tape.

Figure 4.9: *Photo showing the position sensor mounted on the experimental setup.*

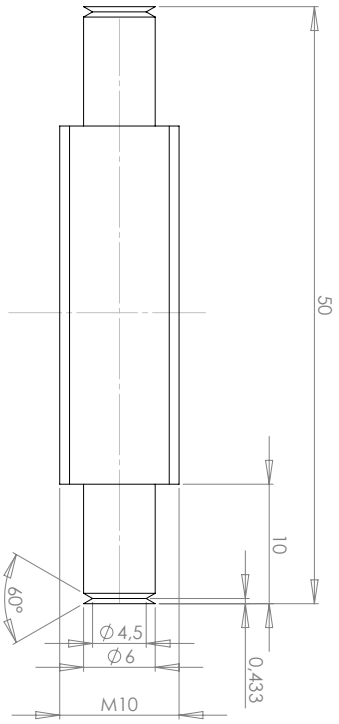

Figure 4.10: *Technical drawing for fabrication of threaded bases for the sensors. The thread is for mounting purposes, and the grooves are for coil mounting.*

4.4.5 Instrumentation amplifier

The Inamp is ideal for measuring the output of a bridge, but because the bridge is excited by a $1MHz$ sine wave, the bandwidth must at least match this frequency. Of the ready available components, this is the case for the AD620 [Analog Devices, AD620, 2011]

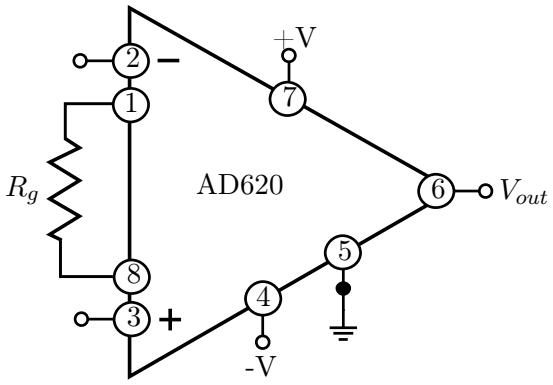

Figure 4.11: *AD620 Instrumentation amplifier used for measuring the shift in the AC impedance bridge. Furthermore it is used to condition the DC voltage to the correct range and offset.*

The symbol of the Inamp is shown in Figure 4.11, and this will be the starting point for a brief introduction. First of all the device must be supplied with both positive and negative voltage, a so-called rail-to-rail voltage, up to $\pm 18V$ (4&7). The Inamp outputs the voltage difference between the inverting and non-inverting pins (2&3), at the V_{out} pin

(6), referenced to pin (5) - the reference pin. This signal can be amplified by choosing the appropriate R_g, for the desired gain. For DC signals, gains from $1 - 10,000$ can be chosen, but at a frequency of $1MHz$ the gain is limited to 1 by the Inamp bandwidth.

In this application R_g is left unconnected, resulting in a gain of 1, inverting and non-inverting inputs are connected to points D and B of Figure 4.6 respectively and the reference pin is connected to GND.

4.4.6 Operational amplifier

Operational amplifiers are used in two of the stages, refer to Figure 4.7, that is the inverting gain stage and as a precision rectifier. The inverting gain configuration is presented Figure 4.12, where the ratio between R_1 and R_2 yields amplifier stage gain. An important parameter in this application, and often specified in Opamp datasheets is the Gain-bandwidth product (GB), which is defined by:[Sedra and Smith, 2004]

$$GB = f_b \cdot G_a \tag{4.4.13}$$

Where f_b is the bandwidth, and G_a is amplifier gain. With a signal of $1MHz$, the GB is equal to the gain that the device can deliver. Of the available amplifiers, the AD844 has a sufficient GB, up to $320MHz$ depending on the configuration of the amplifier.

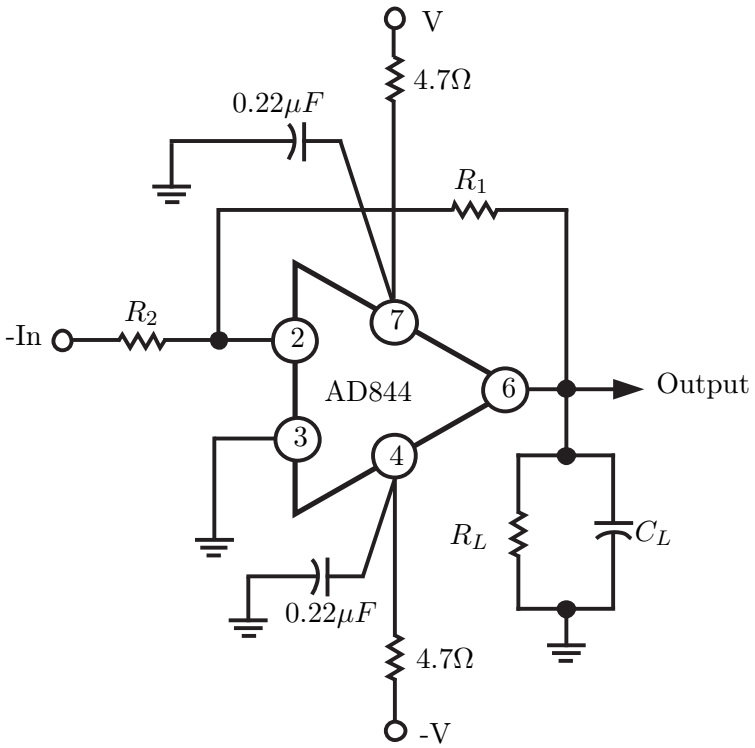

Figure 4.12: *AD844 operational amplifier, configured in an inverting gain configuration according to manufacturer.[Analog Devices, AD844, 2009]*

The inverting amplifier is set up to deliver a gain of -75.

The $AD844$ is also used for another purpose, namely the precision rectifier that is necessary to convert the signal to a DC signal. Using the topology proposed in [Ducu, 2011,Improved Op Amp Half-Wave Rectifier], utilizes few components and has

the necessary performance when combined with the AD844. The application note also recommends Schottky diodes, for fast recovery time and low voltage drop. The rectifier in the mentioned configuration is seen in Figure 4.13.

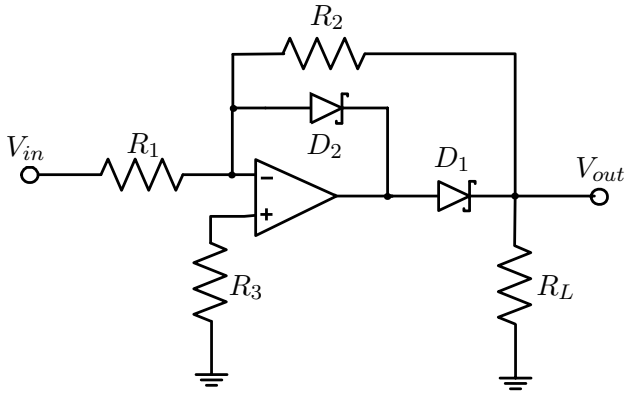

Figure 4.13: *Halfwave Inverting Rectifier. Active rectifier able to gain and rectify a signal with an Opamp and two Schottky diodes.[Ducu, 2011]*

Because this is a half wave rectifier only, half of the potential signal is rejected. Using a single Opamp full wave rectifier is less robust, more difficult to tune and a full wave rectifier using two stages increases component count, complexity and cost. Furthermore the chosen configuration can be configured with a gain, just like the inverting gain of Figure 4.12, by the ratio between R_1 and R_2, compensating for the loss of the rejected signal and potentially amplifying the signal further.

4.4.7 Filtering

The half wave rectified signal needs to be filtered to a point, where the ripple in the signal does not affect the Least Significant Bit (LSB) of the ADC. In other words the ripple should not affect the measurement, and thus must be smaller than the resolution of the ADC. A passive Butterworth low-pass filter has been chosen for filtering the rectified signal, because of its flat pass-band characteristics and simple design. A set of requirements for the filter is set up, before designing the filter.

Specifications:

- Settling time, $T_s < 50\mu s$.
- Stop band frequency, f_{SB}, $1MHz$.
- Pass band frequency, f_{PB}, depends on T_s.
- Stop band attenuation, G_{SB}, $< -100dB$.
- Pass band gain, G_{PB}, $> -6dB$.

The graphical interpretation of the specifications for the filter can be seen in the next Figure, 4.14

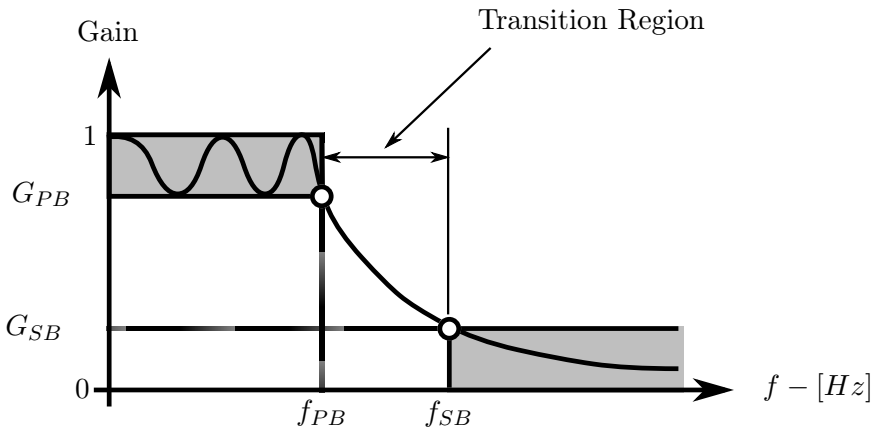

Figure 4.14: *Specifications for a low-pass filter.[Allen, 2008]*

Using MATrix LABoratory (MATLAB)s Filter Design and Analysis Tool (FDATool), it becomes clear that a $4th$ order Butterworth filter with a cutoff frequency, or f_{PB}, of $50kHz$ meets the desired requirements for the filter. This is implemented according to the procedure described in [Hagen, 1996]. The principle of this is to start out with one of two networks with capacitors and inductances, depending on the order of the filter. For even order filters like this case, the network is based on the topology of Figure 4.15, that handles N-order even filters.

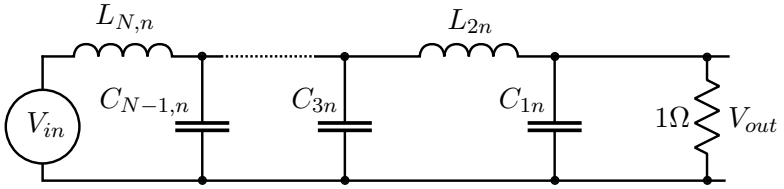

Figure 4.15: *Topology for a N-order low-pass filter, n indicates normalized values.[Allen, 2008]*

The values for the components are tabulated for a normalized filter, with a cutoff frequency of $1Hz$ and a impedance of 1Ω. The magnitude of the component values must then be adjusted to match the corner frequency and impedance of the filter.

Table values:

$$C_{1n} = 0.382F$$
$$L_{2n} = 1.0824H$$
$$C_{3n} = 1.5772F$$
$$L_{4n} = 1.5307H$$

Z_0 is a factor for the wanted filter impedance, a unit-less quantity chosen as 1000, to get a filter impedance of $1k\Omega$. The pass-band frequency,f_{PB}, is also used for scaling, unit-less.

The scaling is done according to the following:

$$C_i = \frac{C_i n}{Z_0 \cdot f_{PB} \cdot 2 \cdot \pi} \tag{4.4.14}$$
$$L_j = \frac{Z_0 \cdot L_j n}{f_{PB} \cdot 2 \cdot \pi} \tag{4.4.15}$$

$i = odd; j = even$ The result of this can be seen in Figure 4.16

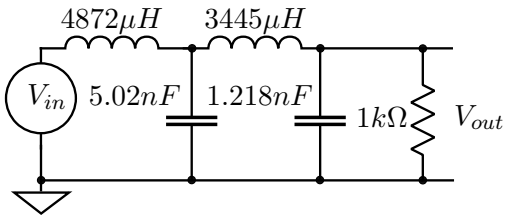

Figure 4.16: *Ideal implementation of a 4th order Butterworth filter in LTspice IV.*

This poses some challenges, as components with exact values can be hard to find or construct. A SPICE model with available components as close as possible to the ideal can be seen in Figure 4.17, which also incorporates the resistances of the actual components, and a approximate value for the resistance in the PCB. Notice that the values are rounded as a result of matching with available components.

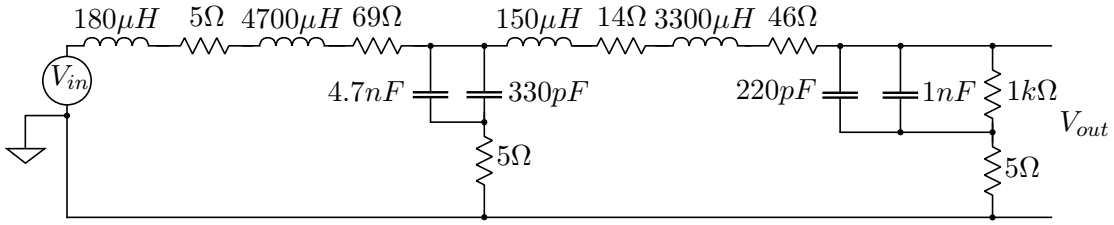

Figure 4.17: *SPICE model of the Butterworth filter with ohmic resistances and actual components values.*

An AC sweep is performed on this circuit in LTSpice, to construct a Bode plot of this model, and the result is shown in Figure 4.18. Furthermore all values have been multiplied by a factor of k, to see how sensitive the filter is to component tolerances. The k values are chosen for a 10% change of value, and can be identified with the figure legend. The plot labeled "ideal" is the sweep of the network of Figure 4.16.

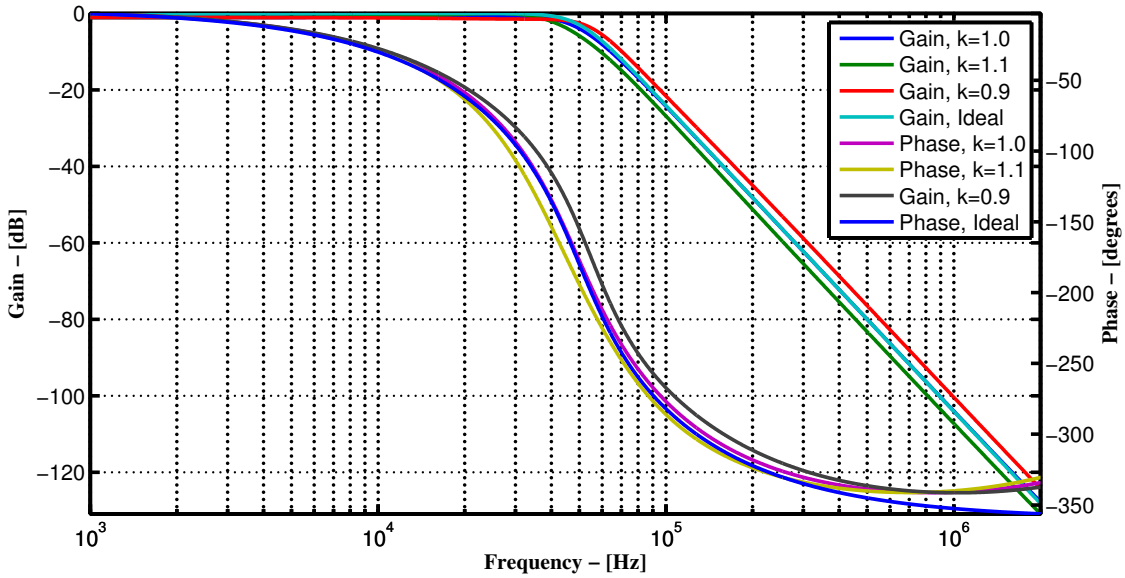

Figure 4.18: *Bode plot of the filter responses shown with regard to varying filter component values, as a measure of robustness against potential varying component values.*

The same is repeated for a step-response of the filter Figure 4.19.

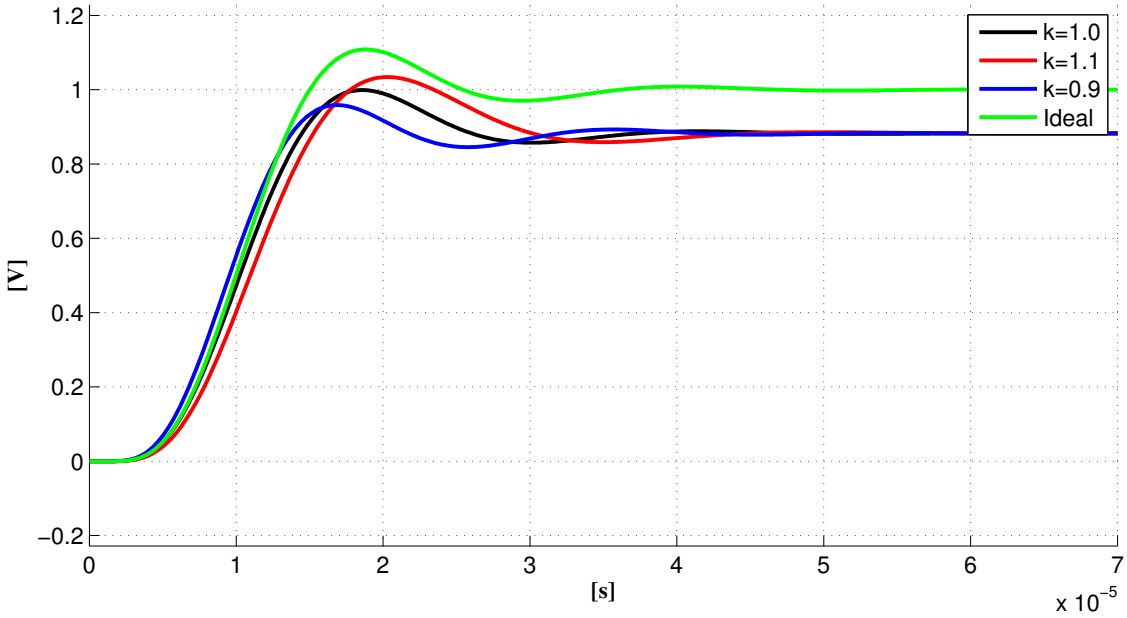

Figure 4.19: *Step-response of the designed filter to an applied step of* $1V$*. Step was applied at time* $1\mu s$*.*

The overall characteristics of the filter are not changed dramatically, attenuation at the stop band frequency and settling time are not affected beyond the specified. The most significant change, is the pass band attenuation when ohmic impedance in the filter is accounted for, this is seen in the steady state error of the step response. Although all permutations of tolerances are not trialed, component tolerances are 1%. The filter design is accepted, because the specifications presented in the beginning of this subsection are fulfilled.

4.4.8 DSC protection

The last active stage of the system is an instrumentation amplifier with a rail-to-rail voltage of $\pm 15V$.According to the datasheet of the DSC, the device is not damaged when voltage outside the range of $0-3V$ are applied to the ADC, but as an extra safety measure, components are added to restrict the output to this range. This is done by means of a Zener diode to restrict the upper range, and a PNP transistor to restrict the voltage from swinging into the negative. This is shown in Figure 4.20, which is an extract of the full schematic.

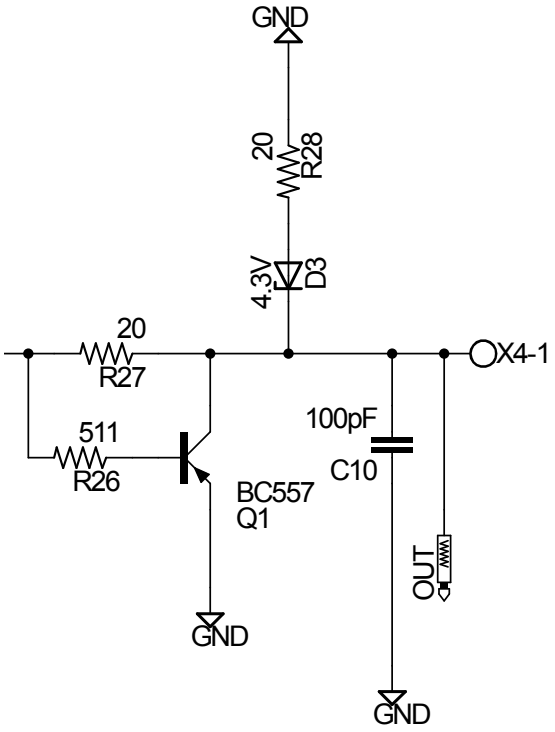

Figure 4.20: *Voltage limiting circuit protecting the DSC from over-voltage.*

This simple approach does not confine the range strictly to $0 - 3V$, but rather $-0.7V$ to $4.3V$ which will not damage the ADC. Decreasing the breakdown voltage of the Zener diode, increases leakage, and results in an increased error in the measurement.

4.4.9 Decoupling capacitors

To reduce noise in the output of the system, it must be decoupled effectively. There are two reasons for adding decoupling capacitors: Shorting high frequency noise away from a sensitive component, and acting as a reservoir on the power supply trace. [Analog devices, Decoupling Techniques, 2009]

Appendix C.1 has the full schematic for a distance sensor, and $C8$ and $C9$ are added as reservoir capacitors. In the layout of the components on the PCB, these capacitors are placed closer to the components than the supply.

For shorting high frequency noise away from the active components, $100nF$ ceramic capacitors are added according to Figure 4.21 and 4.22

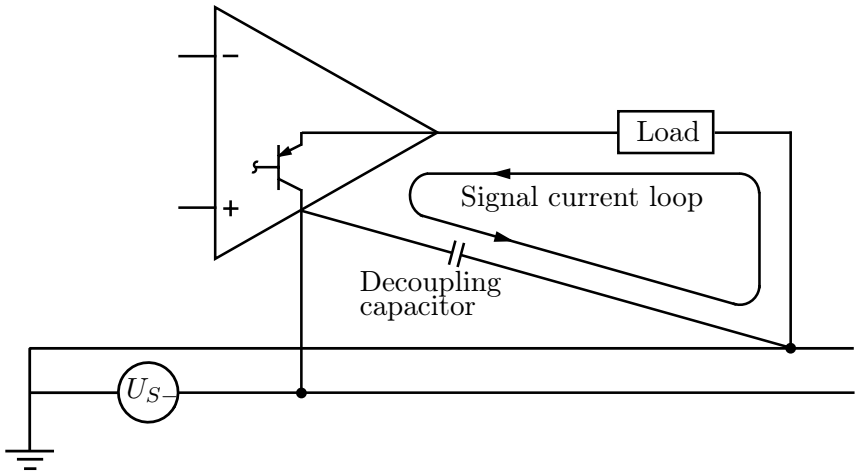

Figure 4.21: *Decoupling a grounded load driven by an Opamp.[Brokaw, 2000,Figure 3b]*

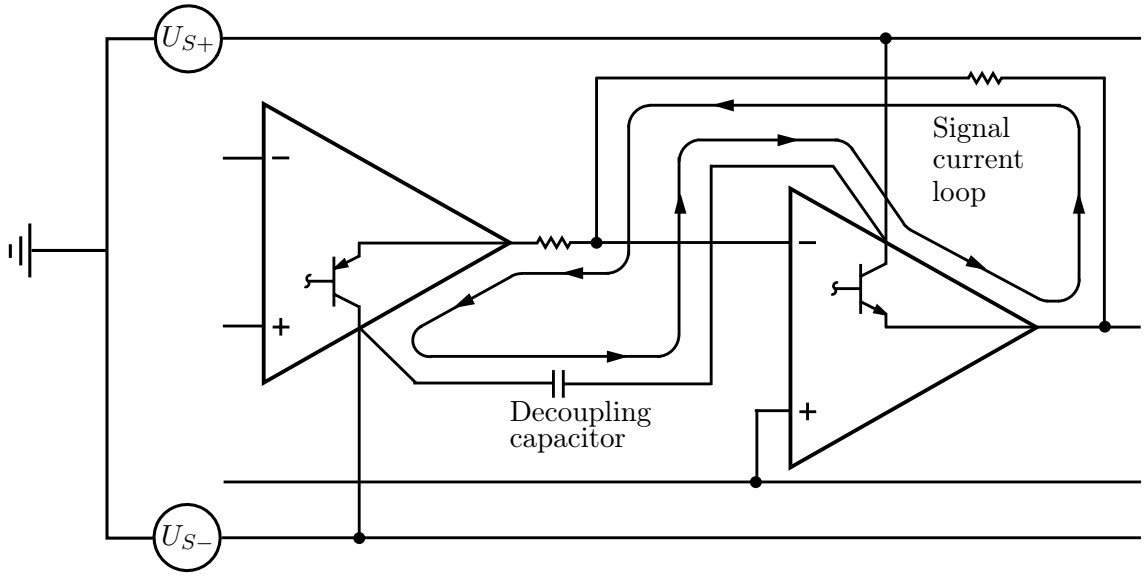

Figure 4.22: *Decoupling between two Opamps in series, also known as virtual ground.[Brokaw, 2000,Figure 3c]*

Operational amplifiers are decoupled according to Kitchin and Counts [2006,Figure 5-2], which are used in both cases of operational amplifiers as seen in appendix C.1.

Furthermore, when adding capacitors to a circuit, and realizing it on a PCB that has stray inductances resonant circuits also appear. These unwanted oscillations are damped by adding 5Ω resistors in series with the U_{S-} and U_{S+} pins of all Integrated circuits (ICs).

4.4.10 PCB considerations

Depending on the sensitivity of the circuit that are designed, the PCB design can make or break a circuit. This is because of the network of resistances, capacitances and inductances that make up a PCB, and thus affects the performance of the system. Generally all impedances must be kept as small as possible, by using wide traces for power and ground, or ideally dedicating a plane on the PCB for each. Routing the traces by hand is critical, e.g. the decoupling capacitors for the Opamp of Figure 4.21 is merely connected in

parallel between ground and the power supply - if interpreted solely from the netlist. The decoupling must be connected right at the power pins to bypass the current around the supply. Power and signal ground must be separated, and connected in a star to avoid large and varying voltage drops in the signal traces as suggested by Brokaw [2000]. The star ground topology also prevents ground loops, where currents looping in the circuit instead of running through the power supply, can cause a grounding problem for the components locally where the loop is. [Rich, 1983]
Guards are implemented at the amplifying stages, to sink stray currents. [Zumbahlen and Analog Devices, 2008,Chapter 12]

4.4.11 Carrier signal line driver

The AC bridge in the sensor circuit is driven by an external function generator, but in order not to draw any significant current from the function generator, a line driver is configured on the PCB to drive the current through the bridge. This is done with an AD841, and it is simply configured as a voltage follower with a gain of one according to the datasheet.[Analog Devices, AD841, 1988]

4.4.12 Sensor performance

The performance of the sensor in terms of both response time and noise, should be governed solely by the $4th$ order Butterworth filter, designed in section 4.4.7. After testing the sensor in the experimental setup, it is clear that the system itself in practice introduces a lot of noise, e.g. the PCB design, diodes and wiring in the box where the electronics are assembled. This drastically reduces the resolution of the distance sensors, that theoretically is only limited by the resolution of the ADC. A steady state measurement on channel 1 has been conducted with an oscilloscope over a period of 0.2 seconds, and the results from this measurement is presented in Table 4.2.

	Channel 1
s_{x1p-p}	$26.07\mu m$
σ	$2.59\mu m$
Resolution, s_{x1p-p}	36.43
Resolution, σ	60.95

Table 4.2: *Laboratory results for the four distance sensor resolutions, when idling for 0.2s.*

Where the peak to peak position is defined as:

$$s_{x1p-p} = s_{x1max} - s_{x1min} \tag{4.4.16}$$

And the standard deviation as:

$$\sigma = \sqrt{\frac{1}{n}\sum_{i=1}^{n}(s_{x1i} - \overline{s_{x1}})^2} \tag{4.4.17}$$

Resolution, s_{x1p-p}: The axle travel divided by the peak to peak voltage, as a worst case scenario for the numbers of discrete points that can be determined by the position sensor.

Resolution, σ: The axle travel divided by six times the standard deviation, which contains 99.73% of the data [Walpole et al., 2007].

Even though this resolution is inferior to the theoretically counterpart, it represents a resolution of 60.95 in 99.73% of the cases, which again represents a resolution of $15.58\mu m$ and can be accepted as a useful sensor.

4.4.13 Sensor change log

After using the distance sensor channels for an extended period of time, it became clear after troubleshooting the circuit that the AD620 was unstable, and that reducing the overall driving frequency from $1MHz$ to $500kHz$ dramatically increased the robustness of the system. Overall this has two impacts on the system, firstly that the signal from the bridge is reduced, and secondly that the filter damping of the driving signal is reduced. Because the system itself also introduces noise, also below the $50kHz$ cutoff frequency, the added noise from the driving sine wave through the filter is comparatively small, and is not the frequency seen in the data in the preceding section 4.4.12.

The smaller signal from the bridge is compensated by increasing the total gain, more specifically the gain in the first stage.

The problem: After installing the position sensors, the control system was assembled and everything was powered up. This step rendered the distance sensors useless, because noise was introduced that was beyond the reach of a filter. This was due to unforeseen phenomena, and the changes to the overall system are all mentioned here.

1. Initially an aluminum box was constructed to house all the electronics, which resulted in EMI from the H-bridges to reach the position sensor. The small distance between the power electronics and the sensor equipment, was increased and resulted in less noise.
2. A large contribution of the noise was due to the parasitic capacitance of the optocouplers. As earlier stated, this effect was completely removed by changing to a fiber-optic cable connection, which also made it possible to have a larger distance between the position sensors and the power electronics.
3. All the electronics were designed with decoupling capacitors to some degree. Further decoupling of the DC-supply, before it was distributed to the sensors, also reduced the noise. Large capacitors was already installed, but adding smaller ceramic capacitors, resulted in better high frequency decoupling.
4. Separating the electronics created a new unnoticed problem, namely that ground loops were formed with the wires that connected the current sensors to the DSC, now moved to the experimental setup. This created antennas the EMI can induce a voltage in, and thus increase the noise. These loops were removed by rewiring.
5. Noise was increased in the current sensor signals, because they had their measuring resistances placed on the same PCB as the sensor modules themselves, which is found on the attached CD. These resistances were moved close to the DSC. This way the voltage that are induced by noise, are not measured across the resistance, only the voltage drop from the sensor current.

6. While moving the measuring resistances, analogue low-pass filters were also implemented. This reduces high frequency signal noise in the signal. The main problem seemed to be that the hall elements have a significant capacitance, causing the high frequency voltage from the power electronics to pollute the measurement signals. Adding snubbers, documented in section 4.2.1, reduced ringing in the PWM voltage, and thus also the amplitude of this signal shown on the sensor side.

4.4.14 Position sensor calibration

An initial calibration of the position sensors is necessary to determine whether the sensors are linear, or can be approximated as linear. Secondary objectives of this calibration are to ensure that the sensors are within range of the ADC and to measure the actual clearance between axle and rotor. To calibrate the sensors two dial gauges are mounted on the frame of the experimental setup, and set up to measure the x translation, and then relocated to measure y. This approach was used to account for the angle, e.g. θ_y of the axle while calibrating one axis at time. Ideally four gauges would be permanently installed, but only two were available. The setup is shown in Figure 4.23. As shown in the figure, the dial gauge in the x-direction measures in the same direction as the sensor, and the dial gauge in the y-direction measures in opposite direction of the sensor. Also the axes of the sensors and gauges are offset, due to the limited space available on the experimental setup. As mentioned this potential error is minimized by calibrating one axis at a time, and keeping θ_y and θ_x small.

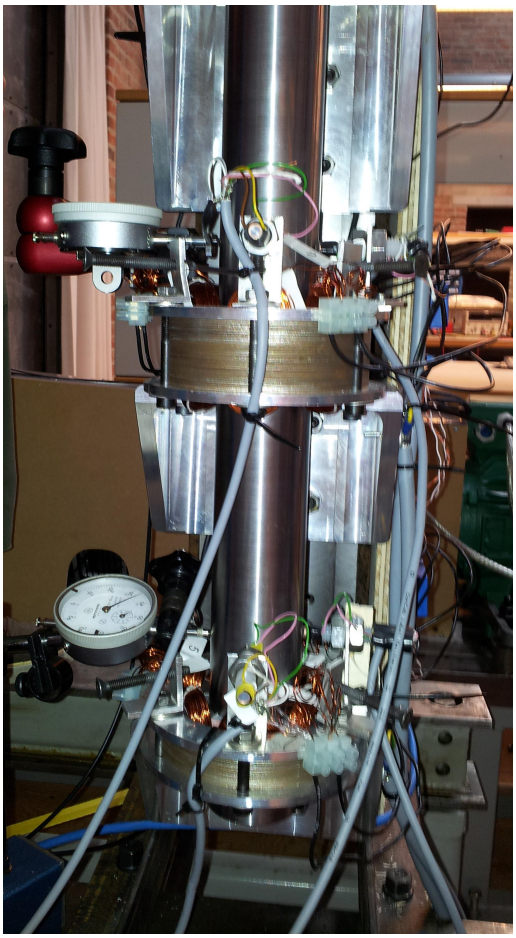

(a) Picture of the dial gauges mounted in the y direction during the calibration procedure.

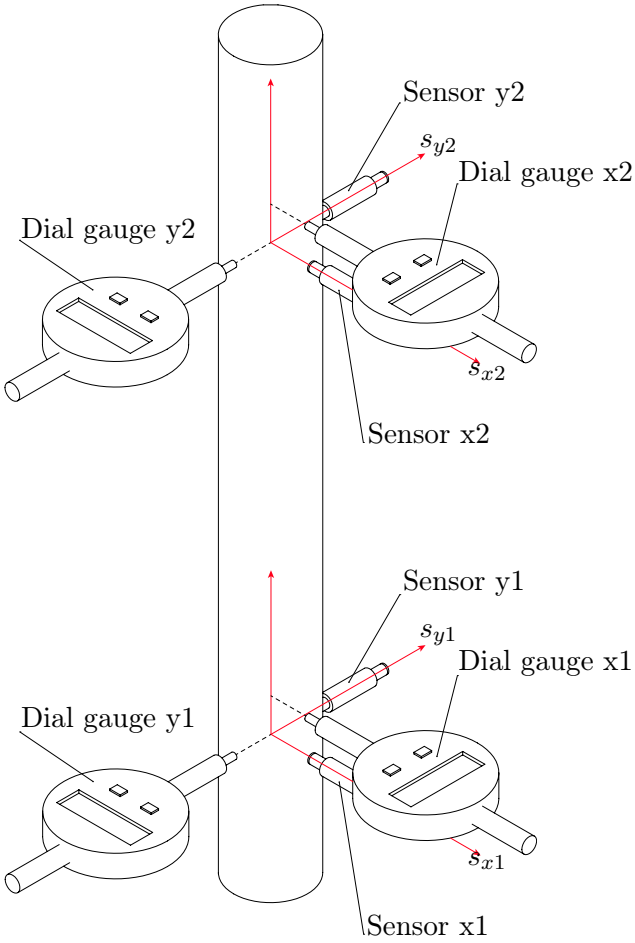

(b) Overall sketch of the calibration procedure, note that the sensors and the gauges are not on the same axis in the x direction.

Figure 4.23

For a certain number of positions the indicated gauge measure, and the sensor voltage is noted. The measurements for sensor x_{1gauge} and x_{2gauge} are shown in Figure 4.24.

The measurements show that the sensor output is not linearly dependent on displacement, this is disregarded for simplicity.

The x_{1gauge} measurement is in the span $x1 = [0mm; 0.78mm]$, which yields an air gap of $l_{gx1} = 0.39mm$. The relation between the sensor voltage and the gauge measurement can be described by:

$$U_{Sx1} = 3.2520 \cdot x_{1gauge} + 0.092686 \tag{4.4.18}$$

The relation between the gauge and the sensor coordinates can be described using the relation:

$$x_{1gauge} = s_{x1} - l_{gx1} \tag{4.4.19}$$

And the sensor voltage to coordinate transformation is:

$$s_{x1} = \frac{1}{3.2520} \cdot U_{Sx1} - l_{gx1} - \frac{0.092686}{3.2520} \tag{4.4.20}$$

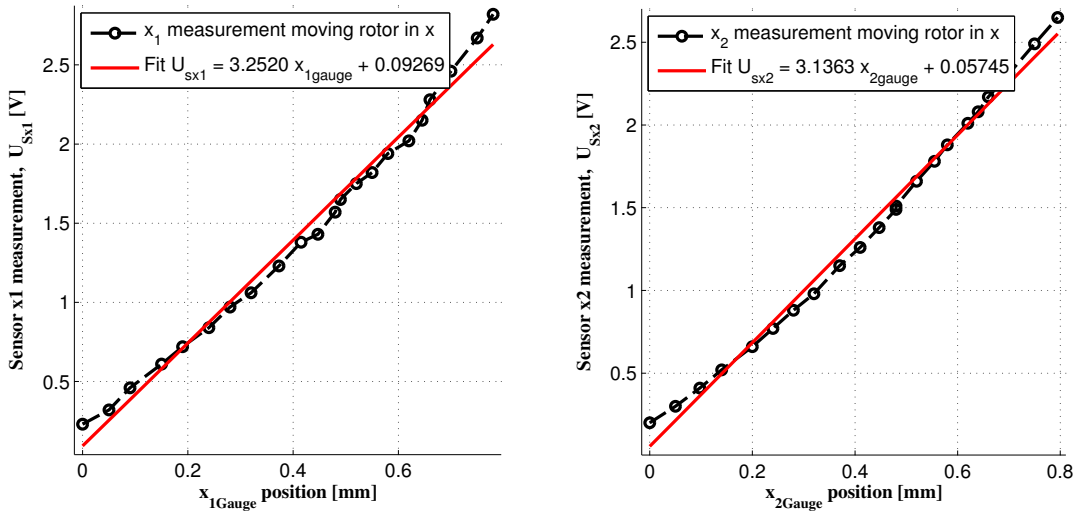

(a) *(b)*

Figure 4.24: *Sensor s_{x1} and s_{x2} calibration measurements.*

The gauge measurement x_{2gauge} spans $x_{2gauge} = [0mm; 0.795mm]$, which yields an air gap of $l_{gx2} = 0.3975mm$. The sensor voltage to coordinate transformation is:

$$s_{x2} = \frac{1}{3.1363} \cdot U_{Sx2} - l_{gx2} - \frac{0.057449}{3.1363} \tag{4.4.21}$$

The measurements for sensor y1 and sensor y2 are shown in Figure 4.25.

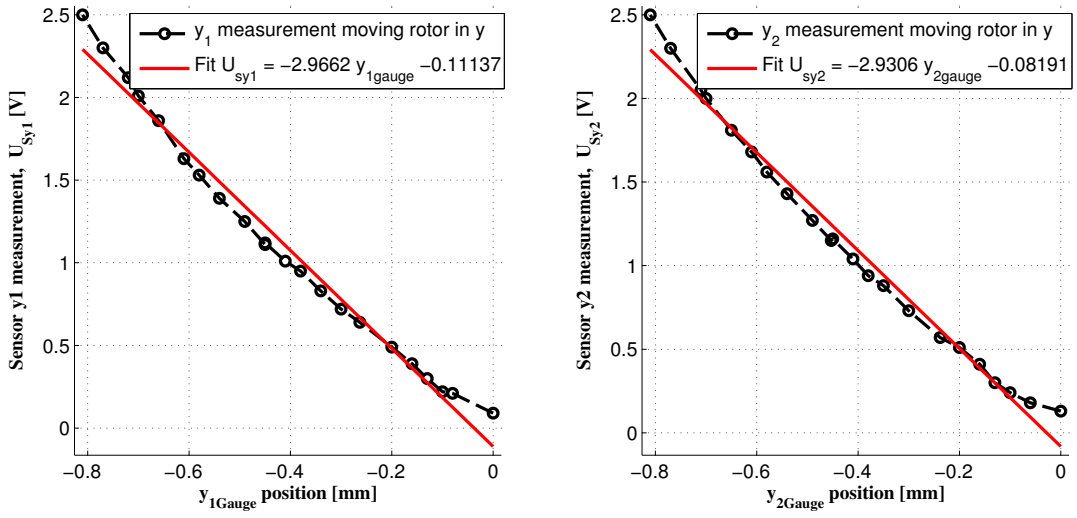

(a) *(b)*

Figure 4.25: *Sensor $y2$ and $y2$ calibration measurements.*

For the y-direction the relation between gauge and model coordinates is the opposite because of the anti-parallel measurement:

$$y_{1gauge} = s_{y1} + l_{gy1} \tag{4.4.22}$$

And the sensor voltage to coordinate transformations are described by:

$$s_{y1} = \frac{1}{2.9662} \cdot U_{Sy1} + l_{gy1} - \frac{0.11137}{2.9662} \tag{4.4.23}$$

$$s_{y2} = \frac{1}{2.9306} \cdot U_{Sy2} + l_{gy2} - \frac{0.081918}{2.9306} \tag{4.4.24}$$

And the airgaps are measured to $l_{gy1} = 0.415mm$ and $l_{gy2} = 0.4425mm$. Misalignment of the bearings is expected to be the source of this measurement being different from the airgap of $0.475mm$ measured in the experimental setup, section 3.

Practical recalibration experiences

During the development and use of the experimental setup it has been necessary to redo the calibration of the sensors, because the sensor calibration is easily ruined by simply touching the sensor wires or the sensors themselves, due to compliant brackets that was not designed to be an integrated part of the experimental setup. During these re-calibrations it was found useful to mount the dial gauges as shown in Figure 4.23 and then use the magnetic bearings to keep the axle fixed. The axle position can then be altered by changing the reference position of the bearing controller. This gave more accurate and less time consuming calibrations since the axle is hard to fixate otherwise. When using this approach only points within $\pm 200\mu m$ of the center are used, and then linearly interpolated. This increases the precision of the calibration at the center of the bearing, which is an advantage when used for verification of the model.

4.4.15 Relating sensor coordinates to bearing coordinates

Using the geometric relation between sensor coordinates and bearing coordinates, described in section 5.1.4, and the relation between sensor voltage and sensor coordinates, described in the previous section, a total transformation for implementation on the DSC can be described.

Recapitulating from equation (5.1.33) and (5.1.30) that the transformation from bearing coordinates to sensor coordinates can be described as:

$$\vec{s} = \mathbf{T_3} \cdot \mathbf{T_2}^{-1} \cdot \vec{x} \tag{4.4.25}$$

Rearranging this, the bearing coordinates are described by:

$$\vec{x} = \mathbf{T_2} \cdot \mathbf{T_3}^{-1} \cdot \vec{s} \tag{4.4.26}$$

Inserting the geometric transformations and the voltage to sensor transformations yield:

$$\vec{x} = \begin{bmatrix} 0.3804 & 0 & -0.0756 & 0 \\ 0 & 0.4171 & 0 & -0.0809 \\ 0.0758 & 0 & 0.2403 & 0 \\ 0 & 0.0831 & 0 & 0.2572 \end{bmatrix} \cdot \begin{bmatrix} U_{Sx1} \\ U_{Sy1} \\ U_{Sx2} \\ U_{Sy2} \end{bmatrix} + \begin{bmatrix} -0.4191 \\ -0.3687 \\ -0.4165 \\ -0.4054 \end{bmatrix} \tag{4.4.27}$$

This sensor rotation is used for control purposes and implemented on the DSC, which is described in the next section.

4.5 DSC

Controllers are digitally implemented with a Texas Instruments (TI) $TMS320F28335$ DSC, as it can manage this task and because of its availability. Overall a DSC is built for control purposes, meaning that it can convert data from analog to digital, and vice versa, while performing the floating point operations that are required for solving the difference equations of various filters and controllers. The primary features of the unit, and those that will be used extensively in this project is:

- 16 channels for ADC, operated by two ADC modules, operating independent of other modules.
- 6 PWM channels, operated by three PWM modules, operating independent of other modules.
- Timers for interrupt purposes.

The 16 channels for ADC is enough to read all currents, forces and positions of the system, but six channels of PWM is only enough to control the two bearings, and thus a separate DSC must be configured for the load actuator. The timing circuit will be used to control the frequency at which the controller updates the controller output, by changing the duty cycle of the PWM.

4.5.1 ADC

An ADC on a TI $TMS320x2833x$ can be set up in different configurations based on a series of combinations. For this application the module is set up to read all 16 channels sequentially, when an timed interrupt enables the Start of Conversion (SOC). The speed of the conversion itself has to be configured, and this is done by defining the time for each operation of the acquisition:

1. Sample-and-Hold (SH), charging a capacitor, is preformed during the "acquisition window" .
2. The ADC module "reads" the capacitor voltage, using one ADC clock.
3. Writing the read value to the registers, included in the "C1" time together with the ADC.

This is shown in Figure 4.26.

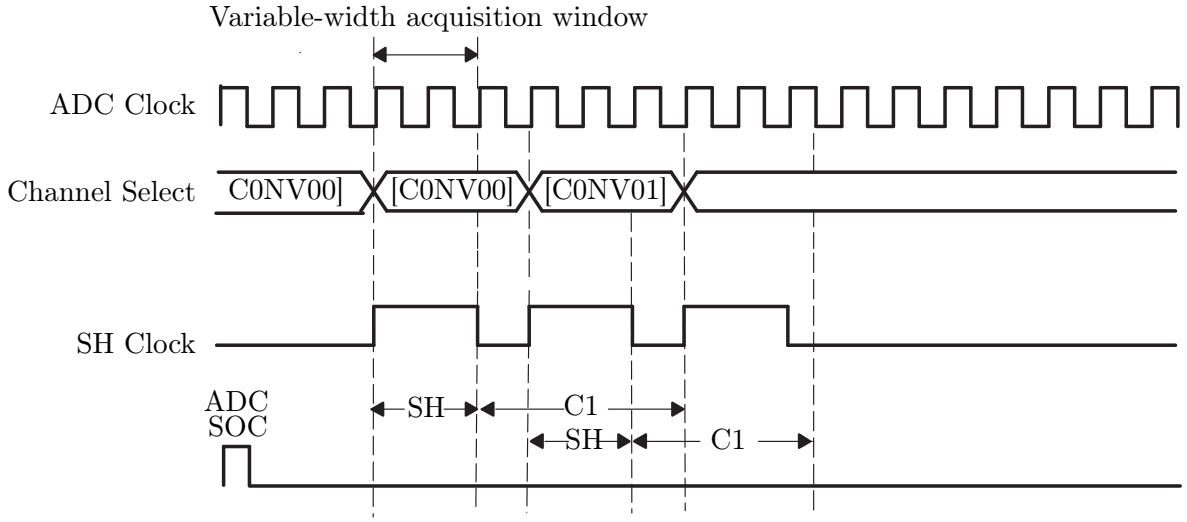

Figure 4.26: *Timing of the DSC module as it executes the ADCs after the SOC signal has been given.*

In this configuration there are two main parameters that controls the timing of the ADC, namely the clock frequency of the ADC itself, and the time window for the SH. Both can be seen in Figure 4.27, as ADCCLK and SH respectively. Depending on the resistance and inductance of the wire from the signal source, and the signal source itself, to the capacitor, these timings must be setup by scaling them relative to the main frequency, High-Speed Prescaler Clock Frequency (HSPCLK), in the ADC module. As the name implies, the HSPCLK is already a fraction of the CPU frequency, scaled from $150MHz$ to $25MHz$

The SH time is set as a integer, that multiplied by the period time of the ADCCLK, gives the SH time window, this integer is Acquisition Prescaler (ACQ_PS) in Figure 4.27. The ADC clock is HSPCLK divided by the ADC Clock Frequency Prescaler (ADCLKPS) and Core clock prescaler (CPS)

All these bits are part of the *ADCTRL* registers.

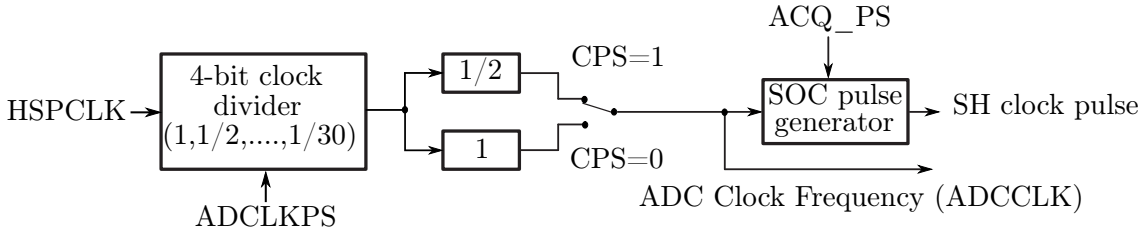

Figure 4.27: *How the ADC Core Clock are set, for the purpose of determining a total conversion speed.*

$$ADC_{clock} = \frac{HSPCLK}{2 \cdot ADCLKPS} \cdot CPS = \frac{25MHz}{2 \cdot 1} \cdot 1 = 12.5MHz \tag{4.5.1}$$

The ACQ_PS is set to 7 which gives a SH window of 8 clocks, which according to Figure 4.26 gives a sample time per channel of:

$$T_{1channel} = \frac{1}{ADC_{clock}} \cdot (8 + 1) = 0.72\mu s \tag{4.5.2}$$

Where the extra clock is the conversion itself.

This yields a sample time for all 16 channels of:

$$t_{sample} = 11.5\mu s \tag{4.5.3}$$

When using this in a control loop, the sampling time must be taken into account depending on the application of the conversions. This module runs independently from the CPU, and does not take up any of the main processors computing power. Generally though, the values are inserted into a table for use with the filter, which requires computation time from the CPU.

4.6 Control system summary

At this point the required hardware for closed loop control of both the current and the position are set up. With an additional DSC a closed loop force control can also be configured.

The actuators was set up starting with a fiber-optic connection from the DSC to separate the sensor common point from the common point of the power system. A H-bridge driver was set up to control the H-bridges, to ensure that the upper MOSFET is turned probably on with a $15V$ voltage difference between Gate and Source, despite varying voltage at the Source.

The H-bridges was designed and snubbers added, based on measurements on the PCB to reduce the ringing in the circuit. This reduced the propagation of the $\frac{dV}{dt}$ signal through parasitic capacitances to acceptable levels.

Current sensors was initially installed close to the DSC, but did pose some challenges. After moving the sensors to the experimental setup close to the coils, the signal quality was increased to acceptable levels by moving the measuring resistances to the DSC, while implementing a analogue filter and removing ground loops.

Position sensors was designed from scratch, and an eddy current sensor was chosen. Four physical sensors was built, and the circuits for amplifying and conditioning the signal designed. The sensors were initially unstable and noisy, but a revision of the entire electrical system reduced both problems to acceptable levels. During tests the brackets for the sensors were the weakest link, as they were simply to compliant. This increased the effects of the structural dynamics, and required re-calibration even after slight mechanical adjustments

The DSC was introduced, and the ADC module was configured to convert the analogue values from the sensors to a digital value.

5 Modeling

To investigate the dynamics of an AMB, a mathematical model is derived. In this chapter the model is derived part by part. First the mechanical part of the model is derived. First for a rigid rotor and then for a flexible. Then the magnetic part of the model is derived and last the electrical part of the model is derived.

Before modeling the active magnetic bearing, its context is introduced. The AMB experimental setup will act as a reference for the mathematical model, and a verification, by comparing the actual dynamic response to the model will show the strengths and the limitations of the model.

The knowledge that accumulates when modeling and comparing theory with practice, will later in the project serve as a foundation for bearing design advise with regards to the DeepWind project. The experimental setup and the mathematical model will continuously be used in the further work of testing control strategies, as these strategies will have an large impact of the durability of the system.

The experimental setup, presented in the previous chapter, is depicted in Figure 5.1, where coordinate systems and measures used in the model are shown.

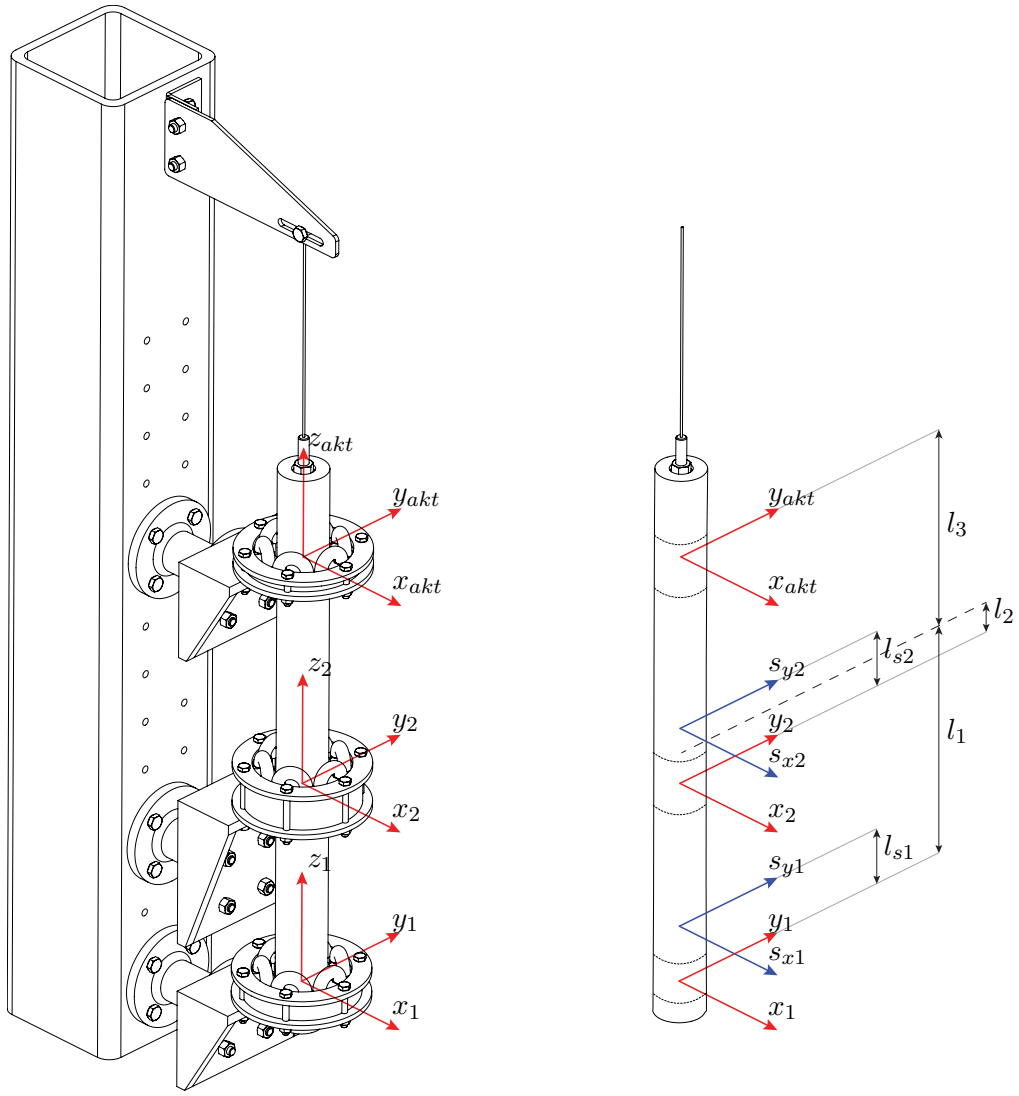

Figure 5.1: *Coordinate systems defined for the model. The red coordinate systems defines the bearing coordinates, and the blue coordinate systems defines the sensor coordinates. In the right figure dimensions are given. The lengths defining the sensor coordinates are related to the nearest bearing, and the bearing lengths are related to the center off mass, which is shown by a dashed line.*

At this point the objective is to model an axle, that represents the axle of the wind turbine in its own coordinate system. If needed this coordinate system can later be referenced from another coordinate system, e.g. the sea bed, and the forces that are present in this environment - waves, wind etc. could be modeled. Furthermore a magnetic bearing is modeled, and initially an old electric motor is used, so geometry is not a variable in this phase.

First a mechanical model is derived, and then a magnetic and electrical model for the system. These parts are presented in the next section, and thereafter interconnected.

5.1 Mechanical model

In this section the mechanical behavior of the magnetic bearing system is derived. This is done based on the experimental setup coordinate definitions and measures presented in

Figure 5.1. First it is assumed that the axle is a rigid body, and thereafter flexibility is taken into account. For this the Lagrange formulation, as shown in equation (5.1.1), is used [Calkin, 1996].

$$\frac{\mathrm{d}}{\mathrm{d}t}\left(\frac{\partial \mathcal{L}}{\partial \dot{\vec{q}}}\right) - \frac{\partial \mathcal{L}}{\partial \vec{q}} = \vec{Q} \qquad , \qquad \mathcal{L} = T - V \tag{5.1.1}$$

Where $\mathcal{L}$ is the Lagrangian, and is defined as the difference between kinetic energy T and the potential energy V. The Lagrangian formulation describes the energy of the system. Therefore all conservative forces are accounted for. Non-conservative forces are included on the right hand side of the equation.

The axle is considered as a free body with five degrees of freedom. Three rotational and two translational (It cannot move in the axial direction). Therefore the generalized coordinates are:

$$\vec{q} = \begin{bmatrix} x & y & \theta_x & \theta_y \end{bmatrix}^T \tag{5.1.2}$$

Where the vector describes the four coordinates of the mass center of body. The last degree of freedom θ_z is not included in the vector (5.1.2), since the rotation velocity $\dot{\theta_z} = \omega_z$ is assumed to be constant and the description of the system, because of the rotation symmetry around the z-axis, does not depend on the θ_z coordinate.

The force vector $\vec{Q}$ of the right hand side in equation (5.1.1) corresponds to the generalized coordinates and is described by forces and torque in the center of mass:

$$\vec{Q} = \begin{bmatrix} F_x & F_y & \tau_x & \tau_y \end{bmatrix}^T \tag{5.1.3}$$

To compute the Lagrangian a description, of the potential- and kinetic energy, has to be derived. Because of the limitation that the body will not move in the z-direction, it is seen that there is no change in potential energy, and the term V equals zero. In the next sections expressions for the kinetic energy is derived. Lastly the system Lagrangian is set up.

5.1.1 Rotational kinetic energy

First the rotational kinetic energy for the axle is considered. This is in general described by the three rotational degrees of freedom and their respective inertia:

$$T_{rot} = \frac{1}{2} \cdot \left(I_{xx} \cdot {\omega_x}^2 + I_{yy} \cdot {\omega_y}^2 + I_{zz} \cdot {\omega_z}^2 \right) \tag{5.1.4}$$

Due to symmetry, the moments of inertia I_{xx} is equal to I_{yy}. Though the expression for the kinetic energy can not be used directly in the Lagrangian, since the velocities in (5.1.4) must be time derivatives of angular coordinates referred to a global common coordinate system. The rotations of the body are described by:

- The body is described in global coordinate system $\vec{i_0}$, $\vec{j_0}$ and $\vec{k_0}$. Figure 5.2a.
- The system rotates θ_y around $\vec{j_0}$, and the new axes are named $\vec{i_1}$, $\vec{j_1}$ and $\vec{k_1}$, where $\vec{j_0}$ and $\vec{j_1}$ are collinear. Figure 5.2b.

- The system rotates θ_x around $\vec{i_1}$, and the new axes are named $\vec{i_2}$, $\vec{j_2}$ and $\vec{k_2}$, where $\vec{i_1}$ and $\vec{i_2}$ are collinear. Figure 5.2c
- The system rotates θ_z around $\vec{k_2}$, and the new axes are named $\vec{i_3}$, $\vec{j_3}$ and $\vec{k_3}$, where $\vec{i_2}$ and $\vec{k_3}$ are collinear. Figure 5.2d

The third rotation ϕ is different because it relates to the normal bearing rotation.

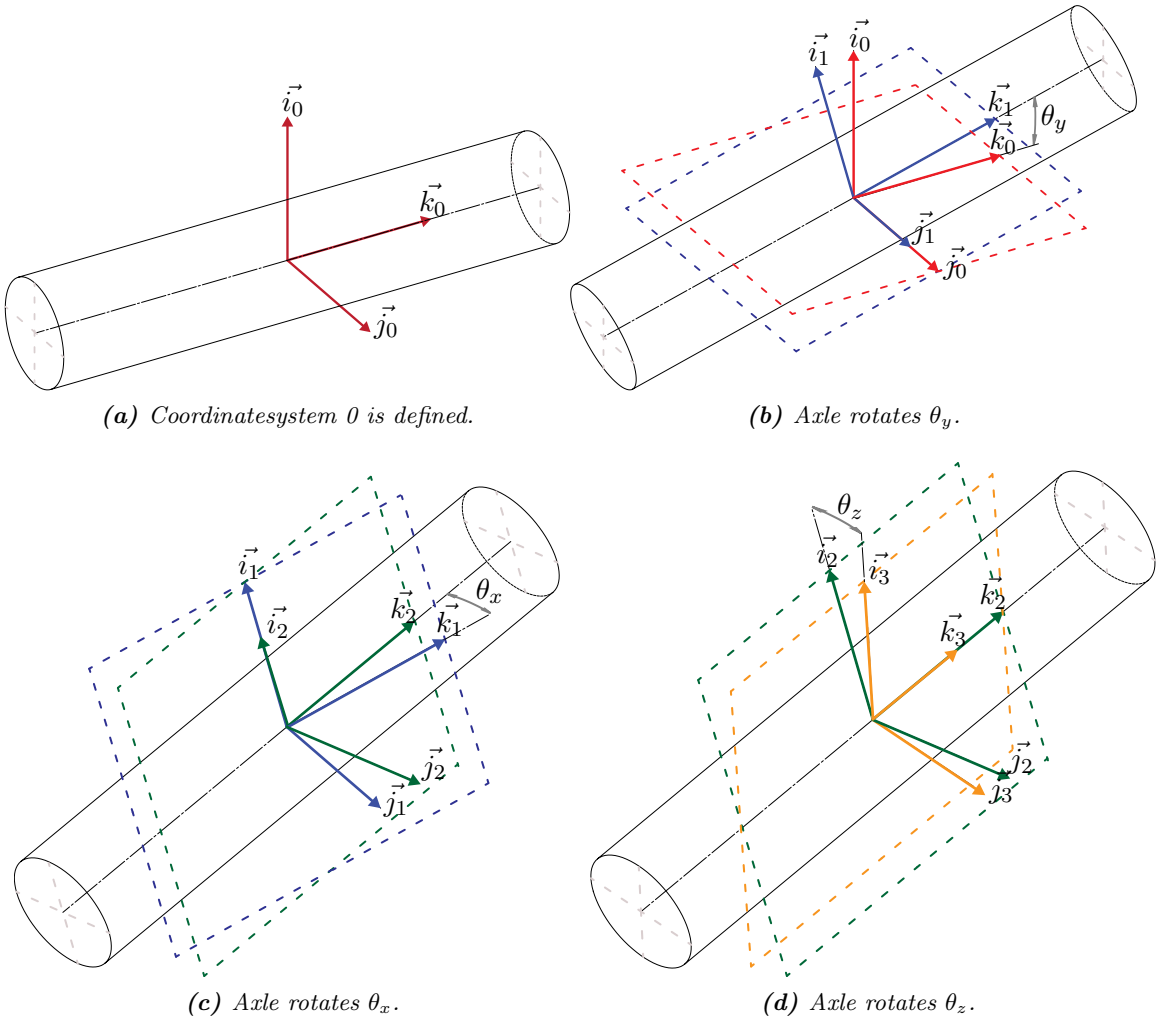

(a) *Coordinatesystem 0 is defined.*

(b) *Axle rotates θ_y.*

(c) *Axle rotates θ_x.*

(d) *Axle rotates θ_z.*

Figure 5.2: *Definition of coordinate systems and rotations of the axle, for the purpose of determining the angular velocities in the general coordinate system.*

The order of the rotations around θ_y and θ_x does not matter due to the symmetrical body. This can be seen in the final equation of the total angular velocity (5.1.16) and the equation for the rotational kinetic energy (5.1.17). The total angular velocity can be described with respect to the axis rotation:

$$\vec{\omega}_{total} = \dot{\theta_y} \cdot \vec{j_0} + \dot{\theta_x} \cdot \vec{i_1} + \dot{\theta_z} \cdot \vec{k_2} \tag{5.1.5}$$

Due to the rotations and the collinear axis definitions this equals:

$$\vec{\omega}_{total} = \dot{\theta_y} \cdot \vec{j_1} + \dot{\theta_x} \cdot \vec{i_2} + \dot{\theta_z} \cdot \vec{k_3} \tag{5.1.6}$$

From this point the angular velocity $\dot{\theta_z}$ will be referred as ω and the rotation ϕ, as the z-rotation is not one of the generalized coordinates and the angular velocity is assumed to be constant.

First the rotation θ_y is described by the Euler rotation:

$$\begin{bmatrix} \vec{i_1} \\ \vec{j_1} \\ \vec{k_1} \end{bmatrix} = \begin{bmatrix} cos\theta_y & 0 & -sin\theta_y \\ 0 & 1 & 0 \\ sin\theta_y & 0 & cos\theta_y \end{bmatrix} \begin{bmatrix} \vec{i_0} \\ \vec{j_0} \\ \vec{k_0} \end{bmatrix} \tag{5.1.7}$$

The rotation θ_x is described by:

$$\begin{bmatrix} \vec{i_2} \\ \vec{j_2} \\ \vec{k_2} \end{bmatrix} = \begin{bmatrix} 1 & 0 & 0 \\ 0 & cos\theta_x & sin\theta_x \\ 0 & -sin\theta_x & cos\theta_x \end{bmatrix} \begin{bmatrix} \vec{i_1} \\ \vec{j_1} \\ \vec{k_1} \end{bmatrix} \tag{5.1.8}$$

The rotation ϕ is described by:

$$\begin{bmatrix} \vec{i_3} \\ \vec{j_3} \\ \vec{k_3} \end{bmatrix} = \begin{bmatrix} cos\phi & sin\phi & 0 \\ -sin\phi & cos\phi & 0 \\ 0 & 0 & 1 \end{bmatrix} \begin{bmatrix} \vec{i_2} \\ \vec{j_2} \\ \vec{k_2} \end{bmatrix} \tag{5.1.9}$$

And the total rotation is described by:

$$\begin{bmatrix} \vec{i_3} \\ \vec{j_3} \\ \vec{k_3} \end{bmatrix} = \mathbf{R}_{\phi} \cdot \mathbf{R}_{\theta_\mathbf{x}} \cdot \mathbf{R}_{\theta_\mathbf{y}} \cdot \begin{bmatrix} \vec{i_0} \\ \vec{j_0} \\ \vec{k_0} \end{bmatrix} = \mathbf{R} \begin{bmatrix} \vec{i_0} \\ \vec{j_0} \\ \vec{k_0} \end{bmatrix} \tag{5.1.10}$$

Inverting the rotation matrix yields:

$$\begin{bmatrix} \vec{i_0} \\ \vec{j_0} \\ \vec{k_0} \end{bmatrix} = \mathbf{R}^{-1} \cdot \begin{bmatrix} \vec{i_3} \\ \vec{j_3} \\ \vec{k_3} \end{bmatrix} \tag{5.1.11}$$

$$= \begin{bmatrix} cos\phi cos\theta_y + sin\phi sin\theta_x sin\theta_y & -sin\phi cos\theta_y + cos\phi sin\theta_x sin\theta_y & cos\theta_x sin\theta_y \\ sin\phi \cdot cos\theta_x & cos\phi cos\theta_x & -sin\theta_x \\ -cos\phi sin\theta_y + sin\phi sin\theta_x cos\theta_y & sin\phi sin\theta_y + cos\phi sin\theta_x cos\theta_y & cos\theta_x cos\theta_y \end{bmatrix} \begin{bmatrix} \vec{i_3} \\ \vec{j_3} \\ \vec{k_3} \end{bmatrix} \tag{5.1.12}$$

Then $\vec{j_0}$ can be found directly

$$\vec{j_0} = \vec{j_1} = \vec{i_3} \cdot sin\phi cos\theta_x + \vec{j_3} \cdot cos\phi cos\theta_x - \vec{k_3} \cdot sin\theta_x \tag{5.1.13}$$

As $\vec{i_1}$ equals $\vec{i_2}$ an expression for $\vec{i_1}$ can be found from

$$\begin{bmatrix} \vec{i_2} \\ \vec{j_2} \\ \vec{k_2} \end{bmatrix} = \mathbf{R}_{\phi}{}^{-1} \cdot \begin{bmatrix} \vec{i_3} \\ \vec{j_3} \\ \vec{k_3} \end{bmatrix} = \begin{bmatrix} cos\phi & -sin\phi & 0 \\ sin\phi & cos\phi & 0 \\ 0 & 0 & 1 \end{bmatrix} \begin{bmatrix} \vec{i_3} \\ \vec{j_3} \\ \vec{k_3} \end{bmatrix} \tag{5.1.14}$$

Then

$$\vec{i_2} = \vec{i_1} = \vec{i_3} \cdot cos\phi - \vec{j_3} \cdot sin\phi \tag{5.1.15}$$

The expression for $\vec{j_2}$ and $\vec{i_1}$ is inserted in the expression for the total angular velocity:

$$\begin{aligned}\vec{\omega}_{total} &= \dot{\theta_y} \cdot \left(\vec{i_3} \cdot sin\phi cos\theta_x + \vec{j_3} \cdot cos\phi \cdot cos\theta_x - \vec{k_3} \cdot sin\theta_x\right) \\ &\quad + \dot{\theta_x} \cdot \left(\vec{i_3} \cdot cos\phi - \vec{j_3} \cdot sin\phi\right) + \dot{\theta_z} \cdot \vec{k_3} \\ &= \vec{i_3} \cdot \left(\dot{\theta_y} \cdot sin\phi \cdot cos\theta_x + \dot{\theta_x} \cdot cos\phi\right) + \vec{j_3} \cdot \left(\dot{\theta_y} \cdot cos\phi \cdot cos\theta_x - \dot{\theta_x} \cdot sin\phi\right) \\ &\quad + \vec{k_3} \cdot \left(-\dot{\theta_y} \cdot sin\theta_x + \omega\right) \end{aligned} \tag{5.1.16}$$

Inserting this in the expression for kinetic rotational energy yield:

$$\begin{aligned}T_{rot} = \frac{1}{2}\Big(&I_{xx} \cdot \left(\dot{\theta_y} \cdot sin\phi \cdot cos\theta_x + \dot{\theta_x} \cdot cos\phi\right)^2 + I_{yy} \cdot \left(\dot{\theta_y} \cdot cos\phi \cdot cos\theta_x - \dot{\theta_x} \cdot sin\phi\right)^2 \\ &+ I_{zz} \cdot \left(-\dot{\theta_y} \cdot sin\theta_x + \omega\right)^2\Big)\end{aligned} \tag{5.1.17}$$

Using that I_{xx} equals I_{zz}

$$\begin{aligned}T_{rot} &= \frac{1}{2} \cdot \Big(I_{xx}\Big(\dot{\theta_y}^2 \cdot sin^2\phi \cdot cos^2\theta_x + \dot{\theta_x}^2 \cdot cos^2\phi + 2 \cdot \dot{\theta_y} \cdot \dot{\theta_x} \cdot sin\phi \cdot cos\theta_x \cdot cos\phi \\ &\quad + \dot{\theta_y}^2 \cdot cos^2\phi \cdot cos^2\theta_x + \dot{\theta_x}^2 \cdot sin^2\phi - 2 \cdot \dot{\theta_y} \cdot \dot{\theta_x} \cdot sin\phi \cdot cos\theta_x \cdot cos\phi\Big) \\ &\quad + I_{zz} \cdot \left(\dot{\theta_y}^2 \cdot sin^2\theta_x + \omega^2 - 2 \cdot \dot{\theta_y} \cdot \omega \cdot sin\theta_x\right)\Big) \\ &= \frac{1}{2} \cdot \Big(I_{xx}\left(\dot{\theta_y}^2 \left(cos^2\theta_x \cdot \left(sin^2\phi + cos^2\phi\right)\right) + \dot{\theta_x}^2 \cdot \left(cos^2\phi + sin^2\phi\right)\right) \\ &\quad + I_{zz} \cdot \left(\dot{\theta_y}^2 \cdot sin^2\theta_x + \omega^2 - 2 \cdot \omega \cdot \dot{\theta_y} \cdot \theta_x\right)\Big)\end{aligned} \tag{5.1.18}$$

Assuming that rotations around $\vec{j_0}$ and $\vec{i_1}$ are small, the equations may be simplified using $cos\theta_x \approx 1$, $sin\theta_x \approx \theta_x$ and $sin^2\theta_x \approx 0$. The same applies for θ_y. Then the rotational kinetic energy, with the rigid body assumption, can be described as:

$$T_{rot} = \frac{1}{2} \cdot I_{xx} \cdot \left(\dot{\theta_y}^2 + \dot{\theta_x}^2\right) + \frac{1}{2} I_{zz} \cdot \left(\omega^2 - 2 \cdot \omega \cdot \dot{\theta_y} \cdot \theta_x\right) \tag{5.1.19}$$

5.1.2 Translational kinetic energy

The translational kinetic energy is much simpler, since it can be described directly in the global coordinate system. And since the axle only has two translational degrees of freedom the translational kinetic energy is:

$$T_{trans} = \frac{1}{2} \cdot m \cdot \left(\dot{x}^2 + \dot{y}^2\right) \tag{5.1.20}$$

5.1.3 System Lagrangian

The Lagrangian is computed by (5.1.1), where the total kinetic energy is the sum of rotational- and translational kinetic energy. Because the rotor can not move in the z-direction the change in potential energy is zero. The system Lagrangian is:

$$\begin{aligned}\mathcal{L} &= T_{trans} + T_{rot} \\ &= \frac{1}{2} \cdot m \cdot \left(\dot{x}^2 + \dot{y}^2\right) + \frac{1}{2} \cdot I_{xx} \cdot \left(\dot{\theta_y}^2 + \dot{\theta_x}^2\right) + \frac{1}{2} \cdot I_{zz} \cdot \left(\omega^2 - 2 \cdot \omega \cdot \dot{\theta_y} \cdot \theta_x\right)\end{aligned} \tag{5.1.21}$$

Finding the derivatives with respect to the generalized coordinates, and the derivatives with respect to the time derivatives of the generalized coordinates:

$$\frac{\partial \mathcal{L}}{\partial \dot{\vec{q}}} = \begin{bmatrix} m \cdot \dot{x} \\ m \cdot \dot{y} \\ I_{xx} \cdot \dot{\theta}_x \\ I_{xx} \cdot \dot{\theta}_y - I_{zz} \cdot \omega \cdot \theta_x \end{bmatrix} \qquad \frac{\partial \mathcal{L}}{\partial \vec{q}} = \begin{bmatrix} 0 \\ 0 \\ -I_{zz} \cdot \omega \cdot \dot{\theta}_y \\ 0 \end{bmatrix} \tag{5.1.22}$$

And the Lagrangian can be set up:

$$\begin{aligned} \frac{\mathrm{d}}{\mathrm{d}t}\left(\frac{\partial \mathcal{L}}{\partial \dot{\vec{q}}}\right) - \frac{\partial \mathcal{L}}{\partial \vec{q}} &= \begin{bmatrix} m & 0 & 0 & 0 \\ 0 & m & 0 & 0 \\ 0 & 0 & I_{xx} & 0 \\ 0 & 0 & 0 & I_{xx} \end{bmatrix} \cdot \ddot{\vec{q}} + \begin{bmatrix} 0 & 0 & 0 & 0 \\ 0 & 0 & 0 & 0 \\ 0 & 0 & 0 & I_{zz} \cdot \omega \\ 0 & 0 & -I_{zz} \cdot \omega & 0 \end{bmatrix} \cdot \dot{\vec{q}} \\ \vec{Q} &= \mathbf{M} \cdot \ddot{\vec{q}} + \mathbf{G} \cdot \ddot{\vec{q}} \end{aligned} \tag{5.1.23}$$

Where the first matrix is called the mass matrix $\mathbf{M}$, and the second matrix is the gyroscopic matrix $\mathbf{G}$, which links the angular velocity ω of the axle into gyroscopic effects. It shows that a change in angular velocity θ_y produces a torque τ_x, and the same for θ_x and τ_y.

5.1.4 Relating equations of motion to bearing coordinates

So far the mechanical model describes the motion of the rotor, by coordinates related to the center of mass. When setting up a full magnetic and mechanical model, it is necessary to be able to relate the center of mass coordinates, and forces to coordinates and forces acting in the bearings.

Figure 5.3 is a simplification of Figure 5.1 and shows the placement of the three actuators, and their relation to the center of mass.

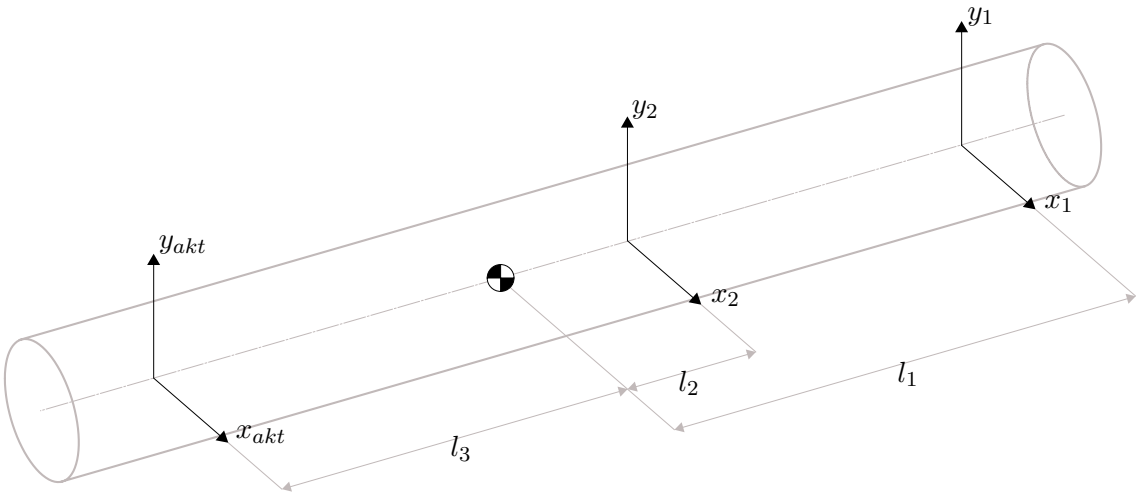

Figure 5.3: *Definition of distances to bearings and load actuator from the center of mass of the axle.*

The force vector $\vec{Q}$ can be related to bearing forces by simple geometrical considerations. Using the sign definitions in Figure 5.3, and summing the forces and moments in the

center of mass yields:

$$F_x = F_{x1} + F_{x2} + F_{xakt} \tag{5.1.24}$$
$$F_y = F_{y1} + F_{y2} + F_{yakt} \tag{5.1.25}$$
$$\tau_x = F_{y1} \cdot l_1 + F_{y2} \cdot l_2 - F_{yakt} \cdot l_3 \tag{5.1.26}$$
$$\tau_y = -F_{x1} \cdot l_1 - F_{x2} \cdot l_2 + F_{xakt} \cdot l_3 \tag{5.1.27}$$

This is written in vector matrix form:

$$\begin{bmatrix} F_x \\ F_y \\ \tau_x \\ \tau_y \end{bmatrix} = \begin{bmatrix} 1 & 0 & 1 & 0 & 1 & 0 \\ 0 & 1 & 0 & 1 & 0 & 1 \\ 0 & l_1 & 0 & l_2 & 0 & -l_3 \\ -l_1 & 0 & -l_2 & 0 & l_3 & 0 \end{bmatrix} \begin{bmatrix} F_{x1} \\ F_{y1} \\ F_{x2} \\ F_{y2} \\ F_{xakt} \\ F_{yakt} \end{bmatrix}$$
$$\vec{Q} = \mathbf{T_1} \cdot \vec{Q_c} \tag{5.1.28}$$

Also the bearing and actuator coordinates are related to coordinates of mass center.

$$\begin{aligned} x_1 &= x - sin\theta_y \cdot l_1 \\ y_1 &= y + sin\theta_x \cdot l_1 \\ x_2 &= x - sin\theta_y \cdot l_2 \\ y_2 &= y + sin\theta_x \cdot l_2 \end{aligned} \tag{5.1.29}$$

Assuming small angles between bearings and axle, and writing the equations in vector matrix form yields:

$$\begin{bmatrix} x_1 \\ y_1 \\ x_2 \\ y_2 \end{bmatrix} = \begin{bmatrix} 1 & 0 & 0 & -l_1 \\ 0 & 1 & l_1 & 0 \\ 1 & 0 & 0 & -l_2 \\ 0 & 1 & l_2 & 0 \end{bmatrix} \begin{bmatrix} x \\ y \\ \theta_x \\ \theta_y \end{bmatrix}$$
$$\vec{x} = \mathbf{T_2} \cdot \vec{q} \tag{5.1.30}$$

By the small angles assumption the time derivatives are expressed as:

$$\dot{\vec{x}} = \mathbf{T_2} \cdot \dot{\vec{q}} \tag{5.1.31}$$
$$\ddot{\vec{x}} = \mathbf{T_2} \cdot \ddot{\vec{q}} \tag{5.1.32}$$

Similarly a transform from sensor coordinates to generalized coordinates $\vec{q}$ can be made

$$\vec{s} = \mathbf{T_3} \cdot \vec{q}$$
$$\begin{bmatrix} s_{x1} \\ s_{y1} \\ s_{x2} \\ s_{y2} \end{bmatrix} = \begin{bmatrix} 1 & 0 & 0 & l_{s1} - l_1 \\ 0 & 1 & l_1 - l_{s1} & 0 \\ 1 & 0 & 0 & l_{s2} - l_2 \\ 0 & 1 & l_2 - l_{s2} & 0 \end{bmatrix} \begin{bmatrix} x \\ y \\ \theta_x \\ \theta_y \end{bmatrix} \tag{5.1.33}$$

Using the transforms (5.1.30), (5.1.31) and (5.1.32) the dynamic equation (5.1.23) can be written in terms of bearing coordinates and bearing forces:

$$\mathbf{T_1} \cdot \vec{Q}_c = \mathbf{M} \cdot \mathbf{T_2}^{-1} \cdot \ddot{\vec{x}} + \mathbf{G} \cdot \mathbf{T_2}^{-1} \cdot \dot{\vec{x}} \tag{5.1.34}$$

$$\begin{aligned} \vec{Q}_c &= \mathbf{T_1}^{-1} \cdot \mathbf{M} \cdot \mathbf{T_2}^{-1} \cdot \ddot{\vec{x}} + \mathbf{T_1}^{-1} \cdot \mathbf{G} \cdot \mathbf{T_2}^{-1} \cdot \dot{\vec{x}} \\ &= \mathbf{M_c} \cdot \ddot{\vec{x}} + \mathbf{G_c} \cdot \dot{\vec{x}} \end{aligned} \tag{5.1.35}$$

With a new mass matrix $\mathbf{M_c}$ and gyroscopic matrix $\mathbf{G_c}$. The mass matrix is not diagonal for this system. It has to be noted that the transformation matrix $\mathbf{T_1}$ is non-square, and therefore inverting the matrix will not yield a unique solution. Though if the actuator forces are not taken into account the matrix is square, and the dynamic system (5.1.35) described in bearing coordinates can be analyzed. Solving the equation for the accelerations:

$$\ddot{\vec{x}} = \mathbf{T_2} \cdot \mathbf{M}^{-1} \cdot \left(\mathbf{T_1} \cdot \vec{Q}_c - \mathbf{G} \cdot \mathbf{T_2}^{-1} \cdot \dot{\vec{x}} \right) \tag{5.1.36}$$

This equation can be solved for a non-square $\mathbf{T_1}$, and is used when setting up the full model described in section 5.5.

5.2 Flexible rotor model

In the previous sections, it has been assumed that the rotor is completely rigid. In this section the rotor is modeled as flexible. The flexibility is modeled in a FEM sense, to be able to add different masses in cross sections of the rotor. Here the model is derived for a Bernoulli-Euler beam element, which is build on standard beam theory, and therefore transverse shear deformation is ignored [Cook et al., 2002]. Here the deflection function is developed for bending in both x- and y-direction.

First the general static deflection of the rotor is expressed as a cubic function:

$$\begin{aligned} \Phi &= a_1 + a_2 \cdot z + a_3 \cdot z^2 + a_4 \cdot z^3 \\ &= \begin{bmatrix} 1 & z & z^2 & z^3 \end{bmatrix} \cdot \begin{bmatrix} a_1 \\ a_2 \\ a_3 \\ a_4 \end{bmatrix} \\ &= \mathbf{z} \cdot \mathbf{a} \end{aligned} \tag{5.2.1}$$

Looking at the limits for the deflection function the following is required:

- $\Phi = \phi_1$ and $\Phi_{,z} = \theta_1$ for $z = 0$
- $\Phi = \phi_2$ and $\Phi_{,z} = \theta_2$ for $z = L$

Where ϕ_1 is the deflection at the left element boundary and θ_1 is the slope of the left boundary. The subscript two refers to the right boundary. Inserting these limits in the

function (5.2.1) yields four equations:

$$\begin{bmatrix}\phi_1\\ \theta_1\\ \phi_2\\ \theta_2\end{bmatrix} = \begin{bmatrix}1 & 0 & 0 & 0\\ 0 & 1 & 0 & 0\\ 1 & L & L^2 & L^3\\ 0 & 1 & 2\cdot L & 3\cdot L^2\end{bmatrix} \cdot \begin{bmatrix}a_1\\ a_2\\ a_3\\ a_4\end{bmatrix}$$
$$\mathbf{d} = \mathbf{A}\cdot\mathbf{a} \tag{5.2.2}$$

Isolating $\mathbf{a}$ yields

$$\mathbf{a} = \mathbf{A}^{-1}\cdot\mathbf{d} \tag{5.2.3}$$

Inserting this in (5.2.1):

$$\begin{aligned}\Phi &= \mathbf{z}\cdot\mathbf{A}^{-1}\cdot\mathbf{d}\\ &= \mathbf{N}\cdot\mathbf{d}\end{aligned} \tag{5.2.4}$$

Where $\mathbf{N}$ is the shape functions, and given as:

$$\begin{aligned}\mathbf{N} &= \mathbf{z}\cdot\mathbf{A}^{-1}\\ &= \begin{bmatrix}1-\frac{3\cdot z^2}{L^2}+\frac{2\cdot z^2}{L^3} & z-\frac{2\cdot z^2}{L}+\frac{z^3}{L^2} & \frac{3\cdot z^2}{L^2}-\frac{2\cdot z^3}{L^3} & -\frac{z^2}{L}+\frac{z^3}{L^2}\end{bmatrix}\\ &= \begin{bmatrix}N_1 & N_2 & N_3 & N_4\end{bmatrix}\end{aligned} \tag{5.2.5}$$

Then the deflection function in the x- and y-direction is described by:

$$\tilde{x} = x_1\cdot N_1 + \theta_{y1}\cdot N_2 + x_2\cdot N_3 + \theta_{y2}\cdot N_4 \tag{5.2.6}$$
$$\tilde{y} = x_1\cdot N_1 + \theta_{x1}\cdot N_2 + y_2\cdot N_3 + \theta_{x2}\cdot N_4 \tag{5.2.7}$$

The time derivatives

$$\dot{\tilde{x}} = \dot{x}_1\cdot N_1 + \dot{\theta}_{y1}\cdot N_2 + \dot{x}_2\cdot N_3 + \dot{\theta}_{y2}\cdot N_4 \tag{5.2.8}$$
$$\dot{\tilde{y}} = \dot{y}_1\cdot N_1 + \dot{\theta}_{x1}\cdot N_2 + \dot{y}_2\cdot N_3 + \dot{\theta}_{x2}\cdot N_4 \tag{5.2.9}$$

The kinetic energy for one element is [Adams, 2001]:

$$T_i = \frac{1}{2}\cdot\frac{M_1^{(s)}}{L_1}\cdot\int_0^{L_i}\left(\dot{\tilde{x}}^2+\dot{\tilde{y}}^2\right)\mathrm{d}z \tag{5.2.10}$$

The potential energy for a rod in bending can be described by:

$$V_i = \frac{1}{2}\cdot E_i\cdot I_i\cdot\int_0^{L_i}\left(\left(\frac{\partial^2\tilde{x}}{\partial z^2}\right)^2+\left(\frac{\partial^2\tilde{y}}{\partial z^2}\right)^2\right)\mathrm{d}z \tag{5.2.11}$$

To introduce the gyroscopic effects on each element, half the polar moment of inertia is transferred to each element boundary, and from (5.1.21) it is seen that this gives the contribution to the kinetic energy as follows:

$$T_{gyri} = \frac{1}{4}I_{zz}\cdot\left(\omega^2-2\cdot\omega\cdot\dot{\theta}_{y1}\cdot\theta_{x1}\right)+\frac{1}{4}I_{zz}\cdot\left(\omega^2-2\cdot\omega\cdot\dot{\theta}_{y2}\cdot\theta_{x2}\right) \tag{5.2.12}$$

Where $\dot{\theta}_{y1}$ and θ_{x1} refers to the left boundary and $\dot{\theta}_{y2}$ and θ_{x2} refers to the right boundary. The Lagrangian can be solved on element basis, where the element Lagrangian is:

$$\mathcal{L}_i = T_i - V_i \tag{5.2.13}$$

$$\frac{\mathrm{d}}{\mathrm{d}t}\left(\frac{\partial \mathcal{L}_i}{\partial \dot{\vec{q}}_r}\right) - \frac{\partial \mathcal{L}_i}{\partial \vec{q}_r} = \mathbf{m}_i \cdot \ddot{\vec{q}}_r + \mathbf{g}_i \cdot \dot{\vec{q}}_r + \mathbf{k}_i \cdot \vec{q}_r \tag{5.2.14}$$

The vector $\vec{q}_r$ is described by the element degrees of freedom:

$$\vec{q}_r = \begin{bmatrix} x_1 & y_1 & \theta_{x1} & \theta_{y1} & x_2 & y_2 & \theta_{x2} & \theta_{y2} \end{bmatrix}^T \tag{5.2.15}$$

And the element mass-, gyroscopic- and stiffness matrices are given as:

$$\mathbf{m}_i = \frac{m}{420} \cdot \begin{bmatrix} 156 & 0 & 0 & 22 \cdot L & 54 & 0 & 0 & -13 \cdot L \\ 0 & 156 & -22 \cdot L & 0 & 0 & 54 & 13 \cdot L & 0 \\ 0 & -22 \cdot L & 4 \cdot L^2 & 0 & 0 & -13 \cdot L & -3 \cdot L^2 & 0 \\ 22 \cdot L & 0 & 0 & 4 \cdot L^2 & 13 \cdot L & 0 & 0 & -3 \cdot L^2 \\ 54 & 0 & 0 & 13 \cdot L & 156 & 0 & 0 & -22 \cdot L \\ 0 & 54 & -13 \cdot L & 0 & 0 & 156 & 22 \cdot L & 0 \\ 0 & 13 \cdot L & -3 \cdot L^2 & 0 & 0 & 22 \cdot L & 4 \cdot L^2 & 0 \\ -13 \cdot L & 0 & 0 & -3 \cdot L^2 & 22 \cdot L & 0 & 0 & -4 \cdot L^2 \end{bmatrix} \tag{5.2.16}$$

$$\mathbf{g}_i = \begin{bmatrix} 0 & 0 & 0 & 0 & 0 & 0 & 0 & 0 \\ 0 & 0 & 0 & 0 & 0 & 0 & 0 & 0 \\ 0 & 0 & 0 & \frac{1}{2} \cdot J_p \cdot \omega & 0 & 0 & 0 & 0 \\ 0 & 0 & -\frac{1}{2} \cdot J_p \cdot \omega & 0 & 0 & 0 & 0 & 0 \\ 0 & 0 & 0 & 0 & 0 & 0 & 0 & 0 \\ 0 & 0 & 0 & 0 & 0 & 0 & 0 & 0 \\ 0 & 0 & 0 & 0 & 0 & 0 & 0 & \frac{1}{2} \cdot J_p \cdot \omega \\ 0 & 0 & 0 & 0 & 0 & 0 & -\frac{1}{2} \cdot J_p \cdot \omega & 0 \end{bmatrix} \tag{5.2.17}$$

$$\mathbf{k}_i = \frac{E_i \cdot I_i}{L^3} \cdot \begin{bmatrix} 12 & 0 & 0 & 6 \cdot L & -12 & 0 & 0 & 6 \cdot L \\ 0 & 12 & -6 \cdot L & 0 & 0 & -12 & -6 \cdot L & 0 \\ 0 & -6 \cdot L & 4 \cdot L^2 & 0 & 0 & 6 \cdot L & 2 \cdot L^2 & 0 \\ 6 \cdot L & 0 & 0 & 4 \cdot L^2 & -6 \cdot L & 0 & 0 & 2 \cdot L^2 \\ -12 & 0 & 0 & -6 \cdot L & 12 & 0 & 0 & -6 \cdot L \\ 0 & -12 & 6 \cdot L & 0 & 0 & 12 & 6 \cdot L & 0 \\ 0 & -6 \cdot L & 2 \cdot L^2 & 0 & 0 & 6 \cdot L & 4 \cdot L^2 & 0 \\ 6 \cdot L & 0 & 0 & 2 \cdot L^2 & -6 \cdot L & 0 & 0 & 4 \cdot L^2 \end{bmatrix} \tag{5.2.18}$$

The mass, gyroscopic and stiffness matrices of the system are assembled, linking the degrees of freedom of each element together. Having a vertical beam geometry, the upper boundary degrees of freedom of one element is connected to the lower boundary degrees of freedom of the element above. This yields system on the following form:

$$Q = \mathbf{M} \cdot \ddot{\vec{q}} + \mathbf{G} \cdot \dot{\vec{q}} + \mathbf{K} \cdot \vec{q} \tag{5.2.19}$$

Where the vector $\vec{q}$ contains all degrees of freedom of the system.
This flexible axle model was not implemented in the experimental setup bearing model, because it would make little sense given the stiffness of the axle. Thus it is not experimentally verified. This flexible axle model is developed for use with the full scale DeepWind VAWT dynamical model.
In the following two sections the magnetic and electric models are set up. In this section a dynamic model of the magnetic circuit of the bearings is developed. The model is based on the six pole sheet steel used in the bearings of the experimental setup . Therefore only the model of a radial bearing is developed in this chapter. Since the same sheets are used in both bearings, the model developed in this section will be a general expression, with the height of the bearings as the only difference. This too goes for the load actuator.

5.3 Magnetic Bearing Model

Two bearing models are studied. First a simple model where only the reluctance of the airgaps are implemented, and then a more detailed Reluctance Network Model (RNM) where a reluctance network, connecting a number of expected flux paths, is developed. The simple model is simpler to derive and linearized for controller design, whereas the RNM is suited for comparison to the FEM model, the experimental setup and numerical simulation.

In the next sections the two approaches of modeling the magnetic circuit of the radial bearing is presented. Then the determination of the air gap reluctances is described.

5.3.1 Airgap reluctance magnetic model

Figure 5.4 shows the stator design and winding scheme of the electromagnets. The flux- and current directions are also defined in the figure.

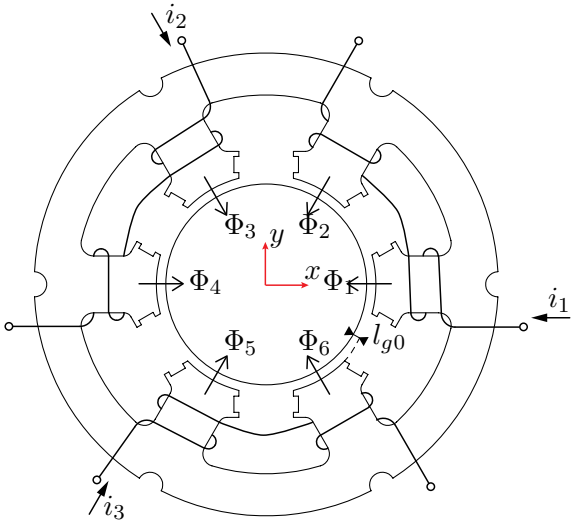

Figure 5.4: *The winding scheme of the radial bearing, along with definition of current and flux directions.*

An equivalent circuit of the radial bearing shown in Figure 5.4 is presented in Figure 5.5. The circuit is an approximation of the radial bearing, saying that reluctances of the air

gaps are by far the largest, and therefore the dominating in the system. As shown in the figure the reluctances are variable and a function of the air gap size.

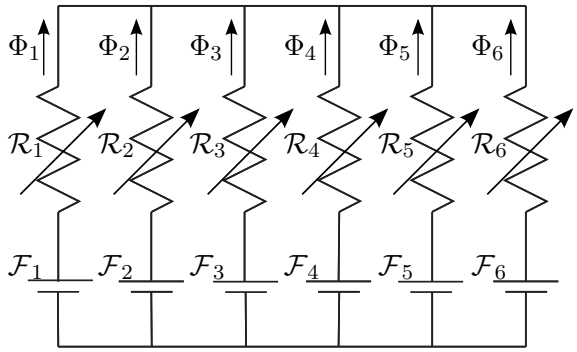

Figure 5.5: *Equivalent magnetic circuit of the radial bearing from Figure 5.4.*

The governing equations for the circuit are found by using the magnetic analogous to Kirchhoff's voltage law (KVL) and Kirchhoff's current law (KCL). The first five equalities sums the MMF in the loops to zero, and the last equations sums the fluxes in and out of the top conductor to zero.

$$0 = \mathcal{F}_k - \mathcal{R}_k \cdot \Phi_k + \mathcal{R}_{k+1} \cdot \Phi_{k+1} - \mathcal{F}_{k+1} \; ; \; k = 1, 2...5 \tag{5.3.1}$$

$$0 = \sum_{k=1}^{6} \Phi_k \tag{5.3.2}$$

Isolating the magnetic fluxes yields six equations showing the relationship between MMF and magnetic flux in the different branches, these are presented in (5.3.3). Because of their size the equations are presented as a sum, where n is an integer from one to six which when inserted gives the six equations.

$$\Phi_n = \frac{\sum_{k=1}^{6} \frac{\mathcal{F}_n - \mathcal{F}_k}{\mathcal{R}_n \mathcal{R}_k}}{\sum_{k=1}^{6} \frac{1}{\mathcal{R}_k}} \; ; \; n = 1, 2...6 \tag{5.3.3}$$

The MMFs are equal to the respective coil currents multiplied by the winding number, thus the circuit MMFs are found using equation (5.3.4). The sign conversion is defined by the winding scheme in Figure 5.4.

$$\begin{aligned} &\mathcal{F}_1 = N \cdot i_1 \quad \mathcal{F}_2 = -N \cdot i_1 \quad \mathcal{F}_3 = N \cdot i_2 \\ &\mathcal{F}_4 = -N \cdot i_2 \quad \mathcal{F}_5 = N \cdot i_3 \quad \mathcal{F}_6 = -N \cdot i_3 \end{aligned} \tag{5.3.4}$$

To relate the magnetic circuit to an electric circuit the inductances has to be determined. Expressing the flux linkages shows the coherence of the current and the flux. By this the inductance can be determined:

$$\lambda = Li = N\Phi \tag{5.3.5}$$

To fully define the inductances of the three coils, an inductance matrix of self and mutual inductances is needed. This is due to the fact that a flux linkage between the coils exists.

How the flux couples are described by equations (5.3.3). The diagonal entries in the inductance matrix are the self inductances, the rest describe mutual inductances. The self inductance of coil one is determined by:

$$L_{11} = \frac{\lambda_{11}}{i_1} \ , \ \lambda_{11} = N\left(\Phi_1 - \Phi_2\right)\Big|_{i_2 \ = \ 0, i_3 \ = \ 0} \tag{5.3.6}$$

λ_{11} is the flux through coil one generated by coil one, times the number of windings. Again the winding scheme causes the fluxes to couple differently, thus Φ_1 couples positively and Φ_2 negatively with coil 1. The remaining self inductances are derived using the same approach. The mutual inductance M_{12} is:

$$M_{12} = \frac{\lambda_{12}}{i_2} \ , \ \lambda_{12} = N\left(\Phi_1 - \Phi_2\right)\Big|_{i_1 \ = \ 0, i_3 \ = \ 0} \tag{5.3.7}$$

M_{12} is the coupling from coil 2 to coil 1, hence M_{21} is the coupling from coil 1 to 2 and so on. Since it does not matter from which coil the coupling is observed, the inductance matrix is symmetric, which results in M_{12} and M_{21} being equal. The full inductance matrix is presented in (5.3.8). Due to the fact that reluctances are dependent of the generalized coordinate, so are the inductances.

$$\mathbf{L} = \begin{bmatrix} L_{11}(\vec{q}_m) & M_{12}(\vec{q}_m) & M_{13}(\vec{q}_m) \\ M_{21}(\vec{q}_m) & L_{22}(\vec{q}_m) & M_{23}(\vec{q}_m) \\ M_{31}(\vec{q}_m) & M_{32}(\vec{q}_m) & L_{33}(\vec{q}_m) \end{bmatrix} \tag{5.3.8}$$

Where the coordinate $\vec{q}_m$ is given as:

$$\vec{q}_m = \begin{bmatrix} x_1 & y_1 \end{bmatrix}^T \tag{5.3.9}$$

As will be shown in section 5.3.3 the reluctances are dependent of the rotor position and -angle. Though a simplifying approximation is made, so that the reluctance is only position dependent. Hence the reluctance model, does not add contributions from the angles θ_{x1} and θ_{y1}. The leakage inductance is assumed to be zero at this point and will be taken into account further on. The equations are only derived for one bearing, as the calculations are similar for the other bearing.

The force generated by the magnetic bearings, is a function of the change of energy in the airgap. Hence the forces are found with respect to the generalized coordinates by differentiation. Since the reluctance of the axle and stator remain constant with relation to the airgap size, the change of energy in the airgap, can be found by evaluating the change in energy stored in the coil. This by using the inductance energy as a function of displacement, as a functional for differentiation [Zhuravlyov, 1992].

$$W = \frac{1}{2} \cdot \vec{i}^T \cdot \mathbf{L}(\vec{q}) \cdot \vec{i} \tag{5.3.10}$$

$$Q_n = \frac{\partial W}{\partial q_n}; n = 1, 2 \tag{5.3.11}$$

5.3.2 Reluctance network model

In this section another, more precise, approach to modeling the magnetic system is derived. In this RNM the reluctance of rotor, stator sheets, and air between poles are added to the model [Antila, 1998]. The circuit is shown in Figure 5.6.

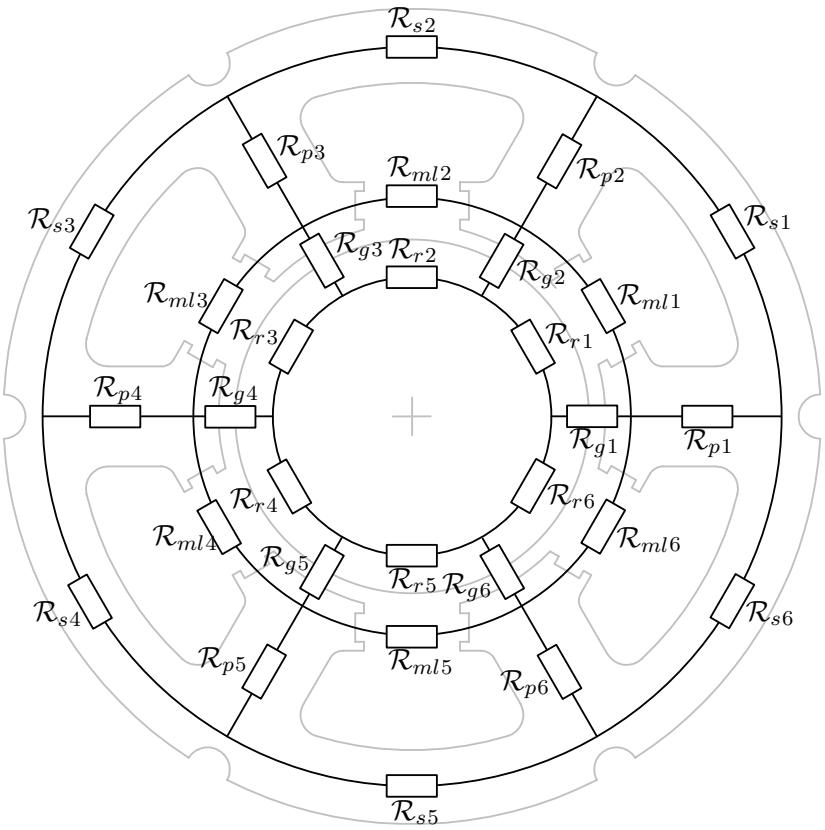

Figure 5.6: *Reluctance network model with added rotor, stator and leakage reluctances for increased accuracy.*

For this circuit it is possible to collect 30 linear independent equations describing the relation between the fluxes and the MMF of the system. The equations are given in Appendix E. Adding a self leakage flux to the system as in Figure 5.7, it yields 36 equations.

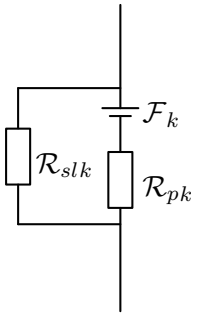

Figure 5.7: *Self leakage path.*

The system can then be described on vector matrix form:

$$\mathbf{R} \cdot \vec{\Phi} = \mathcal{F} \tag{5.3.12}$$

Where $\vec{\Phi}$ is a vector containing all the branch fluxes, and $\mathcal{F}$ is a vector containing the MMF in each branch. When rewriting the equation, the fluxes can be determined:

$$\vec{\Phi} = \mathbf{R}^{-1} \cdot \mathcal{F} = \mathbf{R}^{-1} \cdot \mathbf{N} \cdot \vec{i} \tag{5.3.13}$$

Where $\mathcal{F} = \mathbf{N} \cdot \vec{i}$. The vector $\vec{i}$ contains the three currents, and $\mathbf{N}$ contains the number of windings relating each of the three currents to the $\mathcal{F}$.

Multiplying by a matrix $\mathbf{T}^T$ and using the relation for the flux linkage in equation (5.3.5) yields:

$$\mathbf{T}^T \cdot \vec{\Phi} = \mathbf{T}^T \cdot \mathbf{R}^{-1} \cdot \mathbf{N} \cdot \vec{i} \tag{5.3.14}$$

Where the matrix $\mathbf{T}$ relates the number of turns and the flux, so that the (k,l)'th element of $\mathbf{T}$ is the number of turns of the l'th coil about the i'th flux.

Therefore the inductance matrix can be calculated by:

$$\mathbf{L} = \mathbf{T}^T \cdot \mathbf{R}^{-1} \cdot \mathbf{N} \tag{5.3.15}$$

The force can be calculated from the principle of virtual work [Antila, 1998] as:

$$Q = -\frac{\partial W}{\partial \vec{q}} = -\frac{1}{2} \cdot \vec{\Phi}^T \cdot \frac{\partial \mathbf{R}}{\partial \vec{q}} \cdot \vec{\Phi} = \left[-\frac{1}{2} \cdot \vec{\Phi}^T \cdot \frac{\partial \mathbf{R}}{\partial x} \cdot \vec{\Phi} \quad -\frac{1}{2} \cdot \vec{\Phi}^T \cdot \frac{\partial \mathbf{R}}{\partial y} \cdot \vec{\Phi} \right]^T \tag{5.3.16}$$

Where the derivatives of the reluctance matrices are relatively simple to calculate, since only the air gap reluctances are dependent on the rotor coordinates.

For this model, all the reluctances of all the flux paths has to be calculated. The airgap reluctances $\mathcal{R}_{gk}$ is calculated as described in section 5.3.3. In the following the remaining reluctances are calculated. Because of symmetry in the stator and rotor the constant reluctances are equal in each branch.

$$\mathcal{R}_{pk} = \frac{L_p}{\mu_0 \cdot \mu_s \cdot a_p} \; ; \; k = 1, 2...6 \tag{5.3.17}$$

$$\mathcal{R}_{rk} = \frac{L_r}{\mu_0 \cdot \mu_r \cdot a_r} \; ; \; k = 1, 2...6 \tag{5.3.18}$$

$$\mathcal{R}_{sk} = \frac{L_s}{\mu_0 \cdot \mu_s \cdot a_s} \; ; \; k = 1, 2...6 \tag{5.3.19}$$

Where the lengths L_p, L_r and L_s are the length of the flux paths and a_p, a_r and a_s are the cross section areas of the flux paths through pole, rotor and stator respectively. The cross section area and length of the rotor flux field is not a directly measurable factor. Therefore an approximation of these values are made, saying that the length is $\frac{1}{6} d_{rotor}$ and the area is the same as for the pole.

The size of the mutual leakage- and the self leakage reluctances are also not directly computable, therefore a guess are made, and the model reluctances can be optimized to fit measured data.

$$\mathcal{R}_{sl} = 3 \cdot 10^8 A \cdot Wb^{-1} \tag{5.3.20}$$

$$\mathcal{R}_{ml} = 1 \cdot 10^8 A \cdot Wb^{-1} \tag{5.3.21}$$

5.3.3 Determination of air gap reluctance

The permeance of the magnetic circuit is a function of rotor position i.e. air gap size. It can be written as shown in equation (5.3.22). This is an integral over the stator pole area, with the airgap length expressed as the length of the pole surface normal spanning the airgap [Zhuravlyov, 1992].

$$g = \int_A \frac{\mu_0}{l_g} \mathrm{d}A \tag{5.3.22}$$

And the reluctance is the inverse of the permeance:

$$\mathcal{R} = \frac{1}{g} \tag{5.3.23}$$

Figure 5.8 illustrates the pole angles and the surface normal vector.

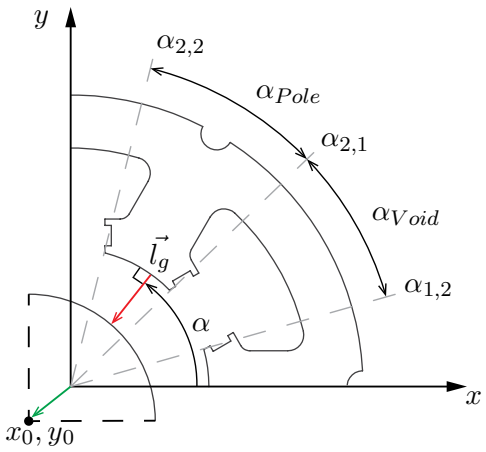

Figure 5.8: *A cutout of the radial bearing, showing the airgap vector(red), displacement position vector(green) and stator pole angles.*

To find the length of the surface normal, the green displacement vector shown in Figure 5.8, is projected onto the red normal vector, and added to the airgap length when the rotor and stator are in concentric position, l_{g0}. Since the rotor both displaces and rotates, the displacement vector is a function of z. Since the rotations are small $sin(\theta_y) \approx \theta_y$ and $sin(\theta_x) \approx \theta_x$. Since the surface normal varies with the angle, the projection of the displacement vector is a function of α. Thus the airgap length is found using equation (5.3.24).

$$l_g = l_{g0} - (x_0 + z \cdot \theta_y) \cdot cos(\alpha) + (y_0 - z \cdot \theta_x) \cdot sin(\alpha) \tag{5.3.24}$$

The integral is rewritten to (5.3.25). r_{SP} is the radius of the stator pole.

$$\mathcal{R}_n = \frac{1}{\mu_0 \cdot r_{SP} \int_{z_1}^{z_2} \int_{\alpha_{n,1}}^{\alpha_{n,2}} (l_g)^{-1} \ \mathrm{d}\alpha \mathrm{d}z}; n \ = \ 1, 2...6 \tag{5.3.25}$$

By this expression it is shown that the reluctance is dependent of the rotor coordinates x_0, y_0, θ_x and θ_y.

The integral for the reluctance (5.3.25) has shown to be hard to compute,. Therefore a simpler expression is developed. Only using the average airgap distance the reluctance yields:

$$\tilde{\mathcal{R}}_n = \frac{\begin{array}{l} l_g - \left(x_0 + \theta_y \cdot \left(z_2 - \frac{z_2 - z_1}{2}\right)\right) \cdot cos\left(\alpha_{n2} - \frac{\alpha_{n2} - \alpha_{n1}}{2}\right) \\ \quad - \left(y_0 + \theta_x \cdot \left(z_2 - \frac{z_2 - z_1}{2}\right)\right) \cdot sin\left(\alpha_{n2} - \frac{\alpha_{n2} - \alpha_{n1}}{2}\right) \end{array}}{\mu_0 \cdot r_{SP} \cdot (\alpha_{n2} - \alpha_{n1}) \cdot (z_2 - z_1)}; n = 1, 2...6 \quad (5.3.26)$$

Setting the reference coordinate system in the center of the bearing, the equation is much more simple, and the term $z_2 - z_1$ is the height of the bearing. The reluctance is the given by:

$$\tilde{\mathcal{R}}_n = \frac{l_g - x_0 \cdot cos\left(\alpha_{n2} - \frac{\alpha_{n2} - \alpha_{n1}}{2}\right) - y_0 \cdot sin\left(\alpha_{n2} - \frac{\alpha_{n2} - \alpha_{n1}}{2}\right)}{\mu_0 \cdot r_{SP} \cdot (\alpha_{n2} - \alpha_{n1}) \cdot h}; n = 1, 2...6 \quad (5.3.27)$$

To compare the simple expression for the reluctance (5.3.27) and the exact expression (5.3.25) influence of the linear motion of the bearing, to the reluctance is plotted. In Figure 5.9 the reluctance $\mathcal{R}_4$ is plotted. Due to alignment of the pole and x-axis, almost nothing happens when moving in y-direction, and the reluctance changes towards infinity, when moving in the x-direction.

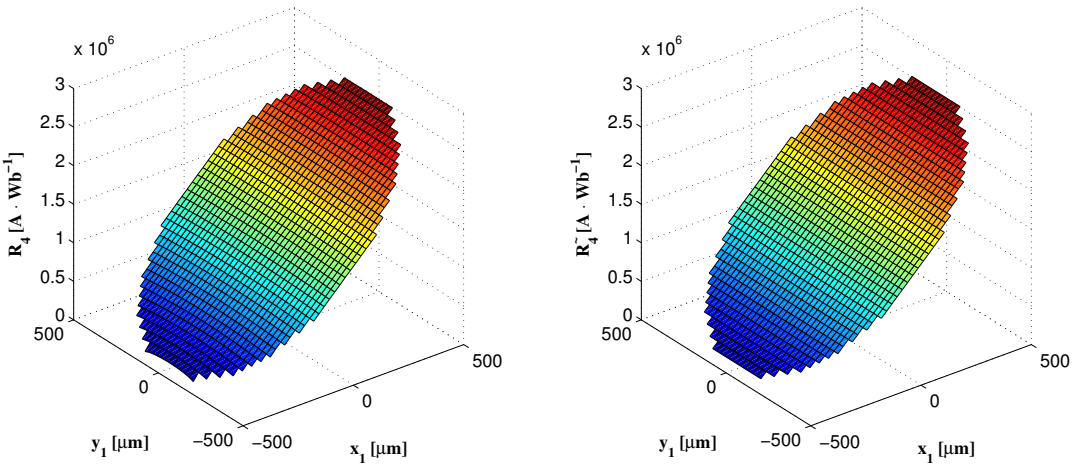

(a) *Exact reluctance.* ***(b)*** *Simplified reluctance.*

Figure 5.9: *Comparison of exact and simplified permeance as function of linear translation of core.*

Likewise the reluctance as a function of rotation θ_x and θ_y is plotted in Figure 5.10a. This shows that the linear translation of the core has a much larger effect on the reluctance.

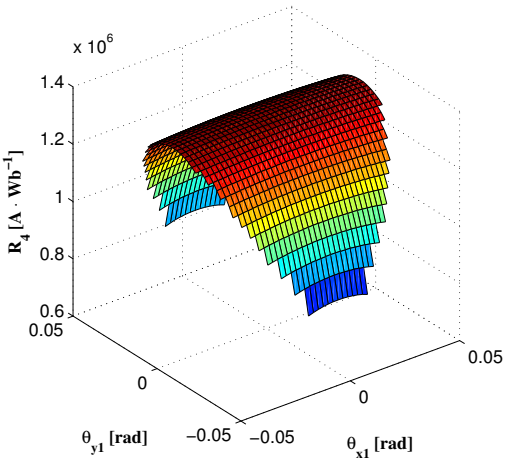

(a) Exact reluctance.

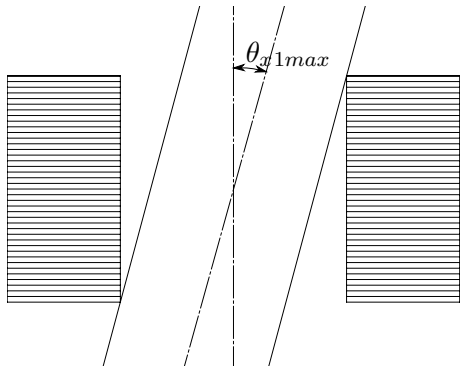

(b) The angle span for the plot is defined by the maximum angle.

Figure 5.10: *The permeance angle dependence.*

The reluctance is evaluated in the possible coordinate domain. Therefore the reluctance tends toward zero when the x_1 coordinate approaches the negative boundary, and the airgap length tends towards zero. The domain of the angles is calculated based on Figure 5.10b. It has to be remarked that physical possible variation in the angle span is significantly smaller than the plotted. The approximation (5.3.27) does not depend on θ_x and θ_y.

The linear translation has a significantly larger effect on the reluctance than the rotation. Thus due to small angles in the bearing and the outlined aspects, the approximate reluctance expression is considered adequate.

5.4 Electric circuit model

The equivalent circuit of one coil is described by the ohmic resistance and the coil inductance. The voltage equation yields:

$$\vec{u} = R_{Ohm} \cdot \vec{i} + \frac{\mathrm{d}}{\mathrm{d}t}\left(\mathbf{L}(\vec{q}) \cdot \vec{i}\right) \tag{5.4.1}$$

Differentiating the flux linkage term with respect to time, equation (5.4.1) yields:

$$\vec{u} = R_{Ohm} \cdot \vec{i} + \mathbf{L}\left(\vec{q}\right) \cdot \frac{\mathrm{d}\vec{i}}{\mathrm{d}t} + \sum_{k=1}^{2}\left(\frac{\partial \mathbf{L}\left(\vec{q}\right)}{\partial q_k}\,\frac{\mathrm{d}q_k}{\mathrm{d}t}\right) \cdot \vec{i} \tag{5.4.2}$$

The summation is from 1 to 2 because of the 2 generalized coordinates ($\vec{q}_m$) the inductance in each bearing is dependent on.

If the inductance is not position dependent, the last term in (5.4.2) does not appear, and the equation only shows the term of self and mutual inductances. Though in this case the last term in (5.4.2) describes the induced Electromotive force (EMF) of rotor movement.

5.5 Non-linear model

In this section the assembled model, containing the mechanical model, the magnetic model and the electric model, is described. For solving the non-linear model, described by a number of differential equations, the MATLAB toolbox Simulink is used. In Figure 5.11 a diagram, collecting the three parts of the model, is shown.

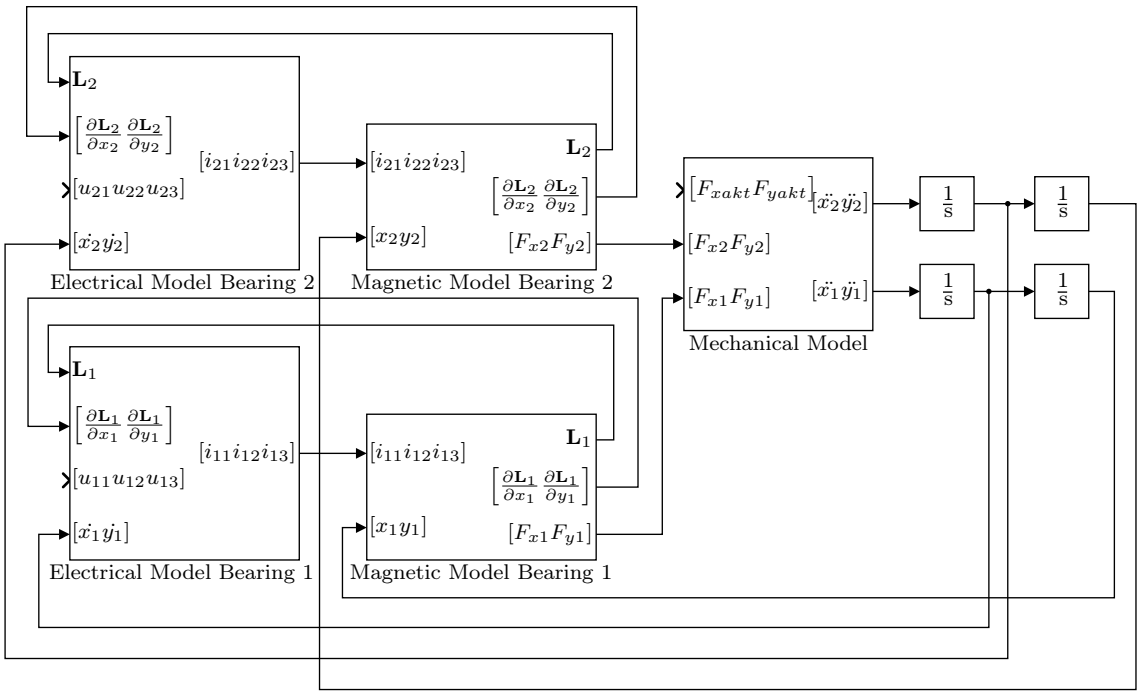

Figure 5.11: *Non-linear Simulink implementation of the model from $\vec{u}$ to $\vec{q}$. The forces from the actuator bearing are left unconnected, resulting in no disturbances.*

The electrical model is in each bearing build up by equation (5.4.2), where the nomenclature in each bearing is shown in the figure.

The magnetic models are set up by equation (5.3.12) calculating the flux in terms of the rotor position and the current, and (5.3.16), where the force is calculated based on the flux. The inductance terms is calculated based on equation (5.3.15).

The mechanical part of the model is described by equation (5.1.36) solving the acceleration based on the forces. It is not shown in the figure, that to include the gyroscopic effect in the model, the axle velocity has to be fed into the mechanical model in bearing coordinates.

5.5.1 Model limitations

In the non-linear model a number of physical conditions are not taken into account. First the saturation of the magnetization is not included in the model. Therefore, if the model should work properly, the flux density must not exceed the linear region of the rotor and stator steel. It is predicted that the saturation of the rotor core represents the limit of the magnetization since it is machined from normal structural ferromagnetic steel.

To get an idea of the size of the limiting saturation current, an approximation is made.

If the model is described by equations (5.3.1) to (5.3.2), where the reluctance of the rotor and stator is neglected. Assuming that the MMF $\mathcal{F}_5 = -\mathcal{F}_6 = N \cdot i_3$ generates the air gap fluxes $\Phi_5 = -\Phi_6 = \Phi$. Then the sum MMF drops yield:

$$2 \cdot N \cdot i_3 = \ 2 \cdot \mathcal{R}_g \cdot \Phi \tag{5.5.1}$$

Dividing each side by the air gap cross section area A gives an expression for the saturation current, described by the position and the maximum flux density:

$$i_{sat} = \frac{A \cdot B_{sat} \cdot \mathcal{R}_g}{N} \tag{5.5.2}$$

Using the expression in (5.3.27) for the reluctance the saturating current is described by:

$$i_{sat} = \frac{B_{sat} \cdot \left(l_g - x_0 \cdot cos\left(\alpha_{n2} - \frac{\alpha_{n2}-\alpha_{n1}}{2}\right) - y_0 \cdot sin\left(\alpha_{n2} - \frac{\alpha_{n2}-\alpha_{n1}}{2}\right)\right)}{\mu_0 \cdot N} \tag{5.5.3}$$

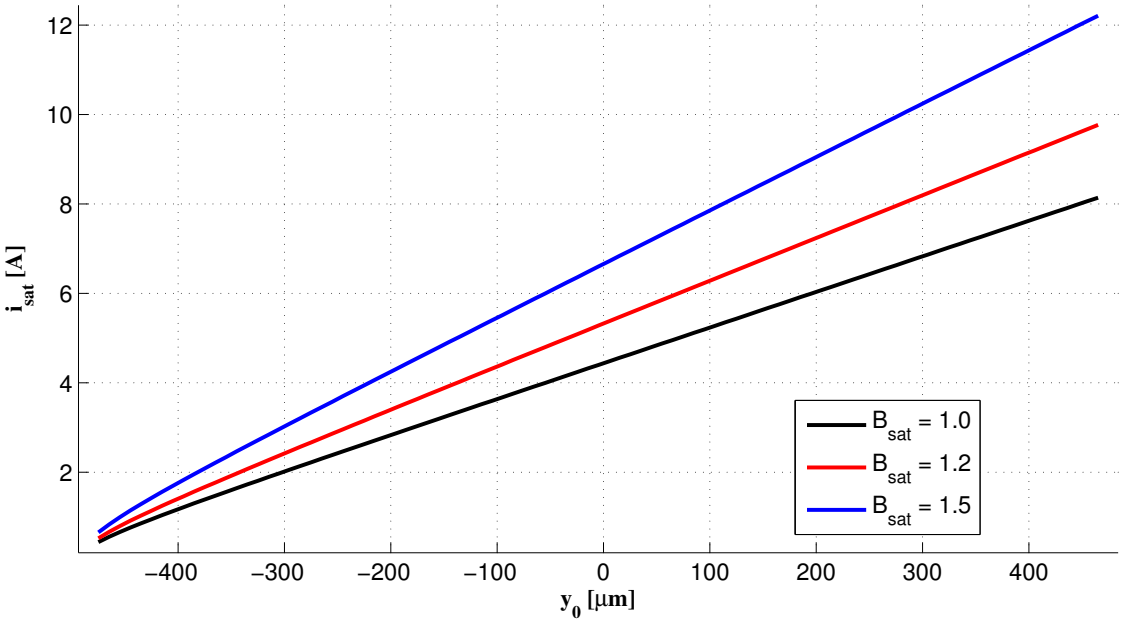

Figure 5.12: *Saturation of current i_3 in bearing 1 for flux density saturating respectively at $B_{sat} = 1.0[T]$, $B_{sat} = 1.2[T]$ and $B_{sat} = 1.5[T]$.*

Nor is the Eddy currents modeled. There are two aspects of Eddy currents in this specific design. When the rotor rotates the flux density in one point in the rotor is changing from $-B$ to B six times per revolution. This effect is less significant because of the low rotor velocity. An eddy current is also induced by the changing field generated by the control system, and should be accounted for in the control design.

Hysteresis is present due to the magnetization and demagnetization does not follow the same B-H curve, and this leads to losses is the iron. Like the Eddy losses this effect is most likely very small due to the low velocities, but are increased by unnecessary control action from the controller.

5.6 Determination of model parameters

In this section the parameters for the model is determined and verified. Measurement data has been acquired using a NI-DAQ, see appendix C.2.

5.6.1 Determination of stator resistance

The stator resistance is determined by connecting a DC voltage source to each coil. The voltage drop over each coil and the current through it is measured, and by Ohms law the resistance in each coil is calculated. All measurements are presented in appendix F.1.

Note that the resistances, used in the model, are a contribution of two coils. So the used resistances are twice the measured. The resistances used for each bearing is as in Table 5.1.

Bearing 1	1.9546Ω
Bearing 2	2.4982Ω
Actuator	1.6454Ω

Table 5.1: *Ohmic resistance for a pair of coils in each bearing.*

5.6.2 Force measurements

In this test the rotor is fixed in the two lower bearings, and the position of the rotor is measured. Exciting one coil in the load actuator to a voltage and measuring the steady state response on the strain gauges, makes it possible to verify the static force response of the model.

The force measurements are made for three different rotor positions, where the x-coordinate is held at $x_{akt} = 0[mm]$, and the y-coordinate is:

$$y_{akt1} = 0.05[mm] \tag{5.6.1}$$
$$y_{akt2} = 0.17[mm] \tag{5.6.2}$$
$$y_{akt3} = 0.35[mm] \tag{5.6.3}$$

A voltage is applied on coil 3 i.e. there should be no force in the x-direction cf. the definition in Figure 5.4. The measured force at different currents is shown in Figures 5.13 through 5.15 for the three positions. The forces are calculated with the gauge factors presented in equation 3.4.2 and 3.4.3. In the figure the results of a Finite Element Method Magnetics (FEMM) model of the bearing is also presented. The FEMM model is documented in Appendix D.

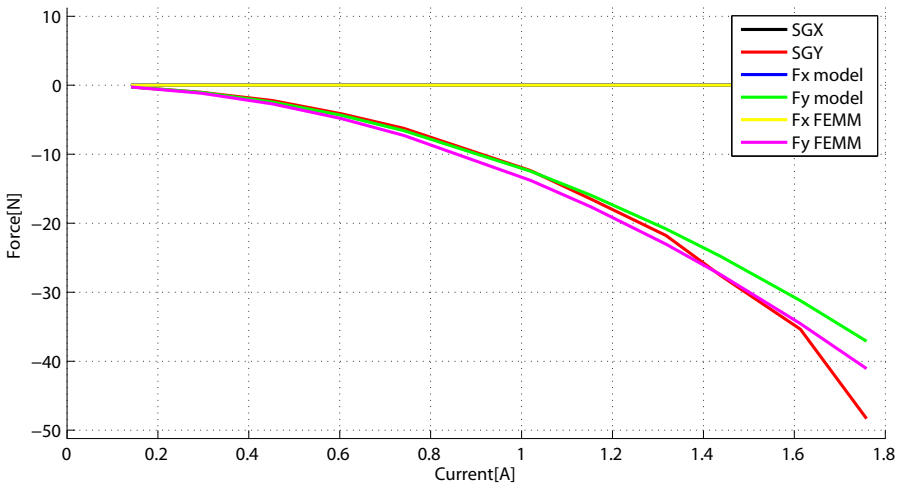

Figure 5.13: *Force by SG measurements, RNM and FEMM at different* $\vec{i_3}$ *at* $y_{akt} = 0.05mm$.

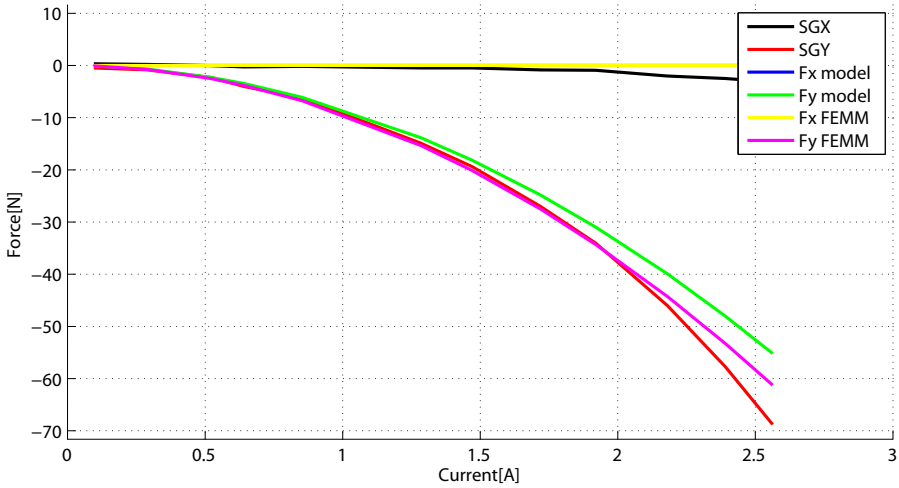

Figure 5.14: *Force by SG measurements, RNM and FEMM at different* $\vec{i_3}$ *at* $y_{akt} = 0.17mm$.

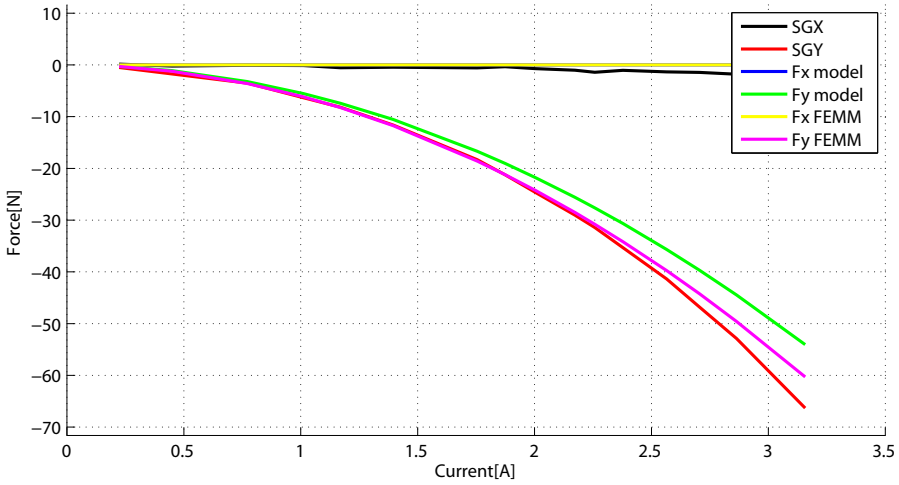

Figure 5.15: *Force by SG measurements, RNM and FEMM at different* $\vec{i_3}$ *at* $y_{akt} = 0.35mm$.

The figure shows that the FEMM model shows a good accordance to the measurements.

The RNM and the FEMM model shows, as expected, no force in the x-direction, though the measurements does show a small force. This is assumed to be because of misalignment in the assembling of the experimental setup.

In general the measurements and the FEMM model shows good accordance in the y-direction, and the RNM tends to give a slight smaller force. The difference between measurements and model force at larger currents, where the measured force is slightly bigger than the model force, might be an effect of rotor movement. Since no position was measured during the tests, this is only an assumption.

To make the model fit the measurements, some modifications has to be done. Due to manufacturing of the stator sheets a consequential damage can be that the magnetic airgap is larger than geometric [Polajzer, 2010]. Therefore increasing the model airgap can give a better fitting model. Though this is not a solution in this case since the RNM shows smaller forces. Furthermore this should also be a problem for the FEMM model.

In the force measurements it is attempted to take into account where on the magnetization curve the tests are performed. This is done by starting the measurements at a large current and then at smaller.

By the considerations in this section it is confirmed that the FEMM model shows a good similarity to the measurements. Therefore the RNM is optimized to show the same response as the FEMM model.

5.6.3 Optimization of model parameters

The FEMM model and results from the experimental setup showed good accordance, and the FEMM model are now used to optimize the RNM. The RNM is used in the solution of the non-linear model, and it is thus advantageous that it has the best fit to the experimental setup. It is convenient to optimize the RNM by using the FEMM model instead of the results from the experimental setup. In Figure 5.16 the force in the y-direction is shown as a dependance of rotor position (only y-coordinate) and current $\vec{i_3}$, both for the reluctance network model and the FEMM model.

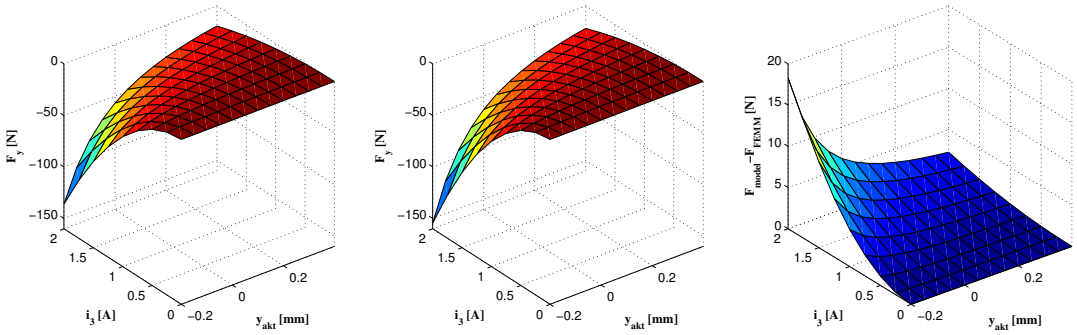

(a) Force by RNM. *(b) Force by FEMM model.* *(c) Difference between RNM force and FEMM force.*

Figure 5.16

To optimize the RNM the algorithm adjust the reluctances of the magnetic circuit to fit

the FEMM model. The specifications of the optimization is described in Appendix G.

The optimization is performed for rotor positions around the center coordinate, and relatively small currents to be sure that no magnetic saturation occurs in the tests. This is verified by the FEMM model, where it is ensured that the flux density does not exceed $\approx 1[T]$. The force of the optimized RNM is shown in Figure 5.17a, and the new reluctances are given in equation (5.6.4) to (5.6.9) as the approximated reluctances from equation (5.3.17) to (5.3.21) multiplied by a factor.

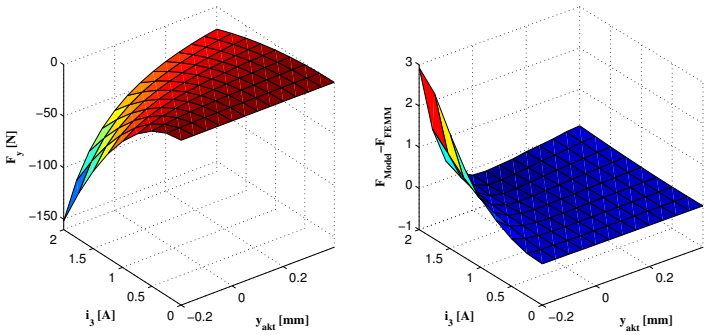

(a) *Force by optimized RNM.*

(b) *Percentage deviation between optimized RNM force and FEMM force.*

Figure 5.17

$$\mathcal{R}_p = 0.8317 \cdot \mathcal{R}_{p,initial} \tag{5.6.4}$$

$$\mathcal{R}_s = 0.7036 \cdot \mathcal{R}_{s,initial} \tag{5.6.5}$$

$$\mathcal{R}_r = 1.4080 \cdot \mathcal{R}_{r,initial} \tag{5.6.6}$$

$$\mathcal{R}_{ml} = 1.6157 \cdot \mathcal{R}_{ml,initial} \tag{5.6.7}$$

$$\mathcal{R}_{sl} = 1.6190 \cdot \mathcal{R}_{sl,initial} \tag{5.6.8}$$

$$\mathcal{R}_g = 0.9023 \cdot \mathcal{R}_{g,initial} \tag{5.6.9}$$

It shows that the mutual leakage reluctance $\mathcal{R}_{ml}$ and $\mathcal{R}_{sl}$ does not have a significant impact on the force, since they are relatively large.

To fit the model of bearing 1 and 2 the reluctances are scaled by the height of the bearings.

Though the optimized RNM shows a remarkable smaller deviation from the FEMM model than for the non optimized, one has to bear in mind that the RNM does not show the effect of saturation. To have an idea of the significance of this, the force of the FEMM model and the RNM model is plotted in Figure 5.18 at different positions. Here a material model for the rotor and stator is chosen to saturate at $1.5T$.

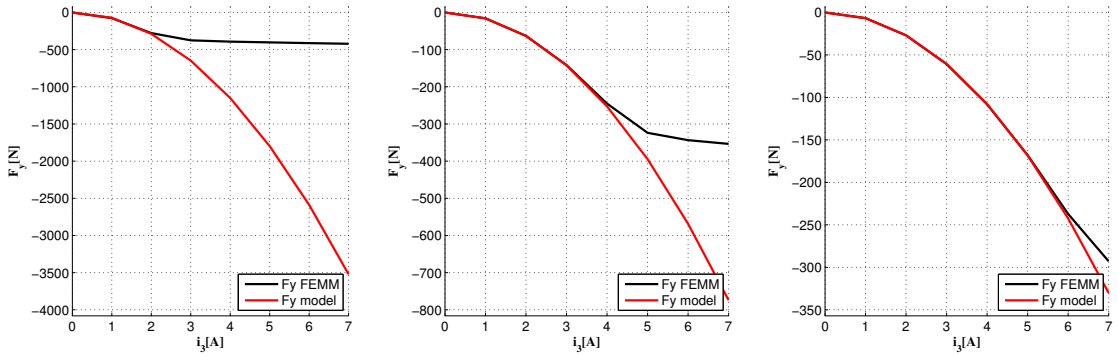

(a) Rotor position $y = -300\mu m$. *(b) Rotor position $y = 0.0$.* *(c) Rotor position $y = 300\mu m$.*

Figure 5.18

This shows clearly that the saturation has a significant effect where the rotor is close to a pole, i.e. saturation occurs at $\approx 2[A]$ in Figure 5.18a, and at a position far from the pole, the saturation first occurs at $\approx 6[A]$ in Figure 5.18c. The model saturating at $1.5T$ is expected to yield even higher saturation currents than for the physical system.

5.7 Dynamic Verification

To verify the model dynamically the system is stabilized using a linear controller. The system is then disturbed by applying a step to the set point of the controller. Figure 5.19 shows the response of different steps of the controller. The controller used is the decentralized PD controller from chapter 6, but less aggressively tuned to minimized the differential noise and make result comparison more accurate. The PD controller gains are shown (5.7.1).

Bearing One:

$$k_p = 1678.5$$
$$k_d = 11.52$$

Bearing Two:

$$k_p = 2228.0$$
$$k_d = 18.20$$

(5.7.1)

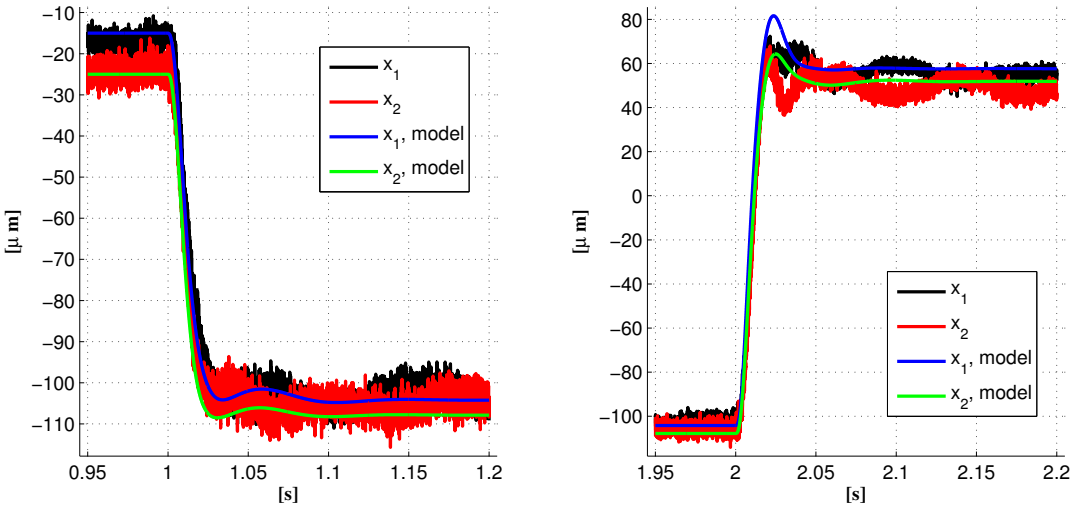

(a) Step of -50 µm. *(b) Step of 100 µm.*

Figure 5.19: *Position for a series of steps for model verification.*

Figure 5.19 shows two steps, with the model response plotted along the measured response from the experimental setup. The model response is slightly offset to compensate for steady state error occurring on the experimental setup, because of axle misalignment the string force is not completely zero. After this alteration it is seen that the model response follows that of the measured response. The steady states are similar. Some oscillations occur in reality which the model does not show, it is expected that these occur because of signal noise or physical oscillations in the experimental setup. The current for the same two steps are shown Figure 5.20 and 5.21.

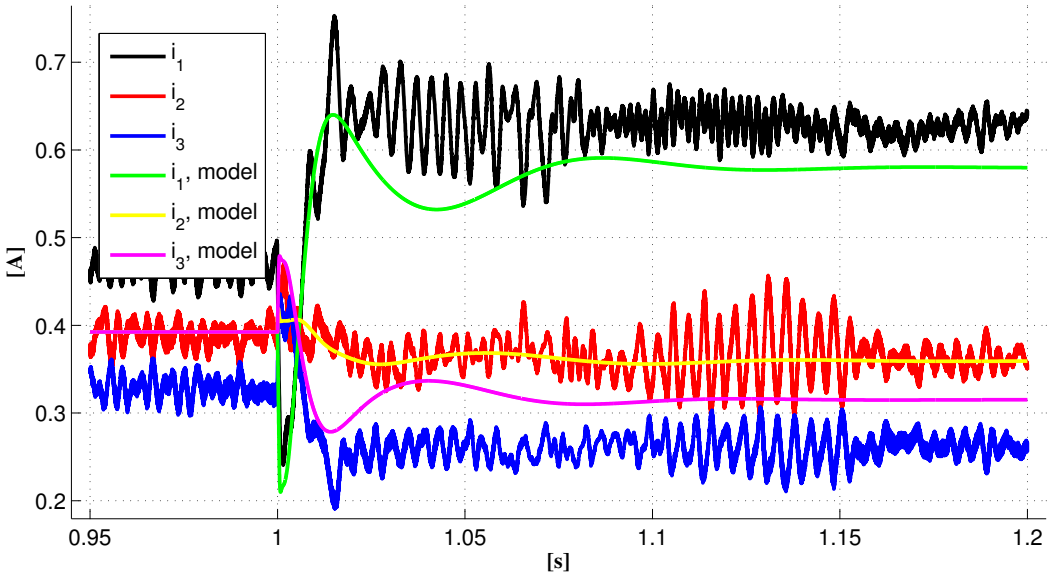

Figure 5.20: *Measured currents of a $-50\mu m$ step.*

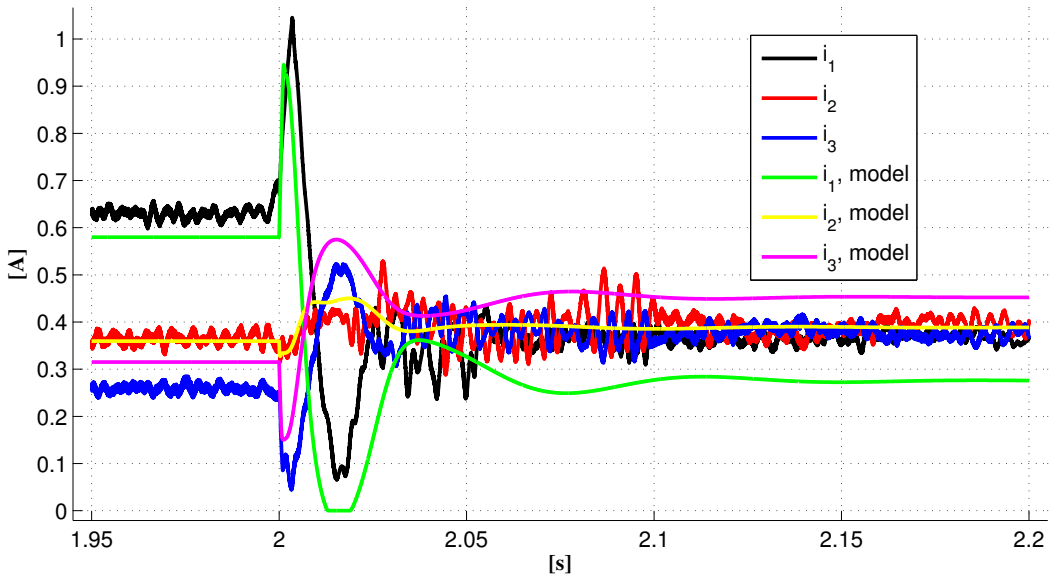

Figure 5.21: *Measured currents of a* $100\mu m$ *step.*

The currents are highly affected by the noise in the position signal, disturbing the differential part of the PD controller. Most of this disturbance does not result in axle movement, because of the mechanical systems time constant, but it makes the comparison between the two signals more difficult. Disregarding the noise in the signals they track the model response. Again an offset exists because the axle is misaligned.

5.8 Linear model

In this section the equations from the previous sections are linearized and connected in a linear model.

5.8.1 Linear mechanical model

From equation (5.1.35) the mechanical model is described by:

$$\begin{aligned}\vec{Q_c} = &\begin{bmatrix} \frac{{l_2}^2 \cdot m + I_{xx}}{k_{mek}} & 0 & \frac{-l_2 \cdot l_1 \cdot m - I_{xx}}{k_{mek}} & 0 \\ 0 & \frac{{l_2}^2 \cdot m + I_{xx}}{k_{mek}} & 0 & \frac{-l_2 \cdot l_1 \cdot m - I_{xx}}{k_{mek}} \\ \frac{-l_2 \cdot l_1 \cdot m - I_{xx}}{k_{mek}} & 0 & \frac{{l_1}^2 \cdot m + I_{xx}}{k_{mek}} & 0 \\ 0 & \frac{-l_2 \cdot l_1 \cdot m - I_{xx}}{k_{mek}} & 0 & \frac{{l_1}^2 \cdot m + I_{xx}}{k_{mek}} \end{bmatrix} \cdot \ddot{\vec{x}} \\ &+ \begin{bmatrix} 0 & \frac{I_{zz} \cdot \omega}{k_{mek}} & 0 & \frac{-I_{zz} \cdot \omega}{k_{mek}} \\ \frac{I_{zz} \cdot \omega}{k_{mek}} & 0 & \frac{-I_{zz} \cdot \omega}{k_{mek}} & 0 \\ 0 & \frac{-I_{zz} \cdot \omega}{k_{mek}} & 0 & \frac{I_{zz} \cdot \omega}{k_{mek}} \\ \frac{-I_{zz} \cdot \omega}{k_{mek}} & 0 & \frac{I_{zz} \cdot \omega}{k_{mek}} & 0 \end{bmatrix} \cdot \dot{\vec{x}} \\ &= \mathbf{M_c} \cdot \ddot{\vec{x}} + \mathbf{G_c} \cdot \dot{\vec{x}} \end{aligned} \tag{5.8.1}$$

Where the constant k_{mek} is defined by:

$$k_{mek} = (l_1 - l_2)^2 \tag{5.8.2}$$

It shows that the mechanical model by it self is all ready linear. This is due to the small angle assumptions from section 5.1.

5.8.2 Linear magnetic and electrical model

The voltage equation (5.4.2) is linearized by a first order Taylor series:

$$\begin{aligned}\Delta u_j = &\sum_{k=1}^{2} \left.\frac{\partial u_j}{\partial q_k}\right|_{\{l_0\}} \cdot \Delta q_k + \sum_{k=1}^{2} \left.\frac{\partial u_j}{\partial \dot{q}_k}\right|_{\{l_0\}} \cdot \Delta \dot{q}_k + \sum_{k=1}^{3} \left.\frac{\partial u_j}{\partial i_k}\right|_{\{l_0\}} \cdot \Delta i_k \\ &+ \sum_{k=1}^{3} \left.\frac{\partial u_j}{\partial \dot{i}_k}\right|_{\{l_0\}} \cdot \Delta \dot{i}_k \\ = &\sum_{k=1}^{2} k_{ujqk} \cdot \Delta q_k + \sum_{k=1}^{2} k_{uj\dot{q}k} \cdot \Delta \dot{q}_k + \sum_{k=1}^{3} k_{uji k} \cdot \Delta i_k + \sum_{k=1}^{3} k_{uj\dot{i}k} \cdot \Delta \dot{i}_k \end{aligned} \tag{5.8.3}$$

Where the set $\{l_0\}$ represents the linearization points given as:

$$\{l_0\} = \{x_{10}\ y_{10}\ \dot{x_{10}}\ \dot{y_{10}}\ i_{10}\ i_{20}\ i_{30}\ \dot{i}_{10}\ \dot{i}_{20}\ \dot{i}_{30}\} \tag{5.8.4}$$

This yields three equations, each with ten linearization constants. Writing the linearized equations on vector matrix form for both bearings yields:

$$\begin{aligned}\begin{bmatrix} u_1 \\ u_2 \\ u_3 \end{bmatrix} = &\begin{bmatrix} k_{u1q1} & k_{u1q2} \\ k_{u2q1} & k_{u2q2} \\ k_{u3q1} & k_{u3q2} \end{bmatrix} \cdot \begin{bmatrix} x \\ y \end{bmatrix} + \begin{bmatrix} k_{u1\dot{q}1} & k_{u1\dot{q}2} \\ k_{u2\dot{q}1} & k_{u2\dot{q}2} \\ k_{u3\dot{q}1} & k_{u3\dot{q}2} \end{bmatrix} \cdot \begin{bmatrix} \dot{x} \\ \dot{y} \end{bmatrix} + \begin{bmatrix} k_{u1i1} & k_{u1i2} & k_{u1i3} \\ k_{u2i1} & k_{u2i2} & k_{u2i3} \\ k_{u3i1} & k_{u3i2} & k_{u3i3} \end{bmatrix} \cdot \begin{bmatrix} i_1 \\ i_2 \\ i_3 \end{bmatrix} \\ &+ \begin{bmatrix} k_{u1\dot{i}1} & k_{u1\dot{i}2} & k_{u1\dot{i}3} \\ k_{u2\dot{i}1} & k_{u2\dot{i}2} & k_{u2\dot{i}3} \\ k_{u3\dot{i}1} & k_{u3\dot{i}2} & k_{u3\dot{i}3} \end{bmatrix} \cdot \begin{bmatrix} \dot{i}_1 \\ \dot{i}_2 \\ \dot{i}_3 \end{bmatrix} \end{aligned} \tag{5.8.5}$$

The linearization of one bearing is shown here. Going through the same procedure for the other bearing, yields an equation of the same form. Collecting the equations for the two bearings yields an equation for the 6 voltages described by:

$$\vec{u}_c = \mathbf{k}_{uq} \cdot \vec{x} + \mathbf{k}_{u\dot{q}} \cdot \dot{\vec{x}} + \mathbf{k}_{ui} \cdot \vec{i}_c + \mathbf{k}_{u\dot{i}} \cdot \dot{\vec{i}}_c \tag{5.8.6}$$

Similarly the expression for the force (5.3.11) is linearized by a first order Taylor series:

$$\begin{aligned}\Delta Q_j = &\sum_{k=1}^{2} \left.\frac{\partial Q_j}{\partial q_k}\right|_{\{l_0\}} \cdot \Delta q_k + \sum_{k=1}^{3} \left.\frac{\partial Q_j}{\partial i_k}\right|_{\{l_0\}} \cdot \Delta i_k \\ = &\sum_{k=1}^{2} k_{Qjqk} \cdot \Delta q_k + \sum_{k=1}^{3} k_{Qjik} \cdot \Delta i_k \end{aligned} \tag{5.8.7}$$

Where each Q has five linearization constants. Writing the linearized equations on vector matrix form yields:

$$\begin{bmatrix} F_{x1} \\ F_{y1} \end{bmatrix} = \begin{bmatrix} k_{Q1q1} & k_{Q1q2} \\ k_{Q2q1} & k_{Q2q2} \end{bmatrix} \cdot \begin{bmatrix} x_1 \\ y_1 \end{bmatrix} + \begin{bmatrix} k_{Q1i1} & k_{Q1i2} & k_{Q1i3} \\ k_{Q2i1} & k_{Q2i2} & k_{Q2i3} \end{bmatrix} \cdot \begin{bmatrix} i_{11} \\ i_{12} \\ i_{13} \end{bmatrix} \tag{5.8.8}$$

Collecting the linearization constants for each bearing, yields an equation on the form:

$$\begin{bmatrix} F_{x1} \\ F_{y1} \\ F_{x2} \\ F_{y2} \end{bmatrix} = \begin{bmatrix} k_{Fx1x1} & k_{Fx1y1} & 0 & 0 \\ k_{Fy1x1} & k_{Fy1y1} & 0 & 0 \\ 0 & 0 & k_{Fx2x2} & k_{Fx2y2} \\ 0 & 0 & k_{Fy2x2} & k_{Fy2y2} \end{bmatrix} \cdot \begin{bmatrix} x_1 \\ y_1 \\ x_2 \\ y_2 \end{bmatrix}$$

$$+ \begin{bmatrix} k_{Fx1i11} & k_{Fx1i12} & k_{Fx1i13} & 0 & 0 & 0 \\ k_{Fy1i11} & k_{Fy1i12} & k_{Fy1i13} & 0 & 0 & 0 \\ 0 & 0 & 0 & k_{Fx2i21} & k_{Fx2i22} & k_{Fx2i23} \\ 0 & 0 & 0 & k_{Fy2i21} & k_{Fy2i22} & k_{Fy2i23} \end{bmatrix} \cdot \begin{bmatrix} i_{11} \\ i_{12} \\ i_{13} \\ i_{21} \\ i_{22} \\ i_{23} \end{bmatrix}$$

$$\vec{Q_c} = \mathbf{k}_{Qq} \cdot \vec{x} + \mathbf{k}_{Qi} \cdot \vec{i_c} \tag{5.8.9}$$

Setting this equal to (5.8.1), and solving for accelerations yield:

$$\begin{aligned} \mathbf{M_c} \cdot \ddot{\vec{x}} + \mathbf{G_c} \cdot \dot{\vec{x}} = & \ \mathbf{k}_{Qq} \cdot \vec{x} + \mathbf{k}_{Qi} \cdot \vec{i}_c \\ \ddot{\vec{x}} = & \ \mathbf{M_c}^{-1} \cdot \mathbf{k}_{Qi} \cdot \vec{i}_c + \mathbf{M_c}^{-1} \cdot \mathbf{k}_{Qq} \cdot \vec{x} - \mathbf{M_c}^{-1} \cdot \mathbf{G_c} \cdot \dot{\vec{x}} \end{aligned} \tag{5.8.10}$$

Solving (5.8.6) for the current derivatives yields:

$$\dot{\vec{i}}_c = \ -\mathbf{k}_{ui}^{-1} \cdot \mathbf{k}_{ui} \cdot \vec{i}_c - \mathbf{k}_{ui}^{-1} \cdot \mathbf{k}_{uq} \cdot \vec{x} - \mathbf{k}_{ui}^{-1} \cdot \mathbf{k}_{u\dot{q}} \cdot \dot{\vec{x}} + \mathbf{k}_{ui}^{-1} \cdot \vec{u}_c \tag{5.8.11}$$

These equations are described on state space form:

$$\begin{bmatrix} \begin{bmatrix} \dot{\vec{i}}_c \\ 6 \times 1 \end{bmatrix} \\ \begin{bmatrix} \dot{\vec{x}} \\ 4 \times 1 \end{bmatrix} \\ \begin{bmatrix} \ddot{\vec{x}} \\ 4 \times 1 \end{bmatrix} \end{bmatrix} = \begin{bmatrix} \begin{bmatrix} -\mathbf{k}_{ui}^{-1} \cdot \mathbf{k}_{ui} \\ 6 \times 6 \end{bmatrix} & \begin{bmatrix} -\mathbf{k}_{ui}^{-1} \cdot \mathbf{k}_{uq} \\ 6 \times 4 \end{bmatrix} & \begin{bmatrix} -\mathbf{k}_{ui}^{-1} \cdot \mathbf{k}_{u\dot{q}} \\ 6 \times 4 \end{bmatrix} \\ \begin{bmatrix} \mathbf{0} \\ 4 \times 6 \end{bmatrix} & \begin{bmatrix} \mathbf{0} \\ 4 \times 4 \end{bmatrix} & \begin{bmatrix} \mathbf{I} \\ 4 \times 4 \end{bmatrix} \\ \begin{bmatrix} \mathbf{M_c}^{-1} \cdot \mathbf{k}_{Qi} \\ 4 \times 6 \end{bmatrix} & \begin{bmatrix} \mathbf{M_c}^{-1} \cdot \mathbf{k}_{Qq} \\ 4 \times 4 \end{bmatrix} & \begin{bmatrix} -\mathbf{M_c}^{-1} \cdot \mathbf{G_c} \\ 4 \times 4 \end{bmatrix} \end{bmatrix} \begin{bmatrix} \begin{bmatrix} \vec{i}_c \\ 6 \times 1 \end{bmatrix} \\ \begin{bmatrix} \vec{x} \\ 4 \times 1 \end{bmatrix} \\ \begin{bmatrix} \dot{\vec{x}} \\ 4 \times 1 \end{bmatrix} \end{bmatrix} + \begin{bmatrix} \begin{bmatrix} \mathbf{k}_{ui}^{-1} \\ 6 \times 6 \end{bmatrix} \\ \begin{bmatrix} \mathbf{0} \\ 4 \times 6 \end{bmatrix} \\ \begin{bmatrix} \mathbf{0} \\ 4 \times 6 \end{bmatrix} \end{bmatrix} \begin{bmatrix} \vec{u}_c \\ 6 \times 1 \end{bmatrix} \tag{5.8.12}$$

The form of the linearized equations is described in this section. In the next the linearization points are discussed.

5.8.3 Linearization points

In this section some considerations about the linearization procedure is performed. First the current-force model (5.8.9) is considered.

Current-force model

As shown in equation (5.3.11) the force is a parabolic function of the current, for a defined rotor position. A plot of this is shown in Figure 5.22. This shows that the non-linear model can not be linearized at a current on $0[A]$, since the tangent at this point is a horizontal line.

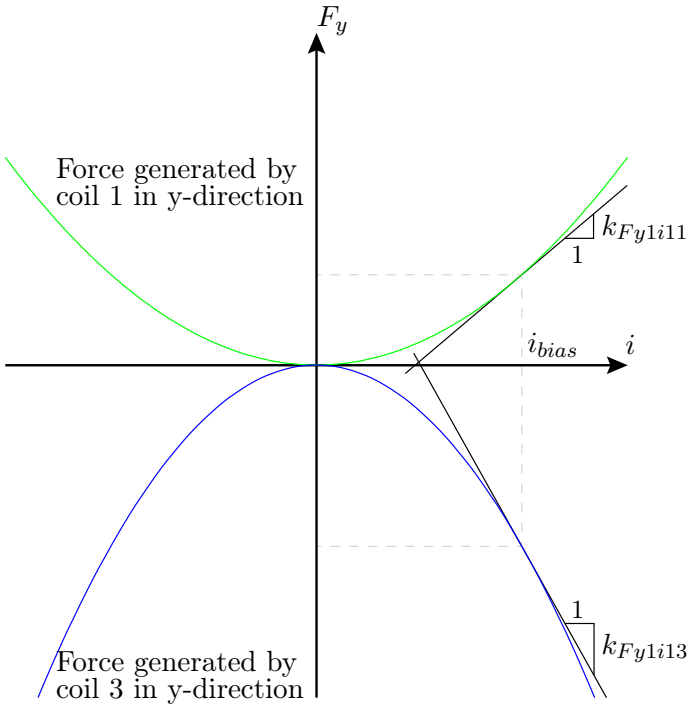

Figure 5.22: *Shows the relation between current and force, at a fixed position. The current stiffness is indicated.*

To avoid this problem a bias current is introduced. Adding this on all coils the resulting force is still zero. In Figure 5.22 the linearization constants k_{Fy1i11}, k_{Fy1i12} and k_{Fy1i13} would be the slopes of the tangents, where $k_{Fy1i11}$and k_{Fy1i12} should be equal.

When linearizing around a bias current, negative and zero currents can be prevented, as long as the control current does not exceed the bias current.

The coordinate linearization points are specified in the zero position, as it will be this position the axle has to maintain. In the next section, the consequence of this is approximation is analyzed.

5.8.4 Study of linearization points

In this section, the consequence of the chosen linearization points are studied. In the following figures the linearization constants of equation (5.8.8) are plotted for a constant bias current and different linearization positions.

First the position stiffness is plotted in Figure 5.23. The stiffness k_{Fx1x1} relates the movement in the x_1 direction to the force F_{x1}, and as it shows it is changing dramatically, when the linearization position x_0 is changed. The position stiffness k_{Fx1y1} has a almost

flat zero value area, when the x_0 and y_0 position is near the center, though near the boundary this constant has a significant influence on the force.

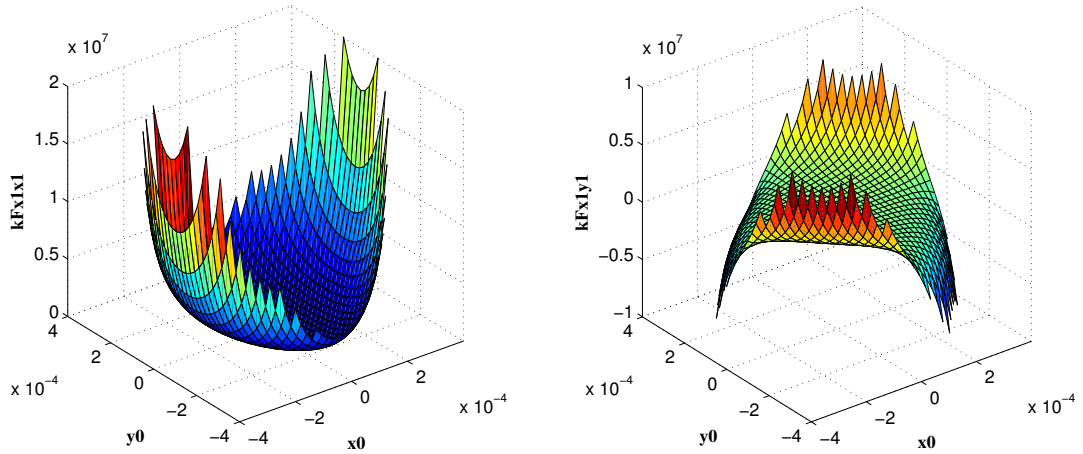

(a) *(b)*

Figure 5.23: *Position stiffness in x direction, for bias of 1A.*

By these considerations the constant k_{Fx1y1} can be neglected when the rotor is near a center position, and only the k_{Fx1x1} has a significant effect.

Next the current stiffness' are plotted in Figure 5.24. In an area around the center all of them has a constant value. The zero value of k_{Fx1i11} is $130\frac{N}{A}$ and the zero value of k_{Fx1i12} is $-130\frac{N}{A}$. The last constant k_{Fx1i13} is zero in the center position, as current 3 has no effect on the x_1 direction, when in the middle position.

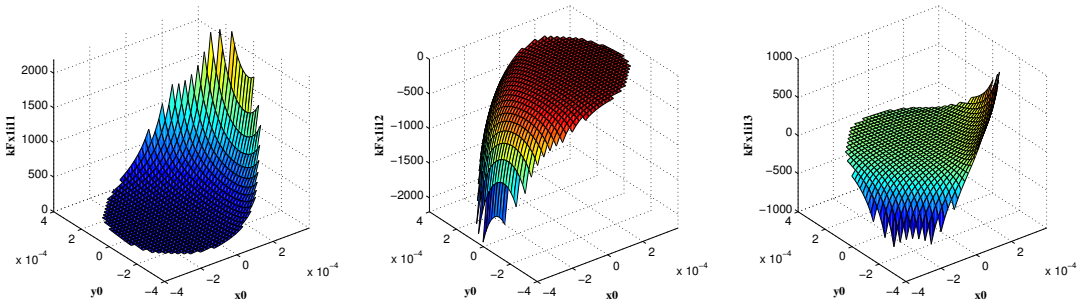

(a) *(b)* *(c)*

Figure 5.24: *Current stiffness in x direction, for a bias current of* 1*A.*

The position stiffness' for the F_{y1} force is similar to the other. The k_{Fy1x1} constant can be neglected when in the center area. The plot of the constants are shown in Figure 5.25.

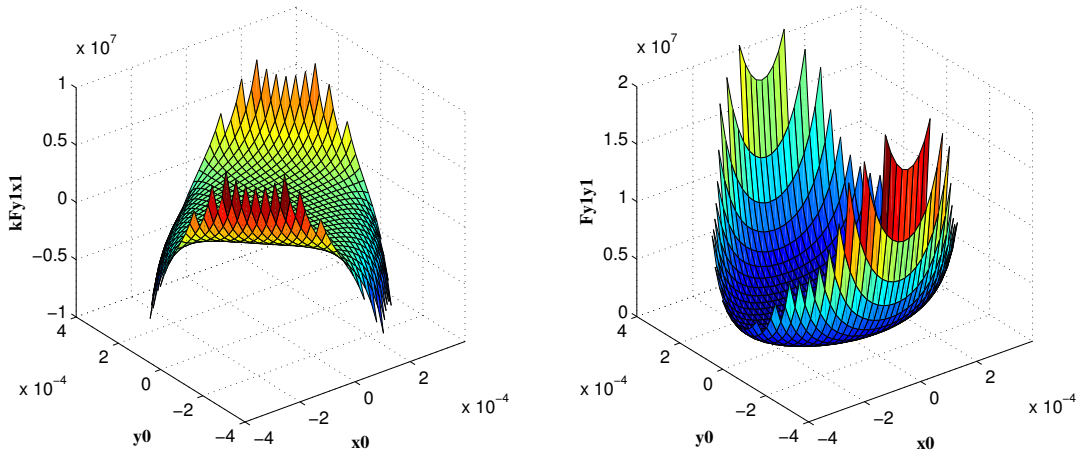

(a) *(b)*

Figure 5.25: *Position stiffness in y direction, for bias on 1A.*

The current stiffness' for F_{y1} are plotted in Figure 5.26. The zero values for k_{Fy1i11}, k_{Fy1i12} and k_{Fy1i13} are respectively $75.04\frac{N}{A}$, $75.04\frac{N}{A}$ and $-150.10\frac{N}{A}$. This corresponds to the fact that the force contributions to F_{y1} from i_{11} and i_{12} is acting in an angle of 60°, and therefore are half the value (negative) of k_{Fy1i13}. Similarly the it shows that the k_{Fx1i11} and k_{Fx1i12} equals $cos(30°) \cdot k_{Fy1i13}$, due to the angle between i_{11} and i_{12} and the F_{x1} force.

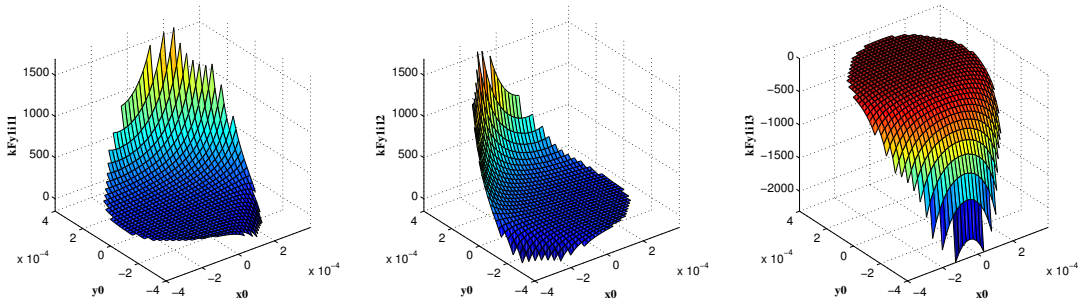

(a) *(b)* *(c)*

Figure 5.26: *Current stiffness in y direction, for a bias current of* $1A$.

Linearizing in $i_{10} = i_{20} = i_{30} = i_{bias}$ and $x_{10} = y_{10}$=0. Remark that in this position the inductance matrix is almost symmetric, and the linearized expression can be written as follows. Though the second order derivatives of the off diagonal elements is not zero in this position.

Then the linearized system for bearing one is described by:

$$\begin{bmatrix} F_x \\ F_y \end{bmatrix} = \begin{bmatrix} k_{Fx1x1} & 0 \\ 0 & k_{Fx1x1} \end{bmatrix} \cdot \begin{bmatrix} x_1 \\ y_1 \end{bmatrix} + \begin{bmatrix} -\frac{\sqrt{3}}{2} \cdot k_{Fy1i3} & \frac{\sqrt{3}}{2} \cdot k_{Fy1i3} & 0 \\ -\frac{1}{2} \cdot k_{Fy1i3} & -\frac{1}{2} \cdot k_{Fy1i3} & k_{Fy1i3} \end{bmatrix} \cdot \begin{bmatrix} i_{11} \\ i_{12} \\ i_{13} \end{bmatrix} \tag{5.8.13}$$

The off diagonal terms in the matrix relating position to force is set equal to zero, as they are much smaller than the diagonal terms, as shown in the position stiffness figures. As long as the rotor is near the center position.

The linearization constants described by the bias current, are presented for each bearing in Table 5.2. Since the only difference of the two bearings is the height, the linearization constants can simply be scaled by the height ratio $\frac{h_1}{h_2}$

Bearing 1		
k_{Fy1i3}	$[\frac{N}{A}]$	$-i_0 \cdot 60.4178$
k_{Fx1x1}	$[\frac{N}{m}]$	${i_0}^2 \cdot 2.2031 \cdot 10^6$
k_{Fx1y1}	$[\frac{N}{m}]$	$-{i_0}^2 \cdot 2.1828 \cdot 10^{-11}$

Bearing 2		
k_{Fy2i3}	$[\frac{N}{A}]$	$-i_0 \cdot 105.7311$
k_{Fx2x2}	$[\frac{N}{m}]$	${i_0}^2 \cdot 3.8554 \cdot 10^5$
k_{Fx2y2}	$[\frac{N}{m}]$	$-{i_0}^2 \cdot 3.8199 \cdot 10^{-11}$

Table 5.2: *Linearization constants for bearing 1 and 2.*

The scope, of the linearization and the discussions in this section, is to be able to design controllers using the linearized system. Also it is important to know the limitations of the linear model discussed. In the next chapter a number of controllers based on the linearized system are developed.

Control 6

In this chapter a number of different control strategies for the AMB is developed, along with a Finite Impulse Response (FIR) filter used for control implementation on the experimental setup. Overall control design with both transfer functions and state space representation are tried. Because of the Multiple-Input and Multiple-Output (MIMO) and non-linear nature of the system, further strategies for the controllers are necessary. These strategies are based on experience with the system, and the fundamental governing equations for the magnetic system. In the last section of this chapter the controllers are compared and the best strategy is chosen.

6.1 Digital filtering

The noise in the position sensors signal was in section 4.4.12 found to be significant. As long as a controller with strictly proportional and integral action is used, this will probably pass unnoticed. In this application, where the system is linearized in a vertical position, there is no force from the string, and the system is thus *unstable* as depicted in figure 1.3, and the differential action of the controller must be implemented to stabilize the system. Using a first order differentiation scheme, like that of an ordinary PID controller, simply is insufficient, and a filter is necessary. For this purpose a FIR filter will be designed and implemented, because of its inherent stability and good phase response. [Chassaing, 2003].

FIR filter design

The filter is designed using MATLAB, where a windowed method is used to generate a low-pass filter. The filter is given in Direct form 1, which provides the coefficients for the filter,$\vec{h}$, in a row vector where $h(0)$ corresponds to the signal $e(0)$, see Figure 6.1.

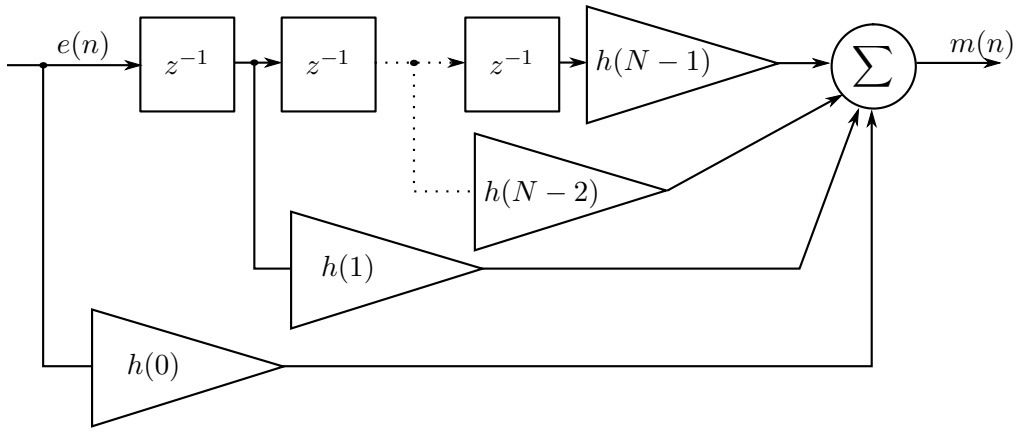

Figure 6.1: *Block diagram of how the sampled signal, $\vec{e}$, is filtered with coefficients $\vec{h}$ to create output $m(0)$. z^{-1} is one sample delay.*

Initially a filter was designed to run with the same frequency as the ADC, but the filter proved to be too computationally demanding, hence a lower order filter was chosen to run with the same timing as the controller. The filter will be chosen with an order and cutoff frequency, that will not cripple the performance of the position sensors, while making the first order differential scheme of the PID applicable. To the filter, the differentiation scheme has simply been applied to a signal that are comprised of a sine wave, with the noise present in the actual system added.

A sine wave with an amplitude of $25\mu m$ and frequency of $100Hz$ has been chosen to illustrate the filter efficiency.

$$x(t) = 25 \cdot sin(100 \cdot 2 \cdot \pi \cdot t) + u_{noise} \tag{6.1.1}$$

$$\frac{dx(n)}{dt} \approx \frac{(u(n-1) + u_{noise}(n-1)) - (u(n) + u_{noise}(n))}{T_{sample}} \tag{6.1.2}$$

With:

u_{noise}(n): The AC noise measured when the system is idling.
T_{sample}: Sample period of $12.5kHz$ sample frequency.

The order of the filter has then been chosen simply by inspecting the results of the numerical differentiation scheme, the scheme is presented in equation (6.1.2), while the input is filtered by filters of different order. The result of a 21th order filter is shown in Figure 6.2. For reference, the analytical solution is also included in the figure.

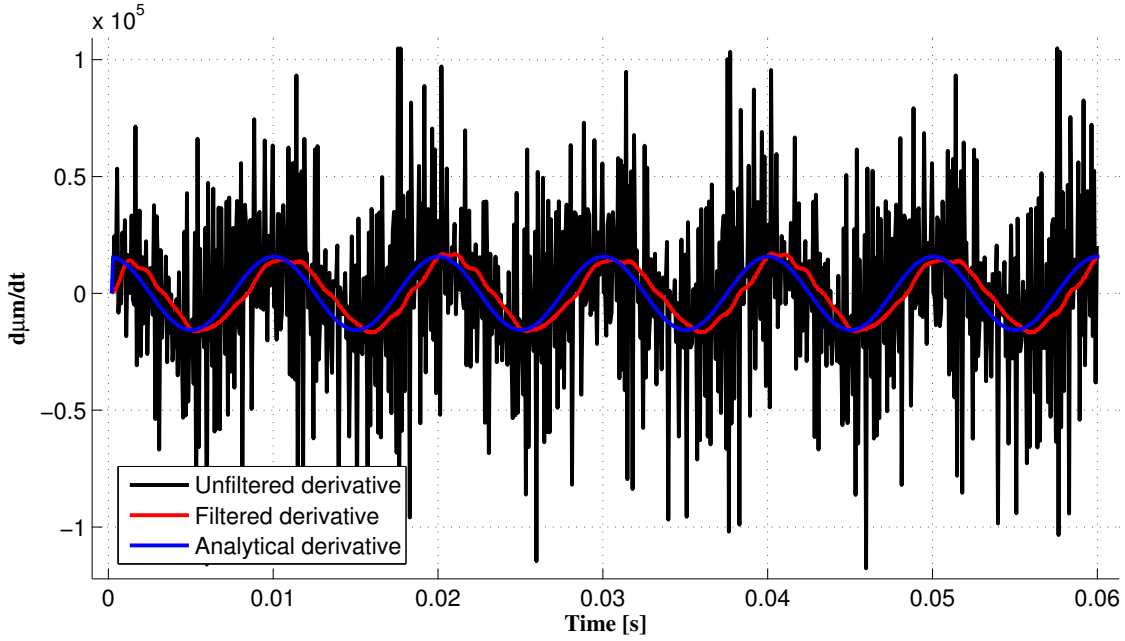

Figure 6.2: *Derivative of the filtered and unfiltered position compared to analytical solution.*

It is clear that the result of the numerical differentiation using the unfiltered data is useless. For small signals, the noise has a relatively high impact, and the differential will produce a signal due to the noise, even if there is no movement. This must be weighed against the order of the filter, which demands more computing power for higher order, and additional phase. The bode plot of the 21th order FIR filter is presented Figure 6.3. This filter is used throughout the control design chapter and implemented on the DSC.

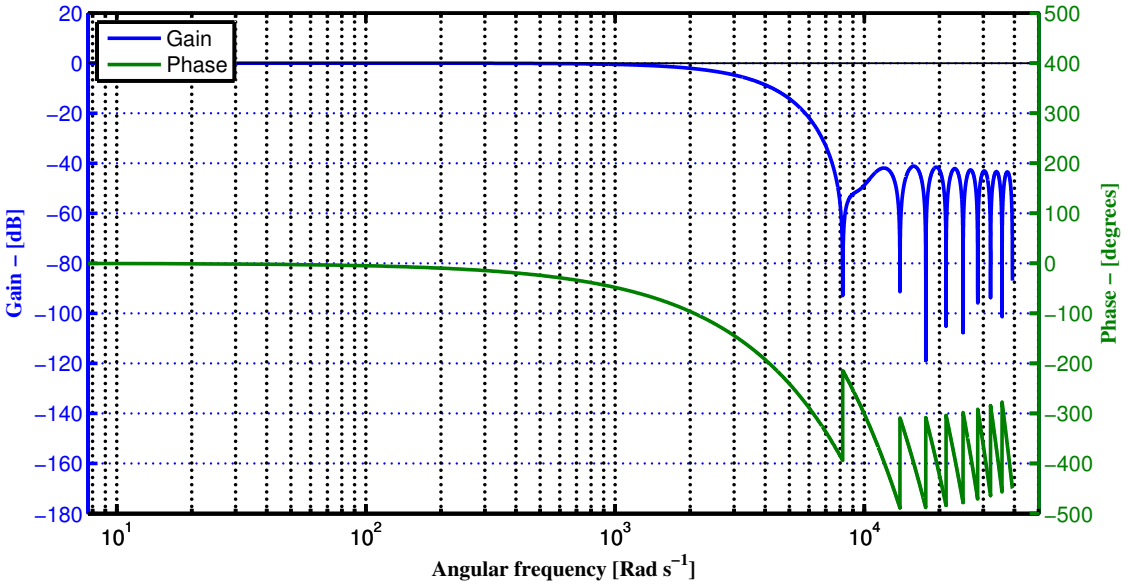

Figure 6.3: *Bode plot of 21st order FIR filter with a cut off frequency of a* $100Hz$ *at a sampling rate of* $12.5kHz$.

6.2 Current proportional controller design

The decentralized PD controller and the Centralized Space Vector control described next in this chapter, both utilize current controllers of the same topology. A current loop is nested in the closed loop of the position loop, which is known as cascaded control. The block diagram of this topology is shown Figure 6.4.

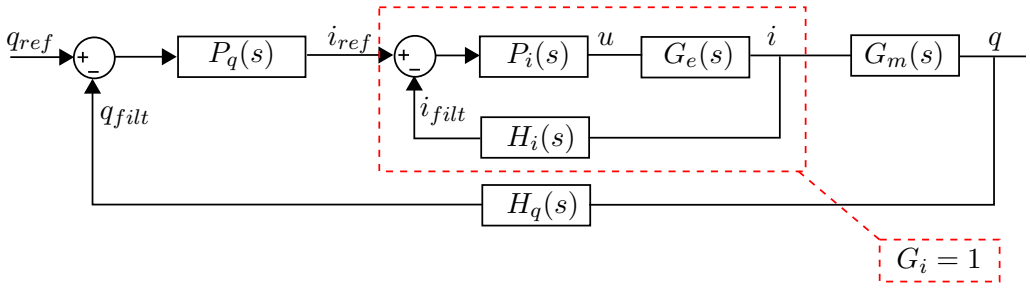

Figure 6.4: *Block diagram of the cascaded control scheme.*

Assuming that the voltage to current control can be described by the system $G_i = 1$, simplifies the control design, by not having to consider the electrical system. This assumption is valid, if the current control is approximately ten times faster than the magnetic and mechanical control system. Thus in this section the electrical system is studied. The governing equation of the electrical circuit in the magnetic bearings were derived in Chapter 5 and is repeated in (6.2.1).

$$\vec{u} = R_{Ohm} \cdot \vec{i} + \mathbf{L}\left(\vec{q}\right) \cdot \frac{\mathrm{d}\vec{i}}{\mathrm{d}t} + \sum_{k=1}^{2} \left(\frac{\partial \mathbf{L}\left(\vec{q}\right)}{\partial q_k} \frac{\mathrm{d}q_k}{\mathrm{d}t} \right) \cdot \vec{i} \tag{6.2.1}$$

To simplify the current controller design, the last term is omitted. This should not affect the controller design much, since the term during the non-linear simulation of different controllers did not exceed approximately $3V$. It is assumed that the current controller can suppress this voltage, which will become evident during the controller testing. Since the inductance varies with position, it is necessary to examine this effect to obtain a useful controller. The sum of inductances for electromagnet one in bearing one and two, is shown Figure 6.5. The sum of inductances in the other electromagnets are similar in magnitude but rotated 120 deg, since the electromagnets are identical. The sum of inductances for e.g. current one is obtained by adding L_{11}, L_{21} and L_{31}.

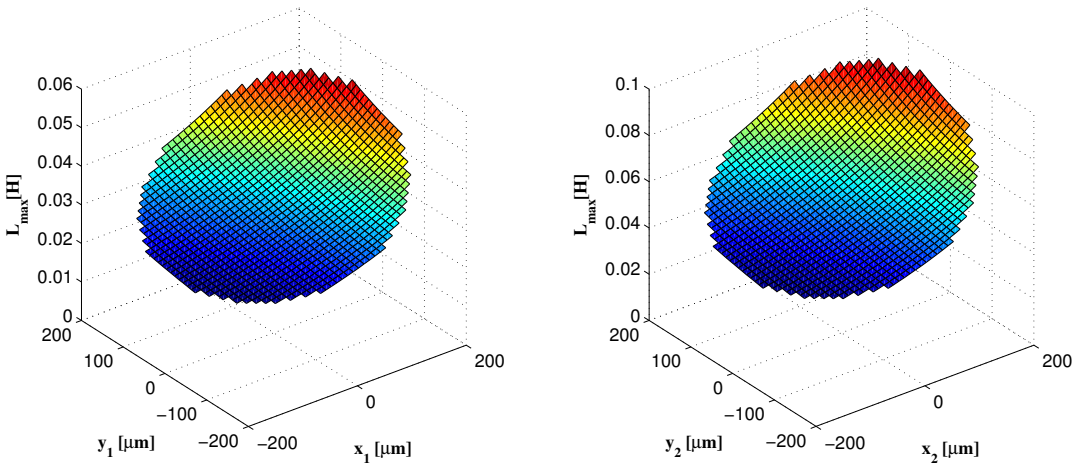

(a) *Bearing one.* ***(b)*** *Bearing two.*

Figure 6.5: *The sum of inductances in one electromagnet with regard to axle position.*

It is deemed sufficient that the controller complies with the bandwidth demands of the position controller at an inductance of $0.06H$ for bearing one and $0.1H$ for bearing two. The controller will then comply with the required bandwidth if the axle position remains within a circle of radius $200\mu m$, from the center in each bearing.

A simple P controller is used, since the steady state error, at the required performance, is insignificant. The bandwidth demand is different depending on the cascaded controller performance. Equation (6.2.2) shows the current controller gain dependent on the bandwidth requirement from the cascaded controller.

$$\begin{aligned} k_{piB1} &\approx 0.06\omega_{bw} - 1.95 \\ k_{piB2} &\approx 0.1\omega_{bw} - 2.50 \end{aligned} \tag{6.2.2}$$

A controller exists for each electromagnet, this amounts to six current controllers. The reason that only two gains are presented (6.2.2) is that the controllers, in each bearing, have identical gains. k_{piB1} is the controller gains for bearing one and k_{piB2} for bearing two.

6.3 Decentralized PD controller

In this section a decentralized PD controller is developed. A decentralized controller is an attempt to create a working controllerÂ¨, without taking the internal model couplings between variables into account. Thus making the controller relatively simple, at the risk of loosing performance or failing in the attempt. To avoid non-linear effects of the system consisting of the fact that the magnets are only able to make an attracting force, a bias current is added as described in section 5.8.3. If the current on one coil consists of a bias current i_0 and a control current, where the control current never exceeds the bias. In Figure 6.6 a system controlling the current in the y-direction is shown. To ensure no current (and thereby force) in the x-direction the currents in coil 1 and 2 has to be equal.

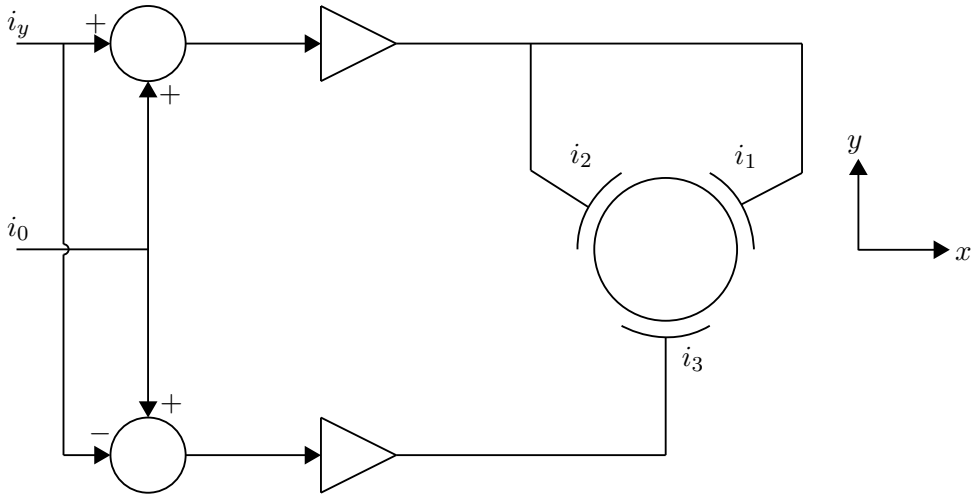

Figure 6.6: *Decentralized control for the control current i_y.*

The three control currents for the y-direction is described as:

$$\begin{aligned} i_{1y} &= i_0 + i_y \\ i_{2y} &= i_0 + i_y \\ i_{3y} &= i_0 - i_y \end{aligned} \tag{6.3.1}$$

Similarly the control system for the x-direction is shown in Figure 6.7. Here the total y-component of the current is zero. To maintain a $1:1$ relationship between the i_x and i_y currents to the resulting current vector a factor $\frac{1}{cos(30)}$ is added the currents in coil 1 and 2. The current $\vec{i_3}$ is controlled so the total current has no y-component.

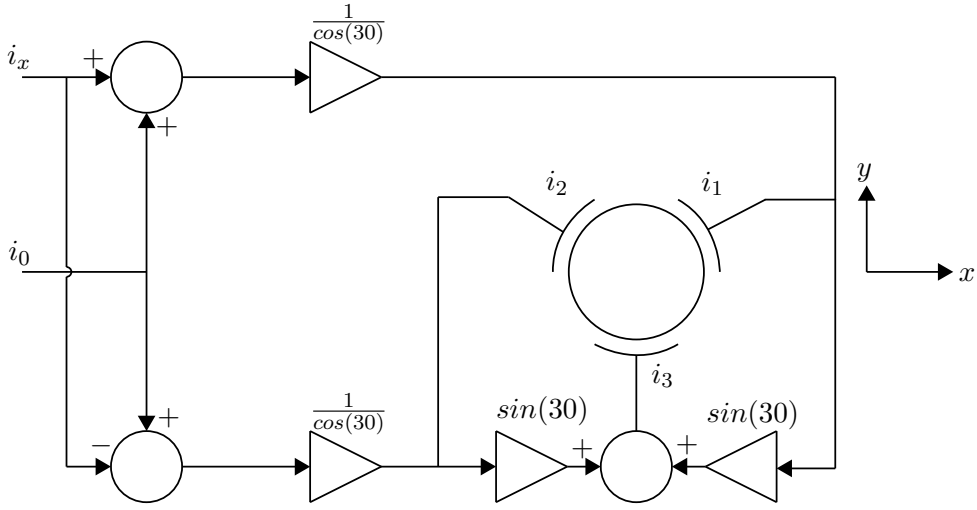

Figure 6.7: *Decentralized control for the control current i_x*

Then the three control currents for the x-direction can be described as:

$$i_{1x} = \frac{1}{cos(30)}(i_0 + i_x) \tag{6.3.2}$$

$$i_{2x} = \frac{1}{cos(30)}(i_0 - i_x) \tag{6.3.3}$$

$$i_{3x} = \frac{sin(30)}{cos(30)}(i_0 - i_x) + \frac{sin(30)}{cos(30)}(i_0 + i_x) = \frac{1}{cos(30)} i_0 \tag{6.3.4}$$

Summing up the currents for the x- and y-direction

$$i_1 = i_0 + i_y + \frac{1}{cos(30)}(i_0 + i_x) = \left(\frac{1}{cos(30)} + 1\right) i_0 + \frac{1}{cos(30)} i_x + i_y \tag{6.3.5}$$

$$i_2 = i_0 + i_y + \frac{1}{cos(30)}(i_0 - i_x) = \left(\frac{1}{cos(30)} + 1\right) i_0 - \frac{1}{cos(30)} i_x + i_y \tag{6.3.6}$$

$$i_3 = i_0 - i_y + \frac{1}{cos(30} i_0 = \left(\frac{1}{cos(30)} + 1\right) i_0 - i_y \tag{6.3.7}$$

Defining a new bias current

$$i_0 = \left(\frac{1}{cos(30)} + 1\right) i_0 \tag{6.3.8}$$

And the three currents are:

$$i_1 = i_0 + \frac{1}{cos(30)} i_x + i_y \tag{6.3.9}$$

$$i_2 = i_0 - \frac{1}{cos(30)} i_x + i_y \tag{6.3.10}$$

$$i_3 = i_0 - i_y \tag{6.3.11}$$

It shows that the sum of the three currents is $3 \cdot i_0 + i_y$, therefore the total power dissipation varies with i_y. Thus the control in the x-direction the current is always constant.

Inserting the results for the three currents in the current force equation (5.8.13) yields:

$$\begin{aligned}
\begin{bmatrix} F_x \\ F_y \end{bmatrix} &= \begin{bmatrix} k_{Fx1x1} & 0 \\ 0 & k_{Fx1x1} \end{bmatrix} \cdot \begin{bmatrix} x_1 \\ y_1 \end{bmatrix} \\
&\quad + \begin{bmatrix} -\frac{\sqrt{3}}{2} \cdot k_{Fy1i3} & \frac{\sqrt{3}}{2} \cdot k_{Fy1i3} & 0 \\ -\frac{1}{2} \cdot k_{Fy1i3} & -\frac{1}{2} \cdot k_{Fy1i3} & k_{Fy1i3} \end{bmatrix} \cdot \begin{bmatrix} \frac{1}{cos(30)} i_x + i_y \\ -\frac{1}{cos(30)} i_x + i_y \\ -i_y \end{bmatrix} \\
&= \begin{bmatrix} k_{Fx1x1} & 0 \\ 0 & k_{Fx1x1} \end{bmatrix} \cdot \begin{bmatrix} x_1 \\ y_1 \end{bmatrix} + \begin{bmatrix} -2 \cdot k_{Fy1i3} & 0 \\ 0 & -2 \cdot k_{Fy1i3} \end{bmatrix} \cdot \begin{bmatrix} i_x \\ i_y \end{bmatrix}
\end{aligned} \tag{6.3.12}$$

Then the system can be approximated by two linear equations:

$$F_x = k_{Fx1x1} \cdot x_1 - 2 \cdot k_{Fy1i3} \cdot i_x \tag{6.3.13}$$

$$F_y = k_{Fx1x1} \cdot y_1 - 2 \cdot k_{Fy1i3} \cdot i_y \tag{6.3.14}$$

Adding a very simple mechanical model, where no connections between the bearings are taken into account, the system can be described as:

$$m_{eq1} \cdot \ddot{x}_1 = k_{Fx1x1} \cdot x_1 - 2 \cdot k_{Fy1i3} \cdot i_x \tag{6.3.15}$$

$$m_{eq1} \cdot \ddot{x}_1 = k_{Fx1x1} \cdot y_1 - 2 \cdot k_{Fy1i3} \cdot i_y \tag{6.3.16}$$

The equivalent masses are found by decomposing the mass matrix of the mechanical model equation (5.8.1), so that the motion in the two bearings have no effect on each other. The equivalent masses for bearing 1 and 2 are therefore respectively:

$$m_{eq1} = \frac{{l_2}^2 \cdot m + I_{xx}}{(l_1 - l_2)^2} \qquad m_{eq2} = \frac{{l_1}^2 \cdot m + I_{xx}}{(l_1 - l_2)^2} \tag{6.3.17}$$

The equivalent mass corresponds to a system where forces in bearing one generates a rotational- and no translational motion in bearing two, and vice-versa. Motion in the other bearing is thereby treated a disturbance to the model. The masses are found from the mass matrix $\mathbf{M_c}$ in equation (5.8.1), where diagonal elements are ignored.

Though examining the elements in $\mathbf{M_c}$, with the dimensions of the experimental setup described in Table B.4, shows how the equivalent mass assumption will influence the control. The mass matrix is evaluated for the geometry of the experimental setup:

$$\mathbf{M_c} = \begin{bmatrix} 4.98 & 0 & -5.48 & 0 \\ 0 & 4.98 & 0 & -5.48 \\ -5.48 & 0 & 14.64 & 0 \\ 0 & -5.48 & 0 & 14.64 \end{bmatrix} \tag{6.3.18}$$

This shows that the equivalent mass assumption is acceptable for bearing two, as the disturbance mass is only a third of the control mass. Though for bearing one, there could occur a problem since the disturbance mass is nearly as large as the control mass. This fact is ignored during decentralized control and the inputs and outputs are paired.

In the next section a general controller is developed for the general system, therefore the relation between the position and force k_{Fx1x1} in equation (6.3.16) is referred to as k_x and the relation between force and current $-2 \cdot k_{Fy1i3}$ is referred to as k_i

6.3.1 PD decentralized control

The transfer function for current to position can be described with use of (6.3.16) as:

$$\frac{x(s)}{i_x(s)} = \frac{k_i}{m_{eq} \cdot s^2 - k_x} \tag{6.3.19}$$

This is shown in Figure 6.8

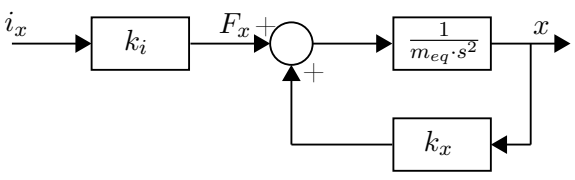

Figure 6.8: *Block diagram for transfering i_x to x.*

Introducing a PD controller and closing the loop, the system will look as in Figure 6.9.

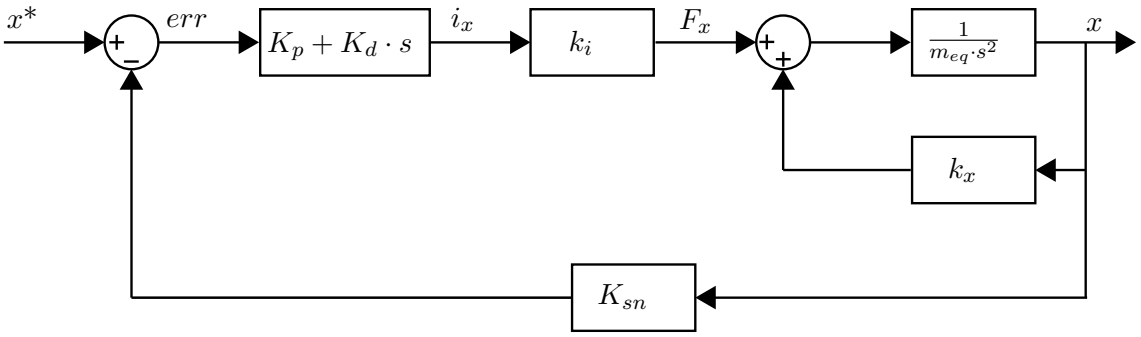

Figure 6.9: *Block diagram for transfering x to x.*

Where K_{sn} is the sensor gain. The open loop transfer function is:

$$G_{OL} = (K_p + K_d \cdot s) \frac{k_i \cdot K_{sn}}{m_{eq} \cdot s^2 - k_x} \tag{6.3.20}$$

And the closed loop transfer function

$$\frac{x}{x_{ref}} = \frac{G_{OL}}{1 + G_{OL}} = \frac{(K_p + K_d \cdot s) \cdot k_i \cdot K_{sn}}{m_{eq} \cdot s^2 + K_d \cdot K_{sn} \cdot k_i \cdot s + (K_p \cdot K_{sn} \cdot k_i - k_x)} \tag{6.3.21}$$

Solving the characteristic equation gives the poles described by:

$$s = \frac{-K_d \cdot K_{sn} \cdot k_i \pm \sqrt{(K_d \cdot K_{sn} \cdot k_i)^2 - 4 \cdot m_{eq} \cdot (K_p \cdot K_{sn} \cdot k_i - k_x)}}{2 \cdot m_{eq}} \tag{6.3.22}$$

To stabilize the system i.e. the poles in left half plane, the following has to apply:

$$-K_d \cdot K_{sn} \cdot k_i < 0 \qquad \Rightarrow \qquad K_d > 0 \tag{6.3.23}$$

And:

$$\begin{aligned} Re\left(\sqrt{(K_d \cdot K_{sn} \cdot k_i)^2 - 4 \cdot m_{eq} \cdot (K_p \cdot K_{sn} \cdot k_i - k_x)}\right) &< K_d \cdot K_{sn} \cdot k_i \\ 4 \cdot m_{eq} \cdot (K_p \cdot K_{sn} \cdot k_i - k_x) &> 0 \\ K_p &> \frac{k_x}{k_i \cdot K_{sn}} \end{aligned} \tag{6.3.24}$$

Introducing a disturbance force F_{xd}, and setting the reference position x_{ref} to zero, the transfer function from disturbance to position is described by:

$$\frac{x}{F_{xd}} = \frac{1}{m_{eq} \cdot s^2 + K_d \cdot K_{sn} \cdot k_i \cdot s + (K_p \cdot K_{sn} \cdot k_i - k_x)} \tag{6.3.25}$$

Comparing this to the standard form of a second order system yields:

$$G(s) = \frac{1}{K_p \cdot K_{sn} \cdot k_i - k_x} \cdot \frac{{\omega_n}^2}{s^2 + 2 \cdot \zeta \cdot \omega_n \cdot s + {\omega_n}^2} \tag{6.3.26}$$

Where

$$\zeta = \frac{K_d \cdot K_{sn} \cdot k_i}{2 \cdot \sqrt{m_{eq} \cdot (K_p \cdot K_{sn} \cdot k_i - k_x)}} \tag{6.3.27}$$

$$\omega_n = \sqrt{\frac{K_p \cdot K_{sn} \cdot k_i - k_x}{m_{eq}}} \tag{6.3.28}$$

Then for a system specified ω_n and ζ the controller gains can be calculated by:

$$K_p = \frac{m_{eq} \cdot {\omega_n}^2 + k_x}{K_{sn} \cdot k_i} \tag{6.3.29}$$

$$K_d = \frac{2 \cdot m_{eq} \cdot \omega_n \cdot \zeta}{K_{sn} \cdot k_i} \tag{6.3.30}$$

6.3.2 Design of PD decentralized controllers

The limiting factor in controller design is the saturation of the actuators and the position signal filtering. The damping is chosen to be 1, meaning the system should be critically damped. Thus the remaining parameter is the systems eigenfrequency. This parameter is limited by actuator saturation and the filtering of the position signal.

To ensure that the system is stable, the bode plot of the open loop system from reference to position is examined. The phase margin and gain margin are used as a measure of stability, and required to be larger than 30° and $6dB$ respectively [Phillips and Harbor, 2000]. This is a rule of thumb not ensuring stability. During testing of the controller on the non-linear model, it was necessary to increase the required phase margin to at least 40°. This is most likely due to the change of the linearization constants of the plant, with position. Making the model error significant when the position and current differs from the linearization point.

The plant and controller are discretized to take the sampling effect into account, and because the filter used is a FIR filter. Thus it is more accurate and simpler to discretize the model and controller than to transfer the filter into the continuous domain.

Using trial and error the eigenfrequency of the system is chosen to be $251.33 rad/s$. Open loop Bode plots are analyzed for each bearing, based on the block diagram of Figure 6.9 with the mentioned plant and controller. The sensor gain K_{sn} is the FIR filter. These are depicted in Figure 6.10 and 6.11.

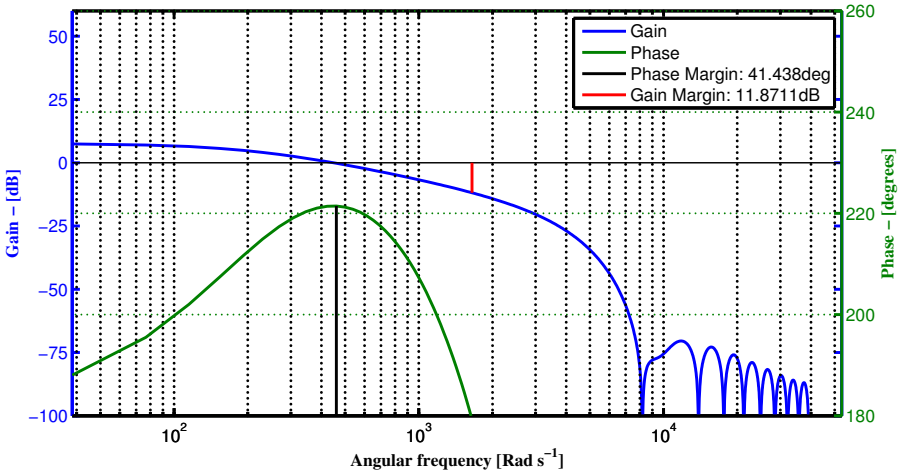

Figure 6.10: *Open loop Bode plot of the plant with designed controller and filtered feedback for bearing one with indicated gain and phase margin.* $k_p = 4352.4$ $k_d = 20.13$

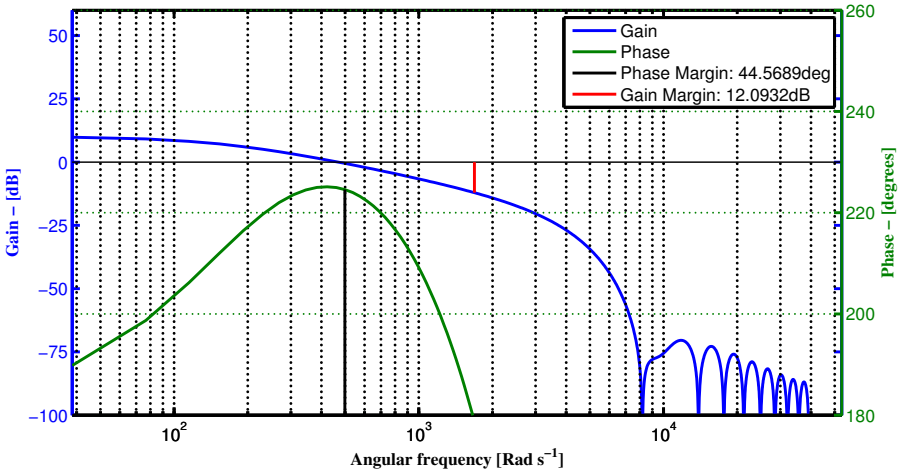

Figure 6.11: *Open loop Bode plot of the plant with designed controller and filtered feedback for bearing two with indicated gain and phase margin.* $k_p = 5816.6$ $k_d = 31.78$.

The controller response is shown in Figure 6.36 section 6.6.

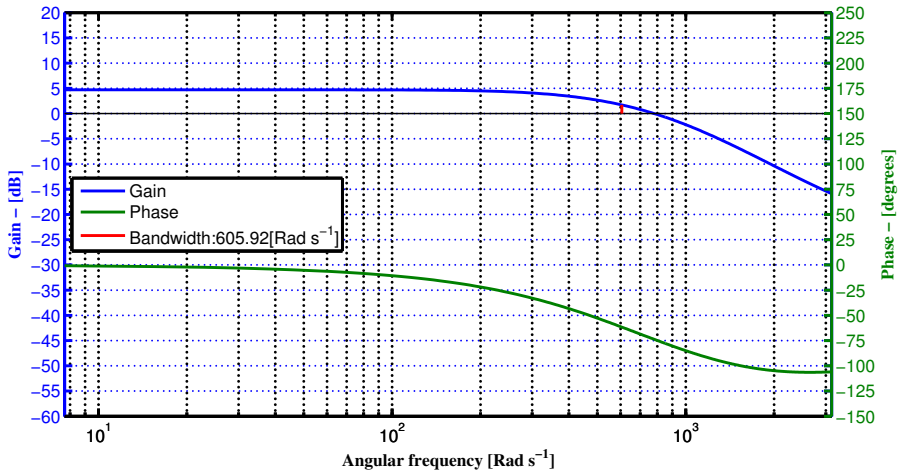

Figure 6.12: *Closed loop Bode diagram of the designed controller, plant and filter.*

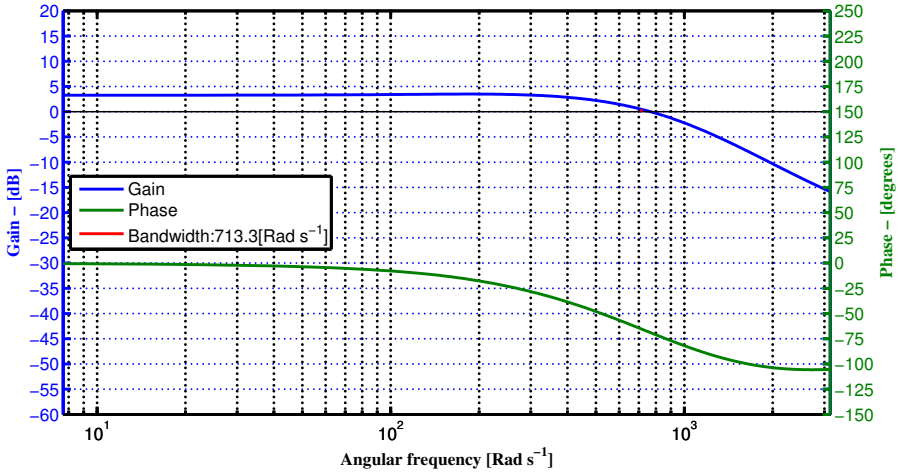

Figure 6.13: *Closed loop Bode diagram of the designed controller, plant and filter.*

The current controller gains are calculated, these are related to the bandwidth of the position controllers. Figure 6.12 and 6.13 shows the closed loop bode plots of a controller, plant and FIR filter. The gains are shown in (6.3.31) and calculated using equation (6.2.2) page 89. Ten times the bandwidth of the position controllers are used to calculate the current controller gains.

$$\begin{aligned} k_{piB1} &= 364.6 \\ k_{piB2} &= 712 \end{aligned} \tag{6.3.31}$$

These gains are relatively large. Especially for bearing two, where it might result in saturation of the voltage. Thus a decrease in the current controller performance is made. It was found by utilization of the non-linear model that a decrease in the current gains to 300, did not result in an unstable controller or severe deterioration in performance.

During the testing and implementation, of these controllers, start-up problems became apparent. If the initial position of the axle was too extreme, the axle would cling to a pole. A feed forward scheme implementing a variable bias was developed, it is available in Appendix H. No change is made to the controller design found in this section, since the feed forward does not alter the linearization constants, used for the controller design.

6.4 Centralized Space Vector Control Scheme

The control schemes, considered so far, all uses a bias current, for linearization of the plant, for controller design. This bias current is constant and applied regardless of what disturbance the bearing is experiencing. The power used to maintain a bias current is essentially wasted. In this section a control method, using a space vector approach, is developed and implemented. The Centralized Space Vector Proportional Derivative (CSVPD). This method does not use a bias current, and the advantage of this is lower power consumption.

Each magnetic bearing consists of three electromagnets. If the axle is positioned near the center, each magnet can be simplified to a single force vector acting along the magnets axis of symmetry. Thus the bearing can create three force vectors directed 120° apart. Figure

6.14 illustrates the largest possible force space vectors the electromagnets can generate. The area of the hexagon spanning the force vectors indicate all the possible vectors which can be generated.

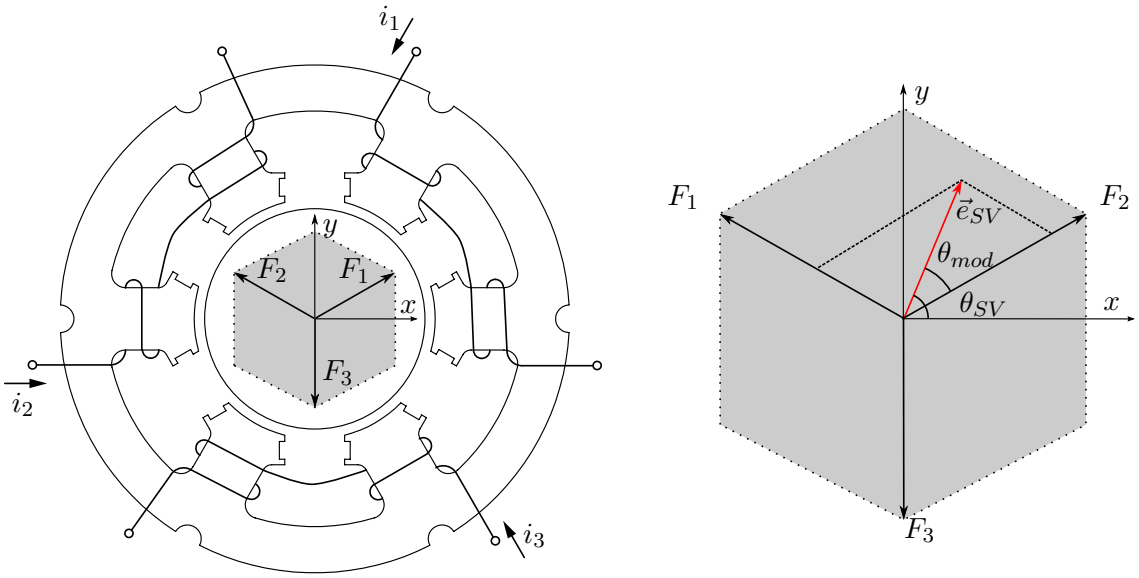

Figure 6.14: *Space vector diagram. F_i are the maximum forces that the respective pole-pair can exert.*

The number of controllers used are still the same, i.e two controllers for each bearing - one for each axis. The PD controller outputs are transformed into three currents using the space vector scheme. Figure 6.15 illustrates the control scheme structure.

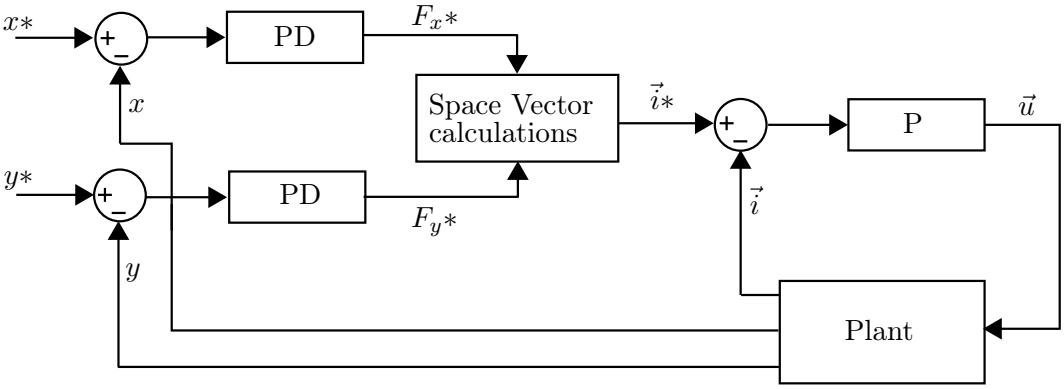

Figure 6.15: *Overview of the Space vector control scheme.*

The PD controller outputs F_x* and F_y* composes an output vector e_{SV}. This challenge is to generate this using a combination of the three magnet forces F_1, F_2 and F_3. It is chosen always to be a combination of the nearest two force vectors.

In equation (6.4.1) the error vector is decomposed into the two adjacent force vectors, shown in Figure 6.16. θ_{mod} is an angle ranging from 0 to $\frac{2\pi}{3}$, beginning at the first force vector encountered going clockwise from the error vector and ending at the error vector itself. This generalization is useful when implementing the decomposition. The same decomposition can be used for each $\frac{2\pi}{3}$ angle span.

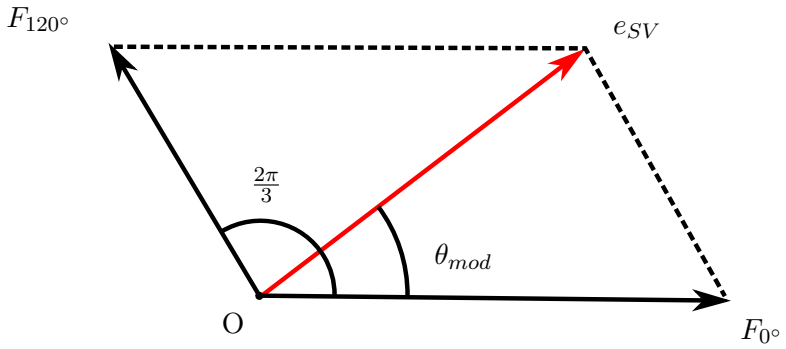

Figure 6.16: *Space vector error vector, $\vec{e}_{SV}$. θ_{mod} is the angle to the error vector from the clock-wise nearest F_i.*

The size of the output force vector is described in terms of the controller outputs:

$$|\vec{e}_{SV}| = \sqrt{F_x *^2 + F_y *^2} \tag{6.4.1}$$

And the relation between the magnet forces and the output force is described in terms of the modulation angle θ_{mod} by:

$$|\vec{e}_{SV}| \cdot cos(\theta_{mod}) = F_{0^\circ} \cdot cos(0) + F_{120^\circ} \cdot cos\left(\frac{2\pi}{3}\right) \tag{6.4.2}$$

$$|\vec{e}_{SV}| \cdot sin(\theta_{mod}) = F_{0^\circ} \cdot sin(0) + F_{120^\circ} \cdot sin\left(\frac{2\pi}{3}\right) \tag{6.4.3}$$

And solving for the magnet forces yield:

$$\begin{aligned} F_{0^\circ} &= \frac{\sqrt{3}}{3} \cdot |\vec{e}_{SV}| \cdot (\sqrt{3} \cdot cos\left(\theta_{mod}\right) + sin(\theta_{mod})) \cdot \sqrt{3} \\ F_{120^\circ} &= \frac{2}{\sqrt{3}} \cdot |\vec{e}_{SV}| \cdot sin(\theta_{mod}) \end{aligned} \tag{6.4.4}$$

To obtain the force the controller is asking for from the electromagnets, a simplification of the force equations from the non-linear model is used. If it is assumed that the axle is positioned at the center, the expression of electromagnet force depending on current reduces to (6.4.5). n is the number of the electromagnet and m is the bearing number. In the centered position $kForce$ only vary depending on the bearing. The current required to deliver the correct force is then directly obtainable.

$$\begin{aligned} F_{n,m} &= kForce_m \cdot i_{n,m}^2 \quad : \quad n = 1,2,3 \quad m = 1,2 \\ i_{n,m} &= \sqrt{\frac{F_m}{kForce_{n,m}}} \end{aligned} \tag{6.4.5}$$

Assuming that the electrical system dynamics can be neglected, by making the system response at least 10 times as fast as that of the mechanical system. The transfer function of the plant reduces to (6.4.6). There exists 4 plant functions, one for each bearing coordinate.

$$\frac{q}{F} = \frac{1}{m_{eq}s^2} \tag{6.4.6}$$

The equivalent mass is found using the same assumptions described in section 6.3.

6.4.1 Controller centralization

In this section the centralization is implemented. As shown in section 6.3 the bearings has couplings through the axle. Saying that a force in bearing 1 results in a reaction in bearing 2. In this section a centralized controller is developed to take these couplings into account. The development is based on the theory for decoupled control in Glad and Ljung [2000].

The system transfer function coupling input u to output y is described by:

$$y = G(s) \cdot u \tag{6.4.7}$$

Introducing the transformation functions $W_1(s)$ and $W_2(s)$ transforming the input and output by:

$$\tilde{u} = W_1(s)^{-1} \cdot u \tag{6.4.8}$$

$$\tilde{y} = W_2(s) \cdot y \tag{6.4.9}$$

Substituting this in the system described in (6.4.7), the compensated system can be described by:

$$\begin{aligned} \tilde{y} &= W_1(s) \cdot G(s) \cdot W_2(s) \cdot \tilde{u} \\ &= \tilde{G}(s) \cdot \tilde{u} \end{aligned} \tag{6.4.10}$$

The plant input and output are made dependent on $W_1(s)$ and $W_2(s)$. The scope is that using the matrices, the plant equations are made as diagonal as possible, thus decoupling the system.

A controller $\tilde{F}_y$ is then designed from $r - \tilde{y}$ to $\tilde{u}$, using the new plant $\tilde{G}(s)$.

$$\tilde{u} = \tilde{F}_y \cdot (r - \tilde{y}) \tag{6.4.11}$$

This decoupled controller can then be transformed using equation (6.4.12). The equation is simplified assuming W_2 is always chosen as the identity matrix. This is a convenient choice since it leaves W_1 free to be chosen as a system inverse, $G(s)^{-1}$.

$$\begin{aligned} u &= W_1(s)\tilde{F}_y \cdot (r - y) \\ &= F_y \cdot (r - y) \end{aligned} \tag{6.4.12}$$

Choosing the $W_1(s)$ as the system inverse should decouple the system completely, but it requires dynamic decoupling, which is more demanding and require a very precise model [Glad and Ljung, 2000]. A simpler way is to design the controller at a stationary point, $W_1(0)$, or at a specific frequency $W_1(i\omega)$ e.g. the crossover frequency.

In this control scheme the transfer function matrix is derived from the mechanical system mass matrix. The controllers are cascaded. A current controller at least ten times faster than the position controllers is used, thus the transfer function of the electrical system can be considered a unity gain.

$$\vec{Q_c} = \mathbf{M_c} \cdot \ddot{\vec{x}} \tag{6.4.13}$$

$$\begin{aligned} \vec{x} &= (\mathbf{M_c} \cdot s^2)^{-1} \cdot \vec{Q_c} \\ &= G(s) \cdot \vec{Q_c} \end{aligned} \tag{6.4.14}$$

W_1 is chosen as the inverse of the system matrix (6.4.15).

$$\begin{aligned} \omega_c &= 1 \\ W_1 &= G(i\omega_c)^{-1} \end{aligned} \tag{6.4.15}$$

In the special case, of designing a controller for this system, it was found that a change in the frequency of the decoupling, ω_c, did not result in different controllers. This is because the frequency is eliminated in the consecutive reverse transformation of the designed controllers. Hence in this special case, the choice of ω_c is simply 1, a positive number different from zero.

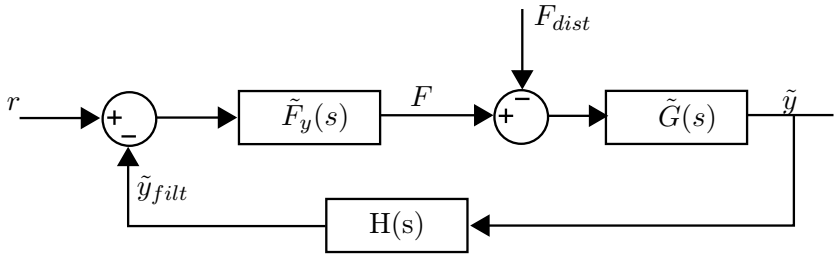

Figure 6.17: *Block diagram of a single centralized controller. F_y is the controller, G(s) the system plant,F_{dist} a disturbance force and H(s) a filter.*

When decoupled, the system matrix is diagonal and fortunately each entry is identical, only one controller needs be designed as the controller criteria are kept identical. The block diagram of one such controller is shown in Figure 6.17. F_y is chosen to be a PD controller, shown in equation (6.4.16).

$$\tilde{F}_y = k_d \cdot s + k_p \tag{6.4.16}$$

Two closed loop transfer functions are of interest. The function from position reference to position (6.4.17) and the function from disturbance force to position (6.4.18).

$$G_{cl(r\to y)} = \frac{\frac{k_p}{m_{eq}} + \frac{k_d}{m_{eq}} \cdot s}{s^2 + \frac{k_d}{m_{eq}} \cdot s + \frac{k_p}{m_{eq}}} \tag{6.4.17}$$

$$G_{cl(F_y\to y)} = \frac{k_p \cdot \frac{k_p}{m_{eq}}}{s^2 + \frac{k_d}{m_{eq}} \cdot s + \frac{k_p}{m_{eq}}} \tag{6.4.18}$$

The two transfer functions are identical except for the zero $k_d \cdot s$ in (6.4.17). This zero causes the dynamics from r to y to be faster than the response from F_y to y e.g. faster rise time and more overshoot. This should be taken into account if the position reference is stepped. In this case the reference is kept zero and for the most part disregarded. It is of more higher importance that the controller has good performance with regards to rejecting the disturbance forces. Thus (6.4.18) is used for controller design.

Since (6.4.18) is relatively simple, k_p and k_d can be made dependent on the required damping and eigenfrequency of the bearing, the derived dependencies are:

$$k_p = \omega_c^2 \cdot m_{eq} \tag{6.4.19}$$

$$k_d = 2 \cdot \omega_c \cdot \zeta \cdot m_{eq} \tag{6.4.20}$$

The damping is chosen to be 1, meaning the system should be critically damped. Thus the remaining parameter is the systems eigenfrequency. This parameter is limited by actuator saturation and the filtering of the position signal. To ensure that the system is stable the bode plot of the open loop system from reference to position is examined. The phase margin and gain margin are required to be larger than 30° and $6dB$ Phillips and Harbor [2000], this is a rule of thumb not ensuring a margin of stability. This margin is verified by implementing the controller on the non-linear model.

The plant and controller are discretized to take the sampling effect into account, and because the filter used is a FIR filter. Thus it is more accurate and simpler to discretize the model and controller, than to transfer the filter into the continuous domain. Using trial and error the eigenfrequency of the system is chosen to be 440.

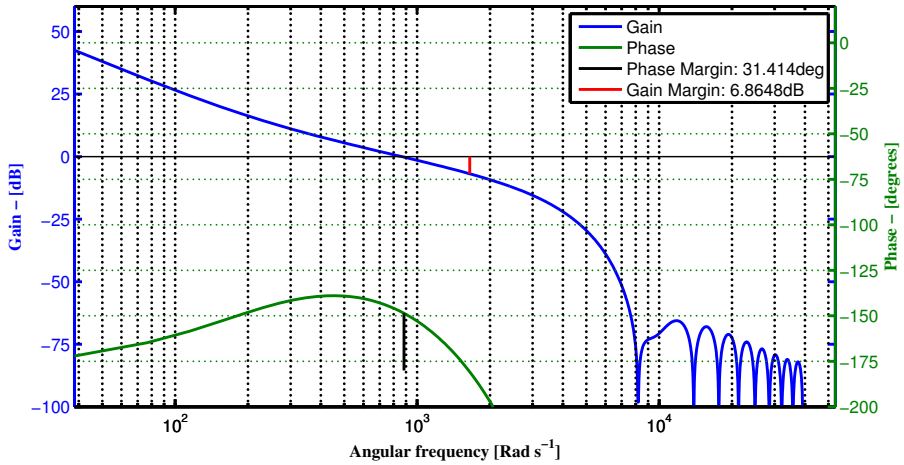

Figure 6.18: *Open loop Bode diagram of the plant with filtered feedback, and the designed controller with indicated gain and phase margin.* $k_p = 1.9600$ $k_d = 0.0089$.

The derived controllers are transformed back using the decoupling matrix and shown (6.4.21).

$$\tilde{F}_y = \begin{bmatrix} \tilde{k}_d \cdot s + \tilde{k}_p & 0 & 0 & 0 \\ 0 & \tilde{k}_d \cdot s + \tilde{k}_p & 0 & 0 \\ 0 & 0 & \tilde{k}_d \cdot s + \tilde{k}_p & 0 \\ 0 & 0 & 0 & \tilde{k}_d \cdot s + \tilde{k}_p \end{bmatrix}$$

$$F_y = W_1(s)\tilde{F}_y$$

$$F_y = \begin{bmatrix} k_{dB1,1} \cdot s + k_{pB1,1} & 0 & k_{dB1,2} \cdot s + k_{pB1,2} & 0 \\ 0 & k_{dB1,1} s + k_{pB1,1} & 0 & k_{dB1,2} \cdot s + k_{pB1,2} \\ k_{dB2,1} \cdot s + k_{pB2,1} & 0 & k_{dB2,2} \cdot s + k_{pB2,2} & 0 \\ 0 & k_{dB2,1} \cdots s + k_{pB2,1} & 0 & k_{dB2,2} \cdot s + k_{pB2,2} \end{bmatrix} \tag{6.4.21}$$

$$
\begin{aligned}
k_{dB1,1} &= 0.979 \cdot 10^6 \\
k_{pB1,1} &= 4154 \\
k_{dB1,2} &= -1.01 \cdot 10^6 \\
k_{pB1,2} &= -4285 \\
k_{dB2,1} &= 2.962 \cdot 10^6 \\
k_{pB2,1} &= 12570 \\
k_{dB2,2} &= -1.01 \cdot 10^6 \\
k_{pB2,2} &= -4285
\end{aligned}
\tag{6.4.22}
$$

Lastly the current controller gains are calculated, these are related to the bandwidth of the position controllers. Figure 6.19 shows the closed loop bode plots of a controller, plant and FIR filter.

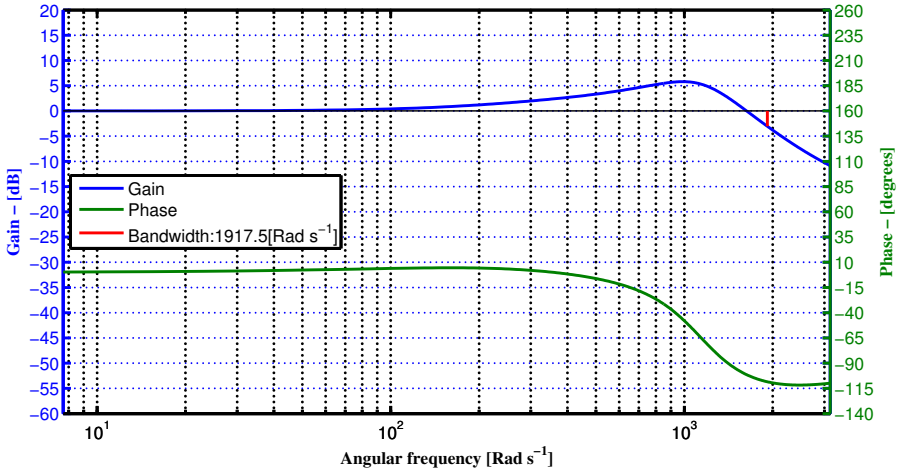

Figure 6.19: *Closed loop Bode diagram of the designed controller, plant and filter .* $k_p = 1.9600$ $k_d = 0.0089$.

With the indicated bandwidth of $1917.5 rad/s$, using (6.2.2) page 89, the current controller gains become:

$$k_{piB1} = 845.62 \tag{6.4.23}$$

$$k_{piB2} = 1409.75 \tag{6.4.24}$$

The problem encountered during the design of the gains for the decentralized PD current controllers, occurs here as well. Therefore 300 is chosen as an acceptable gain for both bearings, and this is verified by simulation using the non-linear model.

The controllers are tested in section 6.6 and the responses are compared to the other controllers.

6.5 Controller design based on the state space representation

Modern control theory is based on a state space representation, or realization of a system, by writing the governing equations of the system on state space form. It requires that the equations are linear, and first order, or can be written as a combination of first order equations. This is an excellent tool for the representation of MIMO systems, and the subsequent design of MIMO controllers [Fadali and Visioli, 2012]. The standard state space representation is shown in (6.5.1), and the linear state space model of the magnetic bearing setup was setup in equation (5.8.12) on page 80. This section will investigate two different controllers based on the state space representation, and their performance should reflect that they take into account the couplings in the system. Unique for the state space representation, is that a Observer can be designed. This uses both model input, the model and the sensor input to estimate the states.

$$\begin{aligned}\dot{\mathbf{x}} &= \mathbf{A}\cdot\mathbf{x} + \mathbf{B}\cdot\vec{u} \\ \vec{y} &= \mathbf{C}\cdot\mathbf{x} + \mathbf{D}\cdot\vec{u}\end{aligned} \tag{6.5.1}$$

Where:

$\mathbf{x}$ is the $n \times 1$ state vector
$\vec{y}$ is the $l \times 1$ output vector
$\vec{u}$ is the $m \times 1$ input vector
$\mathbf{A}$ is the $n \times n$ state matrix
$\mathbf{B}$ is the $n \times m$ input matrix
$\mathbf{C}$ is the $l \times n$ output matrix
$\mathbf{D}$ is the $l \times m$ direct transmission matrix

6.5.1 Full state feedback controller

The poles of the system are the eigenvalues of the state matrix, and the poles of the closed loop system is the eigenvalues of the closed loop state matrix defined by:

$$\mathbf{A}_{cl} = \mathbf{A} - \mathbf{B}\cdot\mathbf{K} \tag{6.5.2}$$

Here $\mathbf{K}$ is the controller gains which can force the poles of the closed loop state matrix to any desired location. This will be the first approach to a controller design. The block diagram of a closed loop state space system is depicted in Figure 6.20. A prerequisite for designing a controller for a system, is that the system is *controllable*. Whether a system is controllable or not, can be determined by evaluating its controllability matrix, (6.5.3), and this must have rank n.

$$\mathscr{C} = \begin{bmatrix}\mathbf{A} & \mathbf{A}\cdot\mathbf{B} & \ldots & \mathbf{A}^{n-1}\cdot\mathbf{B}\end{bmatrix} \tag{6.5.3}$$

This is verified with MATLAB, since equation (6.5.3) yields a 14×84 matrix. A routine for this specific purpose is built into MATLAB, and the command $rank(ctrb(A,B))$ returns 14 which is equal to n, and thus the system is thus controllable.

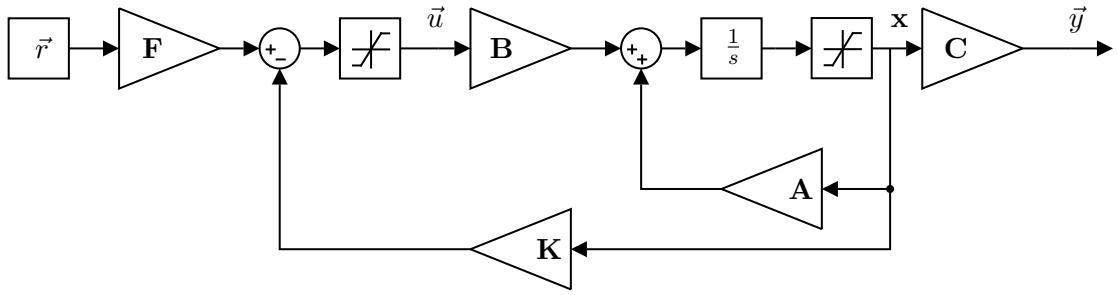

Figure 6.20: *Block diagram of the bearing model on state space form, controlled by* $\mathbf{K}$ *and* $\mathbf{F} * \vec{r}$*. Also modeled is the saturation of* $\vec{u}$ *and* $\mathbf{x}$*, limiting the voltages and currents.*

The vectors of the above figure are presented next:

$$\mathbf{x} = \begin{bmatrix} i_1 \\ i_2 \\ i_3 \\ i_4 \\ i_5 \\ i_6 \\ x_1 \\ x_2 \\ x_3 \\ x_4 \\ \dot{x}_1 \\ \dot{x}_2 \\ \dot{x}_3 \\ \dot{x}_4 \end{bmatrix} \quad (6.5.4) \qquad \vec{r} = \begin{bmatrix} i_1 \\ i_2 \\ i_3 \\ i_4 \\ i_5 \\ i_6 \\ x_1 \\ x_2 \\ x_3 \\ x_4 \end{bmatrix} \quad (6.5.5) \qquad \vec{y} = \begin{bmatrix} i_1 \\ i_2 \\ i_3 \\ i_4 \\ i_5 \\ i_6 \\ s_{x1} \\ s_{y1} \\ s_{x2} \\ s_{y1} \end{bmatrix} \quad (6.5.6) \qquad \vec{u} = \begin{bmatrix} u_1 \\ u_2 \\ u_3 \\ u_4 \\ u_5 \\ u_6 \end{bmatrix} \quad (6.5.7)$$

Reference gain matrix.

The computation of the control value is called the control law, and the simplest controller uses the control law shown in (6.5.8). This controller drives all states to zero, and the controller will reject disturbances by doing so. As the system is highly non-linear, with actuators only able to pull, it is advantageous to add a reference enabling the currents to be biased at a desired current. This can be achieved with the control law of equation (6.5.9). Figure 6.20 is shown with this feed-forward reference. Evident from the block diagram, this reference is open-loop and will thus result in steady state error(s) if model errors or disturbances are significant.

$$\vec{u} = -\mathbf{K} \cdot \mathbf{x} \tag{6.5.8}$$

$$\vec{u} = -\mathbf{K} \cdot \mathbf{x} + \mathbf{F} \cdot \vec{r} \tag{6.5.9}$$

The reference gain, $\mathbf{F}$, is calculated using (6.5.10).[Fadali and Visioli, 2012,(9.24)]

$$\mathbf{F} = \left(\mathbf{C} \cdot (\mathbf{I}_n - \mathbf{A}_{cl})^{-1} \cdot \mathbf{B}\right)^{-1} \tag{6.5.10}$$

Since the inner product of (6.5.10) is a matrix with dimensions 10×6, and thus not square, it cannot be inverted. Therefore the problem is solved with MATLABs $pinv()$, which yields a Moore-Penrose pseudo-inverse of the matrix.

$$\mathbf{F} = pinv\left(\mathbf{C} \cdot (\mathbf{I}_n - \mathbf{A}_{cl})^{-1} \cdot \mathbf{B}\right) \tag{6.5.11}$$

At this point the control gain, $\mathbf{K}$, can be computed by choosing the poles for the closed loop. Using this model with relatively high complexity, did not yield good results. introducing the model saturation on states and control signal and tested the controller on the linear model, it did not stabilize the system.

6.5.2 Linear Quadratic Regulator

This controller is also called the optimal controller, i.e. this method chooses the pole locations for the closed loop poles in a way, such that the response and the input to the plant is optimal, with regards to a chosen cost function. The system and the state, input and output vectors are the same as described in the previous section 6.5.1. The controller gains are found via minimum two weighing matrices, that respectively penalizes the input and the state vector. A third matrix can be added, this penalizes the cross-coupling between input and output. The cost function is:

$$J(u) = \int_0^\infty (\mathbf{x}^T \cdot \mathbf{Q_{lqr}} \cdot \mathbf{x} + \vec{u}^T \cdot \mathbf{R_{lqr}} \cdot \vec{u} + 2 \cdot \mathbf{x}^T \cdot N \cdot \vec{u}) dt \tag{6.5.12}$$

The weighing matrices $\mathbf{Q_{lqr}}$ and $\mathbf{R_{lqr}}$ are to be considered design variables [Glad and Ljung, 2000]. It is the relative values in the matrices that are relevant in this context, and not their absolute values. The obvious issue at hand is to choose the values, such that a desired result is achieved. The initial solution for this problem is given by applying Bryson's rule, where the maximum allowable value for the states are chosen and inserted in (6.5.13). This is repeated for the input vector, and the values are used in (6.5.14). [Franklin et al., 2010,p.537]

$$\mathbf{Q_{lqr}}_{ii} = \frac{1}{max(\mathbf{x}_i^2)} \qquad i \in \{1, 2, ..., n\} \tag{6.5.13}$$

$$\mathbf{R_{lqr}}_{jj} = \frac{1}{max(\vec{u}_j^2)} \qquad j \in \{1, 2, ..., m\} \tag{6.5.14}$$

This is very convenient compared to the pole placement method, as the saturation of the systems can be taken into account directly. When the pole placement method is used this requires quite a lot of experience and simulation effort.

6.5.3 Full state feedback with integral control

This approach is referred to as the servo problem, i.e. the error between the reference and the output. An integrator is added that ensures zero steady state accuracy during constant disturbances or as a result of model errors. For visualization purposes a block diagram is shown in Figure 6.21.

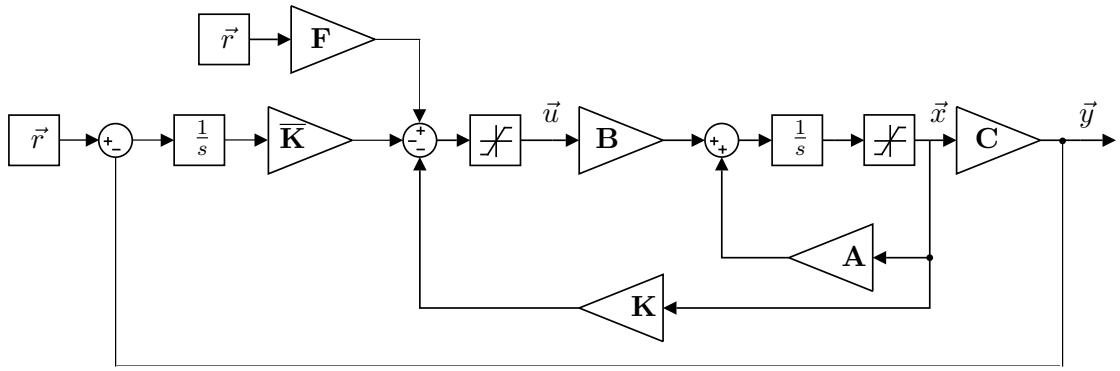

Figure 6.21: *Block diagram for the augmented state space system*

An extra closed loop and additional controller gains are added to the system. By augmenting the state vector with an extra state per paired reference and output (6.5.15), and the state matrix accordingly (6.5.20), the block diagram is reduced to the original, of Figure 6.20. This way the control design procedures are unchanged. The added states are as follows:

$$\vec{w}_i = \int \vec{r}_{i+6}(t) - \vec{y}_{i+6}(t)\mathrm{dt} \qquad i \in \{1,2,3,4\} \tag{6.5.15}$$

The block diagram of Figure 6.21 implies that all entries in $\vec{y}$ are used, but as the above equation shows, the state vector is only augmented with the integrated error of the positions. The augmented state vector is shown in (6.5.16). The vectors for input, output and reference remain unchanged.

$$\mathbf{x} = \begin{bmatrix} i_1 \\ i_2 \\ i_3 \\ i_4 \\ i_5 \\ i_6 \\ x_1 \\ x_2 \\ x_3 \\ x_4 \\ \dot{x}_1 \\ \dot{x}_2 \\ \dot{x}_3 \\ \dot{x}_4 \\ w_1 \\ w_2 \\ w_3 \\ w_4 \end{bmatrix} \tag{6.5.16}$$

$$\vec{r} = \begin{bmatrix} i_1 \\ i_2 \\ i_3 \\ i_4 \\ i_5 \\ i_6 \\ x_1 \\ x_2 \\ x_3 \\ x_4 \end{bmatrix} \tag{6.5.17}$$

$$\vec{y} = \begin{bmatrix} i_1 \\ i_2 \\ i_3 \\ i_4 \\ i_5 \\ i_6 \\ x_1 \\ x_2 \\ x_3 \\ x_4 \end{bmatrix} \tag{6.5.18}$$

$$\vec{u} = \begin{bmatrix} u_1 \\ u_2 \\ u_3 \\ u_4 \\ u_5 \\ u_6 \end{bmatrix} \tag{6.5.19}$$

$$\begin{bmatrix} \begin{bmatrix} \dot{\vec{i}}_c \\ 6\times 1 \end{bmatrix} \\ \begin{bmatrix} \dot{x} \\ 4\times 1 \end{bmatrix} \\ \begin{bmatrix} \ddot{x} \\ 4\times 1 \end{bmatrix} \\ \begin{bmatrix} \dot{\vec{w}} \\ 4\times 1 \end{bmatrix} \end{bmatrix} = \begin{bmatrix} \begin{bmatrix} & & \\ & \mathbf{A} & \\ & 14\times 14 & \end{bmatrix} & \begin{bmatrix} \mathbf{0} \\ 14\times 4 \end{bmatrix} \\ \begin{bmatrix} \mathbf{0} \\ 4\times 6 \end{bmatrix} \begin{bmatrix} -\mathbf{I} \\ 4\times 4 \end{bmatrix} & \begin{bmatrix} \mathbf{0} \\ 4\times 8 \end{bmatrix} \begin{bmatrix} \mathbf{I} \\ 4\times 4 \end{bmatrix} \end{bmatrix} \begin{bmatrix} \begin{bmatrix} \vec{i}_c \\ 6\times 1 \end{bmatrix} \\ \begin{bmatrix} x \\ 4\times 1 \end{bmatrix} \\ \begin{bmatrix} \dot{x} \\ 4\times 1 \end{bmatrix} \\ \begin{bmatrix} \vec{w} \\ 4\times 1 \end{bmatrix} \end{bmatrix} \tag{6.5.20}$$

The implementation of this controller can be found on the attached CD. The block diagram of the implementation is depicted in Figure 6.22. T is a discrete integrator. In the implementation the trapezoidal integration rule is used.

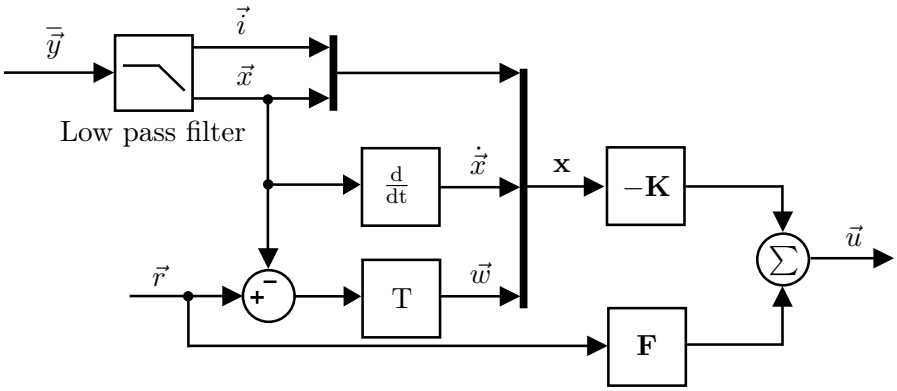

Figure 6.22: *Block diagram for implementation of full state feedback.*

6.5.4 Full order prediction observer

The velocities of the state vector has so far been computed with a first order differential scheme, using the filtered values. This was already implemented as described in section 6.1, for use with the PID-controllers. The observer approach is a method, where the states are estimated not only from the measurements, $\vec{y}$, but also from the control signal and the model. This requires that the system is *observable*. This requires full rank, or rank n,

of the observability matrix, (6.5.21).

$$\mathscr{O} = \begin{bmatrix} \mathbf{C} \\ \mathbf{C} \cdot \mathbf{A} \\ ... \\ \mathbf{C} \cdot \mathbf{A}^{n-1} \end{bmatrix} \tag{6.5.21}$$

Similar to the controllability matrix, (6.5.21) are calculated using MATLABs *obsv*(), which yields a 140×14 matrix. Using *rank*() it is verified that the system is observable. Introducing the observer gain, $\mathbf{L}$, the estimated states are [Glad and Ljung, 2000]:

$$\dot{\hat{x}} = \mathbf{A} \cdot \hat{x} + \mathbf{B} \cdot \vec{u} + \mathbf{L} \cdot (\vec{y} - \mathbf{C} \cdot \hat{x} - \mathbf{D} \cdot \vec{u}) \tag{6.5.22}$$

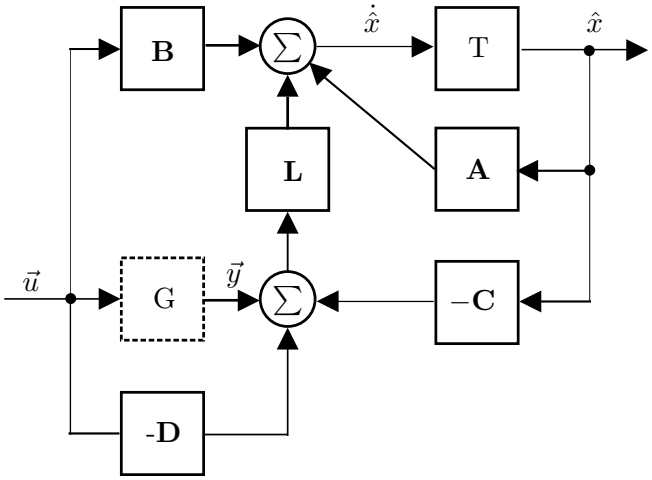

Figure 6.23: *Block diagram for a full order prediction observer. G is the system, and T a discrete integrator.*

The block diagram of (6.5.22) is depicted in Figure 6.23. While estimating the states with an observer, there is no other filter in the system. The observer gain is the filtering effect, and its characteristics are determined by the closed loop poles of the observer. This poses the exact same challenge as choosing the poles of the closed loop for the controller gain, where one solution was to simply place them at immediately advantageous locations, also known as pole placement. Since the job of the observer is to reconstruct states for the controller to react on, and it is recommended to have poles that are $5 - 10$ times faster than the poles in the system[Fadali and Visioli, 2012], the tradeoff that must be considered is that very fast poles will result in less noise attenuation.

Alternatively the poles can be chosen as the poles in a Butterworth filter, as suggested by [Ruscio, 2009]. The controller is designed as earlier described, via LQR on the augmented system, so the four positions have integral action. Implementation of the controller and observer are naturally discrete, and the difference equations for the implementation, control law, observer and integral action respectively are:

$$\vec{u}(k) = -\mathbf{K} \cdot [\hat{x}(k)\ \vec{w}(k)] + \mathbf{F} \cdot \vec{r} \tag{6.5.23}$$

$$\hat{x}(k+1) = \mathbf{A} \cdot \hat{x}(k) + \mathbf{B} \cdot \vec{u}(k) + \mathbf{L} \cdot (\vec{y}(k) - \mathbf{C} \cdot \hat{x}(k)) \tag{6.5.24}$$

$$\dot{\vec{w}}(k+1) = \vec{r}(k) - \vec{y}(k) \tag{6.5.25}$$

A block diagram of the three equations constituting the control approach can be seen in Figure 6.24. The C implementation for this this control approach is located with the rest of the code for this project on the attached CD.

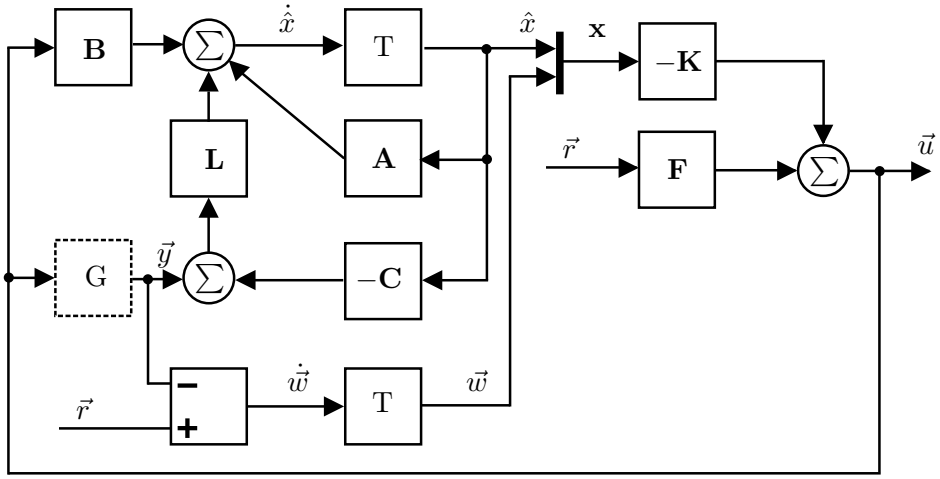

Figure 6.24: *Block diagram for DSC implementation. G is the system, and T a discrete integrator.*

6.5.5 Recapitulation of state space controllers

A short recapitulation of the methods and topologies that has been used and chosen are presented here, before the results of the controller implementations are shown.

Overall two topologies for state space based controllers has been presented throughout this section:

- Full state feedback, with state vector (6.5.4).
- Full state feedback, with augmented state vector (6.5.16).

Full state feedback requires that $\vec{y}$ and $\mathbf{x}$ are of the same length, i.e. all states are measured. Since the velocities are not fed back in this system, some approximation must be made in order to control the system. Two options have been presented to deal with this:

- Filtering and differentiation of the position.
- State estimation with an observer.

Lastly two approaches to the design of the controller itself was presented, i.e. the choice of gains in the control gain matrix, and the resulting poles in the closed loop:

- Pole placement.
- The Linear-quadratic Regulator (LQR)

Three implementations are chosen from different combinations of the above mentioned, but identical for all controllers is that the gains are computed with LQR, since no effective controller could be designed with pole placement. They are:

1. Full State Feedback (FSF), with a first order differential scheme to approximate the velocities from the filtered positions. Poles assigned with LQR.
2. Full State Feedback - Integral Control (FSFIC), with a first order differential scheme to approximate the velocities from the filtered positions. Poles assigned with LQR.
3. Full State Feedback - Integral Control and state Observer (FSFICO), with a full order prediction observer to estimate the full state vector. Poles assigned with LQR.

The implementation of these controllers are found on the attached CD. As an important point related to the implementation of the controllers, the sample frequency of FSF and FSFIC is $12.5kHz$, whereas it is $5kHz$ on the FSFICO. The choice of sample frequency was governed solely by the time needed for the DSC to complete the computations, and the frequency chosen as the reciprocal of the computation time with a sensible margin for variations in the computation time. This margin is also used in order to ensure that the frequency is an integer multiple of the DSC clock frequency, since this is required because of the discrete nature of the system.

So far the FSFIC and the FSF has been tested, and the results are presented here. As for the FSFIC, it is possible to follow a reference even though it is not in the vicinity of the linearization point, and this is exploited with a $0.5s$ ramp, instead of a step. The currents are also following a ramp, from $0.2A$ to $1A$, where the initial values of the position ramps are determined by the axle position at start up.

All controllers are based on models that are linearized at $x_1 = y_1 = x_2 = y_2 = 0.0$, and $i_1 = i_2 = i_3 = i_4 = i_5 = i_6 = 1A$, which is also used as their bias currents. The following three figures, 6.25 6.26 and 6.27, are comparisons of the integral control scheme simulations with the response on the experimental setup. General for all the data is that the response of bearing one deviates more from the model than that of bearing two. This is probably caused by error in the sensor calibration, and the fact that the model does not have any disturbance forces applied to it, but this ideal case is not present in the real system.

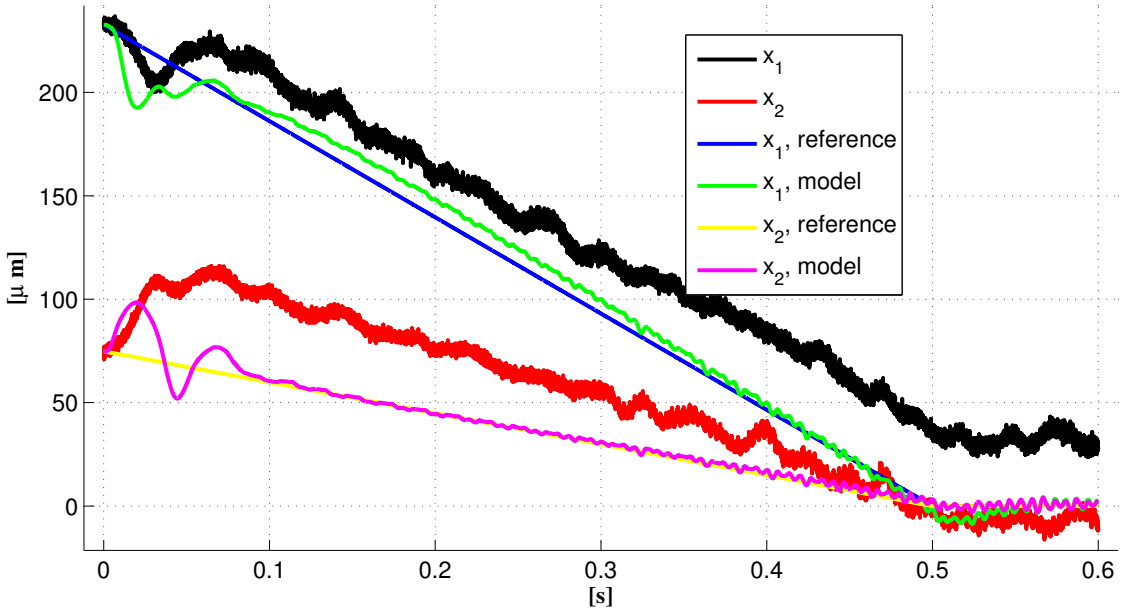

Figure 6.25: *State feedback with integral control, x_1 and x_2.*

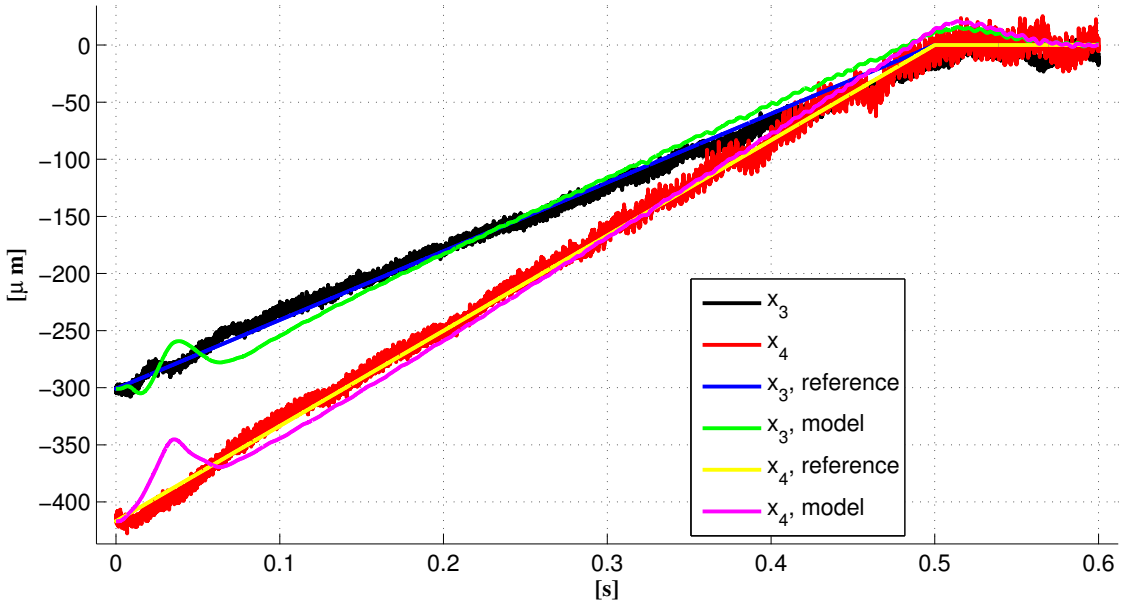

Figure 6.26: *Experimental- and non-linear data comparison for FSFIC controller, x_3 and x_4.*

The currents of the system, shown Figure 6.27, has a steady state error that is expected since the reference for these are purely feed-forward, and without any feedback.

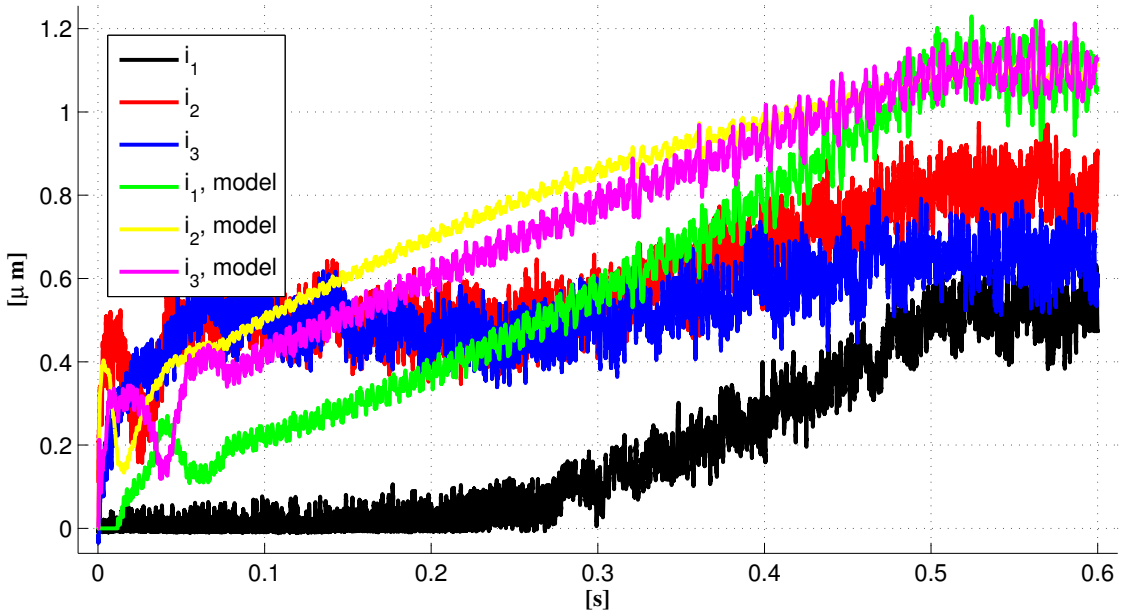

Figure 6.27: *Experimental- and non-linear data comparison for FSFIC controller, i_1, i_2 and i_3.*

When the state space controllers reference are feed-forward only, and no integral action is used, the results from bearing 1 does not match the model for this step. This is seen in Figure 6.28, whereas bearing two Figure 6.29 shown better accordance. Again model error and sensor calibration can contribute with significant errors, with this type of sensitive controllers that does not utilize feedback for the reference.

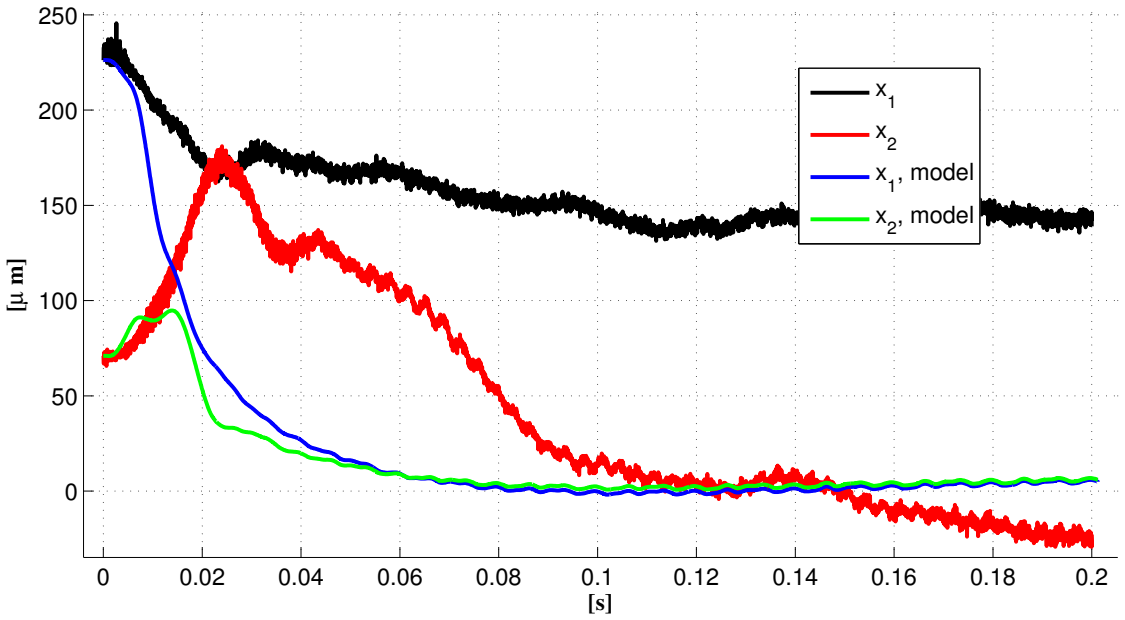

Figure 6.28: *FSF controller, comparison of experimental data and non-linear model, x_1 and x_2.*

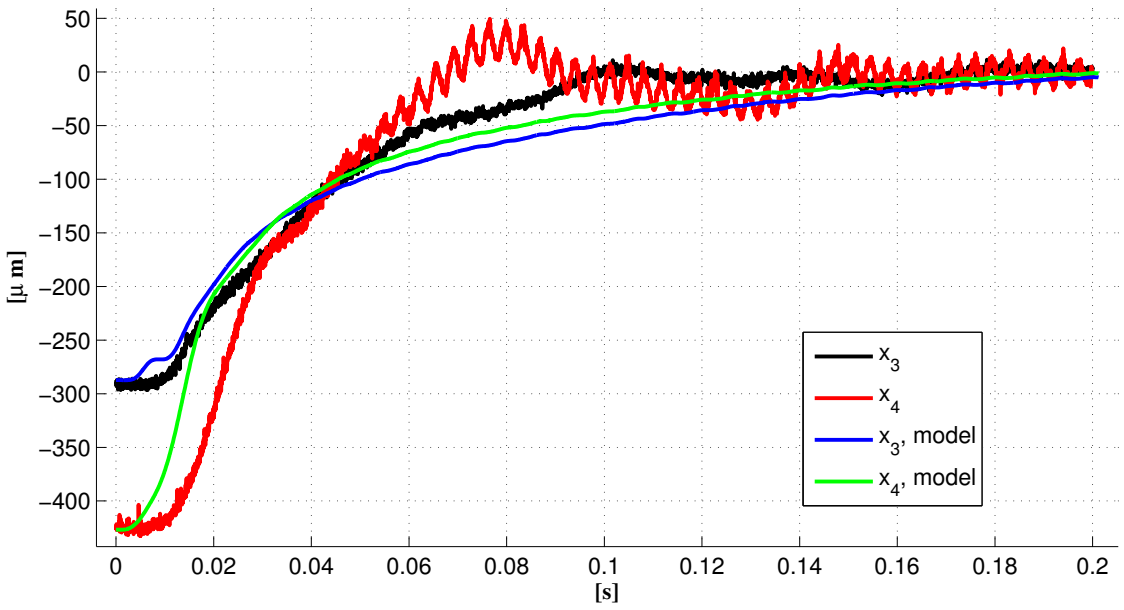

Figure 6.29: *FSF, comparison of experimental data and non-linear model, x_3 and x_4.*

6.6 Comparison of controller performance.

For comparison of the controllers that have been developed for the experimental setup, a test is devised to evaluate the performance of the different control strategies across the range of approaches. A force vector with a fixed point of attack, is applied in the form of three load scenarios: Impulse, step and a ramp, to determine the stall force of the bearing. For each scenario an appropriate measure of performance are set up and compared. The force is applied to the non-linear model, where the load actuator are situated, see Figure 5.1, and at a $-60°$ angle, which is considered to be the most odd angle from an actuator point of view, for the purpose of exciting as much as the dynamics and couplings as possible, see Figure 6.30.

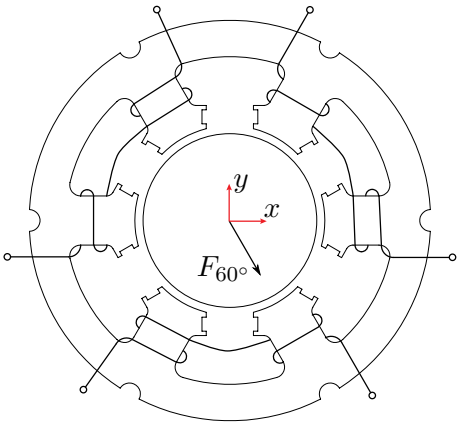

Figure 6.30: *How the test force,$F_{60°}$, for testing the different controls strategies is applied geometrically.*

The resulting forces and moments from the applied force must be transformed into general coordinates,$\vec{Q}$, to be added to the mechanical model, this is done with (6.6.1).

$$\vec{Q} = \begin{bmatrix} cos(60°) \\ -sin(60°) \\ sin(60°) * l_3 \\ cos(60°) * l_3 \end{bmatrix} \cdot F_{60°} \tag{6.6.1}$$

The magnitude of the force varies with time according to Figure 6.31, and as mentioned, it is comprised from an impulse, a step and a ramp. Each load case is analyzed separately, i.e. the performance indicators are applied to all of the load cases.

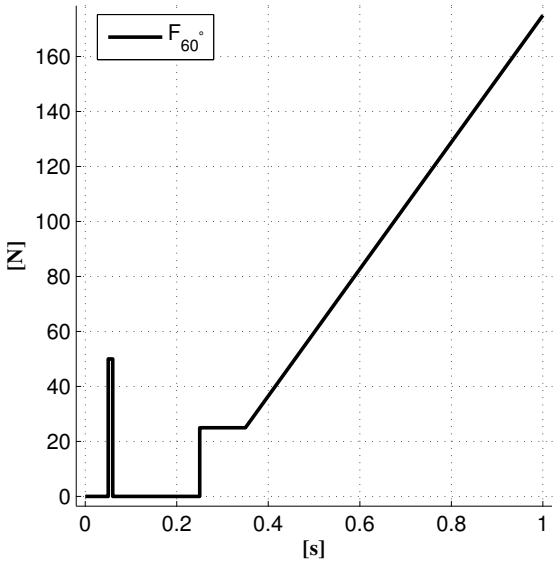

Figure 6.31: *How the force is applied over time.*

The controllers are subjected to similar conditions as in the laboratory, the observer based controller e.g. runs at a frequency of $5kHz$, since it is more computational demanding than the other controllers.

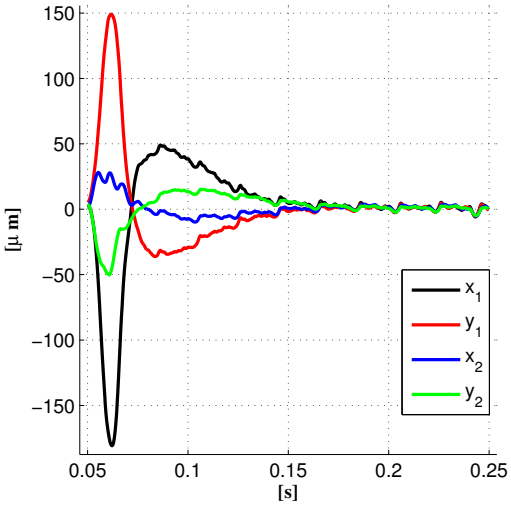

(a) Impulse

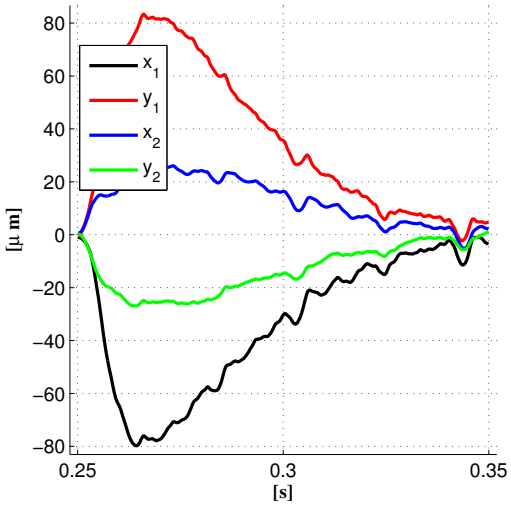

(b) Step

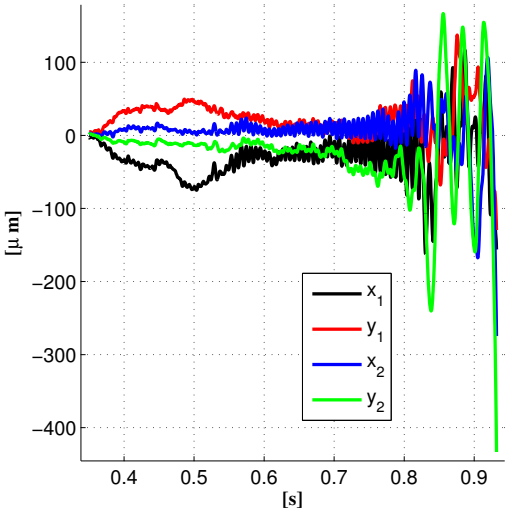

(c) Ramp

Figure 6.32: *FSFICO*

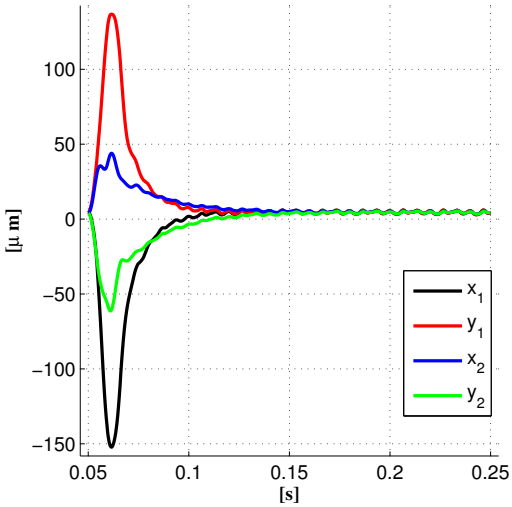

(a) Impulse

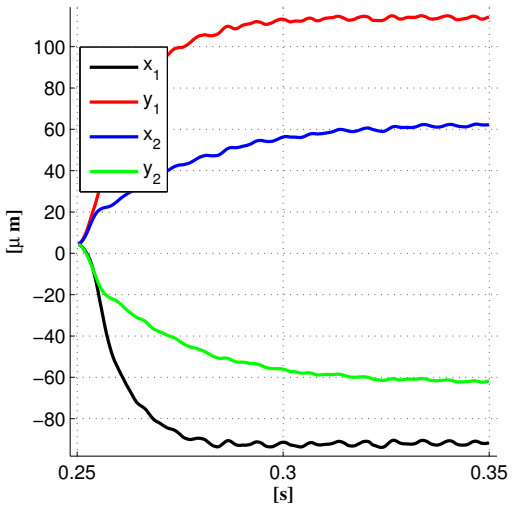

(b) Step

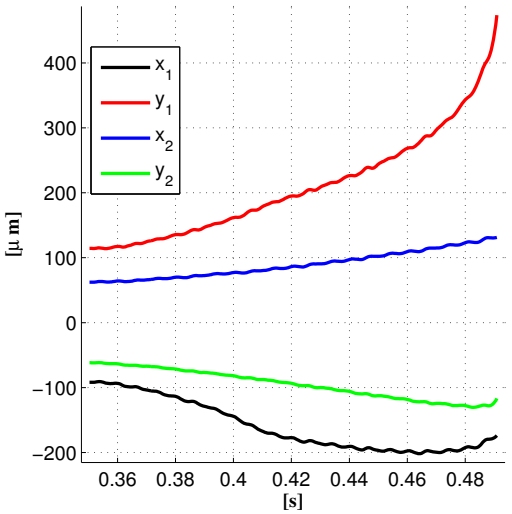

(c) Ramp

Figure 6.33: *FSF*

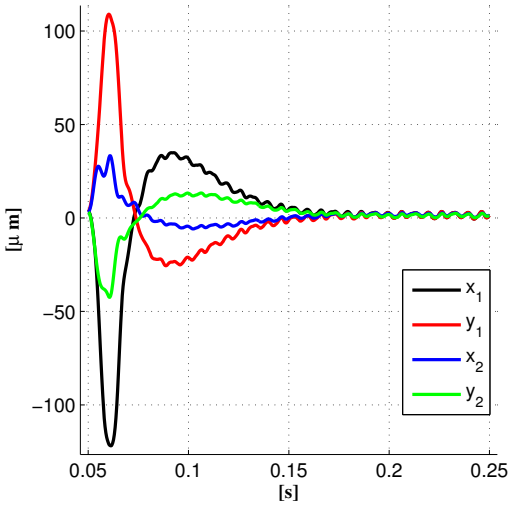

(a) Impulse

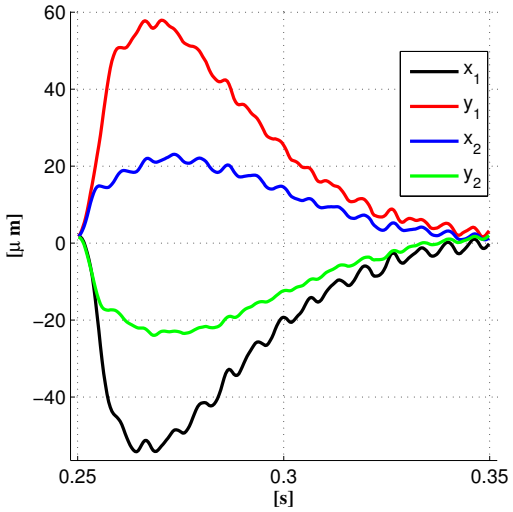

(b) Step

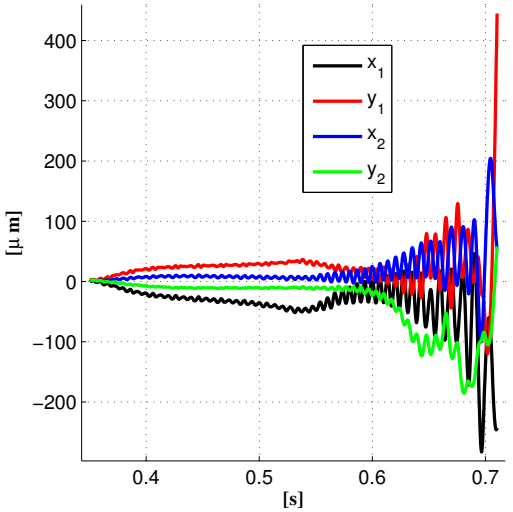

(c) Ramp

Figure 6.34: *FSFIC*

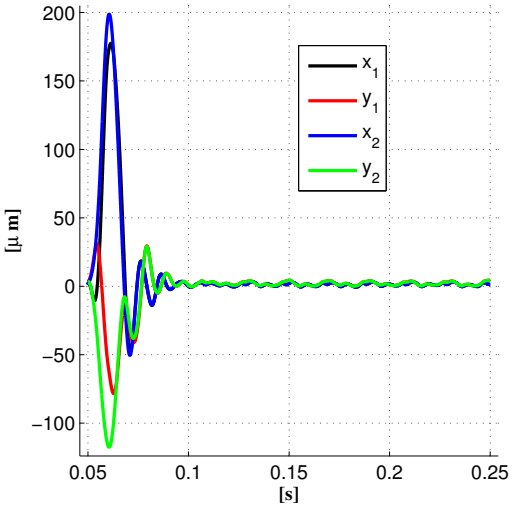

(a) Impulse

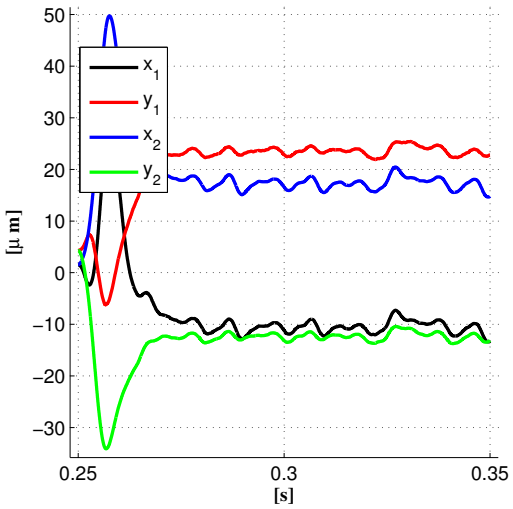

(b) Step

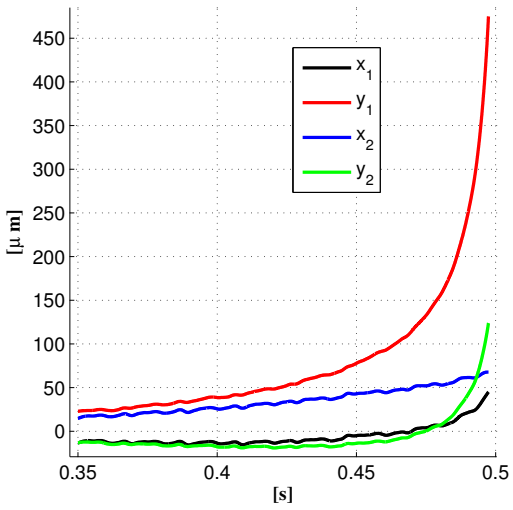

(c) Ramp

Figure 6.35: *Space vector centralized PD*

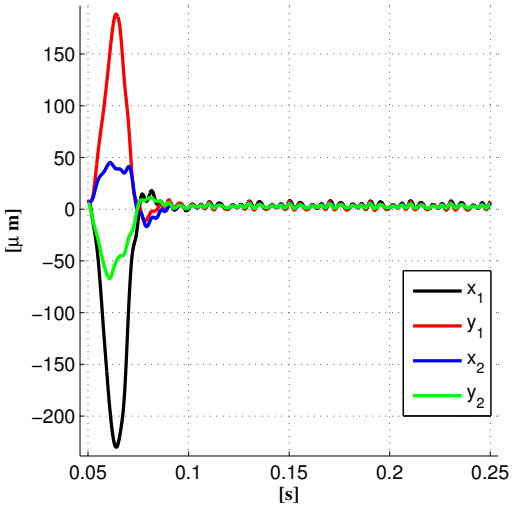

(a) Impulse

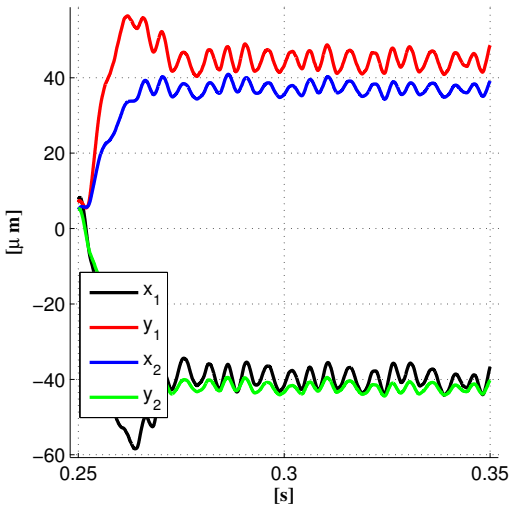

(b) Step

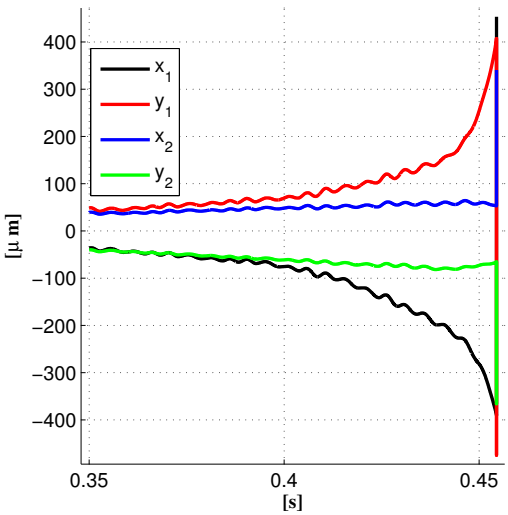

(c) Ramp

Figure 6.36: *PD*

The simulated response of the controllers, with respect to the three load cases are shown Figures 6.32, 6.33, 6.34, 6.35, and 6.36. Five indicators have been chosen as quantitative measures for the performance of the controllers, as a basis for the further work for control strategies of an AMB, they are:

- Overshoot, in bearing coordinates,$\vec{x}$. The measure of the overshoot, will simply be the summation of the overshoot for each entry in $\vec{x}$.
- Maximum recovery time, i.e. the slowest bearing coordinate to return to a chosen value of $< 10\mu m$.
- The summation of the 2-norm for each bearing coordinate in $\vec{x}$.
- Energy consumption.
- Stall force.

With exception of the stall force, each performance indicator is shown for the three load cases, resulting in Table 6.2. NaN is indicated whenever the performance indicator does not make sense e.g. recovery time of a step response, when no integrating action is present in the tested controller.

	Overshoot	**Recovery time**	**2-norm sum**	**Energy used**
	$[\mu m]$	$[ms]$	$[-]$	$[J]$
FSF Impulse	412.05	49.72	2052.51	3.75
FSF Step	351.24	NaN	4616.04	2.07
FSFIC Impulse	386.36	84.08	1580.35	4.51
FSFIC Step	165.27	70.32	1402.33	2.31
FSFICO Impulse	518.67	84.04	2263.93	4.01
FSFICO Step	225.64	94.36	2097.59	2.04
CSVPD Impulse	730.10	33.00	10786.04	0.41
CSVPD Step	162.56	NaN	4764.49	0.81
PD Impulse	589.04	33.22	11620.28	2.71
PD Step	224.17	NaN	11350.06	1.48

Table 6.1: *Performance parameters for the controllers topologies that have been tested.*

	Stall force
FSF	57.52
FSFIC	108.13
FSFICO	159.28
CSVPD	59.02
PD	49.11

Table 6.2: *Stall force for the controllers.*

The result in Table 6.1 are also presented in Figure 6.37.

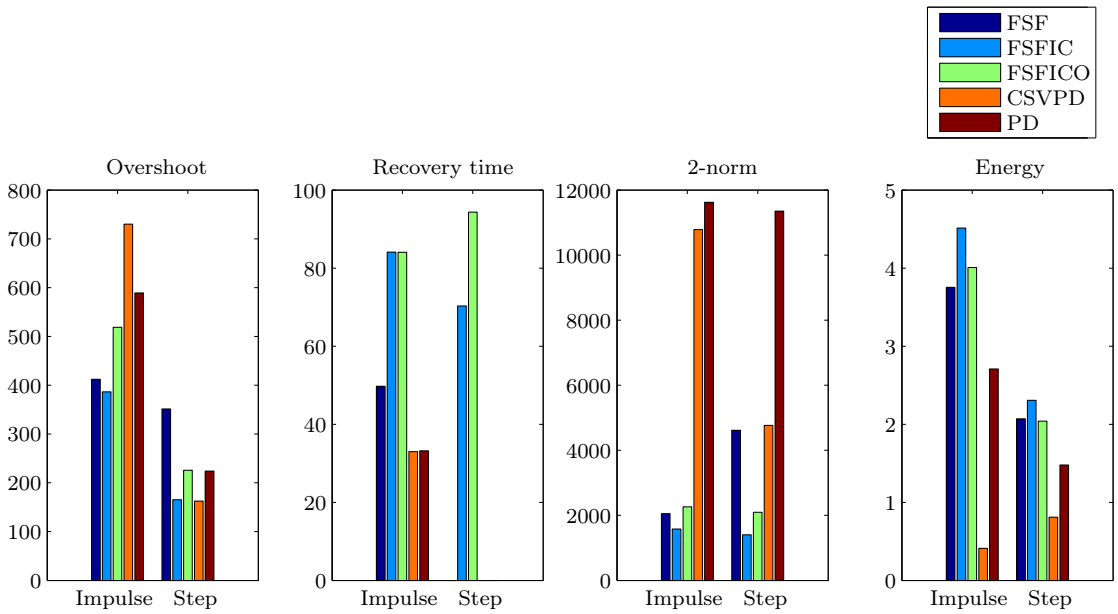

Figure 6.37: *Bar plot of the controllers performance.*

The results are analyzed in the following section, and a conclusion will be drawn. A recommendation for further work that could increase the performance of the controllers are also given.

6.6.1 Choice of control strategy

The overall choice of controller for a full-size bearing, must of course be a very robust design. Apart from being stable and robust, in order to handle unexpected load scenarios, the controller must be economical and able to harness the force that the bearing can exert. As the results show, the loads that the controllers are able to handle before stalling are very different, with more than a factor of three from the minimum to maximum pull-out force. The conclusion here is expected, since the controllers that uses an integral term outperforms the other controllers. With respect to energy consumption, the CSVPD is far superior, since it does not feature a bias current in order to operate linearly. For example this controller has the highest overshoot when an impulse is applied, but it uses by far the least energy as well. This is an indication that if the overall efficiency of the bearing is a high priority, then a scheme without a bias current for linearization should be further investigated.

At this point the FSFICO yields the best performance in terms of stall force, and this must thus be the recommendation. It must be stressed that this is a recommendation at a point where obvious further work for the control strategies lie ahead, this is discussed in section 9.

Designing DeepWind active magnetic bearing

7

In this chapter design considerations for designing an AMB for the DeepWind application is carried out. The knowledge for doing this in a proper manner is by information gained from designing the experimental setup, and by static calculations.

7.1 Design specifications and interfaces

The dimensions of the generator, and the forces supplied are used as a starting point for a preliminary design of an AMB. Therefore the most important interface is the generator, that is sketched in Figure 7.2 with the dimensions supplied. Note that these dimensions are approximate measures.

For a full scale project, emergency- or touchdown bearings are imperative, since the magnetic bearings can be damaged during assembly, start up, maintenance etc. Even though this is an important feature, it is outside the scope of this thesis.

The safety factors for the bearing are considered from two perspectives. One where the classical factor of two is applied to the maximum bearing force, making the bearing able to withstand double the expected maximum. Secondly some redundancy is taken into account, such that two smaller actuators are preferred opposed to one larger. This should provide safe operation, even if a fault in a power amplifier or the coil insulation lead to system failure of one actuator.

It was found during operation of the experimental setup that unintended and unforeseen structural dynamics can enter the control loop via the sensors and severely degrade the performance. This will also apply to the full-scale wind turbine if not taken into account. The static forces will also result in large deflections, that could complicate the position measurements. Local stiffness where the magnets applies their forces are very important, since the energy that are used for local deformation is wasted. Therefore static analysis of the forces close to the bearings must be performed. Dynamic analysis, including an eigenfrequency analysis are necessary, but out of the. Here a topology is presented with no structural support, but simply an electrical and magnetic circuit that can carry the static forces. For an overall idea of the magnitude of the dimensions, a sketch of the full size $5MW$ wind turbine is depicted in Figure 7.1, with a marker where the generator and bearing assembly is located. This lower part of the turbine is shown in a more detailed section view in Figure 7.2, with the dimensions of the generator stator. It goes for turbine dimensions as well as generator dimensions, that they are the preliminary ones supplied

for an AMB design proposal.

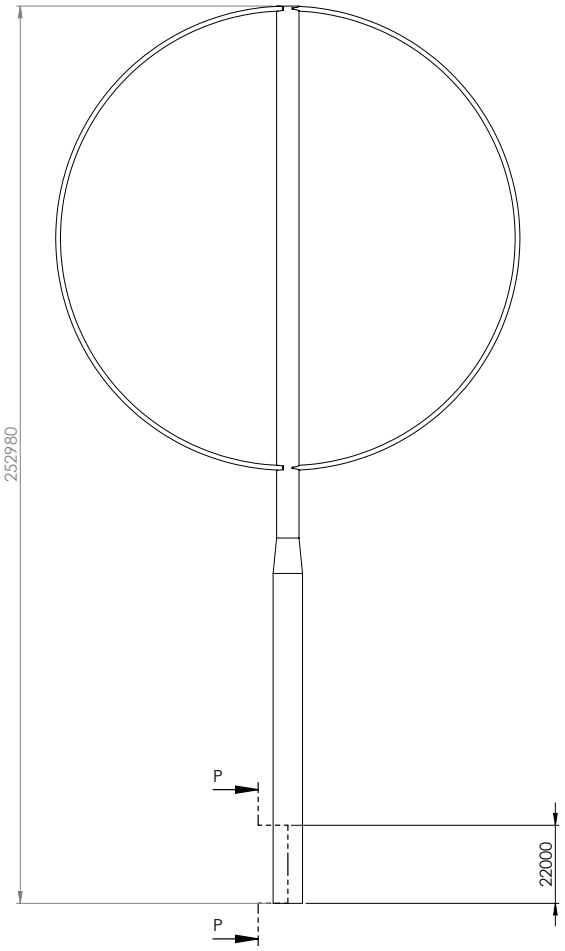

Figure 7.1: *A overview of the entire wind turbine, the circle is the approximate position of the bearing and generator assembly.*

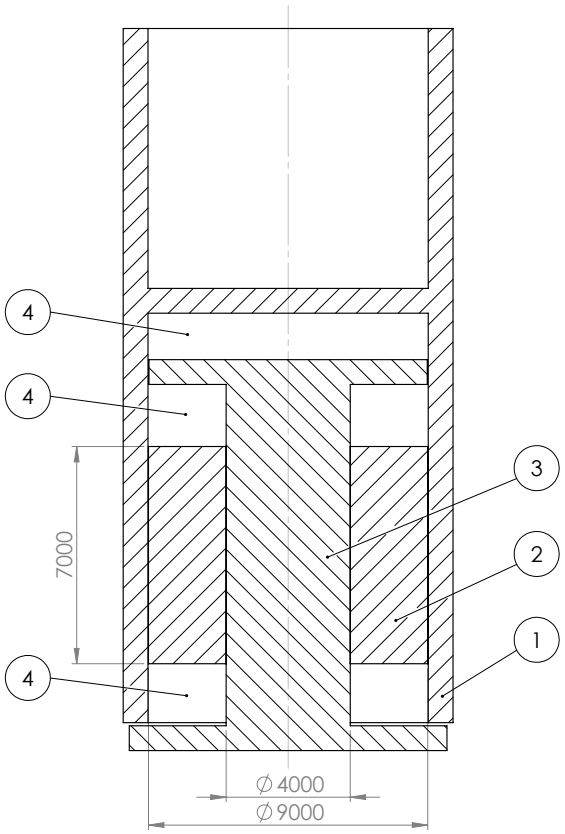

Figure 7.2: *Section view P-P: Sketch of the topology of the generator and bearing assembly. None of the dimensions are true, except for the generator stator, that are approximate numbers for current design revision.*

In this case there are no forces pushing the generator and rotor together, only a force pulling them apart, hence one axial bearing is sufficient. Two radial bearings are placed bellow and above the generator core. The layout of the generator and bearing assembly is shown in Figure 7.2, and the parts are listed below:

1. Rotor, generator.
2. Stator, generator.
3. Generator axle.
4. Room for bearings.

7.1.1 Loads

The forces acting on the wind turbine is acquired from the DeepWind load model [Kragh and Madsen, 2013].

The forces used are from the load the maximum load case. The wind speed is $24\frac{m}{s}$ and the wave amplitude is $14m$ with a period of $16s$ and a current speed of $0.7\frac{m}{s}$

The forces are described by a mean force and a standard deviation. The maximum forces and moments are calculated as the sum of the mean force and the standard deviation multiplied by 3 to account for 99.7% of the normal distribution. The forces acting in the generator are presented in Table 7.1.

Generator loads

	Mean$[kN]$	Std$[kN]$	Max$[kN]$
F_x	-144.01	89.99	-413.98
F_y	228.59	49.95	378.44
F_z	90168.39	643.66	92099.37

	Mean$[kN]$	Std$[kN]$	Max$[kN]$
M_x	1601.27	97.04	1892.39
M_y	-1014.55	246.53	-1754.14

Table 7.1: *Maximum loads in generator are found based on the results from the dynamic simulations performed by Kragh and Madsen [2013].*

The planar force in the bearing is calculated from the mean forces in the x- and y-direction. A similar calculation is carried out to acquire the moments. This yields the mean load scenario in the bearing. The forces and moments are presented in Table 7.2.

Mean planar loads	
$F_{planar}[kN]$	270.17
$F_{axial}[kN]$	90168.39
$M_{planar}[kN]$	1895.62

Maximum planar loads	
$F_{planar}[kN]$	560.89
$F_{axial}[kN]$	92099.37
$M_{planar}[kN]$	2580.34

Table 7.2: *Mean and maximum planar loads.*

Transferring the planar force and the planar moment to act in the radial bearings, yields a mean force in the radial- and axial bearing. This is carried out by use of the following expression:

$$F_{radial1} = \tfrac{1}{2} \cdot F_{planar} + \frac{M}{l} = \tfrac{1}{2} \cdot 270.17kN + \frac{1895.62kNm}{9m} = 345.71kN \tag{7.1.1}$$

$$F_{radial2} = \tfrac{1}{2} \cdot F_{planar} - \frac{M}{l} = \tfrac{1}{2} \cdot 270.17kN - \frac{1895.62kNm}{9m} = -75.54kN \tag{7.1.2}$$

And for the maximum load scenario the maximum radial load is $567.15kN$. The loads, especially in the axial direction, seem excessive, and comparing these to the significantly smaller loads acting on the anchoring system shows that a large mass in the stator/anchoring must contributing to the large axial force.

The large constant axial loads in the bearing limits the applicability of the AMB, since a constant force in this case is suspended, resulting in a similar constant power. The AMB seemed very applicable for this specific application because of an very small expected load situation. If this load situation has to be suspended by an AMB the effective area of the axial magnet has to be $160m^2$, by the force limitation of $573kN/m^2$ calculated in section 7.2. This seems rather implausible since neither safety factor nor fill factor are taken into account. The fill factor in this case being the ratio between effective bearings area and bearings area.

Therefore the project group suggests that an amount of mass is moved from the stator to the rotor. If this is performed in a proper way the axial loads in the bearing should correspond to the loads in the anchoring, which again corresponds roughly to the wind load. The maximum axial force in the anchoring is presented in Table 7.3.

Mean load	
$F_{anchor}[kN]$	1972.38

Maximum load	
$F_{anchor}[kN]$	2389.47

Table 7.3: *Sum of axial loads in anchoring system acquired from [Kragh and Madsen, 2013].*

This maximum force is a sum of the mean y force plus three times the standard deviation, for arm one to three. Note that the y direction of the arms, is parallel with the z axis in this thesis. Having in mind that when the mass is moved to the rotor, the generator must still have a mass that supplies a constant tension in the axial bearing, qua the chosen bearing topology.

The bearing is in the next sections designed for the maximum loads described in this section. This is for the radial bearings a load of $567.15kN$ and an axial load of $2389.47kN$. Furthermore a safety factor of two is added in the design. Afterwards an approximation of the general power use is based on the mean loads.

7.2 General magnetic considerations

A number of factors has to be considered when designing the bearing. The main limitation in the bearing design is the magnetic saturation, which limits the load capacity per area, and therefore has a significant influence on the sizing of the bearing. The magnetic field energy is described by equation (7.2.1) [Zhuravlyov, 1992]:

$$W_f = \int_V \int_0^{\mathbf{B}} H\left(\mathbf{B}\right) \mathrm{d}\mathbf{B}\ \mathrm{d}V \tag{7.2.1}$$

Where the field energy consists of the energy of the air gap fields, the energy of the leakage fields and the energy of the iron fields.

$$W_f = W_g + W_l + W_i \tag{7.2.2}$$

The energy of the air gap fields is highly dependent of the rotor position. The leakage and the iron field energy does not depend on the rotor position. Therefore, describing the force as in (7.2.3), it only depends on the air gap field energy.

$$F = -\frac{\partial W_g}{\partial q} \tag{7.2.3}$$

In an air gap with homogeneous magnetic field and flux density B_g, the force is described by:

$$F = \frac{{B_g}^2}{2 \cdot \mu_0} \cdot A_g \tag{7.2.4}$$

Where A_g the cross section area of the air gap. Saying that if the magnetic saturation occurs at $1.2T$ the maximum force is limited to $\approx 573kN/m^2$.

7.2.1 Mechanical sketch

By the specifications and interfaces described in section 7.1, and the maximum loads specified in section 7.1.1 a preliminary design of the magnetic bearing can be sketched.

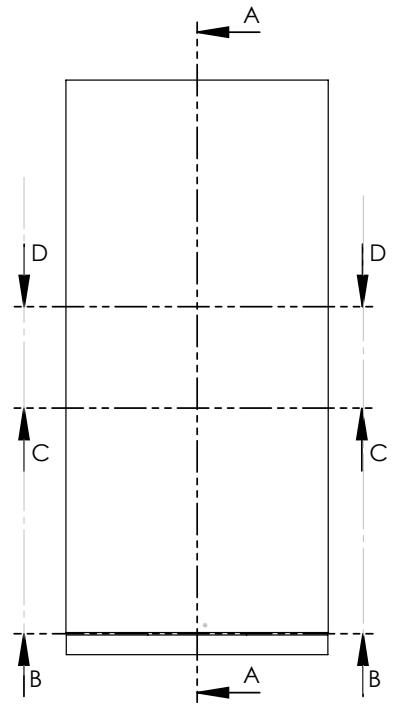

(a) *Bottom of the wind turbine, depicted without the arms for the mooring lines. Sections views A-A to D-D are defined here.*

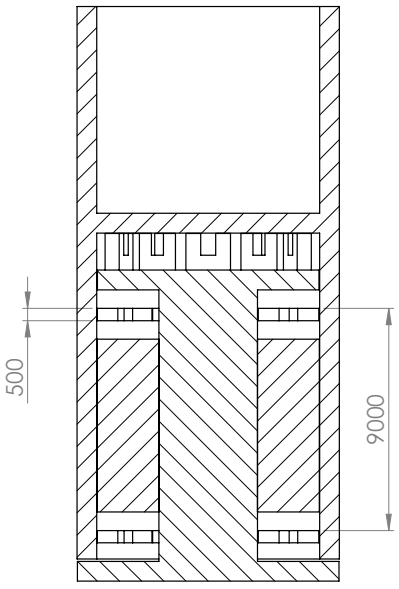

A-A

(b) *Section A-A with the height of the bearing, and the distance between the bearings.*

Figure 7.3

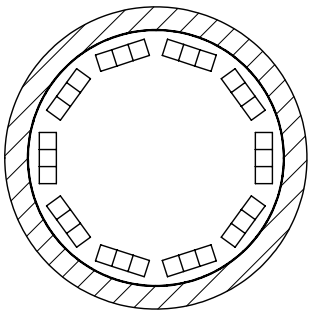

D-D

(a) *Cross section in the airgap of the axial bearing.*

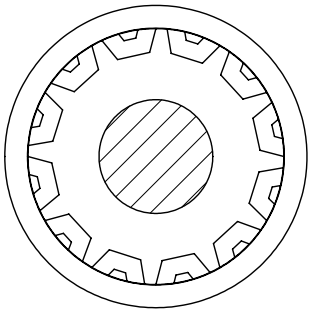

B-B

(b) *Cross section of the lower radial bearing, showing the layout of the electromagnets. Here depicted as floating, they must ofcourse be fixed to the stator axle with an appropriate structure.*

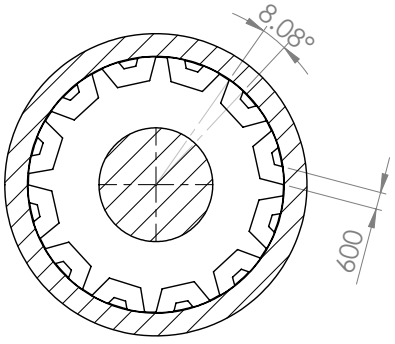

C-C

(c) *View of the upper radial bearing, similar to Figure 7.4b.*

Figure 7.4

First the radial bearing is considered. The angle span of each pole is calculated by the

number of poles by:

$$\alpha = \frac{2 \cdot \pi}{p} \tag{7.2.5}$$

Therefore the minimum possible force described by the number of poles is:

$$F_{radial} = \sum_{n=1}^{p/2} F_{pole} \cdot sin\left(n \cdot \alpha\right) \quad p \in 2\mathbb{N} \tag{7.2.6}$$

Assigning the number of poles to 24, and solving this for the radial force of $771.51kN$ with a safety factor of two, the required maximum force in each pole is described by:

$$F_{pole} = 203.14kN \tag{7.2.7}$$

The area of the air gap is calculated by the rotor diameter d_{rotor}, the pole fill factor FF_{pole} and the bearing height h:

$$A_g = \frac{d_{rotor} \cdot \pi \cdot FF_{pole} \cdot h}{p} \tag{7.2.8}$$

Using the pole fill factor of 0.54 from Figure 7.4c, and using the relation for area and force from equation (7.2.4) limited of a flux density of $1.2T$, the height of the bearing should be:

$$h = \frac{F_{pole} \cdot p}{\frac{{B_g}^2}{2 \cdot \mu_0} \cdot d_{rotor} \cdot \pi \cdot FF_{pole}} = \frac{203.14kN \cdot 24}{573kN/m^2 \cdot 9.03m \cdot \pi \cdot 0.54} = 0.56m \tag{7.2.9}$$

A similar calculation of the axial bearing can be made. The force acting in the axial direction is the sum of all pole forces. The initial design suggests a quadratic pole area and 20 poles. Then the maximum force is:

$$F_{axial} = \sum_{n=1}^{p} F_{pole} \quad p \in \mathbb{N} \tag{7.2.10}$$

$$= p \cdot \frac{{B_g}^2}{2 \cdot \mu_0} \cdot A_{pole} \tag{7.2.11}$$

Having a safety factor of two times the maximum load described in Table 7.3, the required pole area is calculated as:

$$A_{pole} = \frac{2 \cdot 2389.47kN}{20 \cdot 573kN/m^2} = 0.42m^2 \tag{7.2.12}$$

7.2.2 Magnetic draft

A consideration of the necessary flux density can be made. The flux density is described in terms of the MMF and the air gap length by:

$$B_g = \mu_0 \cdot H = \frac{\mu_0 \cdot \mathcal{F}}{l_g} \tag{7.2.13}$$

Thus the smaller the airgap the more economical bearing. Though there would be limiting factors as the speed off the controller. Therefore choosing an appropriate air gap size

should be based on the power dissipation, the time constants in the loads and the time constants in the actuator system. Then specifying a proper airgap length the requested maximum MMF can be calculated. The large geometry of the bearing yields a limitation by the possible tolerances of the stator and rotor. Therefore the air gap length is set to $15mm$. The required MMF is then:

$$\mathcal{F} = \frac{B_g \cdot l_g}{\mu_0} = \frac{1.2T \cdot 0.015m}{\mu_0} = 14323.95A \tag{7.2.14}$$

The MMF is achieved by adding a number of windings or by increasing the current. Though both will have an effect on the ohmic loss. The ohmic loss as a function of current is given by:

$$P = R \cdot I^2 \tag{7.2.15}$$

And the resistance in the windings is:

$$R = \rho \cdot \frac{l}{A_{wire}} \tag{7.2.16}$$

Using that the length of the wire equals length per winding multiplied by the number of windings the power dissipation in the wire is described by:

$$P = \rho \cdot \frac{l/N}{A_{wire}} \cdot N \cdot I^2 \tag{7.2.17}$$

Thus increasing the number of windings the power increases proportionally, and increasing the current the power increases proportionally squared. Though other considerations has to be taken. Firstly it is not possible to increase the number of windings unbounded, because of geometry bounds and fill factor of winding procedure and insulation class. Secondly the heat dissipation in the windings have to be considered. The wire cross section area can be expressed as:

$$A_{wire} = \frac{FF \cdot A_{slot}}{N} \tag{7.2.18}$$

Inserting this in (7.2.17) yields:

$$P = \frac{\rho \cdot l/N}{FF \cdot A_{slot}} \cdot N^2 \cdot I^2 \tag{7.2.19}$$

By this it is shown that the limiting factor is the heat dissipation in the coil. And the maximum MMF is described in terms of the power dissipation:

$$N \cdot i = \sqrt{\frac{P \cdot FF \cdot A_{slot}}{\rho \cdot l/N}} \tag{7.2.20}$$

Besides when choosing the current and winding number, the inductance is affected, since it has the relationship to windings and reluctance given by:

$$L = \frac{N^2}{\mathcal{R}} \tag{7.2.21}$$

This will be an optimization problem, where one has to optimize the speed of the system and the losses. In the specific design, presented in Figure 7.3b and 7.3b, the slot size is not a limiting factor. Therefore the winding number and current can be chosen free. Choosing the maximum current limits the wire cross section, where cooling has to be taken into account.

Choosing the current to $30A$ the number of windings to 500 to maintain the required MMF (7.2.14) in each magnet. Calculating the ohmic power consumption using the in each coil, using $\rho_{20} = 1.68 \cdot 10^{-8}\Omega \cdot m$, the square of the winding $A_{wire} = 1.26 \cdot 10^{-5}m^2$ and $l/N = 2.2m$ using (7.2.17):

$$P = \ 1.68 \cdot 10^{-8}\Omega \cdot m \cdot \frac{2.2m}{1.26 \cdot 10^{-5}m^2} \cdot 500 \cdot (30A)^2 = 1.32kW \tag{7.2.22}$$

In maximum load situation the 12 coils of the radial bearing is turned on, and the power consumption is $15.84kW$. This calculation is per pole basis, so each magnet or pole pair will have 1000 windings.

For the axial bearing the required MMF is the same, therefore the ohmic power consumption can be calculated by the same factors as above, though $l/N = 2.6m$. This yields an ohmic power consumption of $1.56kW$ per pole, and a total on $31.20kW$.

Thus calculated power is the maximum rating of the system.

The power consumption is based on the mean loads in the bearing of the conditions described in section 7.1.1, which is the worst case for normal operation. The power consumption is calculated based on a control scheme where the most effective magnets from a geometric point of view is utilized first, i.e. the ones with the smallest angle to the force.

7.3 Power consumption

The radial forces are described in (7.1.1) and (7.1.2) to $345.71kN$ and $-75.54kN$ respectively. To achieve the forces one pole pair of each radial bearing has to be excited by a current. The necessary flux density of the air gaps is calculated by:

$$B_g = \sqrt{\frac{\frac{345.71kN}{cos(\alpha)} \cdot 2 \cdot \mu_0}{2 \cdot A_g}} \tag{7.3.1}$$

Then the necessary current to achieve this flux density in each air gap can be calculated, and then the power. A similar calculation is made for the axial bearing, though all magnets are excited to achieve the necessary force. The calculated power consumption is presented in Table 7.4.

Mean power consumption	
$P_{radial1}[kW]$	2.10
$P_{radial2}[kW]$	0.46
$P_{axial}[kW]$	11.6

Table 7.4: *Mean power consumption of bearing.*

7.4 Full size design summary

This design outlines the limiting factors when designing the full size bearing. A preliminary magnetic and electrical circuit are presented, and the power requirements seems sensible for a design of this size, but it leaves room for improvements to be done. If it is assumed that the wind turbine can deliver its nominal power of $5MW$ under the windiest conditions that the power consumption for the bearing was computed, then the $14.16kW$ required is equivalent to a power loss of 2.832‰. A simple approach with a safety factor of two has been used, but whether this is adequate must be analyzed further. Also the power loss is computed for the worst case scenario in a static analysis. In a dynamic analysis one should implement the loss of magnetization, the eddy current loss, which primarily would have an effect on the electrical resistivity. Furthermore the losses in the control system electronics could have an significant size.

For the large bearing the eddy currents could have a significant effect. Using coil windings with a large square could introduce skin effect. Also when magnetizing a pole with a large cross section the flux may not be evenly distributed, and a FEM analysis of the geometry would be required.

The designed bearing would be easy to implement in a mathematical model, identical to the RNM described for the six pole bearing. This model showed a good estimation physical system of the experimental setup. Only small modifications were made to the estimated model, thus the reluctances seemed to be underestimated in the model. Also for the axial part of the bearing a RNM could be set up.

Conclusion 8

The objective of this thesis was to develop and analyze modeling tools for AMBs for use in a VAWT application. Furthermore to determine if an AMB is applicable for the loads that are present in this application. This was broken into four main parts, and each conclusion is presented here.

Modeling

Two magnetic modeling approaches were combined and the developed model verified, along with a mechanical axle model. The complete model was verified dynamically and statically. It showed good accordance with the experimental setup. The model developed is described and should be applicable to most AMB designs without much alteration. A mechanical model for a flexible axle is also presented, but not verified. It is believed that the full DeepWind dynamical model can benefit from this model.

Control

Different control strategies were developed, the FSFICO controller was the best performing. It could handle the largest stall force, thus utilizing the full bearing load capabilities. Although several of the PD controller design schemes, might achieve better performance, by simple addition of an integral term. The CSVPD controller has excellent power utilization, thus potentially lowering the energy cost of running the magnetic bearing. The controller development chapter is a solid stepping stone for future work.

Full size preliminary design

Lastly a full size preliminary AMB design was presented. This design yields general figures of the energy consumption and the bearing size. The bearing power consumption was evaluated to $14.16kW$, which is 2.832‰ of the $5MW$ the windmill is designed to produce. This power consumption seems acceptable and the AMB bearing solution worth pursuing.

Experimental setup

The experimental setup was build and is working. During the manufacturing and operation of the setup, many problems occurred, most were solved some still remain. EMI impact on the sensors for both position and current, was one of the biggest problems. The EMI impact was reduced by removing ground loops, reducing the noise source (the H-bridges), decoupling and filtering. The second big challenge encountered was mechanical vibrations, either of the experimental rig itself or merely the position sensors. These were

reduced by stiffening the experimental setup. It is recommended to investigate which eigenfrequency modes can occur during bearing design and either by control or redesign, suppressing these vibrations. The noise was reduced sufficiently for the project group to be able to use the experimental setup for model verification and controller testing.

Further work 9

In this chapter a number of tasks for the continuing work is presented. This is what the project group thinks would serve as a useful addition to the work already performed.

Experimental setup

The experimental setup is at the conclusion of this project in working order, but would benefit from several improvements. A redesign of the power electronics, where special care is placed upon reducing EMI. During the PCB design process, calculating trace inductances and capacitances and accounting for those in the design. Improvement of the position sensors by strengthening the sensor mounts, optimizing the physical sensor coil and improving decoupling from other electrical systems.

Mechanical vibrations could also be removed by redesign or bandwidth improvement of experimental test setup controllers, improving the setup. It is recommended to place accelerometers at relevant positions of the setup to determine the exited vibration modes. A more extensive dynamic verification would be useful. By improving the experimental setup as mentioned before, impulse response and load response of the controllers could be measured and compared with greater success. The current experimental setup signal noise and vibrating makes such tests and comparisons difficult to interpret. With feedback from the strain gauges different load cases can be used to stress test the designed controllers.

Modeling

When more detailed models of the DeepWind turbine dynamics and design become available, the next logical step would be to design an AMB system for the wind turbine. Having the model, and optimizing the design with regard to selective parameters would yield a better bearing design, than the preliminary. When a dynamic model is set up, controllers and their requirements can also be found.

In addition to the presented RNM improvement can be made by implementing the effects of hysteresis and eddy currents. For implementation of hysteresis effects a more precise material model, than the presented, would be necessary. Modeling the effects would give a more precise model of the losses in the machine, and help to choose and optimize a control strategy.

Controllers

The possibilities of the observer are far from fully exploited, and the performance of the FSFICO can thus be further improved. First and foremost, it should be able to at least match the performance of the derivative approach to estimate the velocities in the system. Especially if the optimal linear filter, the Kalman filter, is applied. Finally the observer would be able to use the feedback from an accelerometer, and use this measurement together with the positions for predicting the velocities. Using more inputs should theoretically improve both resolution, speed and reliability of the system.

The integral controllers that yields the best results in stall force, have very oscillating responses before stalling. This is due to the large currents that are drawn, and the linearization of the controller no longer being valid. Amplifying this non-linearity is the fact that currents are larger than the bias current due to the oscillations. A countermeasure to this could be using a gain scheduling strategy. This involving implementation of several controllers on the DSC, which are then selected based on the current.

Higher order controllers should be designed for the transfer function based controllers. As already mentioned the system type should at least be increased to 1.

To decrease the energy spent by the state space based controllers, it should be investigated what performance can be achieved without using a bias current.

Dansk resume 10

DeepWind Projektet er et forskningsprojekt, der omhandler design af en $5MW$ VAWT udelukkende til offshore brug. Forskningsgruppen lokaliseret på Aalborg Universitet er ansvarlig for konstruktion af generator og lejer. Dette speciale er baseret på et projektforslag fra denne gruppe. Specifikt omhandler projektet en undersøgelse af magnetiske lejer og mulighederne for at anvende aktive magnetiske lejer (AMBs) til denne applikation.

For at løse denne opgave bliver en eksperimentel opstilling indeholdende et aktivt magnetisk leje designet og fremstillet. Designet er verificeret ved hjælp af en strukturel FEM analyse, hvor de maksimale udbøjninger er bestemt. Foruden dette er den magnetiske del af forsøgsopstillingen designet og konstrueret. Denne består af to radiallejer og en magnetisk aktuator virkende som last emulator.

Et elektrisk system er også designet. Dette omfatter design og fremstilling af afstandssensorer og effektelektronik, hvor effektelectronikken består af strømsensorer, H-bro drivere og semi passive H-broer.

Endvidere for at kunne opsamle måledata fra systemet bruges en DAQ enhed. For at kunne måle krafterne fra den magnetiske aktuator er der opsat lasttransducere, i form af strain gauges. Styresystemet drives med en DSC, hvor en række regulatorer er implementeret og testede.

En række problemer forekom under fremstillingen og brugen af opstillingen. Et eksempel er den første iteration af et galvanisk isolations system, baseret på optokoblere. Den parasitisk kapacitans i disse enheder gjorde hele sensorsystemet ubrugeligt, på grund af støj. Derfor bruges i stedet en line driver baseret på optiske sendere, ledere og modtagere. Endvidere opstod en række lignende problemer med støj i styresignalerne. Disse er blevet væsentligt mindsket ved at forbedre skærmning og jordforbindelser.

Samtidig med udviklingen af opstillingen, blev en matematisk model udviklet. En Reluktans Netværk Model blev brugt til at beskrive det magnetiske kredsløb. Kræfterne beregnet af modellen er blevet sammenlignet med målinger udført med strain gauges. Ved tuning af modelparametrene blev en god overensstemmelse mellem model og målinger opnået. En mekanisk og en elektrisk model blev også udviklet.

En simpel proportional strømregulator er blevet anvendt sammen med en PD-regulator til at regulere den magnetiske, elektriske og mekaniske model. En dynamisk test af systemet er vist i Figur 10.1, hvor modellen viser god overensstemmelse med målingerne på forsøgsopstillingen.

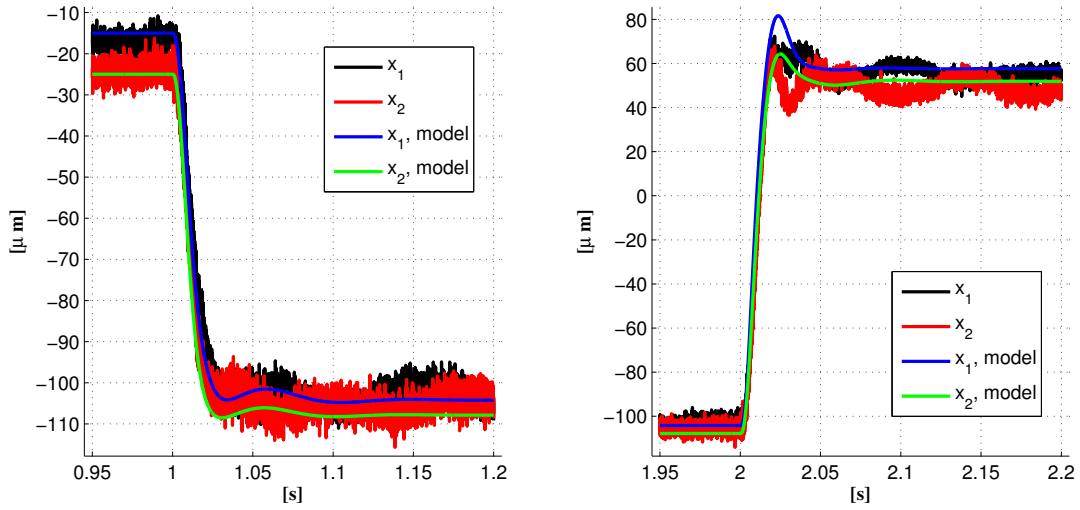

(a) Step pæ−50µm *(b) Step pæ100µm*

Figure 10.1: *Positionsmæling af step for modelverifikation.*

Det eksperimentelle system er ustabilt. Derfor er fem forskellige regulatorer, der stabiliserer systemet udviklet. Disse er udviklet med udgangspunkt i både den klassiske og den moderne kontrol teori. En kvantitativ sammenligningsmetode af regulatorer er udført, og resultaterne er vist i Figur 10.2.

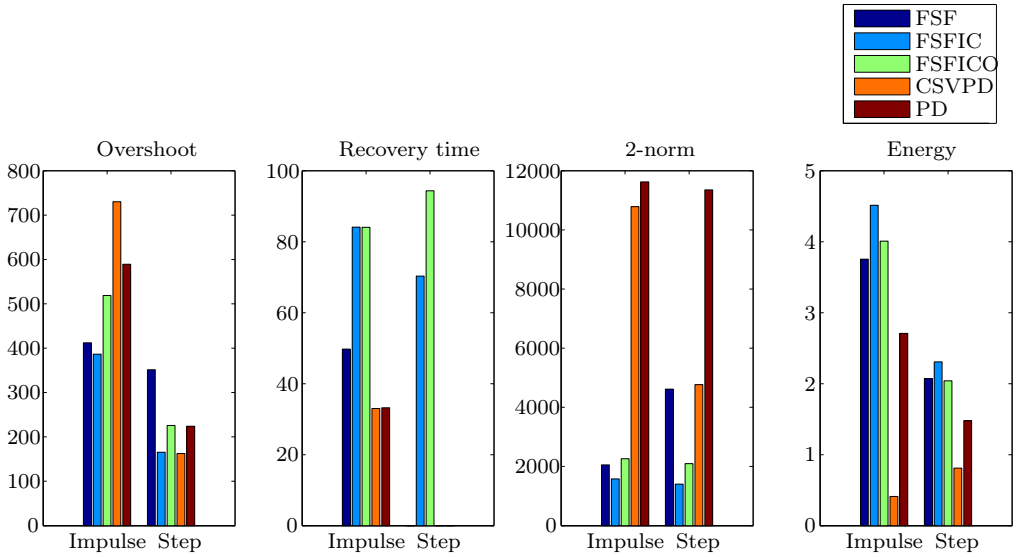

Figure 10.2: *Søjleplot af regulator ydeevne.*

Baseret på dynamiske belastninger beregnet af DeepWind forskningsgruppen, og de mekaniske grænseflader, er et foreløbigt fuld skala design af et magnetisk leje opstillet. Dette specificerer to radiale lejer, hver med 12 polpar og et aksialt leje med 10 polpar. På baggrund af designet og belastningerne er effektforbruget beregnet til $14.16kW$, hvilket er $2,832‰$ af de $5MW$ vindmøllen er designet til at producere. Effektforbruget forekommer acceptabelt og aktive magnetiske lejer virker som en lovende teknologi til brug i denne type vindmøller.

Acronyms

AC	Alternating Current
ACQ_PS	Acquisition Prescaler
ADC	Analog to Digital Conversion
ADCCLK	ADC Clock Frequency
ADCLKPS	ADC Clock Frequency Prescaler
AMB	Active Magnetic Bearing
CAD	Computer Aided Design
CPS	Core clock prescaler
CSVPD	Centralized Space Vector Proportional Derivative
DAC	Digital to Analog Conversion
DC	Direct current
DIN	Deutsches Institut für Normung
DSC	Digital Signal Controller
DTU	Technical University of Denmark
EMF	Electromotive force
EMI	Electromagnetic interference
FDATool	Filter Design and Analysis Tool
FEA	Finite Element Analysis
FEM	Finite Element Method
FEMM	Finite Element Method Magnetics
FIR	Finite Impulse Response
FSF	Full State Feedback
FSFIC	Full State Feedback - Integral Control
FSFICO	Full State Feedback - Integral Control and state Observer
GB	Gain-bandwidth product
HBM	Hottinger Baldwin Messtechnik
HSPCLK	High-Speed Prescaler Clock Frequency
IC	Integrated circuit
Inamp	Instrumentation Amplifier

KCL	Kirchhoff's current law
KVL	Kirchhoff's voltage law
LQR	Linear-quadratic Regulator
LSB	Least Significant Bit
MATLAB	MATrix LABoratory
MIMO	Multiple-Input and Multiple-Output
MMF	Magnetomotive force
MOSFET	Metal-Oxide-Semiconductor Field-Effect Transistor
NI-DAQ	National Instruments - Data Acquisition
Opamp	Operational Amplifier
PCB	Printed Circuit Board
PM	Permanent Magnet
PWM	Pulse Width Modulation
RNM	Reluctance Network Model
RSE	Referenced Single Ended
SG	Strain Gauge
SH	Sample-and-Hold
SOC	Start of Conversion
TI	Texas Instruments
VAWT	Vertical Axis Wind Turbine

Nomenclature

α	Stator pole angle	$[-]$
λ	Flux linkage	$[Wb]$
μ_0	Permeability of vacuum $(4\pi \cdot 10^{-7})$	$[H \cdot m^{-1}]$
μ	Permeability	$[H \cdot m^{-1}]$
μ_r	Relative permeability rotor	$[H \cdot m^{-1}]$
μ_s	Relative permeability stator	$[H \cdot m^{-1}]$
ω	Angular velocity axle	$[s^{-1}]$
ω_n	Natural frequency	$[s^{-1}]$
$\vec{\omega}_{total}$	Angular velocity vector	$[s^{-1}]$
ω_x	Angular velocity around x-axis	$[s^{-1}]$
ω_y	Angular velocity around y-axis	$[s^{-1}]$
ω_z	Angular velocity around z-axis	$[s^{-1}]$
τ_x	Moment around x-axis	$[N \cdot m]$
τ_y	Moment around y-axis	$[N \cdot m]$
ζ	Damping coefficient	$[-]$
$\mathbf{A}$	State matrix	$[-]$
A	Magnetic vector potential	$[V \cdot s \cdot m^{-1}]$
A_g	Air gap cross section area	$[m^2]$
a_p	Pole cross section area	$[m^2]$
a_r	Rotor flux field cross section area	$[m^2]$
a_s	Stator cross section area	$[m^2]$
B	Flux density	$[T]$
$\mathbf{B}$	Input matrix	$[-]$
B_g	Air gap flux density	$[T]$
$\mathbf{C}$	Output matrix	$[-]$
C_{1n}	Normalized capacitance 1, for Butterworth filter.	$[F]$
C_{3n}	Normalized capacitance 3, for Butterworth filter.	$[F]$
$\mathbf{D}$	Direct transmission matrix	$[-]$
d_{rotor}	Rotor diameter	$[m]$
$\vec{e}$	Input vector to a difference equation.	[-]

F_{60°	Force applied to compare controllers.	$[N]$
$\mathbf{F}$	Reference gain	$[-]$
$\mathcal{F}$	Magnetomotive force	$[A]$
f_b	Bandwidth	$[s^{-1}]$
FF_{pole}	Rotor circumference fill factor .	$[-]$
F_{load}	Static load force in experimental setup	$[N]$
f_{PB}	Pass band frequency	$[s^{-1}]$
f_{SB}	Stop band frequency	$[s^{-1}]$
$\mathcal{F}$	Magnetomotive force vector	$[A]$
F_x	Force in x-direction	$[N]$
F_{x1}	Force in x-direction in bearing 1	$[N]$
F_{x2}	Force in x-direction in bearing 2	$[N]$
F_{xakt}	Aktuator force in x-direction	$[N]$
F_{xd}	Disturbance force in x-direction	$[N]$
F_y	Force in y-direction	$[N]$
F_{y1}	Force in y-direction in bearing 1	$[N]$
F_{y2}	Force in y-direction in bearing 2	$[N]$
F_{yakt}	Aktuator force in y-direction	$[N]$
$\mathbf{G}$	Gyroscopic matrix	$[-]$
g	Permeance	$[Wb \cdot A^{-1}]$
G_a	Amplifier gain	$[-]$
$\mathbf{G_c}$	Gyroscopic matrix related to bearing coordinates	$[-]$
G_{OL}	Open loop transfer function	$[-]$
G_{PB}	Gain in filter pass band	$[-]$
G_{SB}	Gain in filter stop band	$[-]$
H	Field intensity	$[A \cdot m^{-1}]$
$\vec{h}$	FIR filter coefficients	$[-]$
h	Bearing height	$[m]$
$\mathbf{I}$	Identity matrix	$[-]$
$\vec{i}$	Current vector	$[A]$
i	Current	$[A]$
i_0	Bias current	$[A]$
$\vec{i_0}$	Direction vector for axis	$[-]$
$\vec{i_1}$	Direction vector for axis	$[-]$
$\vec{i_2}$	Direction vector for axis	$[-]$
$\vec{i_3}$	Direction vector for axis	$[-]$
$\dot{\vec{i}}$	Current velocity vector	$[A \cdot s^{-1}]$
i_l	Current in the left leg of the wheatstone bridge	$[A]$
i_r	Current in the right leg of the wheatstone bridge	$[A]$

i_{ws}	Supply current to wheatstone bridge	$[A]$
$\vec{i}$	Current vector	$[A]$
i_x	x-direction control current	$[A]$
I_{xx}	Mass moment inertia around x-axis	$[kg \cdot m^2]$
i_y	y-direction control current	$[A]$
I_{yy}	Mass moment inertia around y-axis	$[kg \cdot m^2]$
I_{zz}	Mass moment inertia around z-axis	$[kg \cdot m^2]$
J	Current density	$[A \cdot m^{-2}]$
$\vec{j_0}$	Direction vector for axis	$[-]$
$\vec{j_1}$	Direction vector for axis	$[-]$
$\vec{j_2}$	Direction vector for axis	$[-]$
$\vec{j_3}$	Direction vector for axis	$[-]$
$\mathbf{K}$	State space control gains matrix.	$[-]$
$\vec{k_0}$	Direction vector for axis	$[-]$
$\vec{k_1}$	Direction vector for axis	$[-]$
$\vec{k_2}$	Direction vector for axis	$[-]$
$\vec{k_3}$	Direction vector for axis	$[-]$
$\overline{\mathbf{K}}$	State space control gains matrix.	$[-]$
K_d	Differential controller gain	$[-]$
k_i	Linear model current stiffness	$[N \cdot A^{-1}]$
k_{mek}	Constant in mechanical model	$[-]$
K_p	Proportional controller gain	$[-]$
K_{sn}	Sensor gain	$[m \cdot V^{-1}]$
k_x	Linear model position stiffness	$[N \cdot m^{-1}]$
L	Self inductance	$[H]$
$\mathcal{L}$	Lagrangian	$[J]$
$\mathbf{L}$	Observer gain	$[m]$
$\mathbf{L}$	Inductance Matrix for actuator circuit	$[H]$
l_1	Total Length of the shaft	$[m]$
l_2	Length to first bearing force	$[m]$
L_{2n}	Normalized inductance 2, for butterworth filter.	$[H]$
l_3	Length between the two radial bearing forces	$[m]$
L_{4n}	Normalized indutance 4, for butterworth filter.	$[H]$
L_{rotor}	Rotor length	$[m]$
l_g	Airgap length	$[m]$
$\mathbf{L}$	Inductance matrix	$[H]$
L_p	Length of pole flux path	$[m]$
L_r	Length of rotor flux path	$[m]$
L_s	Length of stator flux path	$[m]$

l_{s1}	Length from sensor 1 to bearing 1	$[m]$
l_{s2}	Length from sensor 2 to bearing 2	$[m]$
m	Mass	$[kg]$
$\mathbf{M}$	Mass matrix	$[-]$
m_{eq}	Mass equivalent	$[kg]$
M	Mutual Inductance	$[H]$
$\mathbf{M_c}$	Mass matrix related to bearing coordinates	$[-]$
N	Number of windings	$[-]$
$\mathbf{N}$	Winding matrix	$[-]$
p	Number of poles	$[-]$
Φ	Magnetic flux	$[Wb]$
ϕ	Angle around z-axis	$[-]$
Φ_g	Air gap flux	$[Wb]$
Φ_{ml}	Mutual leakage flux	$[Wb]$
Φ_p	Pole flux	$[Wb]$
Φ_r	Rotor flux	$[Wb]$
Φ_s	Stator flux	$[Wb]$
Φ_{sl}	Self leakage flux	$[Wb]$
Φ	Approximate deflection function	$[-]$
$\vec{\Phi}$	Flux vector	$[Wb]$
Q	Generalized coordinate force and moment	$[-]$
q	Generalized coordinate	$[-]$
$\mathbf{Q_{lqr}}$	State weighing matrix for Linear quadratic regulator.	$[-]$
$\vec{Q}_c$	Generalized coordinates force vector related to bearing forces	$[-]$
$\vec{Q}$	Generalized coordinates force vector	$[-]$
$\vec{q}$	Generalized coordinate vecor	$[-]$
$\dot{\vec{q}}$	Time derivative of generalized coordinate vector	$[-]$
$\ddot{\vec{q}}$	Second order time derivative of generalized coordinate vector	$[-]$
$\mathcal{R}$	Reluctance	$[A \cdot Wb^{-1}]$
$\mathbf{R}$	Rotation matrix for total rotation	$[-]$
r_{SP}	Radius of the stator pole	$[m]$
$\tilde{\mathcal{R}}$	Approximate reluctance	$[A \cdot Wb^{-1}]$
$\mathbf{R_{lqr}}$	Input weighing matrix for Linear quadratic regulator.	$[-]$
$\mathcal{R}_g$	Air gap reluctance	$[A \cdot Wb^{-1}]$
$\mathbf{R}$	Reluctance matrix	$[A \cdot Wb^{-1}]$
$\mathcal{R}_{ml}$	Mutual leakage reluctance	$[A \cdot Wb^{-1}]$
R_{Ohm}	Resistance for actuator circuit	$[\Omega]$

$\mathcal{R}_p$	Pole reluctance	$[A \cdot Wb^{-1}]$
$\mathbf{R}_\phi$	Rotation matrix for rotation ϕ	$[-]$
$R_{pulldown}$	Pull down resistance	$[\Omega]$
$\mathcal{R}_r$	Rotor reluctance	$[A \cdot Wb^{-1}]$
$\mathcal{R}_s$	Stator reluctance	$[A \cdot Wb^{-1}]$
$\mathcal{R}_{sl}$	Self leakage reluctance	$[A \cdot Wb^{-1}]$
$\mathbf{R}_{\theta_\mathbf{x}}$	Rotation matrix for rotation θ_x	$[-]$
$\mathbf{R}_{\theta_\mathbf{y}}$	Rotation matrix for rotation θ_y	$[-]$
$\vec{r}$	State Space reference vector	-
σ	Standard deviation	$[-]$
$\vec{s}$	Sensor coordinate vector	$[m]$
s_{x1}	Bearing 1 sensor x-coordinate	$[m]$
s_{x2}	Bearing 2 sensor x-coordinate	$[m]$
s_{y1}	Bearing 1 sensor y-coordinate	$[m]$
s_{y2}	Bearing 2 sensor y-coordinate	$[m]$
T	Kinetic energy	$[J]$
t	time	$[s]$
$\mathbf{T_1}$	Transformation matrix between generalized force vector and bearing force vector	$[-]$
$\mathbf{T_2}$	Transformation matrix between bearing coordinates and generalized coordinates	$[-]$
$\mathbf{T_3}$	Transformation matrix between sensor coordinates and generalized coordinates	$[-]$
T_{gyr}	Kinetic energy by gyroscopic effect	$[J]$
θ_x	Angle around x-axis	$[-]$
$\dot{\theta_x}$	Angular velocity around x-axis	$[s^{-1}]$
θ_y	Angle around y-axis	$[-]$
$\dot{\theta_y}$	Angular velocity around y-axis	$[s^{-1}]$
θ_z	Angle around z-axis	$[-]$
$\dot{\theta_z}$	Angular velocity around z-axis	$[s^{-1}]$
$\mathbf{T}$	Winding matrix	$[-]$
T_{rot}	Rotational kinetic energy	$[J]$
T_{sample}	Sample time	$[s]$
T_s	Settling time	$[s]$
T_{trans}	Translational kinetic energy	$[J]$
$\vec{u}$	Supply voltage vector of actuator	$[V]$
u	Electromotive force	$[V]$
$U_{control}$	Control voltage	$[V]$
U_{in}	Input voltage	$[V]$

U_{out}	Output voltage	$[V]$
U_{S-}	Negative supply voltage	$[V]$
U_{S+}	Positive supply voltage	$[V]$
U_{Switch}	Switch voltage	$[V]$
$\vec{u}$	Voltage	$[V]$
U_{wo}	RMS output from the wheatstone bridge.	$[V]$
U_{ws}	RMS wheatstone bridge supply	$[V]$
V	Potential energy	$[J]$
W	Energy stored in inductor	$[J]$
W_f	Magnetic field energy	$[J]$
W_g	Air gap field energy	$[J]$
W_i	Iron field energy	$[J]$
W_l	Leakage field energy	$[J]$
$\dot{\vec{w}}$	Tracking error	[-]
$\vec{w}$	Integrated tracking error	[-]
$\mathbf{x}$	State vector.	[-]
x	x-coordinate	$[m]$
x_0	Bearing center x-coordinate	$[m]$
x_1	Bearing 1 x-coordinate	$[m]$
x_2	Bearing 2 x-coordinate	$[m]$
x_{akt}	Axtuator x-coordinate	$[m]$
$\dot{\mathbf{x}}$	State vector derivative.	[-]
$\dot{x}$	Velocity in x-direction	$[m \cdot s^{-1}]$
$\ddot{x}$	Acceleration in x-direction	$[m \cdot s^{-1}]$
$\hat{x}$	Estimated states.	$[m]$
$\dot{\hat{x}}$	Estimated states.	$[m]$
x_{ref}	Position reference input	$[m]$
$\vec{x}$	Bearing coordinate vector	$[m]$
$\dot{\vec{x}}$	Bearing coordinate velocity vector	$[m \cdot s^{-1}]$
$\ddot{\vec{x}}$	Bearing coordinate acceleration vector	$[m \cdot s^{-2}]$
y	y-coordinate	$[m]$
y_0	Bearing center y-coordinate	$[m]$
y_1	Bearing 1 y-coordinate	$[m]$
y_2	Bearing 2 y-coordinate	$[m]$
y_{akt}	Actuator y-coordinate	$[m]$
$\dot{y}$	Velocity in y-direction	$[m \cdot s^{-1}]$
$\vec{y}$	Model output	$[-]$

Z_0	Butterworth filter impedance factor.	[−]
Z_1	Impedance 1 in wheatstone bridge	[Ω]
Z_2	Impedance 2 in wheatstone bridge	[Ω]
Z_3	Impedance 3 in wheatstone bridge	[Ω]
Z_4	Impedance 4 in wheatstone bridge	[Ω]
z_1	z axis related to bearing 1	[-]
z_2	z axis related to bearing 2	[-]
z_{akt}	z axis related to actuator bearing	[-]

Bibliography

Adams, **2001**. Maurice L. Adams. *Rotating Machinery Vibration*. Marcel Dekker, Inc, 2001. ISBN 0-8247-0258-1.

Allen, **2008**. P. Allen. *Continuous Time Filters*. Georgia Tech, 2008. URL `http://users.ece.gatech.edu/phasler/Courses/ECE6414/Unit1/Discrete_02.pdf`. Course notes.

Analog Devices, AD620, **2011**. Analog Devices, AD620. *Low Cost Low Power Instrumentation Amplifier, AD620*, 2011. URL `http://www.analog.com/static/imported-files/data_sheets/AD620.pdf`. Datasheet, rev. H.

Analog Devices, AD841, **1988**. Analog Devices, AD841. *Wideband, Unity-Gain Stable, Fast Settling Op Amp, AD841*, 1988. URL `http://www.analog.com/static/imported-files/data_sheets/AD841.pdf`. Datasheet, rev. F.

Analog Devices, AD844, **2009**. Analog Devices, AD844. *60 MHz 2000* $\frac{V}{\mu s}$ *Monolithic Op Amp, AD844*, 2009. URL `http://www.analog.com/static/imported-files/data_sheets/AD844.pdf`. Datasheet, rev. F.

Analog devices, Decoupling Techniques, **2009**. *Analog devices, Decoupling Techniques*. 2009. URL `http://www.analog.com/static/imported-files/tutorials/MT-101.pdf`. Tutorial, rev. 0.

Antila, **1998**. Matti Antila. *Electromechanical properties of radial active magnetic bearings*. Electrical Engineering Series No. 92. Finnish Academy of Technology, 1998. ISBN 952-5148-73-4.

Bargallo, **2006**. Ramón Bargallo. *Finite elements for electrical engineering*. Universitat Politécnica De Catalunya - Electrical Engineering Department, 2006.

Brokaw, **2000**. Paul Brokaw. *An IC Amplifier User's Guide to Decoupling, Grounding, and Making Things Go Right for a Change*. Analog devices, 2000. URL `http://www.analog.com/static/imported-files/application_notes/AN-202.pdf`. Application note, rev. B.

Calkin, **1996**. Melvin G. Calkin. *Lagrangian and Hamiltonian mechanics*. World Scientific Publishing, 1st edition, 1996. ISBN 981-02-2672-1.

Chassaing, **2003**. Rulph Chassaing. *DSP Applications Using C and the TMS320C6x DSK*. Topics in Digital Signal Processing. John Wiley & Sons, 2003. ISBN 0-471-20754-3.

Cook, Malkus, Plesha, and Witt, **2002**. Robert D. Cook, David S. Malkus, Michael E. Plesha, and Robert J. Witt. *Concepts and Applications of Finite Element Analysis*. John Wiley & Sons, Inc, 2002. ISBN 978-0-471-35605-9.

DTU Risø, **2012**. DTU Risø. *DeepWind*, 2012. URL `http://http://www.risoecampus.dtu.dk/Research/sustainable_energy/wind_energy/projects/VEA_DeepWind.aspx?sc_lang=en`. Downloaded: 01-06-2013.

Ducu, **2011**. Dragos Ducu. *Op Amp Rectifiers, Peak Detectors and Clamps, AN1353*. Microchip Technology Inc., 2011. URL `http://ww1.microchip.com/downloads/en/AppNotes/01353A.pdf`. Application note.

Fadali and Visioli, **2012**. M. Sami Fadali and Antonio Visioli. *Digital Control Engineering: Analysis and Design*. Elsevier Science, 2nd edition, 2012. ISBN 978-0-12-394397-0.

Franklin, Powell, and Emami-Naeini, **2010**. Gene F. Franklin, J. David Powell, and Abbas Emami-Naeini. *Feedback control of dynamic systems*. Prentice Hall, 4th edition, 2010. ISBN 0-13-032393-4.

Gere and Goodno, **2004**. James M. Gere and Barry J. Goodno. *Mechanics of materials*. SI edition. Cengage learning, 7th edition, 2004. ISBN 978-0-495-43807-6.

Glad and Ljung, **2000**. Torkel Glad and Lennart Ljung. *Control Theory: Multivariable and nonlinear*. Control Engineering. Taylor & Francis, 2000. ISBN 0-7484-0878-9.

Hagen, **1996**. Jon B. Hagen. *Radio-Frequency Electronics: Circuits and Applications*. Cambridge University Press, 1996. ISBN 0-521-55356-3.

Hoffmann, **1989**. Karl Hoffmann. *An Introduction to Measurement Using Strain Gages*. Hottinger Baldwin Messtechnik, 1989.

Kaman Sensors, **2012**. Kaman Sensors. *Inductive Technology Handbook*, 2012.

Kitchin and Counts, **2006**. Charles Kitchin and Lew Counts. *A designers guide to instrumentation amplifiers*. Analog devices, 3rd edition, 2006. URL `http://www.analog.com/static/imported-files/design_handbooks/5812756674312778737Complete_In_Amp.pdf`.

Kragh and Madsen, **2013**. Knud A. Kragh and Helge Aagaard Madsen. *2nd Iteration Design Loads for the DeepWind 5MW Turbine*. DTU Wind Energy Report, 2013.

Meeker, **2010**. David Meeker. *Finite Element Method Magnetics User's manual*, 2010. URL `http://www.femm.info/Archives/doc/manual42.pdf`. FEMM reference manual.

Mohan, Undeland, and Robbins, **2003**. Ned Mohan, Tore E. Undeland, and William P. Robbins. *Power Electronics - Converters, Applications, and Design*. John Wiley & Sons, Inc, 2003. ISBN 978-0-471-22693-2.

National Instruments, **2009**. National Instruments. *NI USB-621x User Manual*, 2009. URL `http://www.ni.com/pdf/manuals/371931f.pdf`. Application note, rev. 1.

NXP Semiconductors, **2012**. NXP Semiconductors. *Designing RC snubbers*, 2012. URL `http://www.nxp.com/documents/application_note/AN11160.pdf`. Bus-Powered M Series USB Devices.

Phillips and Harbor, **2000**. Charles L. Phillips and Royce D. Harbor. *Feedback control systems*. Prentice Hall, 4th edition, 2000. ISBN 0-13-949090-6.

Polajzer, **2010**. Bostjan Polajzer. *Magnetic Bearings, Theory and Applications*. Sciyo, 2010. ISBN 978-953-307-148-0.

Rich, **1983**. Alan Rich. *Shielding and guarding*. Analog devices, 1983. URL `http://www.analog.com/static/imported-files/application_notes/41727248AN_347.pdf`. Application note, reprinted from Analog Dialogue.

Ruscio, **2009**. David Di Ruscio. *Linear Polynomial Estimator: The State Observer*, 2009. URL `http://home.hit.no/~hansha/documents/control/theory/state_observer.pdf`.

Schneider, **2000**. Schneider. *Electromagnetic Compatibility, Practical Installation guidelines*. Schneider Group, 2000. URL `http://www.schneider-electric.com/download/dk/da/details/28272763-Electromagnetic-Compatibility-Practical-Installation-guidelines/?reference=deg999en`.

Sedra and Smith, **2004**. Adel S. Sedra and Kenneth C. Smith. *Microelectronic Circuits*. The Oxford Ser. in Electrical and Computer Engineering Series. Oxford University Press, 4th edition, 2004. ISBN 0-19-511690-9.

Walpole, Myers, Myers, and Ye, **2007**. Ronald E. Walpole, Raymond H. Myers, Sharon L. Myers, and Keying Ye. *Probability & Statistics For Engineers & Scientists*. Pearson Education, 8th edition, 2007. ISBN 978-8131715529.

Zhuravlyov, **1992**. Yuriy N. Zhuravlyov. *Active Magnetic Bearings*. Otaniemi, 1992. ISBN 951-22-1314-1.

Zumbahlen and Analog Devices, **2008**. Hank Zumbahlen and inc Analog Devices. *Linear Circuit Design Handbook*. Electronics & Electrical. Newnes, 2008. ISBN 9780750687034.

Part I

Appendix

Appendix contents

CD A

Content of the attached CD is listed here in accordance with folders found on the CD.

Simulink models with implemented controllers

Components data sheets

DSC Code

Technical documentation of the experimental setup

- SolidWorks parts.
- Technical drawings.

PCB documentation

- Schematic files for EagleCAD.
- PCB layout and schematics.

Miscellaneous

- Report.pdf
- Batch Model MATLAB script for FEMM.
- LT-Spice model of position sensor.
- Photos of the experimental setup.

Experimental setup B

B.1 Design drafts for experimental setup

Designing the experimental setup five different examples of bearing configurations are considered. In Figure B.1 the subfigures each shows one experimental setup configuration.

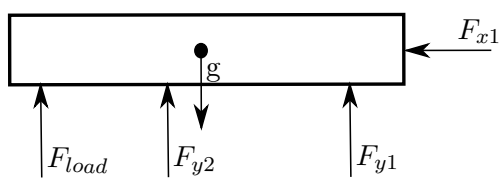

(a) *Horizontal with a force to control the axial displacement.*

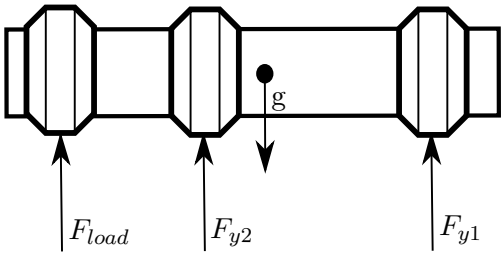

(b) *Horizontal with mechanical control of the axial displacement.*

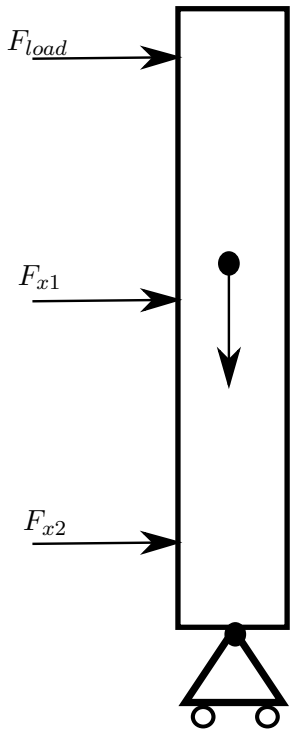

(c) *Vertical with a linear bearing to support the axial displacement.*

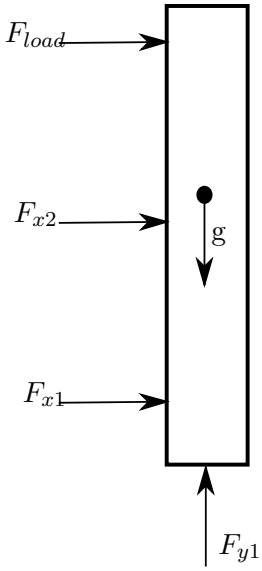

(d) *Vertical with a force to control the axial displacement, similar to B.1a but rotated* $90°$.

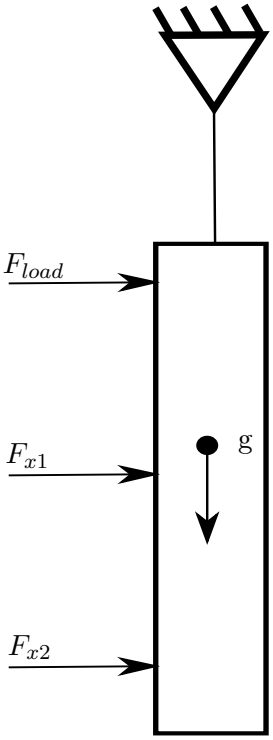

(e) *Vertical with a string to control the axial displacement.*

Figure B.1: *Five proposals for experimental setup topology.*

There are obvious pros and cons with respectively the vertical and horizontal approach, namely that a substantial part of the radial bearings force must be used for canceling the gravitational force in the horizontal case, leaving less force for control purposes. On the other hand, the horizontal approach in Figure B.1b theoretically cancels out the need for an separate axial force, as the shape of the shaft will have an axial force exerted on it, if it moves axially. Looking at the pros and cons of Table B.1. Configuration B.1e is chosen. The simplicity of the configuration is seen as a benefit because of the limited scope of the project and current experience level of the group members within this field of engineering.

Figure	Pros	Cons
B.1a Horizontal	+Full control of all DOF's +Small axial force needed	-Extra control loop for axial displacement
B.1b Horizontal	+Simple handling of axial displacement	-Virtually no axial damping
B.1c Vertical	+Simple handling of axial displacement +Full power for control	-Kinematic constraint has dynamics -Potentially elaborate bearing design
B.1d Vertical	+Full power for control +No kinematic constraints	-Large force needed in a axial control loop
B.1e Vertical	+ Very simple handling of axial displacement	-String has dynamics, and short strings may contribute with considerable radial forces.

Table B.1: *Pros and cons for the five different solutions.*

B.2 Bearing and actuator ratio

In this section the distribution of stator sheets is calculated. The experimental setup is limited of 130 sheets of $0.5mm$ available.

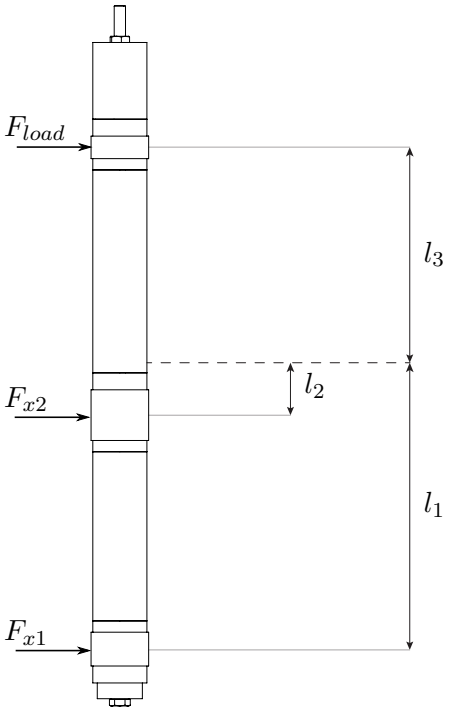

Figure B.2: *Dimension nomenclature for the experimental setup. Lengths are related to the center of mass, represented by a dashed line.*

Figure B.2 shows the experimental setup in a simplified 2D plane making bearing ratio considerations simpler. Due to the limitation of sheets the ratio of sheet steel needs to be calculated. The static equilibrium equations are set up with bearing force as variables and a constant n as the control surplus of the bearings with relation to the load actuator.

It is assumed that the force is somewhat proportional to the number of sheets. So if the sum of forces are set equal to one, saying that we have unity number of sheets.

Solving the force equilibrium equations these equations yields the force ratios necessary to statically fixate the axle. The ratio n is then merely a safety factor or an assurance of control surplus, making the bearings able to create forces larger than the load actuator.

The equilibrium equations are shown (B.2.1). n is chosen to be 2, thus the bearings are able to generate a static equilibrium.

$$\begin{aligned} \sum M_x = 0 &= F_{x1} \cdot l_1 + F_{x2} \cdot l_2 - n \cdot F_{load} \cdot l_3 \\ \sum F_x = 0 &= F_{x1} + F_{x2} + n \cdot F_{load} \\ 1 &= F_{x1} + F_{x2} + F_{Load} \end{aligned} \tag{B.2.1}$$

The calculated ratios are shown in Table B.2.

Load Actuator	0.125
Bearing 2	0.563
Bearing 1	0.3125

Table B.2: *Ratio of individual magnetic actuators.*

Based on this the chosen number of sheets and the height of the corresponding bearing is as shown in Table B.3

Load Actuator	$10mm$	20 sheets
Bearing 2	$35mm$	70 sheets
Bearing 1	$20mm$	40 sheets

Table B.3: *Height and number of sheets of individual magnetic actuators.*

B.3 BH-curves of axle and stator material

The BH curves for the axle steel and the stator material are obtained by creating a varying magnetic flux in the test piece via a coil. Then with a secondary coil measure the induced voltage, which is a function of the flux derivative. The test setup is as shown in Figure B.3.

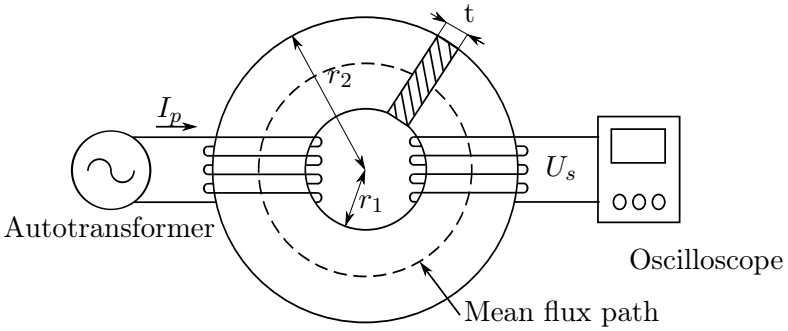

Figure B.3: *BH curve test setup. Primary coil to the left and secondary coil on the right.*

An auto-transformer is used as an Alternating Current (AC) source, 50Hz. Measuring the current in the primary coil, I_p and the voltage in the secondary coil U_s and knowing the number of windings in each coil, N, the BH curves are found using Faraday's law of induction and the direct relation between current, number of windings and MMF. The mean flux path in the test specimen is:

$$l_{MFP} = 2 \cdot \left(\frac{r_2 - r_1}{2} + r_1 \right) \cdot \pi \tag{B.3.1}$$

Where r_1 and r_2 are the inner and outer radius of the test specimen. The cross section area is:

$$A = (r_2 - r_1) \cdot t \tag{B.3.2}$$

(B.3.3)

By this the field intensity and flux density can be calculated:

$$H = \frac{N_p I_p}{l_{MFP}} \tag{B.3.4}$$

$$B = \frac{1}{N_s A} \int U_s(t) dt \tag{B.3.5}$$

The current was varied and several measurement were conducted. The integration of the voltage was carried out in MATLAB using the *trapz*() function, which uses the trapezoidal integration rule. The BH-curves obtained for the sheet steel are as expected and corrolates with the curves presented in Zhuravlyov [1992] for common sheet steels. The BH-curve of the axle is expected to be of similar shape though having large magnetic field values at equivalent flux densities. The axle sample showed a nearly circular hysteresis loop, which might be due to a large cross section area. Since the axle material is not laminated, eddy current are free to flow. Still the curve gives an idea of what flux densities one can expect to obtain using this material as axle steel.

B.4 Constants related to experimental setup

In this section a number of constants related to the experimental setup is presented.

Axle			
L_{rotor}	540.00	[mm]	Total length of rotor
d_{rotor}	51.15	[mm]	Rotor diameter
I_{xx}	0.2103	$[kg \cdot m^2]$	Axle mass moment of inertia around x-axis
I_{zz}	0.0028	$[kg \cdot m^2]$	Axle mass moment of inertia around z-axis
m	8.6550	[kg]	Rotor mass
l_1	222.00	[mm]	Distance from bearing 1 to center off mass
l_2	3.50	[mm]	Distance from bearing 2 to center off mass
l_3	-	[mm]	Distance from actuator to center off mass

Sensors			
l_{s1x}	48.00	[mm]	Distance from sensor 1x to bearing 1 center
l_{s1y}	51.00	[mm]	Distance from sensor 1y to bearing 1 center
l_{s2x}	54.50	[mm]	Distance from sensor 2x to bearing 2 center
l_{s2y}	53.50	[mm]	Distance from sensor 2y to bearing 2 center
m_{eq1}	4.41	[kg]	Equivalent mass bearing 1
m_{eq2}	13.34	[kg]	Equivalent mass bearing 2

Bearing and actuator			
l_g	0.475	[mm]	Airgap neutral
r_{SP}	26.10	[mm]	Radius stator pole
α_{Void}	1.0472	[rad]	Angle span between poles
α_{Pole}	0.5442	[rad]	Pole angle span
α_{Void}	0.5030	[rad]	Angle span og gap between poles
L_p	24.00	[mm]	Pole flux path length
L_s	52.40	[mm]	Stator flux path length
L_r	21.50	[mm]	Rotor flux path length
h_1	20.00	[mm]	Height of bearing 1
h_2	35.00	[mm]	Height of bearing 2
$h_{actuator}$	10.00	[mm]	Height of actuator
N	150	-	Number of windings

Control system C

C.1 Distance sensor full schematic

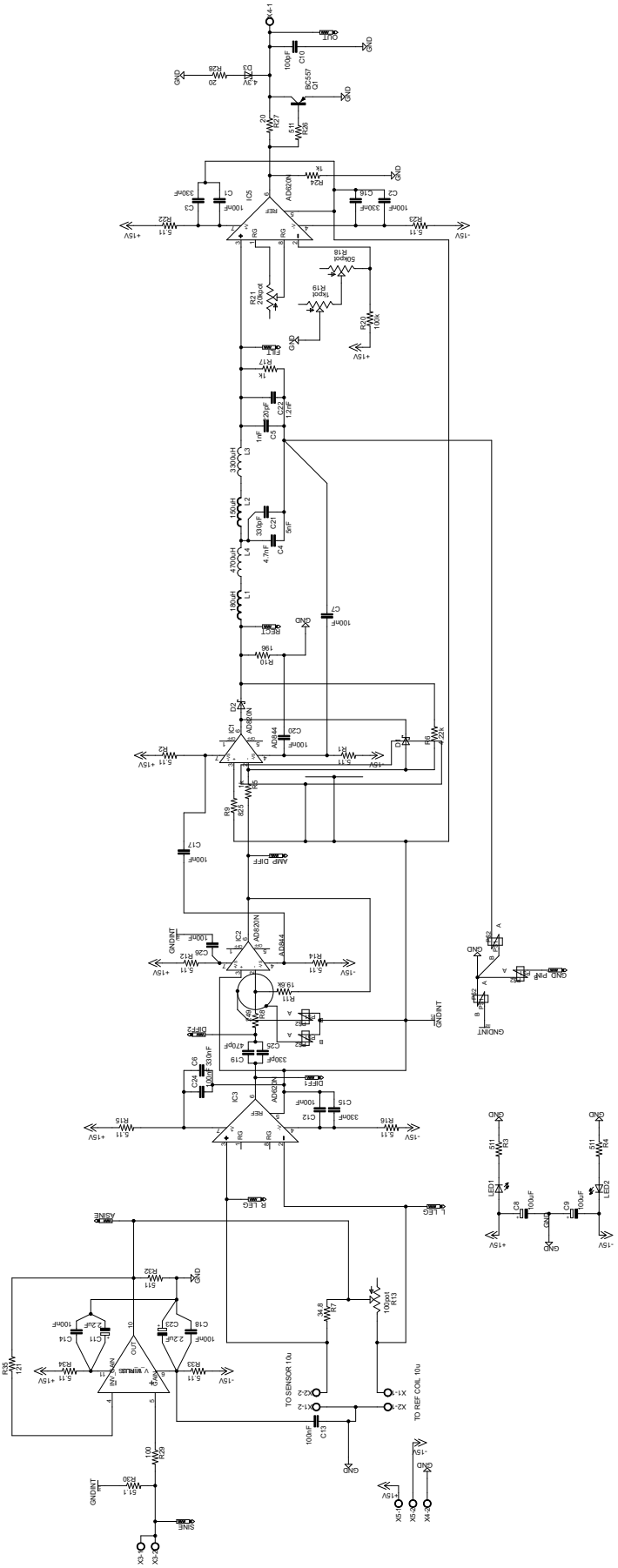

C.2 Data Acquisition

For data acquisition a USB powered $NI - DAQ6215$, has been utilized. This unit inter alia has 16 analog inputs in Referenced Single Ended (RSE) mode, and thus are able to handle the 15 channels of the setup. The unit only has one 16 bit ADC, and a multiplexer is thus implemented in the unit to switch between the channels. When sampling from one channel only, it is able to sample at a rate of 250.000 samples per second, but this speed must be distributed over the 15 channels. This introduces a time delay between each channel sample, that is ignored by the software by only logging one timestamp for 15 samples. In this application a sample frequency of $15kHz$ is chosen, and the time delay between the samples is in the range of microseconds, and thus also chosen to be ignored in this context. [National Instruments, 2009]

The wiring from the various sensors are wired with the shortest possible wires to the DSC, and then to the NI-DAQ via shielded cables, this is illustrated in Figure C.1.

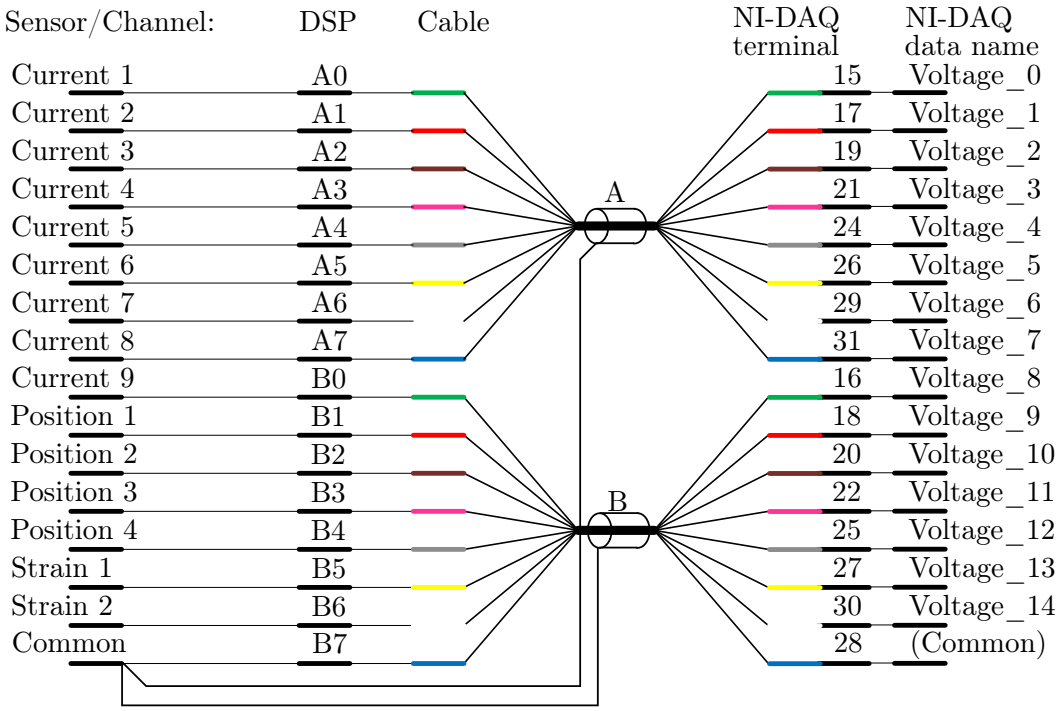

Figure C.1: *Wiring diagram from sensor channels to the NI-DAQ.*

C.3 Line Driver

To control the MOSFETs in each bridge, a driver board is build. The task is to connect the DSC control output to a transistor pair controlling the voltage of each coil. The PWM signal from the DSC is fed through a voltage follower, to ensure that no current is drawn from the DSC. Then the signal is fed to an optocoupler to ensure galvanic isolation between the DSC and the power circuits.

The voltage follower consists of two $10k\Omega$ resistances and a TLC274 Opamp. Since the Opamp has a very high input impedance, this circuit ensures that current is drawn from an external source, and not from the DSC. The voltage follower circuit is shown in Figure C.2. The TLC274 is a single-supply Opamp, supplied by the $+15V$ PSU.

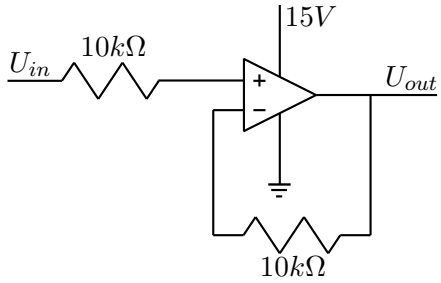

Figure C.2: *Voltage follower with external* $15V$ *supply.*

The amplified voltage is fed through a 90Ω resistor which limits the input current through the optocoupler to approximately $35mA$. The max rating of the optocoupler used in this circuit is $60mA$. The circuit of the line driver is shown in Figure C.3.

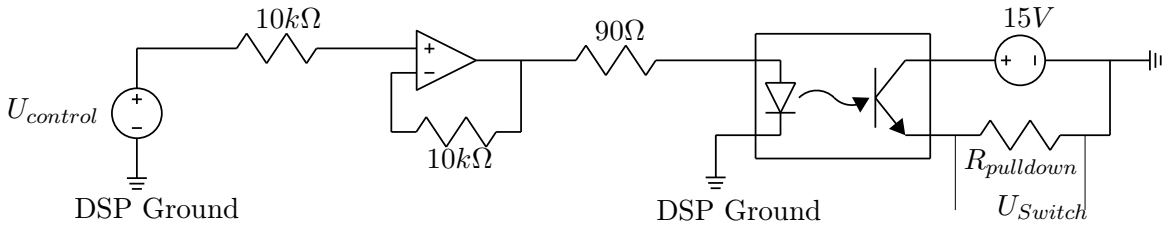

Figure C.3: *DSC-Driver circuit*

To ensure that there is no connection between the DSC and the power circuit, two different grounds are added. In the schematic the DSC ground is marked. A board with twelve channels is build. The schematic for this board can be found on attached CD.

Magnetic finite element model

D

In the program FEMM a finite element model is build to help verify the Simulink model. I addition to FEMM the MATLAB toolbox OctaveFEMM is used to control FEMM via a set of MATLAB functions.

The stator and coils are drawn as a 2D figure in SolidWorks and saved as a .DXF file, which can be imported by the OctaveFEMM functions. The rotor geometry is defined by functions in MATLAB to be able to control rotor diameter and rotor position.

Therefor the problem is set up as a 2D planar magnetostatic problem.

D.1 Model

In Figure D.1a the meshed model is shown, and in Figure D.1b the solution for the flux density solution for one excited coil is shown. The outer boundary is shown in both figures.

For both stator and rotor a linear material model is used, when fitting the RNM. The planar model is valid for both bearings and the actuator, where the only difference is the height. The SG measurements are performed on the actuator. Therefore the model height is set to $h_{actuator}$.

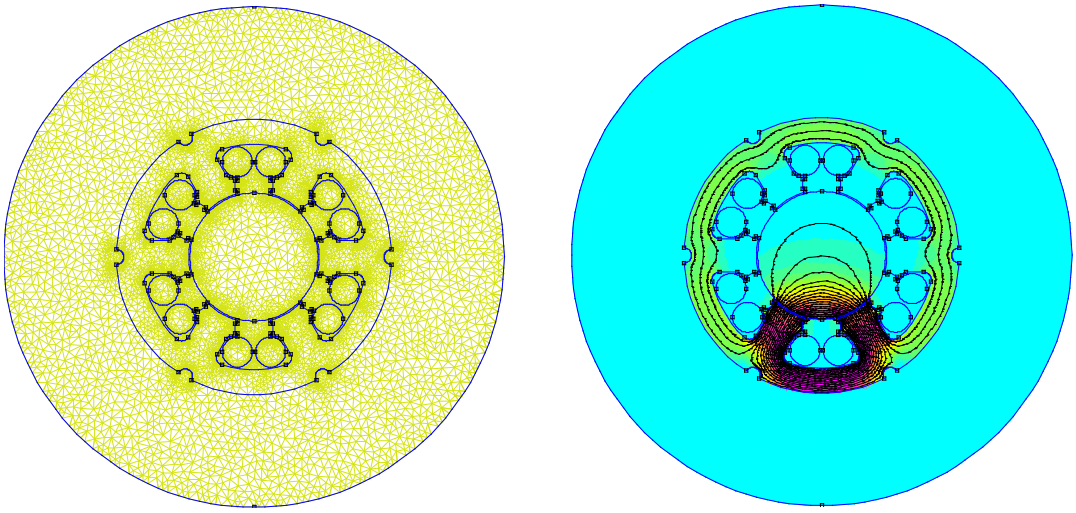

(a) *Mesh of FEMM model*

(b) *Flux density contour plot*

The specifications of the usage of FEMM is described in the next sections based on the User manual of FEMM [Meeker, 2010] and [Bargallo, 2006].

D.1.1 Governing equations

The model is solved as a magnetostatic problem, therefore the model field must satisfy Amperes law (D.1.1) and magnetic flux continuity (D.1.2).

$$\nabla \times H = J \tag{D.1.1}$$

$$\nabla \cdot B = 0 \tag{D.1.2}$$

It also has fulfill the constitutive relation between the flux density B and the field intensity H:

$$B = \mu(B) \cdot H \tag{D.1.3}$$

Where the permeability μ is dependent of the flux density, because most materials has a non-linear relationship between B and H.

The flux density is written in terms of a magnetic vector potential A:

$$B = \nabla \times A \tag{D.1.4}$$

Inserting this into the constitutive relation (D.1.3) yields:

$$\nabla \times A = \mu(B) \cdot H$$

$$\frac{1}{\mu(B)} \cdot (\nabla \times A) = H \tag{D.1.5}$$

This is substituted into Amperes law (D.1.1):

$$\nabla \times \left(\frac{1}{\mu(B)} \cdot (\nabla \times A) \right) = J \tag{D.1.6}$$

$$\frac{1}{\mu(B)} \cdot (\nabla \times \nabla \times A) = J \tag{D.1.7}$$

Using the vector identity:

$$\nabla \times \nabla \times A = \nabla \cdot (\nabla \cdot A) - \nabla^2 \cdot A \tag{D.1.8}$$

And assuming Coulomb gauge condition i.e ($\nabla \cdot A = 0$) yield:

$$-\frac{1}{\mu(B)} \cdot \nabla^2 \cdot A = J \tag{D.1.9}$$

Using the vector potential helps solving the problem i.e, the problem is solved simplified and can be solved for only the vector potential A. Then B and H can be calculated.

D.1.2 Boundary conditions

Due to the symmetric geometry it could be beneficial to use Neumann boundary conditions in the axis of symmetry. This could be applicable because the rotor is only moved in one direction in the model. Though because the geometry of the stator could be imported

directly from a .DXF file, and the computing time of the model is relatively low, this has not been used in the model.

For the magnetic finite element model it is necessary to define a boundary of the model domain outside the geometry, because the air around the geometry is able to conduct flux. In magnetic FEM it is therefore convenient to define an open boundary though by a finite model domain.

To specify the open boundary of this model an asymptotic boundary condition is used. The model domain is defined by a circle around the geometry, and then a mixed boundary condition is added on this boundary. That is by specifying the magnetic vector potential on this boundary.

Alternatively the outer boundary can be applied. Simply specifying the vector potential $A = 0$ on the boundary and using the rule of thumb that the outer boundary radius is five times the radius of the objects of interest [Meeker, 2010]. To decrease the solution time, the mesh near the boundary is set very coarse, relatively to the mesh in the region of interest.

D.1.3 Mesh

The discretion of the model is performed by first order triangular elements. The program is set to auto-mesh, where it refines the mesh near complex geometry. Also the minimum angle is specified to prevent problems when integrating over the element.

A better meshing approach would be to refine the mesh where the solution shows large gradients.

D.2 solving

The output of the model is the force exerted on the rotor by the magnetic field, and the inductance of the coils. To calculate the coil inductance the flux linkage is divided by the current squared. For coil 3 as analyzed in the model this is:

$$L_{33} = \frac{\int A_3 \cdot J_3 \mathrm{d}V}{i_3^2} \tag{D.2.1}$$

This can also be used to determine mutual inductances. To calculate the force on the rotor Maxwells stress tensor is used.

$$\mathrm{d}F = \tfrac{1}{2}\left(H \cdot (B \cdot n) + B \cdot (H \cdot n) - (H \cdot B) \cdot n\right) \tag{D.2.2}$$

Where n is the direction normal to the surface. Integration over the area of the rotor yields the total force acting on the surface. When using the stress tensor line integral a number of precautions has to be taken. If the mesh is made of first order triangular elements, the vector potential solution A will be described by linear functions, and solving for B and H yields constant values over each element. Therefore a problem can occur for areas where the field changes much. This would be avoided by refinement of the mesh. Therefore it is beneficial to have a fine mesh in the air gap.

Reluctance Circuit equations

E

In this section the circuit equations for the reluctance network model is described. Here the 36 linear independent equations are necessary to describe the system.

First the MMF drops in each branch is summed to zero. First five equations describing a loop though stator, pole and mutual leakage path are:

$$\begin{aligned} 0 = & \mathcal{R}_{pk} \cdot \Phi_{pk} + \mathcal{R}_{mlk} \cdot \Phi_{mlk} - \mathcal{R}_{p(k+1)} \cdot \Phi_{p(k+1)} - \mathcal{R}_{sk} \cdot \Phi_{sk} \\ & + \mathcal{F}_k - \mathcal{F}_{k+1} \quad ; \quad k = 1, 2...5 \end{aligned} \tag{E.0.1}$$

A loop through airgap, rotor, and mutual leakage path yields five equations:

$$0 = \mathcal{R}_{gk} \cdot \Phi_{gk} + \mathcal{R}_{rk} \cdot \Phi_{rk} - \mathcal{R}_{g(k+1)} \cdot \Phi_{g(k+1)} - \mathcal{R}_{mlk} \cdot \Phi_{mlk} \quad ; \quad k = 1, 2...5 \tag{E.0.2}$$

A loop through the leakage path, shown in Figure 5.7, yield six equations:

$$0 = \mathcal{R}_{pk} \cdot \Phi_{pk} + \mathcal{F}_k - \mathcal{R}_{slk} \cdot \Phi_{slk} \quad ; \quad k = 1, 2...6 \tag{E.0.3}$$

The MMF drop in the rotor must equal zero:

$$0 = \sum_{k=1}^{6} \mathcal{R}_{rk} \cdot \Phi_{rk} \tag{E.0.4}$$

The MMF drop in the stator loop must equal zero:

$$0 = \sum_{k=1}^{6} \mathcal{R}_{sk} \cdot \Phi_{sk} \tag{E.0.5}$$

And similarly the MMF drop in the leakage path must equal zero:

$$0 = \sum_{k=1}^{6} \mathcal{R}_{mlk} \cdot \Phi_{mlk} \tag{E.0.6}$$

Then, using that the flux into a node must sum to zero. First the five points connecting the stator-, the pole-, the self leakage path is described by five equations:

$$0 = \Phi_{sk} - \Phi_{p(k+1)} - \Phi_{sl(k+1)} - \Phi_{s(k+1)} \quad ; \quad k = 1, 2...5 \tag{E.0.7}$$

The nodes connecting the mutual leakage-, the pole-, the self leakage-, the air gap paths is described by five equations:

$$0 = \Phi_{mlk} + \Phi_{p(k+1)} + \Phi_{sl(k+1)} - \Phi_{g(k+1)} - \Phi_{ml(k+1)} \quad ; \quad k = 1, 2...5 \tag{E.0.8}$$

The nodes connecting the rotor- and the airgap path is described by the five equations:

$$0 = \Phi_{rk} + \Phi_{g(k+1)} - \Phi_{r(k+1)} \quad ; \quad k = 1, 2...5 \tag{E.0.9}$$

Using that the flux into the rotor must equal zero:

$$0 = \sum_{k=1}^{6} \Phi_{gk} \tag{E.0.10}$$

Using that the flux into the stator must equal zero:

$$0 = \sum_{k=1}^{6} \Phi_{pk} + \sum_{k=1}^{6} \Phi_{slk} \tag{E.0.11}$$

Experimental determination of model parameters

F

This chapter concerns the determination of model parameters of the magnetic bearing. In the following sections the results and computations of each test is presented.

F.1 DC test

The resistance of the coils are calculated, measuring the current and voltage across the coil. The measurements for each bearing are presented in the following.

	Coil 1	Coil 2	Coil 3	Coil 4	Coil 5	Coil 6
Measured voltage [V]	3.0582	3.0072	2.9417	2.9379	3.0897	2.9798
Measured current [A]	3.0689	3.0710	3.0751	3.0755	3.0719	3.0709
Calculated resistance [Ω]	0.9965	0.9792	0.9566	0.9553	1.0058	0.9703

Table F.1: *Results of DC test of bearing 1*

The average coil resistance in bearing 1 is 0.9773Ω

	Coil 1	Coil 2	Coil 3	Coil 4	Coil 5	Coil 6
Measured voltage [V]	3.8474	3.8942	3.7841	3.8485	3.8509	3.7536
Measured current [A]	3.0727	3.0596	3.0587	3.0698	3.0676	3.0677
Calculated resistance [Ω]	1.2522	1.2728	1.2372	1.2537	1.2554	1.2236

Table F.2: *Results of DC test of bearing 2*

The average coil resistance in bearing 2 is 1.2491Ω

	Coil 1	Coil 2	Coil 3	Coil 4	Coil 5	Coil 6
Measured voltage [V]	2.5743	2.5254	2.4868	2.5238	2.5021	2.5444
Measured current [A]	3.0709	3.0733	3.0700	3.0721	3.0686	3.0693
Calculated resistance [Ω]	0.8383	0.8217	0.8101	0.8215	0.8154	0.8290

Table F.3: *Results of DC test of actuator bearing*

The average coil resistance in the actuator bearing is 0.8227Ω

Optimization of model parameters

The model parameters in the reluctance network model is in several ways estimated with different degree of accuracy. Therefore an attempt to optimize the parameters of the reluctance network, to make the model fit measured data, is done. The reluctances in the model are calculated based on expected flux path lengths, and the self leakage- and the mutual leakage reluctances are estimated by a rough guess. Therefore it is convenient to optimize these parameters.

Therefore the parameters for the optimization algorithm is described by the vector:

$$\vec{x} = [\mathcal{R}_p \;\; \mathcal{R}_r \;\; \mathcal{R}_s \;\; \mathcal{R}_{ml} \;\; \mathcal{R}_{sl} \;\; \mathcal{R}_g]^T \tag{G.0.1}$$

Where the reluctances are set equal in each branch of the reluctance network because of the symmetric rotor. Furthermore to be able to adjust the airgap reluctance the $\mathcal{R}_g$ is also in the optimization, where it will be multiplied by a factor.

The starting point for the optimization is the values of the vector (G.0.1) calculated in section 5.3.2. Then the starting point is given by:

$$\vec{x}_0 = [\mathcal{R}_{pinitial} \;\; \mathcal{R}_{sinitial} \;\; \mathcal{R}_{rinitial} \;\; \mathcal{R}_{mlinitial} \;\; \mathcal{R}_{slinitial} \;\; \mathcal{R}_{ginitial}]^T \tag{G.0.2}$$

The optimization is performed by the function fmincon in MATLAB. On each parameter an upper and lower bound is defined. Each of the parameters is only allowed to change by a factor of 3. Also the parameters is scaled because of the large difference in reluctance.

The optimization is based on a least square of the relative error:

$$f = \sum_{i=1}^{n} \left(\frac{F_{model} - F_{FEMM}}{F_{model}} \right)^2 \tag{G.0.3}$$

Because of the factor of three, an algorithm that can handle this is chosen. $fmincon()$ implemented in MATLAB can handle constraints of various type, and a simple upper and lower bound is needed for this problem. $fmincon()$ internally features four different algorithms, that can be chosen depending on the problem. It is recommended to start with 'interior-point', where the solver can switch between a trust-region and a line-search method. The algorithm is second order and approximates the Hessian by a dense quasi-Newton approximation by default. This is also known as the Broyden-Fletcher-Goldfarb-Shanno method.

Feed forward H

When using a bias current to make linear control design possible, the magnetic force is highly dependent on position as well as current. As the axle moves closer to the bearing poles their respective attractive force increases and the axle is pulled towards the pole. This pull is compensated by the controller if the controller gain is sufficient. If not the axle "sticks" to one or several poles of the bearing and remains stationary. Dependency of the bearing position can be removed by making the bias current variable with position. This is achieved by using knowledge from the model to create a feed forward current that keeps the sum of forces near zero. This feed forward current is added to the control signal input to the current controller, working as along side the control signal, but only affected by position. The expression for bearing force is non-linear and difficult to manipulate into an analytical expression easily solved with respect to force, another approach using optimization and regression is therefore utilized. Using optimization with sum of forces as the object function and the coil currents as the variables a combination of currents, i_1, i_2 and i_3 that yields minimum force is found for various positions. Since several positions has an infinite number of currents that yield minimum force, e.g. in the centered position where the current can simply be lowered or raised. A linear constraint is needed to avoid this. The linear constraint limits the sum of currents (H.0.1). A sensible choice of sum is the sum of the bias current used earlier, assuring the current still operated around those values.

$$A = i_1 + i_2 + i_3 \tag{H.0.1}$$

Using the $fmincon()$ function in MATLAB, a short description of this function is found appendix G, the object function is minimized. The object function is shown in equation (H.0.2). The object function forces are found using the non-linear model from chapter 5. A lower bound of zero on each current is also applied.

$$f(i) = F_x(i)^2 + F_y(i)^2 \tag{H.0.2}$$

Figure H.1 shows the force plotted for different positions with a constant bias current. The force varies considerably with position and causes the problems mentioned earlier.

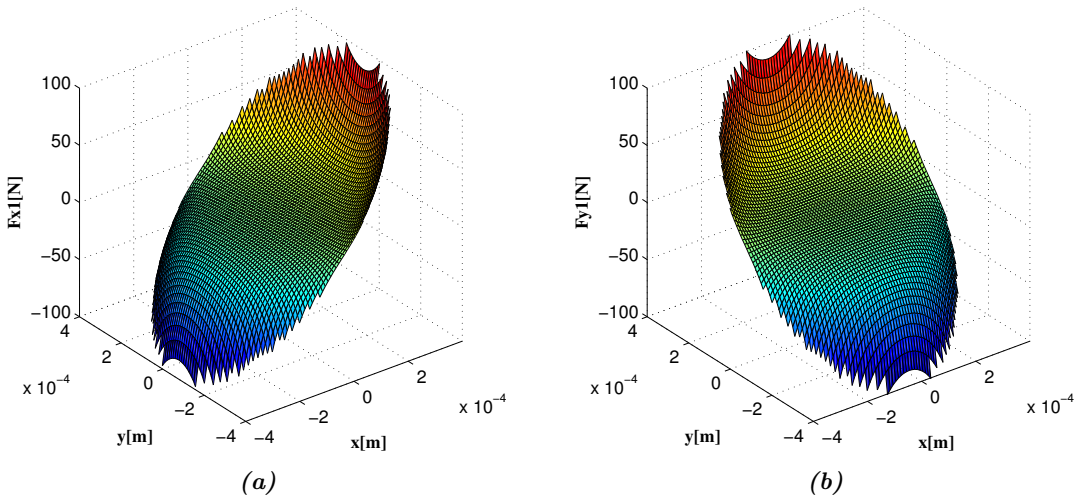

Figure H.1: *The bearing force in the x and y direction respectively, shown with regards to position. Without feed forward bias current.*

Figure H.2 shows the predicted force with the bias current enabled.

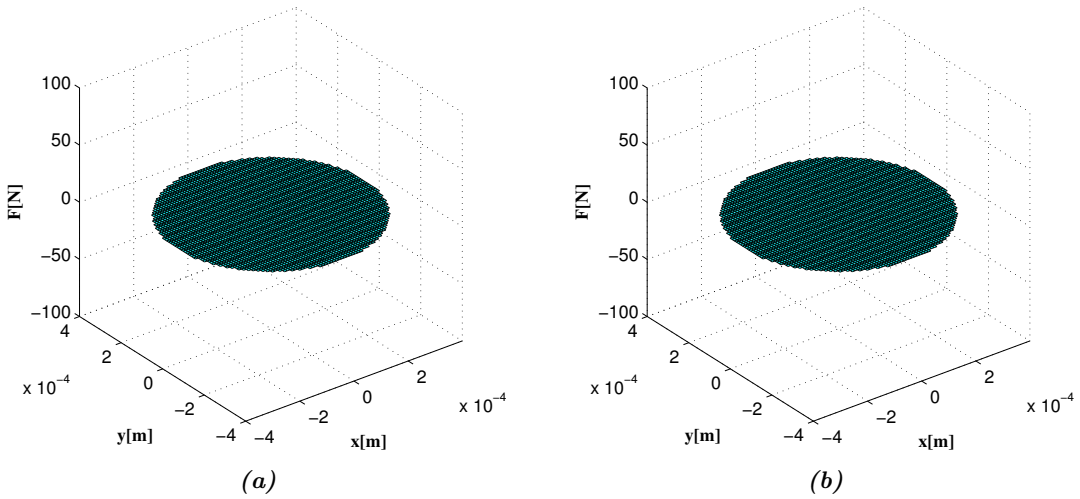

Figure H.2: *The bearing force in the x and y direction respectively, shown with regards to position. With feed forward bias current.*

Figure H.3 shows the position stiffness with feed forward enabled, provided that the model is accurate the position stiffness is now constant.

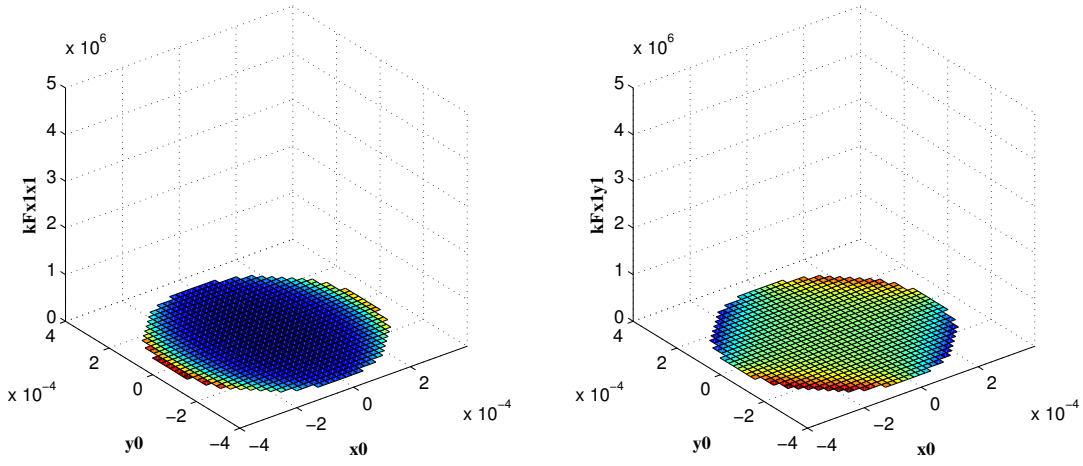

(a) *(b)*

Figure H.3: *Position stiffness with feed forward current.*

Figure H.4 and H.5 shows the current stiffness without and with feed forward enabled respectively. The change in current stiffness has also become smaller.

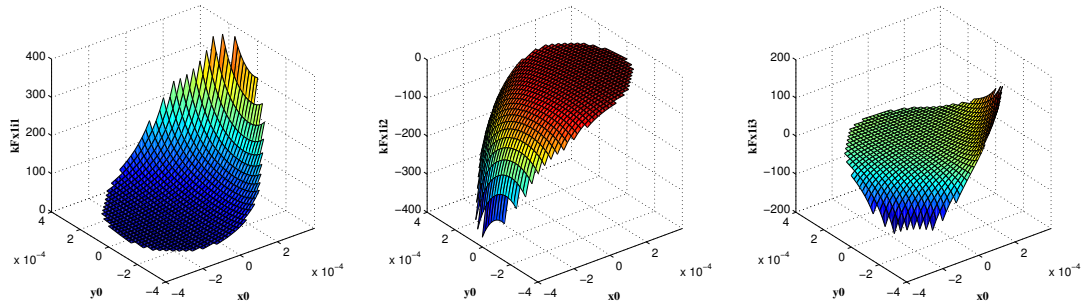

(a) *(b)* *(c)*

Figure H.4: *Current stiffness with constant bias current.*

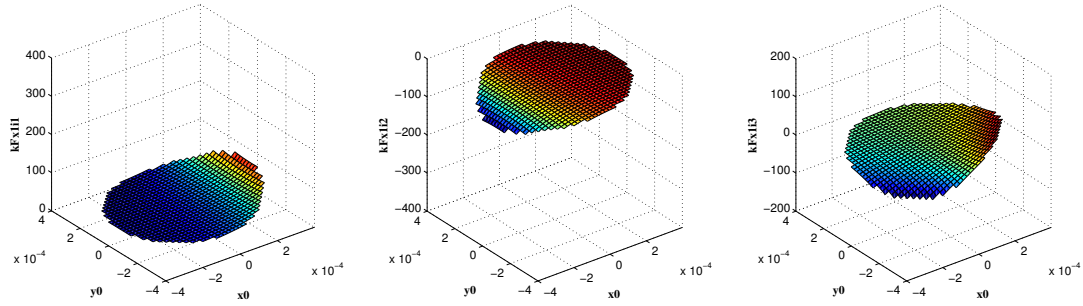

(a) *(b)* *(c)*

Figure H.5: *Current stiffness with feed forward bias current.*

The feed forward current is only shown available at discrete points in space. It is advantageous to approximate the feed forward current by polynomial regression of a surface to the points. This simplifies implementation of the feed forward on the DSC, because of its limited memory. Had the feed forward current dependence on position been

more complex a tabular implementation might have been advantageous with respect to speed of calculation. Since the position and current stiffness does not change when the axle is centered the performance of the controller is not significantly improved by use of a variable bias current. Thus the feed forward current is a start up scheme, making the bearing able to stabilize the axle wherever it is starting position is.